This is to certify that the
dissertation entitled

CHARACTERIZATION OF DEFORMATION IN Sn-Ag LEAD-FREE SOLDERS DURING THERMOMECHANICAL FATIGUE USING ORIENTATION IMAGING MICROSCOPY

presented by

ADWAIT U TELANG

has been accepted towards fulfillment
of the requirements for the

Doctoral degree in Materials Science Engineering

Thomas R Bieler
Major Professor's Signature

7 Dec 04
Date

CHARACTERIZATION OF DEFORMATION IN SN-AG LEAD-FREE SOLDERS DURING THERMOMECHANICAL FATIGUE USING ORIENTATION IMAGING MICROSCOPY

Volume I

By

ADWAIT U. TELANG

A DISSERTATION

Submitted to
Michigan State University
in partial fulfillment of the requirements
for the degree of

DOCTOR OF PHILOSOPHY

Department of Chemical Engineering and Materials Science

2004

ABSTRACT

CHARACTERIZATION OF DEFORMATION IN SN-AG LEAD-FREE SOLDERS DURING THERMOMECHANICAL FATIGUE USING ORIENTATION IMAGING MICROSCOPY

By

Adwait U. Telang

Eutectic Sn-Ag solder joints with copper substrate with different joint geometries were subjected to isothermal aging, creep at room and elevated temperature, and thermomechanical fatigue (TMF). Orientation Imaging Microscopy (OIM) studies reveal how the crystallographic orientations are correlated with microstructural features in the solder joints. Certain misorientations appear to be energetically favored during solidification, which have twin and Σ boundary type relationships. Changes in the crystallographic orientations, grain size and misorientation angles between grains, occurring due to subsequent heating and/or deformation were documented and analyzed. This study shows that the lead-free solder joints are multi-crystals, so that deformation is very heterogeneous and sensitive to crystal orientation, strain and the temperature history. High temperature processes caused polygonization of dislocations into low angle grain boundaries that slid. Special boundaries also show sliding, which adds to the deformation. Mechanisms that cause grain boundary sliding and pop-up are presented and discussed.

Dedicated to

My Mother, Grand Mother,

Priya and Aseem

ACKNOWLEDGMENTS

I would like to sincerely thank my advisor, Dr.T.R.Bieler whose constant support and guidance provided the driving force for this research project. I have enjoyed the discussions we have had and learnt a great deal from him. His excellent tutelage during the course of my Ph.D. dissertation has allowed me to flex my thinking and has been a rewarding experience during the course of my graduate studies, for which I am extremely grateful.

I would also like to thank my committee members Dr.J.P.Lucas for his support and allowing me to use his laboratory facilities, Dr.K.N.Subramanian for his positive criticisms, Dr.P.Duxbury for his insights, and Dr.C.N.Tomé for his invaluable suggestions and support.

Finally, my deepest gratitude to my family who has always stood by me, providing me the much needed perspective, faith and the inspiration to keep going. I would like to thank my mother for supporting me in all my endeavors and instilling her strength in me, my grand mother for showing me by example that anything is possible if the will power exists, my brother Aseem for his positive outlook towards life and the courage to fight, and my wife Priya for understanding me and giving me the much needed support to pursue my dreams and help me strive for the best.

TABLE OF CONTENTS

LIST OF TABLES

LIST OF FIGURES

Images in this thesis are presented in color

CHAPTER 1

INTRODUCTION

The following is a study to examine the deformation behavior of Sn-3.5wt.%Ag lead-free solders using Orientation Imaging Microscopy (OIM), primarily in thermomechanical fatigue (TMF) as experienced by solders in service. The introduction and rationale for this study is presented along with relevant background, followed by the specific aims, experimental procedures, results and discussion.

1.1 RATIONALE

Soldering is as an integral part of the electronic assembly because it connects devices to printed circuit boards (PCB). Lead-based solder (esp. Pb-Sn) has been used for several decades as the interconnect material [1]. However, the toxicity of lead, environmental concerns and international trade restrictions have warranted its eradication from all electronic systems by 2006 [1-5]. Consequently, eutectic tin-silver (96.5Sn-3.5wt.%Ag) based solders have gained particular interest in recent years due to their comparable wetting and mechanical properties to 37Pb-63wt.%Sn solders [1, 3, 6, 7]. There is sufficient data on mechanical properties, microstructural details and deformation behavior of lead-based solders, however relatively less is known about tin-based solders. Therefore the selection of the appropriate solder alloys to replace Sn-Pb solders is still in the embryonic stages because deformation characteristics and failure modes for eutectic Sn-Ag have not been fully characterized. Further, several processes could simultaneously occur during service and contribute to damage accumulation that leads to failure, which implies that, certain solders appropriate for one application might not be

applicable for others. Hence there is need to further investigate Sn-based solders to determine the cause of failure and qualify their usefulness as good interconnects.

About 70% of failures in most electronic circuitry is related to the failure of the solder interconnect. With miniaturization in electronic packaging and the concurrent reduction of the joint dimensions, solder joints serve dual purposes; as electrical connections and mechanical supports for surface mount components. The smaller electronic packaging imposes additional constraints on the solder. The temperatures experienced by solder interconnects ranges from -40°C to 150°C on a printed circuit board (PCB) in an automotive under-the-hood type of application and can reach up to 85°C in household electronics like computers due to Joule heating experienced during service [8]. These temperatures are above $0.5T_m$ (T_m of tin = 232°C) where creep and aging is expedited and the microstructure evolves continuously [9]. This necessitates better inherent properties in the solder material to prevent failure in service.

In solder alloys, there is a strong correlation between the microstructure and mechanical properties [2, 10, 11]. The microstructure of solder joints made with Sn-3.5wt.%Ag solders has a small volume fraction of sub-micron size hard Ag_3Sn intermetallic particles interspersed in the eutectic matrix. Compared to pure metal these particles provide particle strengthening, as a result of dislocation interactions during stress application, thermal cycling, and microstructural evolution. These intermetallic particles are also known to coarsen with time and temperature [12], and affect grain boundary mobility; models for grain growth limited by Zener drag of particles that grow by Ostwald Ripening have been developed for particle strengthened high temperature deformation [12-17]. Joint reliability has been found to depend on factors such as

temperature to which the joint is exposed and temperature fluctuations that it experiences [18], the dwell period at a particular temperature [18], the stresses experienced by the joint due to the thermal expansion mismatch between the substrate, solder and the component, the extent of the external load imposed and the inherent anisotropy of tin.

Extensive prior characterization of this Sn-3.5wt.% Ag solder using single shear lap joint specimens [19, 20] identified changes in properties after creep, stress-relaxation, reversed-shear and thermomechanical fatigue (TMF). These changes were correlated with the **heterogeneous grain boundary sliding and surface relief** that developed in the microstructure [21-30]. Grain boundary sliding is important for superplastic deformation phenomena, which occurs in a limited range of strain rate/temperature conditions. Thus the wide range of strain rates and temperatures encountered by solder joints implies that grain boundary sliding will more likely cause damage rather than plastic deformation. As important as deformation of the tin phase is to solder joints, the vast majority of research on the microstructure of solder joints has focused on intermetallics and not on the tin phase with only a few exceptions, e.g. Ref. [31, 32].

Although deformation in tin has been studied for many decades, the information available on deformation mechanisms in tin is not complete. There are 7 slip system families of interest and taken together they provide 26 slip systems (not counting at least one twinning system family, which is not considered in this study because twinning is most likely at low temperatures/high strain rates, which are not relevant to solder joints in electronic applications). The critical resolved shear stresses and hardening behavior have been partially characterized [33-35]. Some of the more recent studies have shown that

slip is quite complex with the hardening behavior depending on the pre-existing populations of dislocations and their type [36].

Characterization of microstructural evolution in Sn-Ag solder alloys is challenging, since the grain size is difficult to identify in the solidification microstructures of the eutectic Sn-Ag matrix. SEM imaging is fruitful only to the extent of giving topographical information (using secondary electrons) revealing surface damage. However since grain boundary sliding has been the obvious deformation mechanism it is important to characterize misorientations between grains and the grain boundary character along which sliding has occurred. **Since failure of solder joints occurs by deformation and fracture in *tin*, it is necessary to understand the role of crystal orientation and misorientation across grain boundaries that slide, as well as the role of slip and recovery processes occurring in the joint, before failure processes can be characterized, in order to develop the foundation on which physically based deformation models can be developed.** Hence, there is a need to identify a suitable methodology for measuring microstructural evolution in Sn-Ag solders, and characterizing the interaction between the stress and the microstructural evolution, following which modeling strategies can be developed to predict the reliability of lead-free solders.

Due to a strong correlation between the microstructure, properties and the crystallographic orientations that go with the microstructure, it is known that crystallographic orientations can affect fracture behavior and mechanics, corrosion resistance, precipitation and recrystallization [2, 10, 11]. Macrotexture studies on metals have been carried out for decades using X-rays and the technique has allowed theories to

be developed that describe how preferred crystallographic arrangement in the material evolves during service conditions [37-43]. Orientation Imaging Microscopy (OIM) using automated Electron Backscattered Diffraction Pattern (EBSP) indexing is a valuable measurement tool in the texture arena, and provides an ideal method to investigate the microstructure evolution phenomena. With this technique, crystallographic orientation and shape of the grains and their misorientations with each other (collectively called mesotexture) can be simultaneously measured. Thus the phenomenon of microstructural evolution resulting from processes such as solidification, recrystallization and grain growth can be tracked.

The following sections will develop the theoretical background for the current investigation followed by the rationale behind the research, the experiments carried out, results obtained, followed by the discussion and conclusions.

1.2. BACKGROUND AND SIGNIFICANCE

A) Thermal and Mechanical Processes Experienced by a Solder Joint:

(1) Aging: Aging is inevitable with time in such solders where room temperature is greater than half the absolute melting temperature, and this results in the alteration of the microstructure. However, the rate of aging is dependent on the temperature to which the solder joint is exposed during service. Higher temperatures naturally cause faster evolution of the microstructure. Solder joints in typical automotive under-the-hood service conditions are exposed to temperatures of around 150°C, while those in computer related applications experience temperatures of 50-80°C. Such high temperatures cause

dynamic recrystallization and grain growth to occur within the solder microstructure in Pb-Sn solders [44-48]. The constant evolution of the microstructure alters the properties of the solder joint and changes the way the solder material would otherwise respond to further deformation processes.

In eutectic Sn-Ag solder joints aging produces coarsening of the Ag_3Sn particles in the solder matrix [23]. The intermetallic layers of Cu_6Sn_5 and Cu_3Sn also grow in thickness, from approximately 0.7μm initially to about 10μm after aging at 150°C for 1000 hours [23]. The intermetallic compound grows faster in liquid solder. Jang et. al. observed a 2μm thick Cu_6Sn_5 layer after a 60 seconds reflow of a eutectic Sn-Ag solder at 250°C, with no intermetallic present initially [49].

The material in the joint configuration can undergo two basic types of stress / strain history: 1) time dependent monotonic loading e.g. tensile loading, shear loading, creep and stress relaxation, and 2) cyclic deformation as in fatigue [49]. However, due to the low melting temperatures of these solders, during thermomechanical fatigue, a combination of all deformation modes listed above in 1) occur in a cyclic manner.

(2) Creep: Creep is the progressive deformation that a material experiences under constant stress at an elevated temperature, usually greater than half the absolute melting temperature. It is known that material strength decreases with rise in temperature, due to a corresponding influence of diffusion processes that come into play at elevated temperatures. Higher temperatures also give additional mobility to dislocations that can climb as well as additional slip-systems can come into play [50]. For materials being

used at elevated temperatures, the strength of the material depends on the strain rate and the amount of deformation with time that the material has undergone.

The creep experiment involves loading a tensile specimen at a constant temperature ($>0.5T_m$) and at a constant load. The strain / extension of the material is measured as a function of time. Hence studies based on creep experiments can take several hours to years to achieve the desired information. A typical creep curve is shown in Figure 1.1. The curve can be ideally divided into three regions; primary, secondary and tertiary creep. The creep rate given by $d\varepsilon/dt$, decreases rapidly with time initially during primary creep and is approximately constant in the secondary creep region. The initiation of tertiary creep is an important point on the creep curve since after this point the creep rate increases steadily until the specimen ultimately fractures. A long secondary creep period or a very low minimal creep rate is essential for longer service life of the specimen.

The creep curves are explained using the diffusional creep theories or the dislocation based creep theories [51]. Both theories are able to explain many of the strain and strain rate features one sees in a typical creep curve. The diffusion-based theory is explained by the diffusion of atoms through the bulk, grain boundaries or interfaces to sinks in the material, which depends on the activation energy for the process of diffusion (volume, grain boundary and surface). At high temperatures bulk diffusion or lattice diffusion is more active and also has higher activation energy, whereas at lower temperatures ($0.4T_m$) other preferential paths of diffusion (short circuits in the diffusion path), such as grain boundary diffusion or diffusion along dislocation cores, becomes more predominant.

Dislocation creep theories are based on creation and annihilation of dislocations and their subsequent re-arrangement in the material into a substructure. These theories consider the balance between work hardening and recovery phenomena to explain changes in the typical creep curve. Primary creep involves the increase in the number of dislocations, which get tangled up and hence harden the material (causing a decrease in the strain rate). Two types of primary creep curves are observed in alloys; normal transients are seen in class M (pure metals or alloys where the n value (n is the stress exponent) does not change with increasing the amount of the alloying element, and inverse (abnormal) transients are seen where the value of n decreases with increasing alloy content, which is accompanied by a decrease in the creep rate. The decrease in the value of n is associated with the solute atoms forming a cloud around the dislocations cores, which now have to drag the solute cloud to achieve the same strain. Hence the creep rate is governed by the dislocation density and their average velocity [51]. During secondary creep, the overall stress and strain rate remain constant when the rate of hardening is balanced by the rate of recovery. Dislocations rearrange themselves in to substructures. The creation and movement of dislocations leads to work hardening, whereas their climb and cross slip permits recovery by annihilation or re-arrangement into low energy substructures. In tertiary creep, instability is reached, where cavities or microcracks are formed (due to dislocation pile-ups or local tensile regions where vacancies condense. Formation of microcracks or cavities further increase local high stress concentrations and decrease the load carrying capacity of the material. The strain rate increases rapidly with stress, which ultimately leads to the failure of the material.

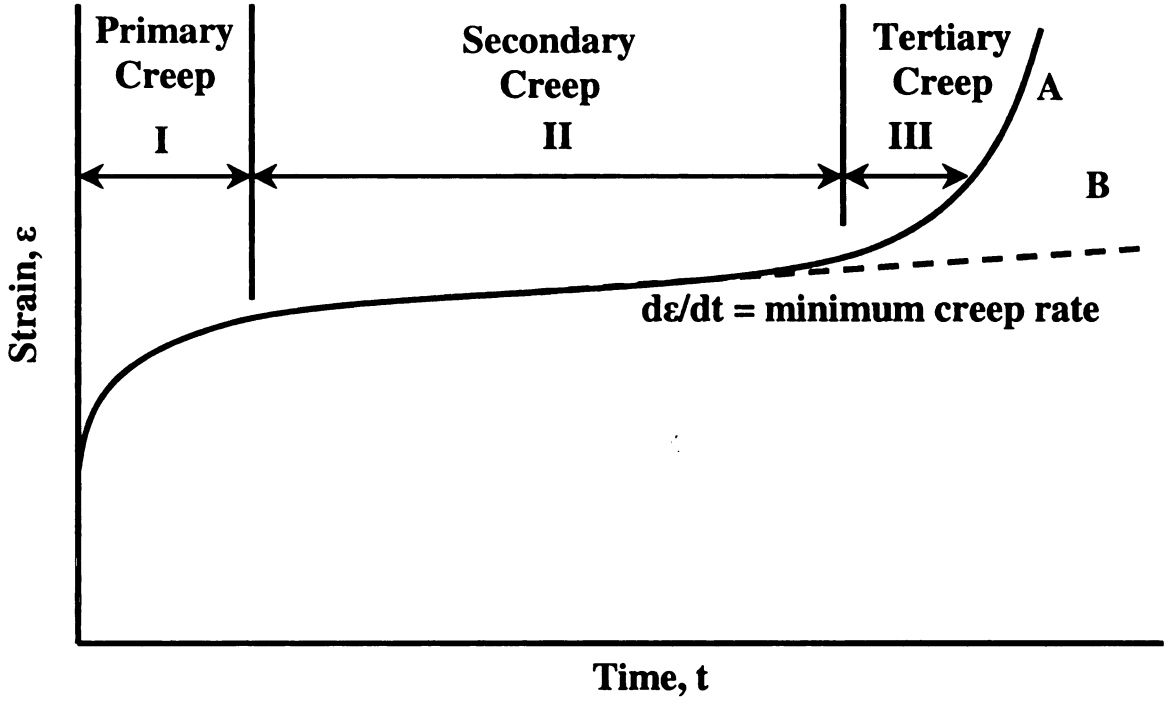

Figure 1.1. Typical creep curve showing the three stages of creep. Curve A is constant-load test; curve B, constant-stress test[50].

A quasi-empirical relationship developed by Mukherjee, Bird and Dorn [52] is commonly used to describe the secondary creep deformation [52, 53] and is given by: $\dot{\varepsilon} = \frac{AGb}{RT}\left(\frac{\tau}{G}\right)^n \left(\frac{b}{d}\right)^p D_0 \exp\left(\frac{-Q}{RT}\right)$ where, where $\dot{\varepsilon}$ is the steady state strain rate, G is the shear modulus, $\boldsymbol{b}$ is the Burger's vector, R is the gas constant, T is the absolute temperature, d is the grain size, τ is the applied stress, D_0 is a frequency factor, Q is the activation energy for the deformation process, n is the stress exponent (n=1 diffusional creep, n=2 grain boundary sliding, n=3-4 dislocation glide or drag by solute atoms, n=5-7 diffusional climb of dislocations around barriers, n>7 creep of dispersion strengthened alloys, with a threshold stress term which could cause the higher stress exponent in several cases), p is the grain size exponent, and A is a constant characteristic of the underlying micromechanism (that depends on the microstructure and the rate limiting deformation mechanism). Most metals and metal alloys have several strain rate regimes where one or the other deformation process could occur depending on the stress and temperatures imposed. Transition points are often observed in logarithmic plots of $\dot{\varepsilon}$ versus σ for materials that deform, with mechanisms that depend on several sequential deformation processes, such as glide and climb; the deformation mechanism that has slowest strain rate will control the flow behavior. When there are multiple independent processes occurring, such as different rates of deformation in different phases, the faster process will dominate the creep deformation.

Tensile tests are commonly used to find the total strain to failure in solder joints. However the recovery processes occurring during creep are not captured in a normal tensile test (unless they are done at a very slow strain rate). Data can be collected at

different temperatures to determine conditions where recovery occurs. Stress relaxation that occurs at the end of tensile tests is a useful way to characterize recovery that occurs after straining. Figure 1.2 shows stress strain curves obtained for Sn-3.5Ag solder joints at room temperature and 150°C. At high strain rate and low temperature, work hardening occurs due to the lack of time for recovery, while at low rate and high temperature, recovery more rapidly than dislocation accumulation that causes work hardening. Extensive softening in these curves implies recovery, recrystallization, and/or damage, but in what proportion, is not yet understood. At higher rates and lower temperature where recovery contributes less than plastic deformation processes to the total strain, more uniform strains are possible.

(3) Thermomechanical Fatigue (TMF):

Fatigue is experienced by a material which is subjected to repeated fluctuating stress states, from which it can fail at a stress significantly lower than that required to cause failure in a single application of load [50]. Figure 1.3 shows examples of several types of fatigue cycles. Figure 1.3(a) shows a sinusoidal curve with complete reversal of stresses. Figure 1.3(b) shows repeated reversals in stress, however the stress state never changes sign and is always on the tensile side in this particular case. Figure 1.3(c) shows a random fatigue cycle and Figure 1.3(d) shows cyclic deformation with hold times. The stress state for solder interconnects is very complex. Depending on the geometry and initial stress state during fabrication, one or a combination of all of the above mentioned fatigue processes can occur in the joint.

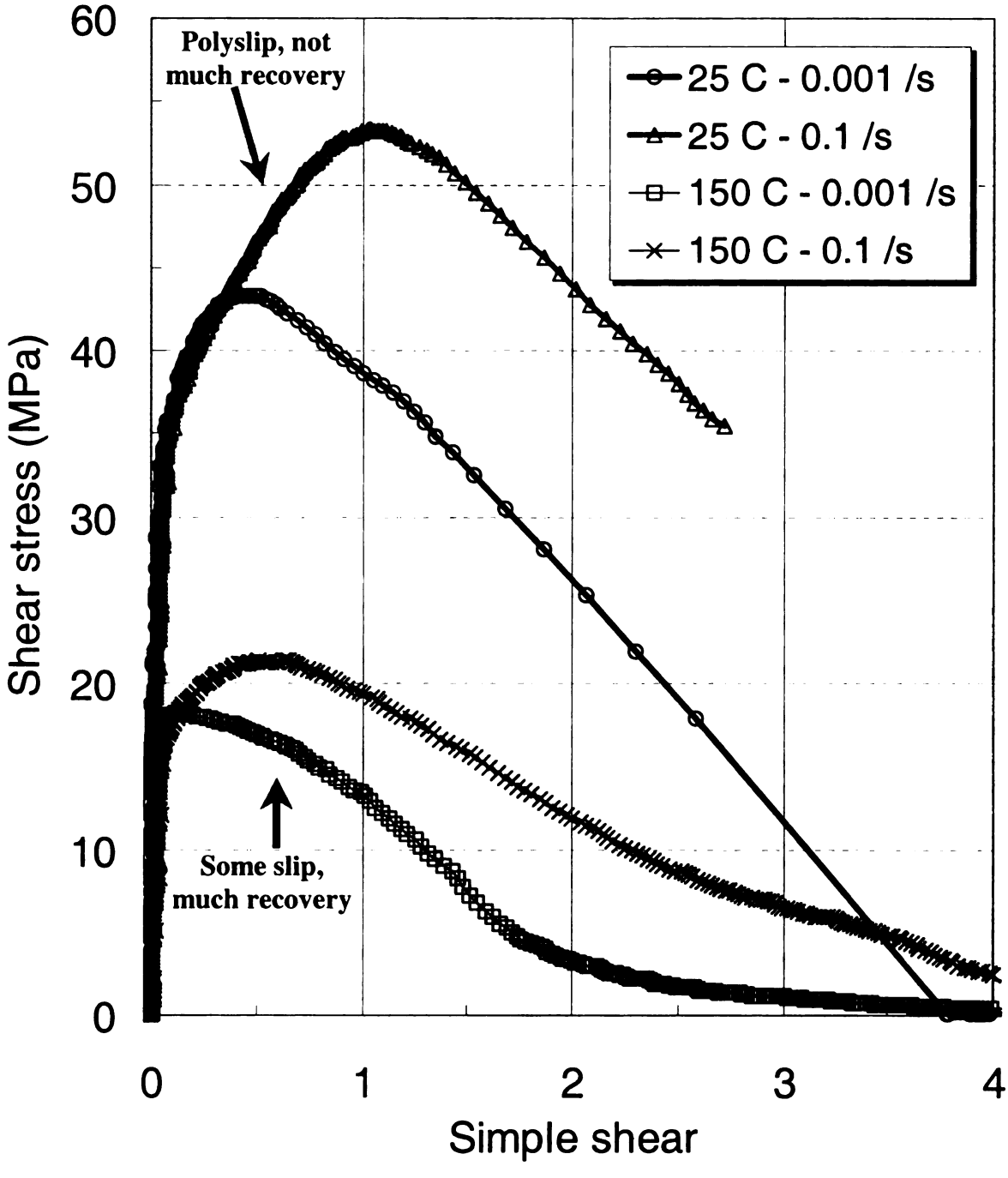

Figure 1.2. Shear stress versus simple shear for single shear lap solder joint obtained from Ref.[54].

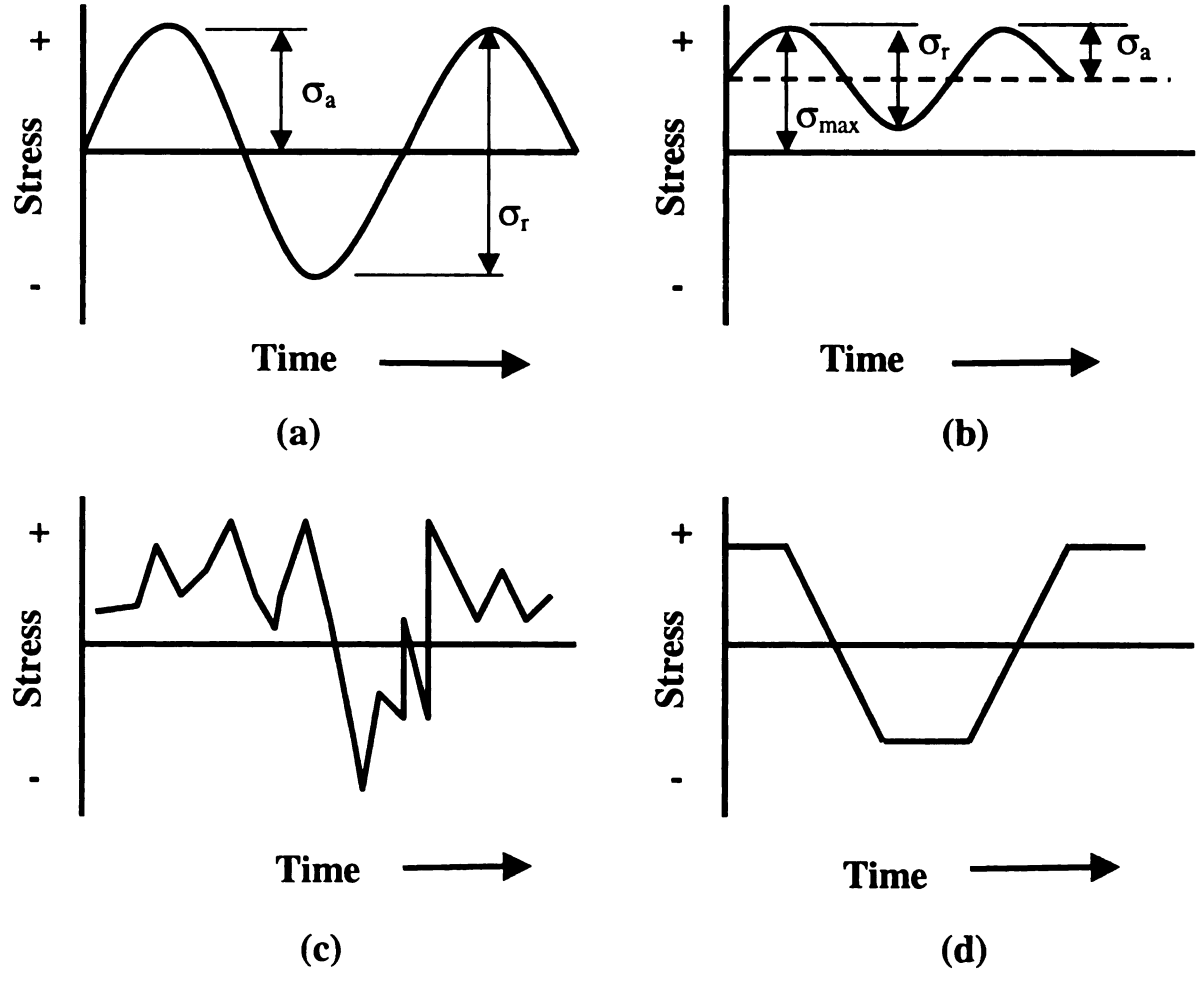

Figure 1.3. Examples of fatigue stress cycles. (a) Repeated reversed sinusoidal stress curve with complete reversal of stresses, (b) repeated stress reversals with same positive (tensile) stress state, (c) random fatigue cycle and (d) cyclic deformation with hold times.

The Coffin-Manson equation is given by $N_f = C_3 \Delta\varepsilon^k$, where N_f is number of cycles to failure, C_3 and k are constants and $\Delta\varepsilon$ is the plastic strain range. When the law is used for low melting temperature solder alloys, fatigue cracking is not only dependent on the cumulative plastic strain, but is related to the equivalent strain amplitude and changes in the properties that occur as a function of time and temperature. The fracture process is not only dependent on the fatigue strain undergone by the joint but also on creep at such temperatures [55]. Harada and Satoh [55] developed an empirical equation to estimate the thermal fatigue life of 96.5Sn-3.5Ag solder. Their equation gives a modeling approach to crack growth as a result of fatigue. It does not attempt to model crack nucleation, which is a more critical phenomenon with reference to solder interconnects [56, 57]. The equation is given by $N_f = C \ln\left(\frac{(A_{af} + B)}{B}\right) f^m . \exp(Q/kT_{\max}) \Delta\varepsilon_{eq\max}^{-n}$ where, N_f = thermal fatigue life, $\Delta\varepsilon_{eq\max}$ = maximum equivalent strain range, Q = activation energy, T_{max} = maximum temperature, f = frequency of temperature cycle, k = Boltzmann's constant, A = 5.87, B = 1.40 x 10^3, C = 0.234, n = 1.2, and m = 0.33.

The fatigue strength of a material usually increases with a decrease in temperature. At higher temperatures, transition from fatigue failure to creep can occur and transcrystalline fatigue failure may change to intercrystalline creep failure [50]. In general, a material with high temperature creep strength will have better fatigue properties at high temperatures [50]. A fine grain size gives better fatigue properties at lower temperature since the length of the dislocation pile-ups in small grains is smaller giving rise to a smaller localized stress concentration, which might not exceed the

theoretical shear stress. In larger grain materials, the opposite is true and higher stresses can cause a locally enhanced state of stress, which can give rise to micro cracks. As the temperature increases, the differences in fatigue properties of coarse and fine grain sized materials are reduced until high temperatures are reached. At high temperatures creep dominates and hence a large grain size is preferred for creep resistance.

The stresses produced during fatigue need not only be mechanically induced. Fluctuating thermal stresses induced by differential heating and cooling and due to differences in the coefficient of thermal expansion (CTE) in the material can lead to stress accumulation, which leads to failure of the material. Repeated application of cyclic thermal stresses of low magnitude that leads to failure is called thermomechanical fatigue. A simple equation showing the stress developed in a constrained material cycled between two different temperature extremes is given by: $\sigma = \alpha E \Delta T$, where σ = stress developed in the material, α = coefficient of thermal expansion, E = elastic modulus, and ΔT = change in temperature.

Fatigue failure usually can be divided into four different regimes [50]: 1) Crack initiation that includes the development of fatigue damage early in the life of the solder joint. However this can be removed by a proper annealing treatment. 2) Slip band crack growth, which includes growth of the initial cracks and this, occurs on planes of high shear stresses (Stage I crack growth). 3) Crack growth on planes of high tensile stress, which involves crack growth in direction perpendicular to the maximum tensile stress. 4) Ultimate ductile failure wherein the crack length is long enough such that the component has lost its load bearing capacity. However, in most cases fatigue failure is seen to initiate from the free surface of the specimen. Gough [58] has shown that in fatigue, slip

lines are seen in certain grains and not in others. More damage occurs with further cycling and cracks are seen to occur in regions of heavy deformation. Wood [59] developed the concept of intrusion and extrusion of slip bands which leads to formation of notches and regions of high stress concentration which act as stress raisers with notch roots of atomic dimensions. This could initiate a fatigue crack which then propagates through the specimen.

The life prediction of a solder joint is dependent on the susceptibility of a solder joint to TMF. TMF in a solder joint can occur due to the cyclic changes in the temperature experienced by the joint. Also the various constituents in the electronic assembly play an important role during such temperature fluctuations, since different constituents have different CTE. The plastic strain accumulation is thus a function of the total change in the temperature, the rate and the magnitude at which this change occurs and the inherent constraints in the electronic assembly and its interaction with the time dependent and cyclic deformation processes occurring in the solder alloy [60]. A constitutive equation taking into account these several processes is needed and a model for this needs to be developed. In his PhD dissertation, Lee has taken a closer look at some of these effects [18].

B) Eutectic Sn-3.5Ag Solder

(1) Crystal Structure and Directional Properties:

Eutectic Sn-Ag solder (96.5%Sn-3.5%Ag in wt.%) consists of two phases, the β-Sn and the Ag_3Sn intermetallic phase. The β-Sn has a squashed Body-Centered Tetragonal (BCT) unit cell with a=b=5.8197 Å, c=3.175 Å [61], with c/a = 0.5456. The four atoms occupy positions 0 0 0, 0 ½ ¼, ½ 0 ¾, ½ ½ ½ in the unit cell as shown in Figure 1.4 [61].

The four directions in the Sn unit cell with the highest linear atomic density are as follows [62]: [001], [111], [100] and [101] (linear densities of these planes are 0.95, 0.69, 0.52 and 0.46 respectively) and the four planes with highest planer density are [62]: (100), (110), (101) and (121), with densities of 0.775, 0.548, 0.742, and 0.127 respectively. At different temperatures the relative activity of slip systems differs, as indicated in Table I. Twin formation is seen frequently in tin and Table I also shows the possible twinning plane and direction for tin. Twins have low energies associated with their coherent boundaries and if a twin is formed during solidification, internal strains at its boundaries are so small or absent that recrystallization is not promoted in these locations [63, 64].

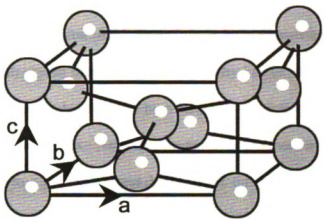

Figure 1.4. β-Sn unit cell (lattice parameters, a=b= 5.8197 Å and c=3.175 Å [61]).

Table I. Possible Slip And Twin Systems In β-Sn.

Glide / Slip Systems					Twinning Systems	
	Low Temp. (~20°C)		High Temp. (~150°C)			
Slip Plane	**Slip Direction**	**Critical Stress, kg/mm^2 ***	**Slip Plane [62, 64]**	**Slip Direction**	**Plane [63]**	**Direction [63]**
(100)	[001]	0.19	(110)	[-111]	(301)	[-301] 62°@[010]
(110)	**[001]**	**0.13**			(101)	[10-1] 59°@[010]
(101)	[10-1]	0.16				
(121)	[10-1]	0.17				

* Critical stress in kg/mm^2 at 20°C and 0.01% impurity.
All data can be found in Ref.[33], except the ones specially marked.

The Young's Modulus in the a-direction is 54 GPa and in the c-direction is 85 GPa as shown in Table II [65]. The CTE for tin in the a-direction is 15.45 x 10^{-6} /°C and 30.5 x 10^{-6} /°C in the c-direction [65]. Hence, tin is highly anisotropic and the value of modulus changes with crystal direction as calculated by Lee et. al. [66]. The anisotropy of tin in the solder joint can lead to very high stress accumulation, which can contribute to the failure of the solder joint. Note that tin expands the most in the direction that is stiffest which leads to significant stress build-up in the adjacent grains that leads to plastic deformation to accommodate the shape change.

The Ag_3Sn has an orthorhombic structure with a=5.968 Å, b=4.7802 Å, c=5.1843 Å [67]. The Ag_3Sn undergoes a transformation at about 60°C [67]. However the nature of this transformation is unknown and X-ray studies have shown that there is no lattice change [68].

Table II. Constants For Various Solder Joint Constituents [65].

	Cu (Polycrystal)	**Sn** (Single crystal)		**Cu_6Sn_5** (Polycrystal)	**Cu_3Sn** (Polycrystal)
		a-dir.	**c-dir.**		
Young's Modulus, GPa	117	85	54	85.56	108.3
Shear Modulus, GPa	--	--		50.21	42.41
Hardness, GPa	2.94	0.98		3.71	
Thermal Expansion, x 10^{-6}/°C	17.1	15.4	30.5	16.3	19.0
Thermal Diffusivity, cm^2/sec	--	--		0.145	0.24
Resistivity, μΩ-cm	1.7	11.5		17.5	8.93
Density, g/cc	8.9	7.3		8.28	8.9

(2) Solidification and Microstructure Of Eutectic Tin-Silver:

The eutectic Sn-3.5Ag solder can have various microstructures depending on the cooling rate. Figure 1.5 shows a part of the Sn-Ag binary phase diagram. Line A-B is the eutectic composition. At 250-280°C the silver dissolves in the liquid Sn phase. Equilibrium cooling along A-B will lead to formation of a eutectic microstructure with the Ag_3Sn precipitates embedded in the Sn matrix as shown in Figure 1.6 (regions interspersed between tin cells). However, the mix is usually not in equilibrium and hence in usual practices, considerable under cooling (as much as 20-50°C depending on the cooling rate [69]) is required to initiate solidification. Due to such a high amount of under cooling, the primary tin nuclei grow very rapidly to form dendrites and sometimes, secondary dendrite arms. As the dendrites thicken, they reject the Ag solute into the remaining liquid, which eventually solidifies with a hyper-eutectic composition surrounding the tin cells. Solid solubility of Ag in Sn is 0.06wt.% at 210°C and 0.02wt.% at room temperature [68]. The under cooling required to start solidification is said to be *explosive* [69], such that it is difficult to obtain a nucleus of critical radius and once a critical nucleus is formed it grows rapidly to consume the entire joint. The heat content in the entire system and the rate of dissipation of this heat would ultimately decide the size of these dendrites and tin cells. Rosenberg and Winegard [70] studied the rate of growth of tin dendrites in pure tin and they saw 1-8cm long tin dendrites depending on the amount of undercooling. A 3° undercooling gave rise to a growth rate of 3cm/sec whereas it increased to 25cm/sec with 10.5° of under cooling. From their study, a log plot of the curves indicated that the rate of dendrite growth varies with under cooling raised to 1.8. The dendrite growth follows the <110> crystallographic direction

[63] and the cells adjacent to each other should have the same crystal orientation, except in regions where two dendritic interfaces intersect. In case of incomplete mixing or no diffusion in the liquid phase, there is also a possibility of formation of concentrations that are slightly off-eutectic in local regions. In this case, the first solid to solidify will do so at a higher temperature than the eutectic composition. In hyper-eutectic compositions, Ag_3Sn particles will precipitate out which will lead to less of the Ag solute in the liquid Sn.

The microstructure of eutectic Sn-Ag solder in joints fabricated in a manner similar to manufacturing practices, consists of β-tin cells surrounded by Ag_3Sn precipitates embedded in a eutectic matrix as shown in Figure 1.6. The grain boundaries are difficult to reveal especially in the joint configuration, since the explosive growth implies near-single crystal orientations with only low angle boundaries. Depending on the cooling rate one can obtain variations of this basic microstructure. Slower cooling rates give rise to dendritic arms in the microstructure. With rapid cooling one sees an equiaxed microstructure, with the eutectic mixture surrounding the β-tin cells. Microstructures of eutectic Sn-Ag solder joint are given in Figure 1.6. It is evident that a microstructure produced with a low soldering temperature and a fast cooling rate would yield an optimal solder joint since a low soldering temperature implies less superheat in the system and similarly a fast cooling rate would prevent dendrite formation and produce a more equiaxed microstructure [23, 71]. However, rapid cooling is undesirable because it can cause thermal shock damage in ceramic components.

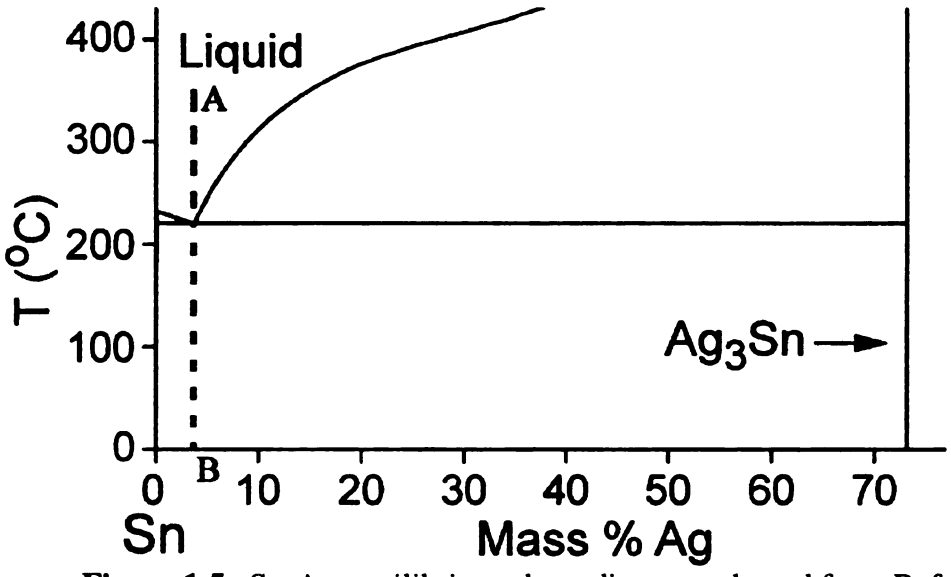

Figure 1.5. Sn-Ag equilibrium phase diagram adapted from Ref. [68]

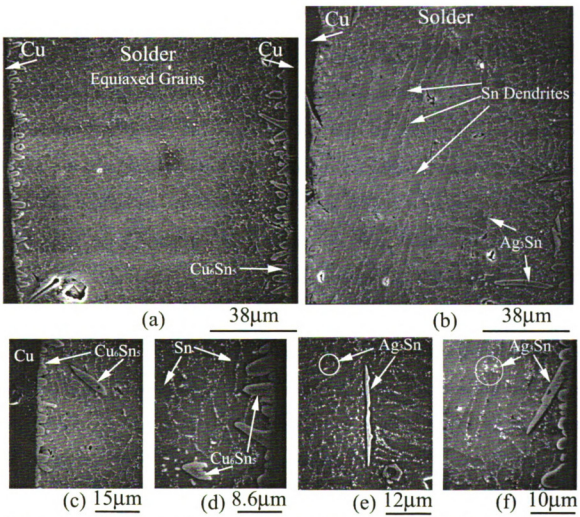

Figure 1.6. SEM micrographs revealing microstructure of eutectic Sn-Ag solder. (a) Solder joint showing equiaxed Sn-cells surrounded by Ag_3Sn intermetallic, (b) same joint revealing dendritic Sn-cells in another region and (c,d,e and f) higher magnification micrographs of particular regions of the same joint. These features are common to all solder joints, with variations depending on the maximum temperature reached during soldering and the cooling rate.

A joint with copper substrates gives rise to scallop shaped Cu_6Sn_5 and Cu_3Sn intermetallic phases at the copper-tin interface as well as dispersed hexagonal rod-like Cu_6Sn_5 precipitates in the tin matrix due to the dissolution of copper into tin when the solder is molten. Cu_6Sn_5 is found at the interface with the Sn-matrix and the Cu_3Sn found between Cu and Cu_6Sn_5 (closer to the Cu substrate phase to maintain thermodynamic equilibrium). The lattice parameters for hexagonal Cu_6Sn_5 are as follows: a = 4.192 $\mathring{A}$ and c= 5.037 $\mathring{A}$ [67]. The thickness of this intermetallic layer is dependent on the heating and cooling rate used during joint fabrication. As explained by Guo et. al. [72], depending on the amount of heat input into the system during the entire soldering process, the total volume of the secondary intermetallic phases of Cu-Sn can be controlled. Higher heat input (thermal flux) as well as higher temperature allows greater diffusion of copper from the substrate into the tin, which combines to form a thicker intermetallic interphase layers. Aging at higher temperatures also increases the thickness of this layer as well as the size of Cu_6Sn_5 precipitates.

The properties of the solder are affected by the microstructure and the constraints imposed by the copper substrate in the joint configuration. The microstructure can be changed and controlled by addition of several alloying elements (Cu, Ni, Ag, Bi, Sb, In) in minute proportions. The Ag_3Sn in the eutectic Sn-Ag solder matrix increases the hardness and strength of the solder. Copper addition (up to 1wt.%) slightly adds to the strength of Sn-3.5Ag solder joint [73]. The intermetallic Cu_6Sn_5 formed due to the dissolution of the Cu substrate increases the strength of the solder joint even more with a loss in ductility.

C) Lead-based Solders

(1) Microstructure Of Lead-based Solders:

Lead-free solders have posed several metallurgical challenges to the research community. Addition of secondary constituents like copper, nickel, bismuth, etc. to the eutectic Sn-Ag solder matrix to enhance wettablility and decrease the melting point, has led to the formation of intermetallics at the interphase / boundary and in the solder matrix. These intermetallics change / affect the microstructure of the joint during formation and results in variation of performance that are not yet fully understood. Much more is known about how the microstructure of Pb-based solders affects the fatigue properties of the solder [11]. Hence there is need to study the evolution and changes that occur in the microstructure and mechanical properties due to processing history and alloy composition. *Lead-based solders are well studied in this regard and though there is a distinct difference in the behavior of lead-based solders and lead-free solders with respect to microstructure and its evolution, the knowledge and insight gained from studying lead-based solders can greatly enhance our understanding of how the microstructure of lead-free solders evolve / change.*

(2) Microstructure of the Sn-Pb eutectic alloy (63%Sn-37%Pb):

Eutectic Sn-Pb is one of the most popular solders being used and the microstructure is well studied. The solder joint is a composite with a relatively harder tin phase surrounded by the relatively softer lead phase. The solidification microstructure is governed essentially by the rate of cooling. Faster cooled joints reveal a fine equiaxed microstructure whereas slower cooling leads to a lamellar microstructure. Smaller joints

cool faster and therefore exhibit a finer microstructure as compared to thicker joints (~0.5-1mm thick), which reveal a coarse lamellar microstructure. A faster cooling rate implies a lesser time for diffusion and hence slower growth of the lamellae [2]. The microstructure and properties evolve with time at high homologous temperatures in service.

Morris et. al. [10] and Mei et. al. [11] found that with relatively slow cooling, eutectic Sn-Pb solders give rise to a microstructure that consists of lamellae of the two solid solutions simultaneously crystallizing and forming parallel plate-like colonies when the two phases are present in approximately equal volumes which is the classic "eutectic" microstructure. However very rapid cooling results in Pb-rich and Sn-rich phases, which solidify as equiaxed grains interspersed with each other. Intermediate cooling rates give rise to variations between these two extremes. If one of the two phases dominates then the other forms a rod-like morphology within the matrix of the larger volume phase. Typically PCBs and on ceramic chip components show the eutectic lamellar microstructure whereas solder joints for surface mount components reveal a fine equiaxed microstructure [73] (surface mount components have a smaller mass and faster heat dissipation as compared to PCBs and large ceramic chip leads).

(3) Evolution of Sn-Pb Microstructure:

After solidification of the solder, when the temperature is lowered below the eutectic temperature, the equilibrium solute content of the primary solid solution is greatly decreased. The super saturation of the solute results in the precipitation of the solute in the matrix as fine particles since solid-state diffusion is relatively slow. Hence one finds small crystallites of Sn distributed in the Pb-rich phase [2]. The Sn-rich phase

is more "pure" than the Pb-rich phase due to the small solubility of Pb in Sn. The volume fraction of the Sn rich phase to the Pb rich phase is 73:27 for 63Sn-37Pb solders [2].

Unlike the Sn3.5Ag solders where the Ag_3Sn particles are mostly spherical (except larger intermetallic plates) and have a lower surface energy, the eutectic microstructure with plate-like lamellae is out of equilibrium with respect to lowering the total surface energy of the interfacial area per unit volume. The reduction in the surface energy occurs in two ways to achieve thermodynamic equilibrium with respect to interfacial energy. In the first method, the lamellae are converted into spheroidal particles, which coarsen and grow with time. Such spherodization usually starts at the boundary between the colonies of the eutectic microstructure, where there are several differently oriented colonies intersecting each other (Pb-Sn solder joints are typically "polycrystalline", consisting of many colonies). The spherodization once initiated at such boundaries slowly consumes the entire grain. The second way the microstructure can change is when the joint undergoes plastic deformation at high homologous temperatures. In such a case the solder material recrystallizes and evolves into finer equiaxed grains [44-48]. The recrystallization occurs preferentially along shear bands that develop due to inhomogeneous deformation in the joint. This sudden change can deteriorate the fatigue life of such solder joints drastically. As Morris et. al. [10] point out, fine, equiaxed microstructures obtained by rapid solidification have higher interfacial surface area per unit volume as compared to a deformed microstructure, which in turn helps to lower interfacial surface energy. Such grains do not undergo recrystallization under load, since deformation causes grain boundary sliding and dislocation activity that helps keep the grain size small. However they can grow and coarsen which can affect the

creep properties and other properties related to grain size. The shear band formed has high stored energy, causes localized dynamic recrystallization, which then generates a band of fine grain microstructure that is less creep resistant, which further causes strain enhancement, stimulating more dynamic recrystallization that keep the grain size small and hence creeps faster.

Finally, at high homologous temperatures, the rate of diffusion, from the Cu (from component) to Sn (in the solder) via the gaps in between the bumps of the intermetallic Cu-Sn layer is high and these locations serve as paths for easy diffusion. This causes a thickness increase in the intermetallic layer and simultaneously depletes the Sn from the intermetallic region, which gives rise to a Pb-rich layer/band near the interface. This Pb-rich layer is soft compared to the Cu_6Sn_5 intermetallic layer and hence there is a greater chance of crack nucleation, de-bonding and failure in this region. Thus a chemically inhomogeneous solder is created near the joint interfaces.

(4) Effect of Eutectic Sn-Pb Microstructure on the Mechanical Properties of Solder Joints:

Creep: In the high stress regime, the stress exponent is in the range of 4-7 and the activation energy is close to that of bulk diffusion. The deformation within the grains is controlled by bulk diffusion and dislocation climb within the grains is the controlling creep mechanism. At slightly lower stresses, the stress exponent is 2 and the activation energy is close to grain boundary diffusion. One sees deformation predominantly concentrated at the grain boundaries, which makes grain boundary sliding the creep rate / deformation controlling mechanism. At still lower stresses the stress exponent has a value of about 3. The activation energy has a value close to that of bulk or solute

diffusion. The creep rate controlling mechanism is believed to be bulk deformation, from dislocations that drag solute atoms, which accommodates deformation concentrated near the grain boundaries and hence maintains contact between grains.

The microstructure of the solder affects the creep behavior and creep rate. An increase in the size of the colony of the eutectic Sn-Pb solder causes hardening of the solder, especially at lower strain rates [74] and the intermediate (n=2) creep mechanism disappears. This phenomenon is particularly seen in eutectic Sn-Pb compositions, where the microstructure is relatively sensitive to the cooling rate. Addition of other elements can affect the creep rate by changing the grain size and solidification microstructure.

Reynolds et. al. [75] state that the creep behavior is affected by the creep behavior of the individual phases present in the joint [10]. By observing the microstructure the phase dominating the creep behavior can be identified. Hence it is essential to customize the microstructure to obtain the desired mechanical properties in the solder.

Shear Strength: Similar to the dependence of creep behavior on microstructure, the shear stress is also affected by the microstructural changes. A fine-grained joint in shear deforms by grain boundary sliding and it can sustain large deformations prior to failure. In this case the solder behaves in the superplastic manner. The shear strain is heterogeneously distributed throughout the microstructure, which allows partial recrystallization and shear band formation in the solder. The mechanical inhomogeneity causes further redistribution of straining in the joint and finally failure occurs along these shear bands [10]. It is observed that superplastically deformed material can sustain larger amount of strain to failure and hence crack growth rates are not fast.

Fatigue: Morris and Reynolds stated that "microstructure should resist the formation of the *persistent slip bands* that concentrate cyclic deformation and nucleate fatigue cracks. To achieve this goal, one would have to homogenize the deformation and avoid the development of local stress concentrations within the material [10]". From this point of view eutectic Sn-Pb solders are rather not suitable, especially due to the fact that solders usually experience high homologous temperatures in service. Recrystallization due to inhomogeneous deformation into a fine grain size under such conditions would lead to a soft microstructure that causes early nucleation of cracks and subsequent failure. To achieve better fatigue properties in eutectic Sn-Pb solders, it is recommended that the eutectic microstructure be converted into a more equiaxed microstructure to homogenize the strain. This can be achieved by using a fast enough cooling rate so that a more equiaxed and homogeneous microstructure is obtained. However, to achieve a fine equiaxed microstructure so that the joint would be able to undergo superplastic deformation (which is possible in electronic circuitry owing to the usually low strain rates) and to prevent grain growth (due to the high temperatures experience by the solder joints) which will lead to decrease in the fatigue resistance of the solder joint, addition of other elements, which inhibit the formation of the eutectic microstructure, can prove very useful. Another way to improve fatigue resistance is to introduce a dispersed second phase, which will postpone the deformation of the matrix. However this secondary phase should be softer than the matrix to be able to undergo deformation [76].

To achieve better creep and fatigue properties it is important to achieve a stable fine grain microstructure that does not coarsen with time, so as to facilitate homogeneous deformation in the solder joint. This is comparable to a similar phenomenon occurring in

high temperature superalloys, which were developed for aerospace applications. Hence approaches used by researchers for aerospace alloys could also be used for solder joints. Out of the many such approaches, dispersion strengthening and precipitation hardening are two possible techniques. In precipitation hardening a fine secondary phase precipitates out homogeneously throughout the microstructure from the solid solution. In case of dispersion hardening, a suitable phase needs to be dispersed in the matrix by external means. These dispersed particles should have the appropriate size and the distance between them should be optimized, such that the hard particles can stop the movement of the dislocations and hence hinder slip [77, 78]. Betrabet et. al. [77] discuss the use of such approaches in their paper with respect to the advantages and disadvantages of such dispersoids and properties inherently required by the secondary phases in the eutectic Sn-Pb system.

(5) Comparison of Sn-Pb and Sn-Ag solders:

Satoh et. al. [79], Hwang et. al. [80] and Thwaites et. al. [81] have reviewed the tensile behavior of Sn-Pb solder. In comparison with Pb-Sn solder, tensile properties of Sn-3.5Ag solders have comparable or slightly higher tensile strength [2, 79-81], and shear strengths of Sn-3.5Ag are comparable to those of Sn-Pb. In shear the plastic instabilities of the Sn-Pb solder do not interfere with strength [2]. During elongation experiments [79, 81, 82], Sn-Ag had comparable elongation to Sn-Pb at room temperature and moderate strain rates, and slightly higher strain rate sensitivities [82, 83]. For Sn-3.5Ag solders Mavoori reports m values of 0.083 at high temperature [84].

Creep resistance of Sn-Ag solder is better than Sn-Pb in the 25-100°C temperature range. In isothermal fatigue, eutectic Sn-Pb with a fine-grained equiaxed microstructure has a better fatigue life than one with a lamellar microstructure. Sn-Ag is much better in fatigue as compared to Sn-Pb at high shear strain amplitudes as indicated by Guo et. al. [85]. He attributes the better fatigue resistance of Sn-Ag solder to the resistance of crack initiation, rather than crack propagation, because Sn-Ag has the lowest crack growth resistance for the alloys he studied. Other studies also show that Sn-Ag is more fatigue resistant at room temperature and at about 100°C, compared to Sn-Pb solders [81]. Localized microstructural coarsening occurs in Sn-Pb solders which decreases its fatigue resistance and leads to failure in the joint, which is not the case in Sn-Ag solders [86]. However, more detailed studies are warranted in this respect to assess the mechanisms of thermomechanical fatigue damage in lead free solder.

1.3. THERMOMECHANICAL FATIGUE, CREEP AND AGING IN Sn-3.5Ag SOLDER

There are three main modes of failure in portable electronic products, namely 1) low cycle fatigue due to ambient temperature cycling or power cycling, 2) creep rupture due to flexure of the PCB during assembly and 3) fracture when the PCB is dropped [87]. TMF is one of the most significant deformation processes that a solder interconnect experiences in service. During TMF the solder material undergoes several cycles of repeated stress reversals followed by relaxation as a consequence of temperature

excursions (which can range from sub-zero to 150°C). During service the stress is often due to the CTE mismatches between the solder/substrate/component as well as the anisotropic behavior of Sn [66]. Since tin expands twice as much along the c-axis (CTE in the a-direction is 15.45 x 10^{-6} /°C and in the c-direction is 30.5 x 10^{-6} /°C [65]) on heating as compared to the copper substrate (17.1 x 10^{-6} /°C), leading to a complex stress state in the joint depending on the relative orientations of the crystals [66]. Simultaneously, at high homologous temperatures experienced by the solder, creep and aging processes are continuously present and contribute to the deformation in the joint.

In the case of single shear lap solder joints studied by Choi [23] and Guo [27], the stress state in the joint is truly complex even in these simplified geometries. The complexity comes partially from the geometry and the crystal orientation differences in the joint, though there has been no characterization initiated so far with respect to the latter (excluding this study). Further complications arise due to the presence of Ag_3Sn and Cu_6Sn_5 intermetallics that can act as local regions of high stress concentration since they are heterogeneously distributed. Constraint effects of the joint are also an important factor [88]. Anisotropy further complicates the issue. Retained stresses in the joint can lead to extensive stress accumulation during cycling, which does not relax after prolonged periods [26], and results in nucleation of micro cracks that progress and combine with time to cause failure of the joint [57, 89]. Observations have revealed that most solders fail in regions close to the interface between the solder and copper substrate in the solder matrix.

At high homologous temperatures during TMF both thermal and athermal processes occur. Mavoori et. al. [84] tried to compare the activation energy and stress

exponent for creep, stress-relaxation and monotonic stress-strain at 25° and 80°C in bulk Sn-3.5Ag solder, where thermally activated plastic flow plays a dominant role along with athermal dislocation glide processes. At high temperatures or low strain rate, creep processes dominate since there is sufficient time for recovery required by creep deformation. At low temperatures or high strain rates, athermal processes are more active. Also stress relaxation occurs more at the higher temperature than lower temperatures due to higher thermal energy, though this stress never goes to zero in joints as reported by Jadhav et. al. [26], contrary to the results seen in bulk tin samples by Mavoori et. al. [84]. Such stresses caused due to CTE mismatches between solder and substrate or due to differently oriented highly anisotropic Sn grains [66] can be relieved by fracture, micro crack formation or grain boundary sliding.

Mavoori et. al.'s [84] study showed that in isothermal fatigue tests carried out at 25°C, the number of cycles to failure decreased with increasing hold time up to 120 seconds, beyond which it did not show any decrease in number of cycles to failure. This correlated well with the stress relaxation data, which showed relaxation of stress to a large extent within the first 120 seconds [84, 90]. **This study suggests that during the hold time, damage accumulates on the surface in the form of slip steps due to dislocations emerging out of the surface.** These steps possibly play a crucial part in the cracking and further damage accumulation. Stress relaxation experiments showed two distinct regions; one of rapid stress drop and the other of relatively slower stress drop rate. Hence they introduced a threshold stress term, σ_t, in their stress relaxation equation, $\dot{\sigma} = A(\sigma - \sigma_t)^n \exp(-Q/RT)$ where A is a constant, $\dot{\sigma}$ is the stress relaxation rate, n is the stress exponent, Q is the activation energy, R is the gas constant and T the

absolute temperature. The fits for this curve yielded values of 6, 9.8MPa and 33.5KJ/mol for the stress exponent, threshold stress and activation energy respectively.

Other studies carried out by Murty et. al. [91] have shown that creep in tin and tin-based solders is controlled by climb. However the low activation energy seen at lower temperatures (33.5kJ/mol from Mavoori's work) compared to lattice diffusion (105 kJ/mol) implies that climb is controlled by pipe diffusion in this temperature regime.

Darveaux et. al. [87] in their paper quantified the effect of deformation behavior on reliability prediction using Pb-Sn solders joints. They have also discussed the inherent differences in properties exhibited by solder in joints as compared to bulk [87]. Using Dorn's equation [52], they compared data from their own work, that of Kasyap et. al. [92] and Subrahmanyan ([93] with that of Hall's [94] stress-strain hysteresis loops. Hall in his study had measured the stress-strain response of actual solder joints situated on PCBs. Darveaux et. al. found that at higher strain rates of 10^{-6} the data correlated well with Hall's data, but at lower strain rates the data deviated from that of Hall's study. Thus prediction of a model using data on bulk specimens as well as that from monotonic tensile experiments has to be done with care. Strain rates during conventional tests are in the order of 10^{-4} - 10^{-2} during ramp and can get down to 10^{-8}/sec during dwell which implies that conventional tests are well in the power-law breakdown regime given by $\dot{\varepsilon} = \frac{C_1 G}{T}\left(\sinh(\alpha\frac{\tau}{G})\right)^n \exp\left(\frac{-Q}{RT}\right)$, where α is a curve fitting parameter at which the power law breaks down and C_1 is a constant. To obtain the true activation energy the temperature dependence of the shear modulus must be included $G = G_0 - G_1 T$, where G_0 is the modulus at 0°C and G_1 is temperature dependent and T is temperature in °C. Also

at high stresses $\tau/G > 10^{-3}$, in the linear region of the power law breakdown the stress is dependent on the strain rate and can be equated using $\sigma = c\dot{\varepsilon}^m$, where m is the strain rate sensitivity exponent and c is a constant [84].

One of the main objectives of thermal cycling testing is to predict field-use-reliability from accelerated testing. Darveaux et. al. [87] has found a factor of 3 difference between prediction of lifetime between accelerated testing and field use, using the Coffin-Manson equation given earlier. This implies that accurate knowledge of deformation behavior of the solder, under different conditions is necessary for precise fatigue life prediction.

Solomon [95] in his study performed isothermal fatigue tests with a frequency of 0.3Hz at 35° and 150°C in simple shear on solder layers about 0.19mm thick using Sn-3.5Ag and Pb-Sn solders. Both the solders revealed a decrease in the number of cycles to failure with increasing plastic strain range following the Coffin-Manson relationship stated above.

Though the Coffin-Manson relationship is commonly used to model such solders, the ultimate cause of failure still needs to be determined and controlled. In solder alloys with low melting temperatures, the fatigue behavior is related to the equivalent strain amplitude and change in the properties with temperature. The fracture is not only dependent on fatigue strains undergone by the joint but is also dependent on creep relaxation during dwell times at such temperatures [55]. Further, higher stress exponents observed in joints could imply the presence of several deformation processes occurring in parallel. Grain boundary sliding is frequently observed, but is still an issue since the grain size is large, and no study has been able to track the cause of this form of grain

boundary deformation. Tin exhibits Harper-Dorn creep, which has a strong dependence on the dislocation substructure [96, 97]. Dislocation generation, movement and their interaction with dispersed intermetallic particles in the joint at high and low temperatures are also important. Therefore there could be combined effects of crystal orientation and dislocation substructure, which need to be characterized.

Igoshev et. al. [98] show that accumulation of grain boundary defects start early during creep and last for 70-80% of the specimen's life. Depending on the stress states during creep at high temperatures, failure can take place via transcrystalline (at lower stresses) or inter-crystalline (at higher stresses) cracking. Darvaeux and Banerji [99] have shown that dislocation climb is the main factor contributing to creep deformation, however stress states in the solder joint can change and failure can occur by fatigue. Darveaux and Banerji [99] developed constitutive relations, which describe the behavior of solder joints under a wide range of conditions. They showed that eutectic Sn-Ag solder absorbed larger strain prior than 60Pb-40Sn solder joints. Creep properties are also affected by several factors; higher melting temperature solders exhibit lesser creep deformation if the applied strain is small [24] (which is usually the case in typical electronic packages). Guo et. al. [100] and Choi et. al. [101, 102] have shown that recently developed composite solders and alloyed solders may be more creep resistant than non-composite counterparts due to the intermetallic interphase layer formed between the solder matrix and the composite reinforcement, however the role of the strain history and time duration of the creep test also needs to be addressed where aging and evolution of the microstructure would play significant roles.

Testing solder joints rather than a bulk solder is the best way to study the deformation and microstructural effects of solder, since the microstructure of bulk specimens is different from solder joints. Solder interconnect material in the joint configuration has constraints from the substrate and alloy differences that alter their deformation and ultimate failure in comparison to bulk specimens [99]. Darveaux and Murty's [87] test results show that creep properties of solder in joint configuration is quite different than bulk solder, with joints showing better creep resistance due to the effect of joint constraints.

1.4. SLIP SYSTEMS AND DISLOCATION ACTIVITY IN TIN

Slip is an important mechanism of plastic deformation in crystalline materials. Slip is obtained by dislocation glide, and occurs in closed packed directions on close packed crystal planes. A resolved shear stress greater than the critical resolved stress for that system is needed for slip to occur.

Tin has a body centered tetragonal structure ($a=b\neq c$) with a c/a ratio of 0.5456. The 7 slip system families (excluding at least one twinning system {-301}<301>) and their critical resolved shear stresses are not very well characterized, because creep/recovery processes add complexity to attempts to interpret experimental data on single crystals. What follows is some background on known slip systems in tin and dislocation activities studied so far. Making thin foils of tin is difficult though not impossible and care has to be taken during preparation so as to not introduce or remove

dislocations due to handling. Most of the studies below concentrate on the slip systems possible in tin based using an etch-hillock technique in bulk specimens (mostly bicrystals). In the etch-hillock technique, a hillock is seen where dislocations emerge from the crystal and the motion of dislocations leave a trail of hillocks, which then show the history of dislocation motion on the surface.

Sugawara et. al. [103] in their study on tensile testing of tin single crystals, found square-shaped etch hillocks on the (001) surface with lateral surfaces of (011) planes. Deviation from the (001) plane surfaces yielded no etch-hillocks, implying that the technique was useful for studying dislocations on only certain specifically oriented planes. In a study done by Honda et. al. [104, 105] using the etch-hillock technique, to observe the dislocation structure of boundaries introduced in tin crystals by stretching and annealing. They found polygonized walls of dislocations with a density of about $2x10^5/cm^2$ lying in the [010] direction on the (001) plane. These dislocations were in a step-like fashion consisting of a series of treads and steps. The tread dislocations were of the (010)[100] type and were mobile but step dislocations (1-10)½[111] did not move [104]. On further stressing, these dislocations bowed between immobile segments [104]. Further, kink bands were also seen on deformation with dislocations having the (010)[101] slip systems that further thickened with strain [104].

Fujiwara et. al. [36] from their study believe that the motion of dislocation is hampered by forest dislocations and not due to long-range elastic interactions with other dislocations. The ease of glide is dependent on the stress with lesser stress needed at increased temperatures. They call our attention to three stress regimes; 55-80kPa, 115-140kPa, and 175-210kPa needed to overcome such obstacles. According to them the

(100)[001] slip system glided most easily in the presence of forest dislocation followed by the (110)[001] dislocations.

Duzgun et. al.[34] have carried out substantial work in studying the slip systems in tin. Their paper shows slight differences in the stress-strain curve for several similarly oriented tin single crystals grown by the Bridgman method implying *the presence of many different slip systems operational in the slightly differently oriented single crystals.* In their study slip systems (100)[010], (010)[100], (010)[10-1] and (121)[10-1] are operative with the (121)[10-1] dislocations operative at higher temperatures (383K) only. No other slip systems were operational in their study.

A number of studies on the effect of temperature on activation energy have shown a transition at about 150°C [106-108]. Chu et. al. [109] indented tin single crystals in [001],[100] and [110] orientation. At low temperatures they obtained activation energies of 37kJ/mol and 105kJ/mol at high temperature. Pencil slip was also observed at low temperature in the [001] orientation but not at high temperature. Instead, sub-boundaries appeared at high temperature due to climb of the dislocations into partially polygonized dislocation walls. It was also confirmed that the absence of slip lines at high temperature is not due to surface diffusion [109]. They suggest that low temperature processes involve dislocation creep and high temperatures involve dislocations climb due to comparable activation energy as that of self-diffusion, but the low temperature processes occur in parallel with the high temperature. Fujiwara et. al. [110] and Suh et. al.'s studies also support this view and Suh et. al. [111] further suggest that lattice diffusion processes operate above the transition temperature and pipe diffusion below [53, 91]. Fiedler et. al. [112, 113] observed only [001] and ½[111] dislocations Burger's vectors in their work

and they calculated the energy of these dislocations using anisotropic elasticity results of Stroh [114]. They found that the energy of [001] and ½[111] dislocations is lower than other types of dislocations and this result is consistent with that of Chu et. al.. This further restricts the number of possible slip systems for each crystal orientation. Table III shows the different slip systems observed by several different researchers discussed above. Seven different slip systems are noted with various CRSS values (italicized numbers are from Duzgun [34]). Barret and Fujiwara's values seem to agree well. Schmid's [62] results are opposite to those of Barrets (plane and direction seem to be flipped). Vook [115] in his work on evaporated single crystals of tin found that most of the dislocations had a screw character. From his study, (001) slip had not been reported earlier and he suggests that this slip system might occur only in thin films. He observed cross slip between different slip systems: (100)[011] ↔ (0-11)[011], (100)[011] ↔ (2-11)[011], and (0-11)[011] ↔ (2-11)[011]. Cross slip between non-parallel planes of the same slip system was observed in (1-21)[-101] ↔ (121)[-101]. From consideration of the available qualitative results from his work, he further suggested that the stacking fault energy in tin is relatively high.

Table III. Different Slip Systems For Tin From Refs. [34, 36, 62, 64, 104, 105, 110, 115, 116]

Glide Plane	Direction	CRSS kg/mm^2	Temp / Misc	Ref
100	001	0.19 -	20°C Least resistance to glide through forest dislocation	Barret, Fujiwara
110	001	0.13 -	20°C 2nd least resistance to glide through forest dislocation	Barret, Fujiwara
101	10-1	0.16	20°C	Barret, Schmid, Vook
121	10-1	0.17, *2.31e5 N/m^2* -	20°C *m = 0.489, active at 100 ℃* Can cross slip.	Barret, *Duzgun*, Vook
110	-111	-	150° C, immobile at room temperature	Barret, Fujiwara
010	100	- - *2.7e5 N/m^2* -	RT, EH, SC Least resistance to glide through forest dislocation *m = 0.456* -	Fujiwara *Duzgun* Ojima, Bausch,
010	101	- *2.39e5 N/m^2*	EH, SC *m = 0.498*	Honda, Fujiwara, *Duzgun*
001	110	-	-	Schmid
001	100	-	-	Schmid
101	-121			Schmid
111	-110		Above 150°C	Schmid
100	011			Vook

RT – Room Temperature, EH - Etch Hillock, SC – Single Crystal

Twinning in tin {-301}<301> is commonly observed, particularly in high strain rate low temperature tensile deformation [63, 117] which is not the case during creep or hot deformation of tin. Hence formation of the twins during hot-deformation is less

likely, though solidification or annealing twins present could play a role in deformation. This author [118] observed (101)[10-1] twins oriented at 59° about the [110] crystal axis are also possible, as solidification twins and not deformation twins.

Studies carried out by several different groups on tin prepared in a similar manner, but having only slight differences in composition and / or processing history have shown variations in activation energy from 35-110 kJ/mol [101] implying that microstructural details and processing history should affect dislocation motion. However there has been no definitive study on the effect of crystal orientations and dislocation activity during hot deformation in tin.

1.5. PLASTICITY MODELING USING VPSC SIMULATIONS

Plasticity in symmetric lattices such as FCC polycrystalline aggregates has been modeled using Taylor type model [119-123], though it has been shown that in some instances, the Sachs type models has worked better [124, 125]. The Sachs model assumes uniform stress within each grain and provides a lower bound on the aggregate stress. The Taylor type model assumes uniform strain in all grains and provides an upper bound on the aggregate stress. Hence the Sachs type model ignores local compatibility amongst grains i.e. lack of consideration for grain boundary compatibility. The Taylor type model ignores local equilibrium i.e. grain boundary traction equilibrium. Both models have been used to simulate large plastic deformation and texture evolution in FCC polycrystals. Nevertheless Taylor's assumption is more reasonable for large

deformations where compatibility is more important than equilibrium [121]. However both these models disregard the interactions between grains. Therefore more complex intermediate models such as the relaxed constraints type models of Leffers, Kocks, [126-128] are more realistic and accurate, since they attempt to satisfy compatibility and equilibrium both at local and macroscopic level.

Plasticity and texture development in a low symmetry polycrystalline aggregate is characterized by deformation on several active slip systems present in each grain. Usually five slip systems are needed to accomplish the desired shape change. High anisotropy gives rise to hard and soft orientations, which can give rise to highly preferred deformation in certain grains, which implies that some grains cannot accommodate deformation due to lack of slip on necessary deformation systems. Such hard grains may have less than 5 active slip systems, causing local interfacial stresses to builds up that lead to either intergranular fracture accommodation through plastic deformation by neighboring grains, or some accommodation of the stress in the grain boundary plane itself [129]. Hence a more involved model, which can predict the plastic deformation in such materials, is needed. The visco-plastic self-consistent (VPSC) polycrystal plasticity code version 6.0 developed by Lebensohn and Tomé [130] can simulate deformation in low-symmetry materials. It can be used in the Taylor, Sachs or the VPSC mode that permits modification of stress and strain in each grain, such that the aggregate deforms to satisfy local and overall boundary conditions. The theory upon which the VPSC code is based is explained in [130], and in [43]. To describe the code briefly, (from the manual [131]), a polycrystalline aggregate consists of a weighted set of orientations, where orientations represent many grains statistically, and the weights represent their volume

fraction, which defines the initial texture. Each grain is treated as an ellipsoidal visco-plastic domain surrounded by a visco-plastic medium, both of which are assumed to be anisotropic. The deformation is carried out by applying increments of strain. At each deformation step, a boundary condition is imposed where either the strain rate components or a combination of strain-rate and stress components are applied to the material, and the resulting stress and strain in each grain is then calculated. Subsequently, the grains are reoriented using the shear rates and this constitutes the evolution in crystallographic texture development. The yield stresses (hardening) and the grain shapes (morphological texture development) are also updated simultaneously. The overall stress and strain tensor components are computed by volume averages of the corresponding grain components. Such averaging gives rise to an anisotropic response of properties over the several orientations. Iterations are needed to converge to the strains in each orientation that when summed, satisfies the boundary conditions. The required input consists of 1) the initial crystallographic texture represented by grain orientations and weights obtained through OIM or X-ray measurements, 2) single crystal properties i.e. the active slip and twinning systems, their critical resolved shear stresses, and the related hardening parameters, 3) the initial morphology of the texture i.e. initial grain shapes and shape orientations, 4) the boundary conditions for the deformation process i.e. overall displacement rate components, or overall stress components, and 5) parameters controlling convergence, precision and type of run i.e. either Taylor, Sachs, or Visco-plastic. The output consists of 1) final crystallographic texture and morphology of each orientation, 2) the stress and strain components during or after deformation can be obtained, 3) statistic of the activity of the slip and twinning systems during deformation,

and 4) statistic of average stress and strain-rate components and their standard deviations, average grain shape, and average grain rotation, etc. during deformation. The output texture can be transformed back into the OIM software for a visual representation of the deformation process.

1.6. TEXTURE MEASUREMENT USING ORIENTATION IMAGING MICROSCOPY (OIM)

Texture is defined as *a collective distribution of crystallographic orientations in a polycrystalline aggregate* [132]. Gaining control of texture allows engineering of the material to optimize properties. X-ray diffraction has been the most commonly used technique to determine texture of materials (macro texture). However, X-rays provide no better spatial resolution than the area illuminated by the beam, unless the more expensive and limited synchrotron source is used [133] (it is a high intensity parallel and focused X-ray beam given off a particle accelerator, e.g. at Argonne National Laboratory, Illinois). Hence a technique based on X-rays is usually only good for bulk macrotexture measurements, where no information about misorientations between grains can be obtained.

The transmission electron microscope (TEM) and scanning electron microscope (SEM) using electrons as their primary source can also be used for microtexture determination. Microtexture is defined as *a population of individual crystallographic orientations, which are usually related to one or more features in the microstructure.* It has information about the misorientation, boundary types, and grain orientation in the

region sought. TEM can be used where precise measurements of grain and subgrain orientation or misorientations are desired. However, the TEM process is quite tedious due to the multistage specimen preparation. Since only a small electron transparent region in the foil is obtained, orientation information for only a small fraction of the total volume is obtained, and hence it is difficult to have statistical certainty that observations correlate to the bulk changes and texture in the specimen. Also, TEM needs off-line diffraction pattern indexing, though recently on-line techniques have become commercially available (hkl Channel Acquisition software version 4.2 by HKL Technology, Inc., Blaakildevej, 17k, Hobro, DK-9500, Denmark and OIM data collection software version 3.5 by TSL Laboratories, Draper, UT).

Grain orientations can be measured in the SEM with two techniques, namely Selected Area Channeling (SAC) and Electron Back-scatter Diffraction Pattern (EBSP). In SAC, one uses the ideas of Electron Channeling Contrast Imaging (ECCI), where electron beam is made to rock such that the normally divergent electrons channel through the lattice, and interact with the deeply seated atoms within the material. The difference in the contrast produced between the electron beam interacting with defects and the channeling of the electrons can be used to observe micro defects in the material. A grain with good channeling contrast will be darker with defects appearing lighter on the dark background (S>0). One can measure the orientation of individual grains at high magnification, but the lack of automation and the limited angular range (25°) and spatial resolution of ~15μm are some of the drawbacks. Thus, it is tedious to measure the entire set of local orientations to correlate with the microstructure of the specimen. One can

obtain a "mesotexture" for the larger grains in a smaller area, which provides information about particular grains and their orientation relationships with neighbors (See Figure 1.7).

On the other hand, EBSP has a better spatial resolution (100-300nm) and angular range (up to about 80°), possibly easier specimen preparation and computer assisted acquisition and analysis of data, which allow large regions of the specimen to be analyzed quickly (clocked at 80 patterns per minute) with reasonably good accuracy. The texture one obtains with EBSP is called microtexture, where crystallographic information of individual crystals / grains and the grain boundaries is delineated in the form of a two-dimensional map, where every pixel corresponds to the spot from where it was taken on the specimen during the scan. Hence it has gained popularity in a very short time. This map is called an Orientation Imaging micrograph and this technique is called Orientation Imaging Microscopy (OIM). These maps correlate very well with the microstructural features and give an insight into the crystallographic orientations, which is invaluable for comprehensively studying material behavior. Solder joints are often about 100μm thick; hence conventional X-rays are impractical. SAC is time consuming and hence the EBSP technique is the best technique to rapidly analyze texture in solder joint specimens.

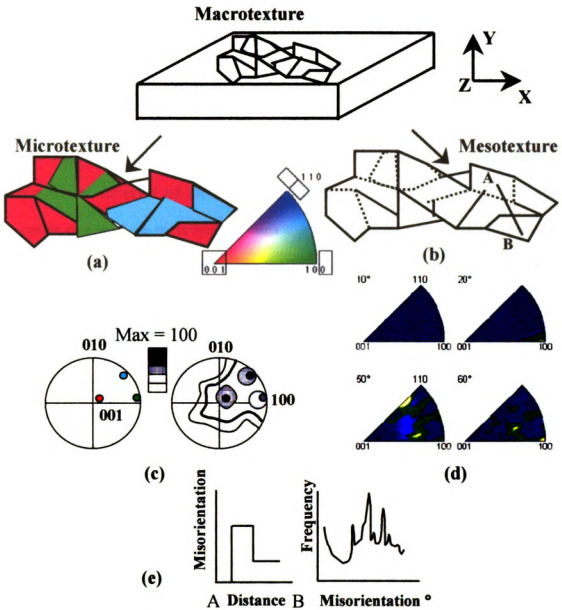

Figure 1.7. An illustration of the relationship between (a) micro and (b) mesotexture. Macrotexture shows 14 grains oriented with respect to the specimen X, Y and Z. (a) Microtexture correlates specific grains and their crystal orientations; three different grain orientations have three different c-axis poles (shown by red, blue and green colored grains)[134] in (c). (b) Mesotexture shows grain boundary relationships (shown by dotted and black thick lines) which help reveal grain boundary character that is statistically described in Figures 1.7(d) by the misorientation distribution function (MODF) and Figure 1.7(e) histograms of misorientation angle. (c) Pole figures with point plots and density plots computed with Gaussian sums of each orientation pixel shows the macrotexture.

a) Electron Back-Scatter Diffraction Pattern (EBSP): Electron beam interaction with a specimen produces many signals, which are useful for imaging. When an electron beam impinges on a specimen, two types of scattering can take place, elastic or inelastic. Elastically scattered electrons are formed when the beam interacts with the nuclei of the atoms and undergoes a large deviation in their path without any energy loss. The electrons are deflected by the positive charge of the nucleus, taking into account the negative charge of the revolving electrons and near collision with electrons. Inelastically scattered electrons are produced when the beam electrons interact with the electrons of the atom, causing slight deviation in their path (small angle deflection) with a loss of energy. In crystalline specimens with preferred orientations, scattering of the electrons occurs in specific directions given by the Bragg's law: $n\lambda = 2d\sin\theta$, where n is an integer, d is the lattice spacing and θ is the angle of diffraction. Backscattered electrons are produced when the elastic interactions between the beam and the specimen produce electrons, which get scattered backwards by multiple large-angle interactions. These electrons are scattered out of the sample from the same side as they entered. About 10-50% of the beam electrons get backscattered. Due to elastic scattering, these backscattered electrons are high in energy and can escape from the entire beam-sample interaction volume*. These backscattered electrons then undergo both elastic and inelastic scattering in the interaction volume before they re-enter the unit hemisphere of solid angle from which they entered [135, 136]. When these inelastic electrons satisfy

* The interaction volume is the volume inside the specimen in which interactions between the incident electrons and those from the specimen take place. This volume depends on 1) the atomic number of the material of the specimen; higher atomic number implies more electron absorbance and hence a smaller interaction volume, 2) the accelerating voltage; higher voltages implies more penetration and generation of a larger interaction volume and 3) the angle of incidence for the electron beam; the greater the angle (further from normal) the smaller the interaction volume.

Bragg's law, the inelastic electrons are scattered outwards in the form of cones which when projected onto a screen in 2-dimension appears to look like parabolas. These parabolas appear as two parallel lines (called Kikuchi lines) if one is to view them near the optic axis. One is excess (brighter, which does not diffract and gets transmitted electrons without diffraction) and the other is deficient (dark, due to diffraction of the back-scattered electrons), however in the Field Emission Gun SEM both lines are equally dark (see Figure 1.8 below). These Kikuchi lines are fixed (both angular and spatial) for a particular crystal structure and they are the projections of the geometry of the lattice planes in a crystal [134]. The angles between the Kikuchi lines (or Kikuchi bands as they are sometimes called) along with the stereographic projection are used to index the Electron Back-scatter Diffraction pattern (EBSP) or Kikuchi pattern (Figure 1.8). Hence the coherent scattering (Bragg scattering) of inelastically scattered electrons in a thick specimen gives rise to Kikuchi patterns. These electrons are sometimes called diffusely scattered electrons.

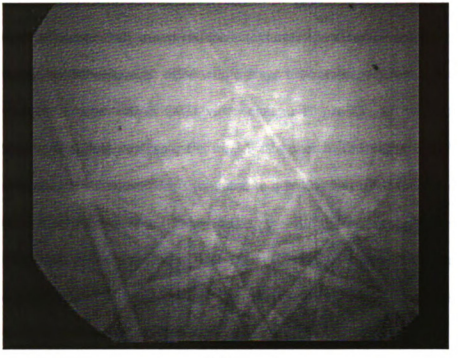

(a)

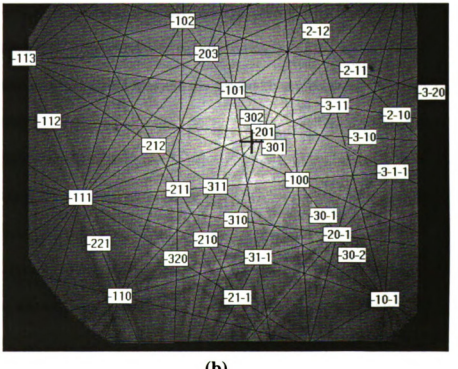

(b)

Figure 1.8. Kikuchi pattern of tin crystal. (a) Pattern showing Kikuchi bands and (b) after indexing.

b) Microtexture Data Collection: Automated EBSP (Electron Backscattered Pattern) is a preferred technique to study micro and meso textures. The essential components for this method of data collection are an SEM with a stage tilt control with a coherent beam, a phosphor screen viewed with a CCD video camera and a TV, all interfaced with a computer for on-line data analysis. Figure 1.9 is a sketch illustrating EBSP formation and data collection. The specimen is mounted in a holder and tilted to an angle of 70°. The rastering electron beam trajectory strikes the surface of the specimen emitting backscattered electrons which undergo Bragg scattering, and illuminate the phosphor screen transmitting light pulses through the optical fiber cable to the outside of the microscope chamber, which are then reconverted into an electronic signal using a photomultiplier tube (PMT) and is then projected on a TV screen. The computer captures the screen image (which is typically averaged to improve resolution) and indexes the pattern in real time to give a crystal orientation recorded in terms of "Euler" angles. The beam then moves to the next spot and the procedure is repeated.

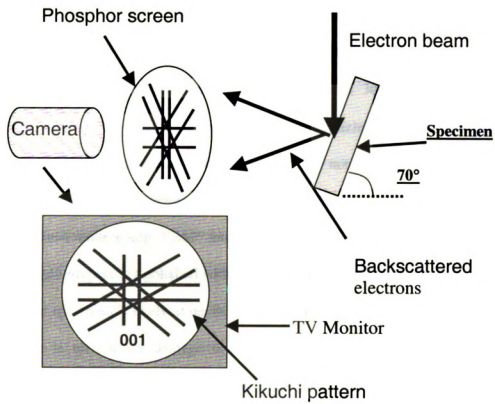

Figure 1.9. Typical setup for EBSP.

c) Sample Preparation and Mounting: The sample preparation for EBSP is relatively straightforward. The surface need not be absolutely flat, though it needs to be free from any oxide layer, impurities and contamination since the penetration depth for back-scatter electrons is approximately 0.5μm (depends on the accelerating voltage and atomic number of the material). This can be accomplished by metallographic polishing or electropolishing, followed by ultrasonic cleaning, plasma cleaning (in cases where high temperatures is not a problem since surface temperature of 300°C can be reached) followed by storing the specimen under a non-oxidizing environment [137]. Metallographically prepared specimens are sometimes not suitable for EBSP and additional steps are required to achieve a good surface. As a general rule it is proposed that all specimens undergoing EBSP analysis be either chemically etched, electro polished or metallographically polished with 20nm silica particles in an alkali suspension [138]. Once the specimen is ready, it needs to be mounted onto the sample holder taking care that there is no surface damage or contamination during mounting. Surface deformation can cause difficulty in indexing the EBSP pattern (which may be distorted or in distinct due to surface damage) and there are various levels of deformation, which can be tolerated for indexing in a pre-deformed specimen. Since the angular relationships between bands remains unchanged, it might be possible to index the EBSP, however the confidence in indexing depends on the extent of deformation, as the intensity of the Kikuchi bands decreases with increase in deformation. High dislocation densities create large elastic distortion and local misorientations. As a consequence, the indexing gets distorted because image quality and contrast is low.

The specimen is mounted in a specimen holder such that the surface of the specimen makes an angle of about 70° [134] with the horizontal axis. Precise tilt is an integral part of the calibration setup. Calibration is achieved using a Silicon single crystal with [001] as the surface normal. The geometrical aspects and procedure for calibration can be found in Ref [134].

Spatial resolution is dependent on the acceleration voltage, probe current, working distance and tilt angle. Higher acceleration voltage is preferred to increase the size and depth of the interaction volume, however 20-25kV seems to be an optimum value. Probe currents of the order of about 5mA or higher are considered optimal. Shorter working distances are preferred to minimize focusing problems. A decrease in the angle from 75° to 60° results in the increase in spatial resolution, with a loss in the proportion of backscatter electrons to absorbed electrons [139, 140]. Hence a 70° angle is considered most favorable [141] in the majority of cases, though in a particular system one can obtain better conditions by tweaking one of these parameters with a trial and error approach.

d) Pattern Recognition: The EBSP pattern can be used to identify crystal structure. The EBSP pattern first obtained is studied for rotation angles and mirror planes which can be easily accomplished by looking at the intersecting Kikuchi bands. Further, calculations of angles between various bands on the EBSP and the spacing between parallel bands can be determined. Further information on crystallographic details that can be obtained from an EBSP is found in Refs. [137, 142, 143].

Once all the above steps are completed and a region of interest is located, the beam is rastered over a chosen area of specimen. The scan coils of the SEM are turned

off (i.e. to obtain the spot mode), and the beam interacts with only a small volume of the specimen to display an image of the EBSP on a low-light TV monitor. The computer program identifies the zone axes from intersection of the Kikuchi bands and measures the inter-axial and inter-planer angles. The orientation is determined in real time and a pixel of orientation data is stored before the beam is automatically positioned to the next spot and the process repeated. Being an automated process, several such areas can be scanned one after the other. The dataset is subsequently post-processed to generate maps and plots.

OIM assigns color to particular crystal orientation, so that a given crystal orientation has the same color. Misorientations between grains can be visualized by the degree of color difference. Thus microstructure and crystal orientation are simultaneously displayed on a map. Figure 1.7 shown earlier reveals the different ways information obtained from an OIM scan can be processed for better understanding and visual representation of the data. Figure 1.7 shows crystal orientations being expressed using color-coded maps and inverse pole figures. Grain size, shape, distribution, etc., are available and can be deduced with the software. The distribution of grain boundary misorientations (i.e. high, low, twin, special boundaries) is expressed as misorientation distribution functions (MODF) or histograms of misorientation angle.

The fast and relatively easy automated setup, along with simple sample preparation and user friendliness, allows researchers to explore topics such as recrystallization, grain size, grain growth and microstructural evolution. The software allows textural representation in pole figures or OIM maps. The grain boundary distribution can be studied with the help of misorientation distribution functions (MODF)

and histograms of misorientation angles. The plots along with the OIM maps serve as effective tools to understand grain boundary formation and changes. Hence OIM is an indispensable tool for better understanding and characterization of microstructures, especially the highly dynamic microstructure of solder joints.

1.7. GRAIN BOUNDARY ENGINEERING AND SPECIAL BOUNDARIES IN TIN

The presence of grain boundaries in crystalline materials during deformation at high temperature affects the deformation behavior. Interest in grain boundaries has only grown since Andrade [144] first noted their presence in 1914, stating that "*Even in the purest metals there are well-defined crystals separated from one another by thin walls of crystalline material*". Grain boundaries can be beneficial or harmful; beneficial by allowing super plastic deformation and formability needed to form complex shapes, or harmful, if they cause intergranular cracking and failure.

Properties of a polycrystalline aggregate are largely controlled by their structure and the interfaces that they contain, particularly grain boundaries. Grain boundary engineering is a new concept in Materials Science and Engineering first proposed by Prof. T.Watanabe in the early 1980s to improve material properties by controlling the grain boundary character distribution. The idea is to promote a high proportion of special grain boundaries, since they are resistant to failure in many cases [145], [146]. More will be discussed on the formation of such special boundaries in following sections.

Special grain boundaries are different from general grain boundaries, characterized by a particular misorientation at which there are extensive areas of good atomic fit along the grain boundary plane. Special boundaries have some coincident lattice sites (or a CSL), such that the reciprocal of the density of coincident sites between the two adjoining grains is represented by Σ# [147]. This implies that there is a lower distortion of atomic bonds at the grain boundary plane, and hence a lower energy and a smaller free volume for the special grain boundary configuration.

The orientation of the grain boundary plane and the distribution and proportion of special grain boundaries are two important factors that can be used to control the properties. Cleavage fracture within a grain can be arrested at the grain boundary if the same type of crystallographic plane in the neighboring grain is not parallel. A high proportion of contiguous special grain boundaries can also improve the properties of materials, which usually are stronger boundaries (low energy boundaries). Palumbo et. al. [146] point out that the probability of intergranular crack propagation and length can be significantly reduced by increasing the fraction of special grain boundaries in Ni-15Cr-10Fe alloy. He further points out that the probability of the crack propagating beyond five grain diameters in a material with 15% special grain boundaries is approximately 35%, and it is reduced to less than 0.001% in a materials containing 75% special grain boundaries.

With this in mind, the concept of grain boundary engineering becomes important, where properties such as tensile strength, creep, and recrystallization can be controlled by controlling the distribution of the special grain boundaries.

Special Boundaries in Tin: Preliminary studies of tin-based solders [118] as well as some earlier studies have shown presence of several special grain boundaries in tin [148, 149] and tin-based solders [118]. Tin-based solders predominantly fail by grain boundary sliding [2, 22, 23, 27, 53, 91, 100, 101, 150]. Hence the presence of such special boundaries (as well as ordinary boundaries) should definitely play a role in the deformation behavior and the ultimate failure of such solders. The following is a summary of investigations of special boundaries in tin.

Grain Boundary Sliding and Migration in Tin Bicrystals: Puttick et. al. [149] studied the effect of grain boundary migration during sliding of grain boundaries in tin bicrystals. They prepared bicrystals of tin and performed two types of deformation tests, shearing and compression. The bicrystals were prepared such that one crystal had an orientation of (001)<100> ((c-axis normal to the plane of paper and a-axis along horizontal x-axis) and the other crystal had an orientation of (001)<-100>. On shearing in the <100> direction the bicrystal at 225°C for 12 hours at a shear stress of 1500g/cm^2 (147kPa), the boundary between the two grains migrated especially on the surface perpendicular to the boundary and normal to the direction of shear. Rounded steps were seen on the surface that were formed where the boundary migrated due to surface tension differences between the boundary and the surface of the specimen, which are not in equilibrium. Such rounded steps were also seen and similarly explained by Mykura [151] using an interferometric technique.

During grain boundary migration, there should be an initial energy difference across the boundary. Also since boundary migration only occurs in these specimens when they are stressed, it is reasonable to assume that the dislocation generated during

deformation can supply the necessary driving force. These dislocations could be randomly arranged or in arrays of low energy which is most likely at such high temperatures (due to climb). Puttick and King [152] observed that sub-boundaries form near the boundary prior to grain boundary migration, that played a role in the local grain boundary migration. The dislocations that supply the energy for migration may be formed due to sources activated by the external shear stress in the interior of the crystal or from places on the boundary itself, where the local grain boundary sliding seized and acted as regions of stress raisers. If these dislocations are produced independent of the grain boundary sliding, then it should be possible to observe boundary migration if the bicrystal is loaded such that there is normal stress on the grain boundary and a resolved shear stress on the operative slip systems which is similar to that imposed during the shear tests in Puttick's work [149]. Puttick then tested this by compressing the bicrystal with load of 5040g/cm^2 (494kPa) applied normal to the grain boundary at 225°C [152]. However after two hours the interference pattern showed no changes and no signs of plastic deformation and no sign of boundary migration. When a shear stress of 1200g/cm^2 (117.6kPa) at 225°C was imposed, there was much more grain boundary migration. It was noted that the resolved shear stresses were smaller in shear tests than the compression experiment for all slip systems studied. *They suggested that the boundary migration does not occur without sliding and there are fewer dislocations moving from the interior of the grain to the boundary in the compression test causing less grain boundary sliding.*

Puttick et. al. [152] presumed that the dislocations were produced by the grain boundary sliding process [153, 154]. When the grain boundary region was studied more

closely in shear by Mykura [151], the interferrometry fringes showed dramatic changes along the grain boundary as soon as grain boundary sliding started. Up to 0.05mm on either side of the boundary, one could see corrugations of the order of 10^{-5} cm. No deformation was observed elsewhere. The initial step height was about 1μm, which increased to 60μm after 1 hour of deformation. These features were explained as follows: initially dislocations were generated by the boundary sliding process. When taken along with the grain boundary migration, in the early stages of sliding most of the dislocations escape by climb and glide, and the ones near the surface disappear completely. Some of the dislocations are retained near the boundary, *which form arrays of low energy that eventually help in grain boundary migration.* In short, local grain boundary migration was observed along with grain boundary sliding. *The strain energy of dislocations provides the activation energy for the migration.* The free surface energy also affects migration, with step formation.

Effect of Pressure and Temperature on Migration of Tilt boundaries in Tin Bicrystals: The mechanisms operating during grain boundary migration have not been investigated in detail. Theoretically, the grain boundary migration / mobility is understood to be dependent on temperature, however less is known about the driving force needed for migration. The introduction of the activation volume V^* parameter (which is defined as the increase in volume in the original state to reach the activated state) in the presence of a hydrostatic pressure would help us understand the driving force necessary for migration of a grain boundary. The dependence of the activation volume on the misorientation angle i.e. ordering of the grain boundary could also be studied.

Molodov et. al. [155] carried out such experiments on tin bicrystals to study the mobility of <001> tilt boundaries and this is discussed next.

Molodov et. al. [155] studied the motion of differently misoriented grain boundaries using a constant driving force for migration technique. This is represented by the formula: $\Delta F = \sigma \cdot \Omega / a$, where σ is the surface energy of grain boundary, Ω is the atomic volume and a is the width of the grain to be consumed [156]. The boundaries they measured were both special boundaries, (22.5, 28 and 37° @ [001]) and general boundaries (25, 33.5 and 41°).

Molodov et. al. [155] derived a boundary mobility term 'A' given by the equation, $A = \frac{v}{(1/a)} = A_0 \exp(\frac{-G}{kT}) = A_0 \exp(\frac{-E}{kT}) \exp(\frac{-PV^*}{kT})$, where v is the velocity of migration, A_0 is the pre-exponential factor, G is the free activation energy of the migration process, E is the activation energy for migration, P is the pressure, V^* is the activation volume. They showed the changes in the activation energy E and pre-exponential factor A_0 for several different boundary misorientations for both special and general boundaries. The special boundaries are more mobile for a given hydrostatic pressure as compared to general boundaries and the hydrostatic pressure affected the grain boundary mobility significantly. The slope of the straight line in the mobility (A) versus pressure (P) plot was used to calculate the activation volume (V^*). Special boundary misorientations have the smallest activation energy for migration (V^* as well as E and A) and these parameters decrease in value as the degree of coincidence increased (Σ decreases).

Comparing this result with the absolute rate theory, where the rate of migration is given by the equation $V = b\nu \frac{\Delta F}{KT} \exp(\frac{-G}{KT})$, where ν is the Debye frequency and b and ΔF are the boundary displacement due to act of atomic transition and driving force respectively, the question that arises is whether the act of atomic jump or transition across the boundary is one comprising of single atom jumps or if several atoms jump simultaneously [155]. For the mechanism of individual transitions, they concluded that the activation energy for migration is much higher than bulk self-diffusion. Also the activation volume for special boundaries is closer to that of bulk self-diffusion whereas for general boundaries it exceeds that of lattice diffusion. Hence it was not possible to explain the experimental values of the migration parameters based upon single atom jumps. For a group transition, [155] they assumed that a group of say n atoms jump into the boundary and then jump from the boundary in to the other grain to make the transition across the grain boundary. The activation migration parameters for this two step process were derived and are shown in Table IV. Using two independent parameters based on the activation energy E (n_E) and the pre-exponential factor A_0 (n_S), in the mobility equation above and shown in Table IV, the n values obtained were very close (see n_E and n_S). This enabled the determination of the change in atomic volume during the transition, $\Delta V = V^* / n$ as indicated in the table. All special boundaries had a value of ΔV close to 0.24 x 10^{-3} m^3/kg.atom and general boundaries had values close to 0.42 x 10^{-3} m^3/kg.atom, almost twice that of special boundaries. Hence there is a distinct activation difference in the migration behavior and structure of special boundaries compared to non-special ones.

Table IV: Analysis Of Experimental Results Obtained By Molodov et. al. [155] With The Group Mechanism Theory For Grain Boundary Migration.

	φ (°)	$n_E = \frac{E\lambda}{\sigma_0\Omega}$	$n_S = \frac{\ln A_0 \lambda K T_c}{\sigma_0\Omega}$	$\Delta V = \frac{V^*}{n_E}(10^{-3}\frac{m^3}{kg.atom})$
Σ = 13	φ = 22.5°	20	17	0.24
	φ = 25°	28	24	0.41
Σ = 17	φ = 28°	21	18	0.24
	φ = 33.5°	31	28	0.42
Σ = 5	φ = 37°	13	10	0.24
	φ = 41.5°	25	22	0.42

Regions of existence of Special and Non-special grain boundaries: In the light of the work done by Molodov et. al. [155], special grain boundaries are considered important and their presence can play a significant role in the behavior of the material. Shvindlerman et. al. [148] studied the regions of existence of special and non-special boundaries and the conversion of one type into the other. As seen earlier, and from studies done in other materials, properties of special boundaries vary significantly from the general ones (non-special) [157-161]. Most of the special boundaries or CSL boundaries are characterized by lower energy values than general boundaries. Although the CSL nature is violated when one deviates slightly from the CSL misorientation angle, the special boundary character is maintained up to a certain finite deviation from the CSL misorientation. *This is attributed to the special boundary structure, which is accommodated by the presence of grain boundary dislocations* [162, 163]. The Burger's vector for such grain boundary dislocations is determined using the DSC (Displacement Shift Complete) lattice [164] and the length of this vector 'b' decreases with increasing Σ value. The maximum value of Σ up to which such special boundaries demonstrate

distinct properties is still under question and it is still not clear as to how these properties depend on temperature and whether they remain special at higher temperatures. Hence it is important to know what establishes the range of misorientations angles and temperature over which a special boundary would maintain their special behavior.

Gleiter et. al. [165] found that the number of special boundaries increase with decreasing temperature as well as with increasing pressure [166]. Also, studies based on Brandon's model [162, 167] indicate that the departure from a perfect special grain boundary misorientation due to a network of dislocations is also considered to be special. The acceptance angle $\Delta\varphi$, for which boundaries exhibit Σ-boundary-like properties is given by $\Delta\varphi = \Delta\varphi_0\Sigma^{-m}$, where $\Delta\varphi_0$ is usually 15° and m= -½. [167-170]. Beckmann et. al. [171, 172], Balluffi et. al. [173], and Wagner et. al. [174] have shown more correctly in their work the presence of special boundaries in an angular interval of ±0.01°. Hence, generally special boundaries defined as those boundaries with $\Sigma<29$, whereas boundaries including $\Sigma>29$ are considered random or general in cubic metals. This differentiation has been deduced by correlating the special fractions with the observed properties (special fraction is the total number of boundaries ($1<\Sigma<29$) / total number of boundaries). The representation of the Σ distribution of boundary types on a map is called the grain boundary character distribution. It is seen that there is a threshold Σ, above which the grain boundaries lose their special properties [168].

Hence one would treat special boundaries as those consisting of equilibrium network of grain boundary dislocations with Burger's vectors corresponding to the DSC-lattice (see explanation of CSL above) but also those that reveal local grain boundary dislocations; maybe formed due to dissociation of boundary-absorbed lattice dislocations.

Good examples are given by Balluffi et. al. [173-175] in their paper on <001> twist boundaries in gold and magnesium oxide.

By looking at data from several experiments in different materials Shvindlerman et. al. [148] came to the conclusion that special boundaries with low Σ are present as special up to a certain temperature T (close to T_m). Boundaries with less ordering (higher Σ) show special properties only up to a certain finite (lower) temperature. Also the existence of angular interval over which such boundaries show special nature decreases with growing Σ. Based on the theory of Pokrovski and Talapov [176], as one moves away ($\pm\Delta\theta_\Sigma$) from the special boundary misorientation θ_Σ, there are dislocation structures present that can accommodate the deviation. As $\Delta\theta_\Sigma \rightarrow 0$, the spacing between the grain boundary dislocations tends to infinity, and at a small $\Delta\theta_\Sigma$, there is no misfit dislocation observed. This is shown by work of Papon et. al. [177] where for a Σ=9 boundary and $\Delta\theta_\Sigma$=0.005°, no misfit dislocations were observed, whereas for $\Delta\theta_\Sigma$=0.1°, they were observed [178, 179]. As the $\Delta\theta_\Sigma$ value increases, the energy of the misfit-dislocation system increase and at a particular value of $\Delta\theta_\Sigma$, the general grain boundary behavior is realized. See Ref. [177] for a figure showing this result for a Σ=9 boundary (not in tin). Also it is seen that the transition temperature from special to non-special boundaries drops with increasing Σ and that the special properties are manifested only by boundaries with $\Sigma <$ a certain Σ_{max} as described above. Zisman and Ribin [180] give a good overview of this phenomenon in their paper. Shvindlerman [148] also found that the angular interval of existence of special boundaries decreases with increasing Σ. Hence there are regions of special and non-special boundaries present. Presence and behavior of such boundaries at high temperatures, and the changes in their behavior can significantly

affect the overall performance of the material. How the transition occurs between the two is still not fully characterized and understood, and will be discussed in the following sections.

Transformation of Σ17 Special Tilt Boundary to General Boundaries in Tin: It was shown by Shivinderman et. al. [148] that the width of the misorientation angle interval within which the boundary possesses a special structure as well as the special properties exhibited by such boundaries decreases exponentially with increase in Σ. The maximum temperature at which such special boundaries can maintain their special behavior also decreases with increasing Σ. Hence at a distinct temperature, only certain boundaries with $\Sigma < \Sigma_{max}$ will show the special structure and properties. Maksimova et. al. [181] conducted detailed studies about the effect of thermodynamical and kinetic properties of the Σ17 special tilt boundary in tin, to determine the misorientation angle and temperature at which such a phase transition from special to general grain boundary transition occurs.

The grain boundary phase transition is manifested by changes in the surface tension of the boundary. Figure 1.10 shows the change in surface tension between a special σ_{sp} and general boundary σ_g. In general, $(\partial\sigma/\partial T)_g > (\partial\sigma/\partial T)_{sp}$ since special grain boundaries are more ordered and hence their entropy is smaller: $(\partial\sigma/\partial T)_g = -S$. Hence boundaries with misorientation angle slightly deviated from the exact CSL angle can exist, but in different structural modifications described later.

It is known [182] that for a single component system, the total number of phases existing at a grain boundary should equal 3. In actuality, the surface tension of each boundary is not measured, but the ratio of the σ_g to the surface free energy is measured, by a thermal grooving technique or by using triple points. Maksimova et. al. [181]

studied the surface tension of tilt boundaries with misorientation angles ranging from 25-30° which were near the special misorientation of 28.07° (Σ17). The specimen contained two general grain boundaries (30-32°, which were beyond the special misorientation) and one special boundary. The ratio of the angle at the triple point gave the energy of the boundaries. Also, the special grain boundary with misorientation angle θ_1 ranging from 26.5-29.5° contained secondary grain boundary dislocations [183, 184] (discussed later) such that the misorientation angles for the general grain boundaries θ_2 and θ_3 would lie outside the interval 26.5-29.5° when $32° \geq \theta_1$. See Figure 1.11 (discussed below).

The plot of the temperature dependence of σ_1/σ_g for 10 different [001] tilt boundaries in the range of 25.5 to 30° at a temperature of $0.85T_m$ to T_m shows that the σ_1/σ_g (specific/general) ratio increases, reaches maximum at 28.3° and then starts decreasing before finally becoming flat again. The maximum was seen to reach at 28.3°, which is close to the 28.07° for the CSL angle. This implies that the position of the humps in the curves is independent of the driving force, the temperature sequence (heating or cooling) followed, and the misorientation angle of the general grain boundaries. Hence the position of the critical temperature T_c peaks with respect to the σ_1/σ_g ratio is dependent only on the misorientation angle of the special boundary and is independent of other thermodynamical, geometrical and kinetic factors. The presence of these humps at temperature T_c implies the transition of the Σ17 boundaries into a general boundary. The shape of this curve matches fairly well with the schematic shown in Figure 1.10 for the first order transition. Figure 1.11 shows the critical temperature as a function of the misorientation angle adapted from Ref. [181]. Semicircles mark the regions where the grain boundary behaves as a general boundary. The line demarcates

the region of special boundaries from the general boundaries and has a symmetrical bell shape with the peak at 28.3°. From the orientation dependence of the surface tension, it was also seen that the special boundaries have a lower surface tension than the general ones.

Summary on Special Boundaries in Tin: It is seen from the above results that rotation of one lattice say L_1 with respect to another L_2 by an angle θ, may give rise to an ordering of the structure. For small misorientations (<15°), the grain boundary consists of lattice dislocations, which are separated by regions of almost perfect lattice. The spacing between the dislocations is determined by the 0-lattice period $C_1 = P_{01} = b_1 /[2\sin(\theta/2)]$, where b_1 is the Burger's vector of the lattice dislocation. For larger misorientation angles (θ between 15 to 60°), the idea of individual dislocations loses sense because d_1 (the spacing distance) is in the range of 2-0.5nm. These grain boundary dislocations with lattice Burger's vectors are called primary grain boundary dislocations. The equilibrium boundaries consisting of only the primary grain boundary dislocations are termed as general boundaries. Hence through experiments it has been seen that at a fixed position of the misorientation axis and invariable grain boundary position, the structure of a general grain boundary is practically fixed. The geometry of the network of grain boundary dislocations remains fixed (the Burger's vector and type are fixed), only the spacing between them changes.

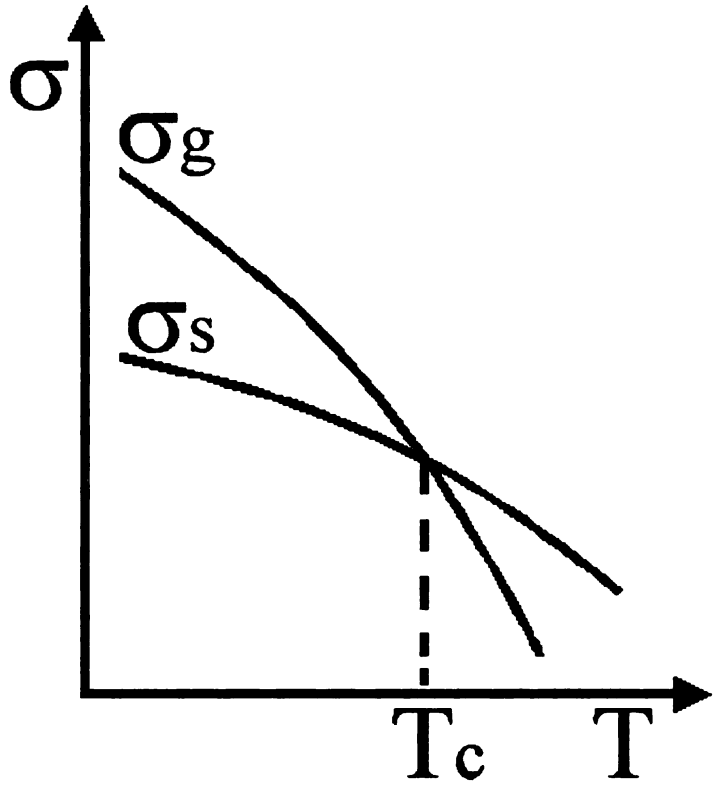

Figure 1.10. Schematic of the temperature dependence of surface tension of special σ_s and general boundaries σ_g adopted from Ref. [181]. The first type of phase transition occurs at the critical temperature T_c. Above T_c the structure of general boundaries is realized and below T_c the special boundary structure is realized.

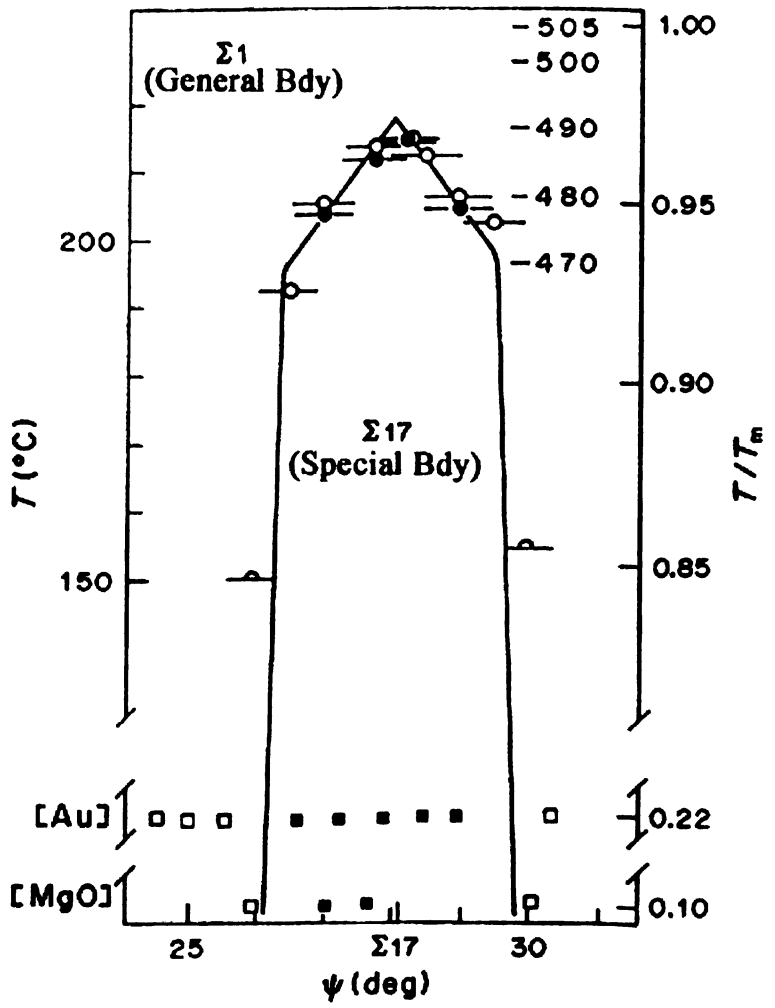

Fig. 8. Phase equilibrium like of Σ17 special boundaries and Σ1 general boundaries in tin constructed with respect to T_c. Open circles stand for the T_c values obtained by as from the temperature dependences of the surface tension [2], solid circles—from the temperature dependences of the boundary migration rate. The lower part of the figure presents the published data on the investigation of the structures of the special Σ17 twist boundaries in gold at $T/T_m = 0.2$ [12] and in magnesium oxide at $T/T_m = 0.1$ [13]. Solid squares correspond to the boundaries which exhibited secondary GBD's, open squares—to the boundaries formed by primary GBD's alone (from the diffraction data).

Figure 1.11. Adapted from Ref. [181]. Phase transformation of Σ17 special boundaries to general boundary.

At some special misorientation angles $\theta = \theta_{sp}$ the 0-lattice sites for the two lattice L_1 and L_2, are coincident with $\Sigma > 1$. In this case $P_{01} = \frac{m}{n}a$, where a is the L_1 and L_2 lattice period. Such special boundaries have lower energies and their properties are significantly different from general boundaries. The low energy of such special boundaries makes them highly favorable, and hence even for small deviations from the special misorientation angles θ, their structure is preserved. The structure of such special boundaries is also different from the general boundaries; Figure 1.12 shows that they have special boundary structure separated by grain boundary dislocations to complete the unit. The Burger's vector for these dislocations is not equal to b_1 (also for small variations from the perfect θ angle). These are termed as secondary grain boundary dislocations, and their Burger's vectors are the basal vectors on the DSC-lattice for that particular Σ. In this case $d_2 = P_{02} = b_\Sigma / [2\sin(\Delta\theta/2)]$ and the Burger's vector b_Σ for the secondary grain boundary dislocation is related to the Burger's vector for the lattice dislocation by: $b_\Sigma = b_1 / \sqrt{\Sigma}$. These *secondary* grain boundary dislocations are seen in electron micrographs, though networks of such dislocation have not been seen so far. The spacing between such secondary grain boundary dislocations is in the range of 50-250Å, which exceeds those between primary grain boundary dislocations by 5-20 times. Hence the structure of the general grain boundary is different from the special boundaries: the special boundaries have primary grain boundary dislocations alternating with the secondary grain boundary dislocations whose Burger's vector is smaller than the primary dislocations and is derived from the value of Σ.

To summarize the above discussion, at a particular value of misorientation angle θ, close to a special boundary condition, $\theta = \theta_{sp} + \Delta\theta$, two different boundary structures can exist; one involving primary dislocations alone with a period $d_1 = d_1 (\theta = \theta_{sp} + \Delta\theta) = b_1 / [2\sin(\theta/2)]$, or one which consists of special boundary portions with the periodicity $d_{1sp} = d_1 (\theta_{sp}) = b_1 / [2\sin(\theta_{sp}/2)]$ separated by secondary grain boundary dislocations having the period $d_2 = d_2 (\Delta\theta) = b_\Sigma / [2\sin(\Delta\theta/2)]$. One of the two structures is realized depending on the energetics of the system. With an increase of $\Delta\theta$, the energy of the secondary grain boundary dislocation is increased and at a specific $\Delta\theta$, the grain boundary structure changes. This is the phase transition that was mentioned earlier. Such a transition can also be seen with temperature since the free energy of general boundaries decreases more rapidly as compared to special boundaries.

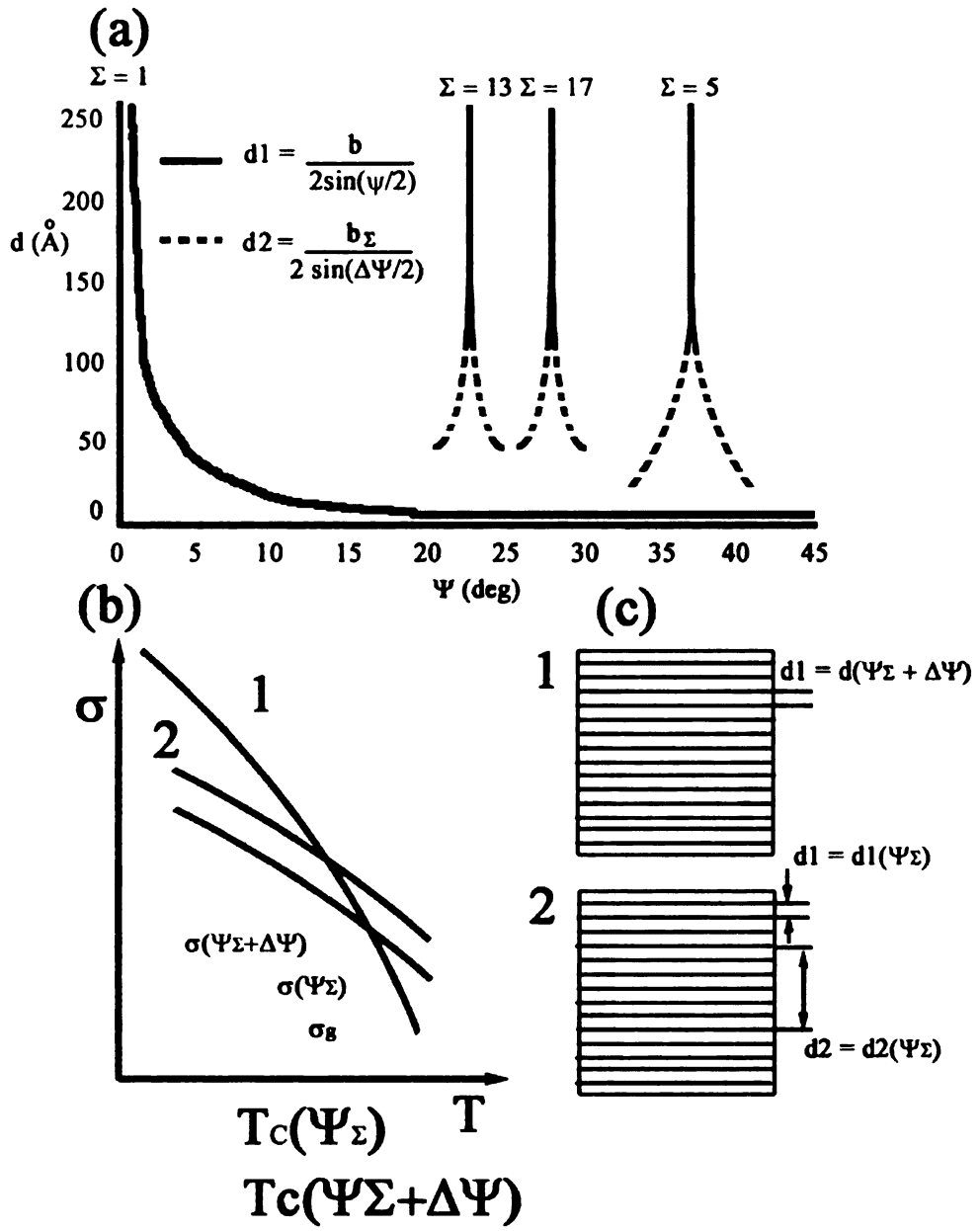

(a) Spacing between primary d1 and secondary d2 grain boundary dislocations as a function of the misorientation angle (Ψ), from the data of [12].
(b) Change of surface tension.

Figure 1.12. Adapted from Ref.[181]. Illustration showing the interaction between grain boundary dislocation and secondary dislocation at CSL lattice.

Grain boundaries play an important role in the deformation of Sn-based lead-free solders. Knowing the grain boundary character is one way to identify the impact of the grain boundaries in different deformation processes. Puttick's study above reveals that the grain boundary migration does not occur without sliding. Dislocations are needed for the sliding / migration process and these are formed close to the grain boundary prior to grain boundary migration. Several special boundaries are found in tin, though only simple CSL boundaries were used in studies listed above. These studies lay the background for the proposed work.

CSL boundaries seem to obey the special characteristics and the special behavior is seen up to a few degrees on either side of the CSL. It was ascertained that special boundaries about the [001] axis also have high mobility with lower activation energy than general boundaries, which could have implication on the overall sliding characteristics. The mobility of twin boundaries in tin are not characterized, so nothing is known about their mobility and activation energy.

Sn-Ag based lead-free solders have a large number of special boundaries [9, 118] thus it becomes imperative to understand their impact on several deformation processes experienced by solder interconnects. CSL boundaries are observed in such joints, along with solidification twins. The above studies lay some of the ground work needed to study the grain boundary sliding seen in these solders, and implies that if the grain boundary character contains a considerable number of the special boundaries, micro texture measurements are needed to ascertain their presence in order to determine their impact on deformation processes.

1.7. SPECIFIC AIMS

On the basis of this state of understanding, the main objective of this study is to characterize deformation processes in Sn-Ag solders and study their effect on the mesotexture evolution in solder joints, and its relationship to damage nucleation and failure during thermomechanical fatigue (TMF). Deformation in Sn-Ag solder interconnects is often coupled with grain boundary sliding, so it is necessary to understand how grain boundary sliding / damage accumulation occurs and evolves during TMF.

The specific aims of this study are:

1. **To characterize the microstructural evolution of Sn-Ag solder joint in aging, creep, and TMF testing using Orientation Imaging Microscopy and to understand the impact of deformation on the mesotexture evolution.**

Crystallographic orientations play a fundamental role in deformation of a material. Due to the lack of knowledge of mesotexture development in Sn-Ag solder interconnects, initial in-depth characterization during different processes was carried out to ascertain if texture and certain grain boundary types contribute to the damage. Preliminary studies had shown that small solder joints consist of multicrystals (anywhere from 2-4 grains), which implied that the deformation should be strongly influenced by the orientation of the crystals.

Since most of the joints undergo thermal cycling in service, actual component type joints were fabricated. The intention was to study three different joint geometries; each with a different stress state on fabrication, to study the effect of the inherent stresses

present in such joints on the TMF behavior and their influence on the mesotexture. As supporting studies, micro textural changes during creep and aging are also carried out because solders experience high temperatures in service, where creep and aging are important parts of the deformation history that affects joint reliability. To understand the more fundamental aspects of grain boundary character in tin and tin-based solders (Sn-3.5Ag and Sn-3.7Ag-0.7Cu), equilibrated microstructures of bulk specimens were also studied using OIM.

2. **To identify the modes of damage and determine existence of a correlation between the damage and the mesotexture. Thereafter, examine the probable cause for such damage and determine the contributing factors to failure of such joints.**

Once the deformation in the joint is carefully characterized, it is important to determine if there is a correlation between the damage seen on the surface from scanning electron micrographs (slip bands and grain boundary sliding / decohesion) and the mesotexture. This was carried out through several steps: a) Firstly, analysis was done to determine the distribution and the total fraction of the different boundary types present in the mesotexture and ascertain if certain boundary types are more closely associated with damage. This gave some statistical basis to determine whether grain boundary sliding and decohesion is related to certain specific boundary types. b) Secondly, using a Schmid factor analysis and the crystal orientation obtained from aim 1, it was possible to determine if certain slip systems are preferentially activated and contribute to the damage (in the form of slip bands seen on the surface) as well as sliding. c) Once sufficient

analysis was carried out causes that contribute to damage could be identified. This will satisfy aim 2.

3. **To model the deformation of the solder joints using the VPSC code to provide further insight for identifying the deformation mechanisms in Sn-based solders.**

The data collected above in aim 1 was also used for modeling the deformation using a VPSC simulation to accomplish aim 3. To accomplish this aim, a) the stress state in the joint and b) the operative slip systems were identified. Using a finite element analysis, the stress state in the joint was determined. Quasi-static shear testing at higher rates was carried out to determine how slip activity varied with stress and strain rate. This enabled comparison of the experimental data obtained from two different strain rate tests with the VPSC code, and the ability to identify relative activity of different slip systems in different conditions. The completion of this study contributes significantly to our understanding of deformation behavior of Sn-Ag solders, and identifies the contributing processes to failure, which can be used to identify strategies to counteract damage and improve solder joint reliability.

1.9 REFERENCES:

1. E. Bastow, Advanced Materials and Processes, Dec 2003. **26**.

2. J.Glazer, J. Electron Mater., 1994. **23**(8): p. 693-700.

3. M.McCormack, and S.Jin, JOM, 1993. **45**(7): p. 36-40.

4. S.Jin, JOM, 1993. **45**(7): p. 13.

5. S.K.Kang, and A.K.Sarkhel, J. Electron. Mater., 1994. **23**: p. 701-707.

6. W.L.Winterbottom, JOM, 1993. **45**: p. 20.

7. A.W.Gibson, S.Choi, T.R.Bieler, and K.N.Subramanian, IEEE 5th International Symposium on Electronics and the Environment, IEEE, Piscataway, NJ, 1997: p. 246.

8. R.N. Wild, Welding Research, 1972: p. 521.

9. A.U.Telang, Masters Thesis, Material Science, Michigan State University, East Lansing, 2002.

10. J. J.W.Morris, and H.L.Reynolds, Design and Reliablility of solders and solder interconnects, edited by R.K.Mahidhara, D.R.Frear, S.M.L.Sastry, K.L.Murty, P.K.Liaw, W.L.Winterbottom, TMS Annual Meeting Warrendale, PA, 1997.

11. Z.Mei, and J. J.W.Morris, ASME Winter Annual Meeting, Atlanta, GA, Dec. 1991.

12. A.W.Gibson, S.Choi, K.N. Subramanian, and T.R. Bieler, Design and Reliability of Solders and Solder Interconnections, edited by R.K. Mahidhara, D.R. Frear, S.M.L. Sastry, K.L. Murty, P.K. Liaw, W.L. Winterbottom, TMS, Warrendale, PA, 1997: p. 241.

13. E.A.Holm, G.N.Hassold, and M.A.Miodownik, Acta Mater., 2001. **49**(15): p. 2981.

14. E.A.Holm, and C.C.Battaile, JOM, 2001. **53**(9): p. 20.

15. M.Miodownik, E.A.Holm, and G.N.Hassold, Scr. Mater., 2000. **42**(12): p. 1173.

16. D.Fan, L.Q.Chen, and S.P.P.Chen, J. Am. Ceram. Soc., 1998. **81**(3): p. 526.

17. A.D.Rollett, D.J.Srolovitz, M.P.Anderson, and R.D.Doherty, Acta Metall. Mater., 1992. **40**(12): p. 3475.

18. J.G.Lee, Doctoral Dissertation, Chemical Engineering and Materials Science, Michigan State University, East Lansing, 2004.

19. F. Guo, Ph.D. Thesis, Michigan State University, East Lansing, MI, 2002.

20. S. Choi, Ph.D. Thesis, Michigan State University, East Lansing, MI, 2002.

21. J.G. Lee, A.U. Telang, T.R. Bieler, and K.N. Subramanian, J. Electron. Mater., 2002. **31**(11): p. 1152.

22. S.Choi, J.G.Lee, K.N.Subramanian, J.P.Lucas, and T.R.Bieler, J. Electron Mater., 2002. **31**(4): p. 292.

23. S.Choi, Ph.D. Thesis, Michigan State University, East Lansing, MI, 2002.

24. D.R.Frear, JOM, May 1996: p. 49-53.

25. H. Rhee, J.P. Lucas, and K.N. Subramanian, J. of Materials Science: Materials in Electronics, 2002. **13**(8): p. 477.

26. S.Jadhav, Master's Thesis, Michigan State University, East Lansing, MI, 2001.

27. F.Guo, Ph.D. Thesis, Michigan State University, East Lansing, MI, 2002.

28. K.N.Subramanian, T.R.Bieler, and J.P.Lucas, J. Electron. Mater., 1999. **28**: p. 1176.

29. J.Siegelko, S.Choi, K.N.Subramanian, J.P.Lucas, and T.R.Bieler, J. Electron. Mater., 1999. **28**: p. 1184.

30. S.Choi, K.N.Subramanian, J.P.Lucas, and T.R.Bieler, J. Elect. Mater., 2000. **29**: p. 1249.

31. T.Y.Lee, W.J.Choi, and J.W.J. K.N.Tu, S.M.Kuo, J.K.Jin, D.R.Frear, K.Zeng and J.K.Kivilahti, J. Mater. Res., 2002. **17**(2): p. 291.

32. Y.Nakamura, Y.Sakakibara, Y.Watanabe, and Y.Amamoto, Soldering & Surface Mount Technology, 1998. **10**(1): p. 10.

33. E.Schmid, Intl. Conf. On Physics, London and Cambridge, 1934. **2**: p. 161-170.

34. B.Duzgun, A.E.Ekinci, I.Karaman, and N.Ucar, J. of Mech. Behavior of Materials, 1999. **10**(3): p. 187-203.

35. P.W.Bridgman, Proc. Of the National Acad. Of Sciences,, 1924. **10**(10): p. 411-415.

36. M.Fujiwara, and T.Hirokawa, J.Japan Inst. Metals, 1987. **51**(9): p. 830-838.

37. B.D.Hong, S.K.Chang, and D.J.Jensen, European Magnetic Materials and Applications, Material Science Forum, 2001. **373**(3): p. 737-740.

38. C.W.Tai, K.Z.Baba-Kishi, and K.H.Wong, Micron, 2002. **33**(6): p. 581-586.

39. F.J.Humphreys, Journal of Microscopy, September 1999. **195**(3): p. 170-185.

40. M.Hasegawa, and H.Fukutomi, Journal of the Japan Institute of Metals, January 2002. **66**(1): p. 40-45.

41. T.R.Bieler, and S.L.Semiatin, Intl. Journal of Plasticity, 2002. **18**: p. 1165-1189.

42. V.Randle, and B.Ralph, Proc. Of the Royal Society of London, Series A, Mathematical ad Physical Sciences,, January 1988. **415**(1848): p. 239-256.

43. U.F.Kocks, C.N.Tomé, and H.-R.Wenk, *Texture and Anisotropy, Preferred Orientations in Polycrystals and their Effect on Material Properties*. Vol. ch.11. 1998: Cambridge University Press.

44. J.F.L.Goldstein, PhD. Thesis, University of California, Berkeley, November 1993.

45. J. J.W.Morris, J.L.F. Goldstein, and Z.Mei, JOM, July 1993. **45**(25).

46. J. J.W.Morris, D.Grivas, D.Tribula, T.Summers, and D.Frear. in *Proceedings of 13th Naval Weapons Electronics Manufacturing Seminar, China Lake, CA*. 1989.

47. J.L.F.Goldstein, and J. J.W.Morris, J. Electron Mater., 1994. **23**: p. 477.

48. D.Tribula, PhD Theis, University of California at Berkeley, June 1990.

49. S.Jang, J.Wolf, O.Ehrmann, H.Gloor, H.Reichl, and K.W.Paik. *Investigation of UBM System for Electroplated Sn/37Pb and Sn3.5Ag Solder ECTC.* in *Paper presented at 51st Electronic Components and Technology Conference ECTC, Lake Buena Vista, Orlando*. 2001.

50. G.E.Dieter, *Mechanical Metallurgy, S.I. Edition*. 1988: McGraw-Hill Book Company.

51. R.W.Evans, and B.Wilshhire, *Introduction to Creep*. 1999, United Kingdom: Oakdale Printing Company Limited, Poole.

52. J.E.Bird, A.K.Mukherjee, and J.E.Dorn, Israel University Press, Jerusalem, 1969: p. 255-342.

53. K.L.Murty, and I.Turlik. *Deformation Mechanisms in Lead-Tin Alloys, Application to Solder Reliability in Electronic Packages.* in *Proceedings of 1st joint conference on electronic packaging ASME/JSME.* 1992.

54. H.Rhee, K.N.Subramanian, A.Lee, and J.G.Lee, Soldering & Surface Mount Technology, 2003. **15**(3): p. 21-26.

55. M.Harada, and R.Satoh, IEEE transactions on Components, Hybrids and Manufacturing Technology, December 1990. **13**(4): p. 736-742.

56. J.G.Lee, F.Guo, S.Choi, K.N.Subramanian, T.R.Bieler, and J.P.Lucas, J. Electron Mater., 2002. **31**(9): p. 946-952.

57. W.D.Kingery, H.K.Bowen, and D.R.Uhlmann, *Introduction to Ceramics.* 2nd edition ed. 1976: John Wiley & Sons.

58. H.J.Gough, Am. Soc. Test. Mater. Proc., 1933. **33**(2): p. 3-114.

59. W.A.Wood, Bull. Inst. Met., 1955. **3**: p. 5-6.

60. C.H.Raeder, J. R.W.Messler, and L.F.Coffin, J. Electron Mater., 1999. **28**(9): p. 1045-1055.

61. R.W.G.Wyckoff. 2nd Edition, Univ. of Arizona, Tuscon, Arizona ed. Crystal Structures. Vol. Volume 1. 1963: Inter Science Publication, New York.

62. E.Schmid, and W.Boas, *Plasticity of Crystals with Special Reference to Metals a translation from the German by F.A.Hughes & Co., Limited, of "Kristallplastizitat mit besonderer Berucksichtigung der Metalle".* 1950, London. 85.

63. B.Chalmers, Proc. Phy. Soc. London, 1935. **47**: p. 733.

64. C.S.Barrett, Trans. AIME, 1945. **161**: p. 15.

65. D.Frear, and H.Morgan, *The Mechanics of Solder Alloy Interconnects*, ed. J.H.Lau. 1994.

66. J.G.Lee, A.U.Telang, T.R.Bieler, and K.N.Subramanian, J. Electron Mater., 2002. **31**(11).

67. P.Villars, and L.D.Calvert, *Pearson's Handbook of Crystallographic Data for Intermetallic Phases*. 2nd edition ed. 1991: Materials Park, OH: ASM International.

68. M.Hansen, *Constitution of Binary Alloys*. 2nd edition, Metallurgy and Metallurgical Transactions, Engg. Series ed. 1958: McGraw Hill Book Company.

69. D.W.Henderson, J.J.Woods, T.A.Gosselin, J.Bartelo, D.E.King, T.M.Korhonen, M.A.Korhonen, L.P.Lehman, E.J.Cotts, S.K.Kang, P.A.Lauro, D.Y.Shih, C.Goldsmith, and K.J.Puttlitz, J. Mater. Res., 2004. **19**(6): p. 1608-1612.

70. A.Rosenberg, and W.C.Winegard, Act. Met., 1954. **2**: p. 342-343.

71. K.C.Chen, A.U.Telang, J.G.Lee, and K.N.Subramanian, J. Electron Mater., 2002. **31**(11).

72. J.G.Lee, F.Guo, K.N.Subramanian, and J.P.Lucas, Soldering and Surface Mount Technology, 2002. **14**(2): p. 11-17.

73. Y.Kariya, Y.Hirata, and M.Otsuka, J. Electron Mater., 1999. **28**(11): p. 1263-1269.

74. Z.Mei, J. J.W.Morris, M.C.Shine, and T.S.E.Summers, J. Electron Mater., 1991. **20**: p. 599.

75. H.L.Reynolds, S.H.Kang, and J. J.W.Morris, J. Electron Mater., 1999. **28**: p. 69.

76. J. J.W.Morris, and Z.Mei. *Solder Mechanics: A State of the Art Assessment Chapter 6.* in *TMS Warrendale, PA*. 1991.

77. H.S.Betrabet, S.M.McGee, and J.K.McKinlay, Scripta Metallurgica et Materialia, 1991. **25**: p. 2323-2328.

78. V.D.Kodgire, *Material Science and Metallurgy*. 5th edition ed. 1997: Everest Publishing House, Pune, India.

79. R.Satoh, *Thermal Stresses and Strain in Microelectronics Packaging*, ed. J.H.Lau. 1993: New York: Van Nostrand Reinhold. 500.

80. J.S.Hwang, and R.M.Vargas, Soldering and Surface Mount Technology, 1990. **4**(2): p. 27.

81. C.J.Thwaites, and W.B.Hampshire, Weld Res. Supp., 1976. **323**.

82. W.J.Timlinson, and A.Fullylove, Journal of Material Science: Materials in Electronics, 1992. **27**: p. 5777.

83. K.S.KIm, S.H.Huh, and K.Suganuma, Mater. Sci. Eng., A, 2002. **333**(1-2): p. 106-114.

84. H.Mavoori, J.Chin, S.Vaynman, B.Moran, L.Keer, and M.Fine, Journal of Electron. Mater., 1997. **26**(7): p. 783-790.

85. Z.Guo, J. A.F.Sprecher, H.Conrad, and M.Kim, Materials Developments in Microelectronic Packaging, ASM, Materials Park, OH, 1991.

86. J.L.Marshall, and S.R.Walter, Intl. J. Hybrid Microelectronics, 1987. **10**: p. 11.

87. R.Darveaux, and K.L.Murty, Proc. Of TMS-AIME Symposium on Microstructures ans Mechanical Properties of Aging Materials, Chicago, IL, Nov. 1992.

88. J.Howell, A.Telang, J.G.Lee, S.Choi, and K.N.Subramanian, Journal of Materials Science: Materials In Electronics, 2002. **13**(6): p. 335-344.

89. J.G. Lee, F. Guo, S. Choi, K.N. Subramanian, T.R. Bieler, and J.P. Lucas, J. Electron. Mater., 2002. **31**(9): p. 946.

90. H.Rhee, and K.N.Subramanian, J. of Electron. Mater., 2003. **32**(11): p. 1310-1316.

91. K.L.Murty, M.D.Mathew, Y.Wang, and F.M.Haggag, Minerals, Metals and Materials Society/AIME, 1998: p. 145-152.

92. B.P.Kashyap, and G.S.Murty, Mater. Sc. and Eng., 1981. **50**: p. 205-213.

93. R.Subrahmanyan, Ph.D. Thesis, Cornell University, 1990.

94. P.M.Hall, I.E.E.E. Trnasaction son Components, Hybrids and Manufacturing Technology,, Dec. 1984. **CHMT-7**(4): p. 314-327.

95. H.D.Solomon, Transactions of th ASME, June 1991. **113**: p. 102-108.

96. M.Y.Wu, and O.D.Sherby, Acta Met. et mat., 1984. **32**(9): p. 1561-1572.

97. F.A.Mohamed, K.L.Murty, and J. J.W.Morris, Metall. Trans., April 1973. **4A**: p. 935-940.

98. V.I.Igoshev, J.I.kleiman, D.Shangguan, C.Lock, S.Wong, and M.Wiseman, J. Electron Mater., 1998. **27**(12): p. 1367-1371.

99. R.Darveaux, and K.Banerji, IEEE, 1992: p. 538-551.

100. F.Guo, J.P.Lucas, and K.N.Subramanian, Journal of Material Science: Materials in Electronics, 2001. **12**: p. 27-35.

101. S.Choi, J.G.Lee, F.Guo, T.R.Bieler, K.N.Subramanian, and J.P.Lucas, JOM, June 2001: p. 22-27.

102. K.N.Subramanian, A.Lee, S.Choi, and P.Sonje, J. Electron Mater., 2001. **30**(4): p. 372-378.

103. S.Sugawara, and J.Watanabe, J. Japan Inst. Metals, 1999. **63**(8): p. 1002-1008.

104. K.Honda, Jpn J Appl Phys, 1979. **18**(2): p. 215-224.

105. K.Ojima, and T.Hirokawa, Jpn J Appl Phys, 1983. **22**(1): p. 46-51.

106. J.E.Breen, and J.Weertman, J Met, 1955. **7**: p. 1230.

107. J.Weertman, and J.E.Breen, J Appl Phys, 1956. **27**: p. 1189.

108. J.Weertman, J Appl Phys, 1957. **28**: p. 196.

109. S.N.G.Chu, and J.C.M.Li, Mater Sci Eng, 1979. **39**(1): p. 1-10.

110. M.Fujiwara, and M.Otsuka, J. Japan Inst. Metals, 1999. **63**(6): p. 760-769.

111. S.H.Suh, J.B.Cohen, and J.Weertman, Metall Trans A, 1983. **14A**(1): p. 117-126.

112. R.Fiedler, and A.R.Lang, J. Mater. Sci., 1972. **7**: p. 531.

113. R.Fiedler, and I.Vagera, Phys. Status Solidi A, 1972. **32**: p. 419.

114. A.N.Stroh, Philos. Mag., 1958. **3**: p. 625.

115. R.W.Vook, Acta Metallurgica, 1964. **12**(2): p. 197-207.

116. K.Bausch, Z.Physik, 1935. **93**: p. 479.

117. M.C.Jon, D.N.Beshers, and W.P.Mason, J Appl Phys, 1974. **45**(9): p. 3716-3719.

118. A.U.Telang, T.R.Bieler, S.Choi, and K.N.Subramanian, J. Mater. Res., 2002. **17**(9): p. 2294-2306.

119. G.I.Taylor, J. Inst. Met., 1938. **62**: p. 307.

120. J.W.Hutchinson, Proc. R. Soc. London, Ser. A, 1976. **348**: p. 101.

121. U.F.Kocks, Metall. Trans., 1970. **1**: p. 1121.

122. R.J.Asaro, and A.Needleman, Acta Met., 1985. **33**: p. 923.

123. S.R.Kalidindi, C.A.Bronkhorst, and L.Anand, J. Mech.Phys. Solids, 1992. **40**: p. 537.

124. G.Sachs, Z. VD1, 1928. **72**: p. 734.

125. T.Leffers, and P.v. Houte, Acta Metall. Mater., 1989. **37**: p. 1191.

126. T.Leffers, Riso Report No. 184 (ICOTOM 1), 1968: p. 1-33.

127. P.v. Houte, L.Delannay, and I.Samajdar, Plasticity 98, ed. A.Khan, 1998: p. 149-152.

128. U.F.Kocks, and G.R.Canova, *How many slip systems and which?*, in *Deformation of Polycrystals, Riso National Laboratory,*, H.e. al., Editor. 1981. p. 35–44.

129. B.J.Lee, S.Ahzi, and D.M.Parks, Journal of Engineering Materials and Technology, Jan 2002. **124**: p. 27.

130. R.A.Lebensohn, and C.N.Tomé, *Code Visco-Plastic Self-Consistent (VPSC).* 1999: Universidad Nacional de Rosario - Argentina and Los Alamos National Laboratory - USA.

131. C.N.Tomé, and R.A.Lebensohn, 2003. **Version 6**.

132. U.F.Kocks, C.N.Tomé, and H.R.Wenk, *Texture and Anisotropy, Preferred Orientations in Polycrystals and their Effect on Material Properties.* 1998: Cambridge University Press. 77.

133. J.Gastaldi, C.Jordan, and G.Grange, Phil. Mag., 1988. **57A**: p. 971.

134. V.Randle, *Microtexture Determination and its Applications.* 1992: The Institute of Materials,.

135. D.E.Newbury, D.C.Joy, P.Echlin, C.E.Fiori, and J.I.Goldstein, *Advanced Scanning Electron Microscopy and X-ray Microanalysis.* 1986: Plenum Press, New York.

136. S.L.Flegler, J.W.Heckman, and K.L.Klomparens, *Scanning and Transmission Electron Microscopy An Introduction.* 1993: W.H.Freeman and Company, New York. 53, 80.

137. K.-B. Kishi, Ph.D. Thesis, University of Bristol, 1986.

138. D.J.Dingley. in *Proc. of ICOTOM8, Eighth Conference on Textures of Materials, Met. Soc. Inc. PA.* 1988.

139. J.A.Venables, and C.J.Harland, Phil. Mag., 1973. **27**: p. 1193.

140. J.A.Venables, and R.B.Jaya, Phil. Mag., 1977. **35**: p. 1317.

141. J.Hjelen, and E.Nes. in *Proceedings XIIth Int. Cong. For Electron Microscopy, Japan.* 1990: San Francisco Press Inc., San Francisco.

142. K.-B. Kishi, and D.J.Dingley, *AEM workshop.* Vol. 425. 1987: Inst. of Metals book. 71.

143. K.-B. Kishi, D.J.Dingley, and V.Randle, *A Crystallographic Atlas of Electron Backscatter Diffraction Patterns.* 1995: Published by the Institute of Physics Publishing, Bristol, U.K.

144. E.N.daC.Andrade, Proc. R. Soc. London, Ser. A, 1910. **84**: p. 1.

145. A.J.Schwartz, and W.E.King, JOM, 1998. **February**: p. 50-55.

146. G.Palumbo, E.M.Lehockey, and P.Lin, JOM, 1998. **February**: p. 40-43.

147. R.W.Balluffi, P.D.Bristowe, and C.P.Sun, J. Am. Ceram. Soc., Jan 1981. **64**(1): p. 23-34.

148. L.S.Shvindlerman, and B.B.Straumal, Acta. Met., 1985. **33**(9): p. 1735-1749.

149. K.E.Puttick, and B.Tuck, Acta. Met., 1965. **13**: p. 1043-1065.

150. J.G. Lee, F. Guo, and K.N. Subramanian, SAE 2003 World Congress, 2003. **SAE Paper Number 2003-01-0621**.

151. H.Mykura, Acta. Met., 1955. **3**: p. 436-441.

152. K.E.Puttick, and R.King, J. Inst. Met., 1952. **80**: p. 537.

153. D.McLean, *Grain Boundaries in Metals.* 1957: Clarendon Press, Oxford.

154. W.L.Bragg, Cavendish Laboratory, 1954.

155. D.A.Molodov, B.B.Straumal, and L.S.Shvindlerman, Scripta. Met., 1965. **13**: p. 1043-1048.

156. V.Yu.Aristov, Ch.V.Kopezky, D.A.Molodov, and L.S.Shvindlerman, Fasika tverdogo tela, 1980. **22**: p. 3247.

157. A.N.Aleshin, B.S.Bokstein, A.L.Petelin, and L.S.Shvindlerman, Metallofizika, 1980. **2**(83).

158. A.N.Aleshin, B.S.Bokstein, and L.S.Shvindlerman, Fizika tverdogo tela, 1977. **19**: p. 3511.

159. V.Yu.Aristov, Ch.V.Kopezky, and L.S.Shvindlerman, Scripta. Met., 1977. **11**: p. 109.

160. E.M.Fridman, Ch.V.Kopezky, and L.S.Shvindlerman, Z.Metallk, 1975. **60**: p. 533.

161. B.S.Bokstein, Ch.V.Kopezky, and L.S.Shvindlerman, Metallurgia, Moscow, 1986.

162. D.G.Brandon, B.Ralph, S.Ranganathan, and M.S.Wald, Acta. Met., 1964. **12**: p. 813.

163. A.N.Orlov, V.N.Perevezentev, and V.V.Ribin, Metallurgia, Moscow, 1980.

164. H.Gleiter, Mater. Sc.Enging, 1982. **52**: p. 91.

165. U.Erb, and H.Gleiter, Scripta Met., 1979. **13**: p. 61.

166. M.Meisser, H.Gleiter, and E.Mirwals, Scripta Met., 1980. **14**: p. 95.

167. D.G.Brandon, Acta. Met., 1966. **14**: p. 1479.

168. G.Palumbo, and K.T.Aust, Acta Metallurgica Et Materialia, 1990. **38**: p. 2343.

169. P.H.Pumphrey, *Grain Boundary Structure and Properties*, ed. D.A.Smith. 1976, New York: Academic Press.

170. Y.Ishida, and M.McLean, Phil. Mag., 1973. **27**: p. 1125.

171. J.J.Backmann, G.Silvestre, M.Petit, and W.Bollmann, Phil. Mag., 1981. **A43**: p. 189.

172. J.J.Backmann, J.P.Millier, M.Petit, and G.Silvestre, Mater. Res. Bull., 1980. **15**: p. 261.

173. R.W.Balluffi, P.J.Goodhew, T.Y.Tan, and W.R.Wagner, J.Phys., 1975. **36**(C4): p. 17.

174. W.R.Wagner, T.Y.Tan, and R.W.Balluffi, Phil. Mag., 1974. **29**: p. 895.

175. R.W.Balluffi, Y.Komem, and T.Schober, Surf. Sci., 1972. **31**: p. 68.

176. V.L.Pokrovsky, and A.L.Talapov, J.E.T.P., 1980. **75**: p. 269.

177. A.M.Papon, M.Petit, G.Silvestre, and J.J.Backmann, Proc. Mater. Res. Soc. Ann. Meet., Boston MA 1981, 1982.

178. O.L.Krivanck, Chemica scripta, 1978-1979. **14**: p. 213.

179. O.L.Krivanck, S.Isoda, and K.Kobayashi, Phil. Mag., 1977. **36**: p. 931.

180. A.A.Zisman, and V.V.Ribin, Poverchnost, 1982. **7**: p. 87.

181. E.L.Maksimova, L.S.Shvindlerman, and B.B.Straumal, Acta Metallurgica, 1988. **36**(6): p. 1573-1583.

182. E.M.Fridman, B.S.Bokstein, A.L.Petelin, and L.S.Shvindlerman, Metallofizika, 1980. **2**: p. 83.

183. T.Y.Tan, S.L.Sass, and R.W.Balluffi, Phil. Mag., 1975. **31**: p. 575.

184. C.P.Sun, and R.W.Balluffi, Phil. Mag., 1982. **A46**: p. 49.

CHAPTER 2

EXPERIMENTAL PROCEDURES

The following sections will outline some of the general experimental procedures that were employed to accomplish the above-mentioned aims. Experimental details specific to a particular experiment will be described in the appropriate chapters in the Results and Discussion.

2.1. SOLDER JOINT PREPARATION:

Three different types of shear lap joint geometries are used in this study – (1) single shear lap joint, (2) dual shear lap joint and (3) component type joint.

(1) The single shear lap joint is an ideal joint to test the solder in shear using a specimen with the shape of a tensile specimen, in creep and quasi-static strain rates, and for stress relaxation following strain imposed in a tension test. Single shear lap specimens were prepared with two copper half-dog bone specimens electro discharge machined (EDM) from as received OFHC Copper sheet 0.5mm thick (shown in Figure 2.1). The copper dog bone halves were dipped in 50% Nitric acid for 2-3 seconds when different color appeared to remove any surface oxide present that could hinder good joint formation due to de-wetting and creating pores. The dog bones were placed in an apparatus using tweezers which eliminated the need for a mask that was required in previous studies [1, 2]. A jig was used to hold the joint during fabrication with 600μm glass plates serving at spacers to limit joint thickness to 100μm and an area of $1mm^2$. The eutectic Sn-Ag solder paste (~$0.2mm^3$ volume) was applied to the end of the copper dog bones and heated to make the joint and cooled on an Aluminum plate. The heating profile is shown in Figure 2.2. Two leads were attached to the ends of the apparatus with screws to measure the temperature. Prior studies with thermocouple attached to the joint

showed that temperature profile was nearly identical based on manual data recording by watching the display manually. When the thermocouple displayed 250° after a count of 5 seconds the tray was picked up and placed in 1-2 seconds on a one square foot 0.5cm thick Aluminum plate to cool down. This method provided the ability to make 100μm thick joints with reasonable consistency (see fixture in Figure 2.1).

OIM studies require the surface to be free of oxide and deformation, so careful polishing is needed. The joint was carefully removed from the fabrication tray and polishing was performed in a special jig (made of Aluminum) that supported the joint so as to minimize mechanical deformation during polishing. Though most of the solder was used to make the joint, some of the solder formed fillets on either side of the joint and some bulged out from the edges when the upper dog bone was overlaid on the solder. This excess was ground off during polishing. Figure 2.3 illustrates the way the joint was placed in the jig for the polishing operation. The jig was designed to support the joint on the flat edges, so that no deformation or bending was induced in the joint. To accommodate the thickness of the joint, two identical copper strips (18mm x 3mm x 0.5mm, from the same stock as the dog bone halves excluding the section used to make the joint) were placed alongside the tabs of the copper dog bone to prevent bending or twisting of the joint during polishing. The edges of these joints were metallographically polished progressively with 600 and 1000 grit sandpapers. Then, the same procedure was repeated on the other side of the specimen, which was then progressively polished up to 0.3μm alumina suspension followed by 0.05μm silica in an alkaline suspension, which was the final step in polishing. The side that underwent final 0.05μm polishing was used to study the microstructural evolution, whereas the other side, which had a flat surface,

facilitated mounting the specimen on the stub for OIM. The specimen was observed under an optical microscope periodically while polishing. All specimens were metallographically hand polished with minimal force application during polishing. The final two steps were achieved by placing the joint (in the jig) with the surface to be polished on velvet paper mounted on a 6cm x 1cm x 0.5cm Aluminum block, applying the polishing media and then moving the jig back and forth without applying any force. The only force applied was that of the weight of the jig, which is about 30 grams. Due to the hand support the force actually applied was in the range of 0.20-0.25N. The solder joint specimen was then cleaned in methanol or acetone in an ultrasonic cleaner and then dried in compressed air and stored in a refrigerator until future testing. The single shear lap joints made with eutectic tin silver (3.5 wt. %Ag) lead free solder had an average solder area of about 1 mm^2 and an average thickness ranging from 100-150μm.

Preliminary OIM studies carried out on polished specimens indicated that no additional electropolishing was necessary to enhance the sharpness of the EBSP's [3-5], since they were sharp enough to determine the crystal orientation for 60-90% [3-5] of the scanned positions. The remaining 40-10% of the non-indexed positions were attributed to porosity, grain or phase boundaries, second phases, oxidation or locally highly deformed regions (for specimens after deformation).

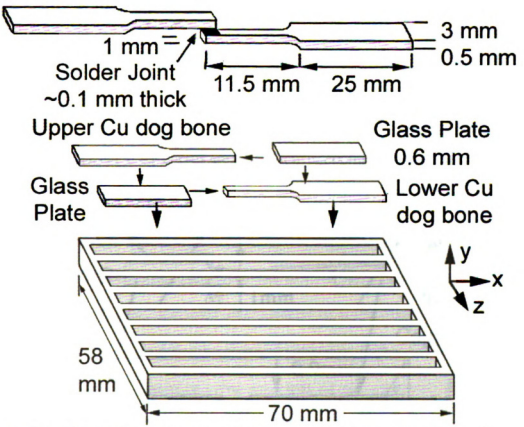

Figure 2.1. Solder joint configuration showing side "A" orientation along with fixture for manufacturing solder joints used in this study. Copper dog bones were about 500μm in thickness, while the glass plate was ground to about 600μm thickness, which facilitates making 100μm thick solder joints with reasonable consistency.

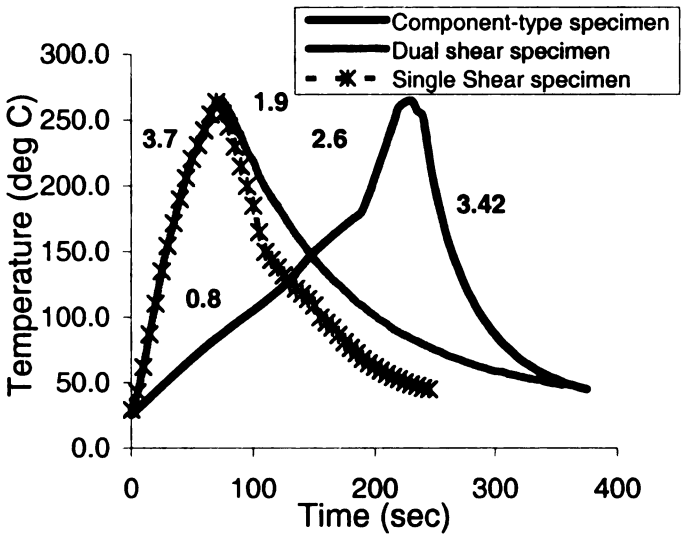

Figure 2.2. The heating profile for three types of specimens. The numbers adjacent to the curves are the heating or cooling rates in °C/sec

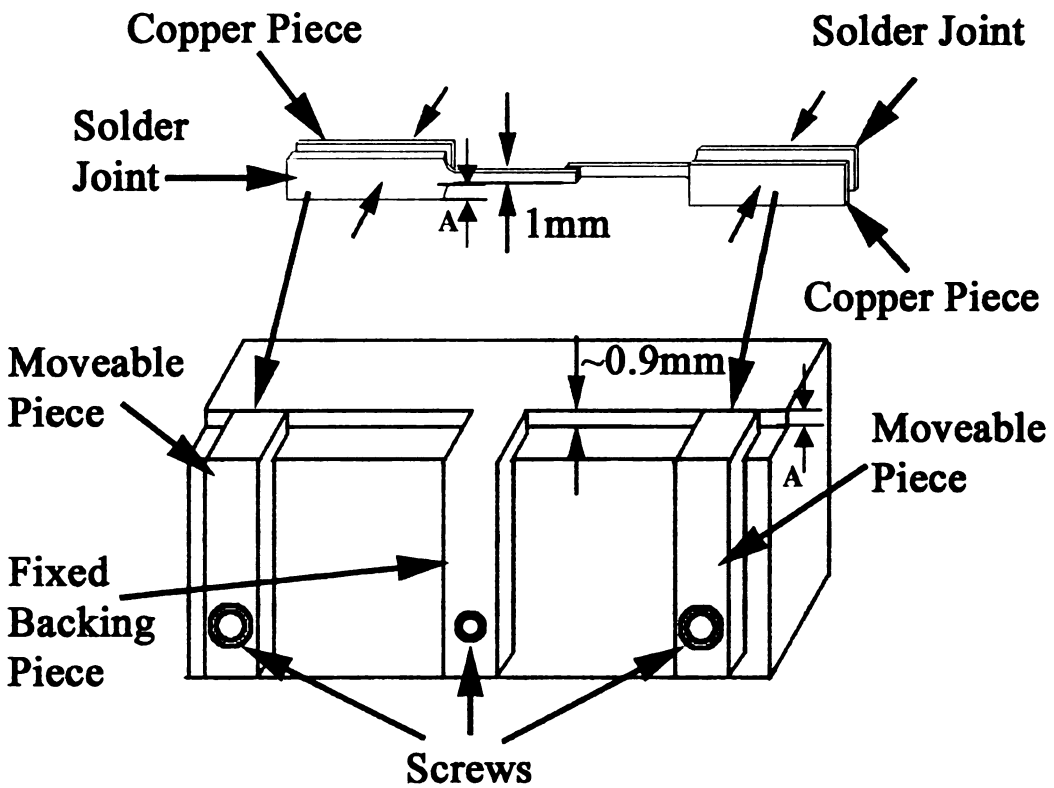

Figure 2.3. Jig used for polishing specimens showing a specimen with copper pieces used as backing to avoid bending and twisting of the joint. Middle piece is not moved because it supports the solder joint during polishing.

(2) Dual shear lap and Component type specimens: These specimen geometries were used to simulate the stresses experienced by actual joints on PCBs. Figure 2.4 shows the dual shear and component type specimen geometries. Both specimens consist of two single shear lap joints made with eutectic Sn-Ag solder having similar dimensions as the single shear lap joint above. Copper functions as the substrate-base and nickel serves as the component. Copper and nickel have different CTE (17×10^{-6} /°C and 12.9×10^{-6} /°C respectively). The 9mm length of nickel simulates the differential contraction that would arise between a printed circuit board and a ceramic surface mount component that is 3-4 mm long. This arrangement also simulates practical applications where underbump metallurgy on the chip side uses nickel as the interfacial layer with the solder. During fabrication, both types of specimens are held in an aluminum jig to help align the joints. The component type specimen is given a two-step heating schedule to allow the flux to work better (as in industrial practices) whereas the dual shear specimen was prepared by a one step heating process, and both specimens were cooled on an aluminum plate (see Figure 2.2). The edges of the joints were carefully polished using the same jig for the single shear specimens discussed above. The primary difference in these two joints is the different stress state achieved after fabrication; the component type joint caused a residual stress state in the solder due to the substrate constraint during cooling, whereas the dual shear lap specimen is assumed to be stress free since it was not constrained during fabrication.

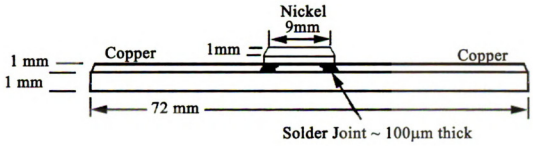

(a)

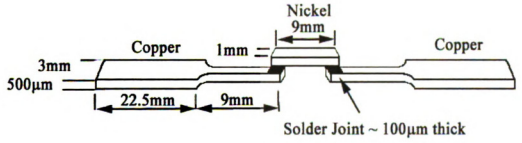

(b)

Figure 2.4. (a) Component type and (b) dual shear lap specimen geometries. The dual shear specimen is fabricated without imposing external stress on the joint, and then it is clamped in a fixture that holds the copper substrates in place while cycling. The nickel piece is 1 mm wide and 0.5 mm thick.

2.2. THERMAL AND MECHANICAL TESTING:

To study the evolution of the microstructure with aging, the single shear lap solder joints were placed in a furnace maintained at either 85 or 150°C (controlled within ±1°) for desired duration ranging from 100 hours to 200 hours. Creep tests were carried out in a special apparatus devised by Guo [2] and Choi [6], which facilitated documentation of the shear strain changes during creep using an optical microscope fitted with a closed circuit digital (CCD) camera. The load was applied to the joint through a cable and pulley system. The entire loading assembly along with the solder joint was placed on an optical microscope fitted with an attached closed circuit digital (CCD) camera. The camera was previously setup in such a manner, so that the solder joint edge remained in focus throughout the test. The computer controlled CCD camera took digital images at specified time intervals so that the amount of local strain experienced by the solder joint could be easily studied and documented. Specimens for elevated temperature creep tests were heated by wrapping a heating element around the copper portion of one of the copper dog bones and heat was transferred to the solder joint by conduction. Figure 2.5 shows the creep setup used. A constant load was applied to one dog bone whereas the other was fixed to the frame. Typically a load of 3.5lbs (~15.6 MPa for a 100μm joint) was used for room temperature creep testing and 2.5 lbs (~11.2 MPa for a 100μm joint) was used for high temperature creep carried out at 85°C. The temperature was controlled at 85°C with ±1°C of accuracy using a variac. Thermocouple wires were wrapped around the dog bones at a distance of about 2 mm from the solder joint (not shown in Figure 2.5).

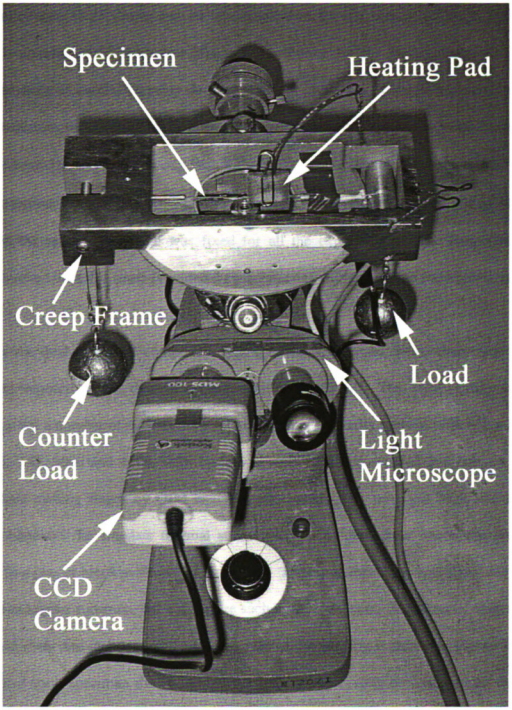

Figure 2.5. Setup for dead weight loading miniature creep testing frame.

The thermomechanical fatigue (TMF) cycling was carried out on all three types of specimens, by subjecting them to thermal excursions between –15°C and 150°C with a heating ramp rate of 25°C/min and 20 min dwell time for the heating segment, and a cooling ramp time of 7°C/min and 300 min dwell time for the cooling segment [7] performed using an automated setup developed by our group [7]. The joints were placed on an aluminum plate sitting on a heater which was set inside a commercial freezer maintained at –15°C. A timer along with a thermostat controlled the time for which the heater stayed on to maintain 150°C temperature at the hot extreme. A voltage regulator controlled the ramp rate, which was fixed for all the experiments. The temperature profile obtained with this setup provided 4 cycles per day using the cycle shown in Figure 2.6.

In the dual shear and component type specimens, a cyclic shear strain cycle of 0.003 was imposed by this thermal cycle for this geometry [8]. The TMF cycling was carried out for a number of cycles on a joint, and then periodically removed (for e.g. after 250, 500, 750, 1000 and 1500 TMF cycles) to assess the deformation and damage at intermediate cycling stages by OIM analysis, after which they were put back into the cycling chamber. To simulate thermal stress cycling, the dual shear specimens were attached to a copper block as shown in Figure 2.7. The component type specimen, due to its common copper substrate, did not require such a substrate base. A schematic diagram of the dual shear and component specimens under cyclic loading is shown in Figure 2.8. For the dual shear specimen shown in Figure 2.8(b), during cycling both ends of the dual shear joints are clamped onto a copper fixture as shown in to obtain the same strain cycle as the component type joint.

These two sample configurations resulted in different strain histories, as follows: Since the dual shear specimen was stress free during fabrication and presumed to be stress free after clamping to the copper base at room temperature, with cooling to -15°C the nickel contracts less than the copper, causing the nickel to be in a state of compression. The opposite happens after heating to 150°C, causing a reversal in the *sign* of the shear stress. For the joints in the component type specimen, since they were stressed during fabrication to put the nickel into compression, cooling to -15°C the joints are further stressed beyond the initial condition at room temperature. Assuming that the stress did not relax much at –15°C due to minimal creep deformation, upon heating, the stress magnitude relaxed with heating to 150°C, where the shape of the joint returned to its geometry shortly after it solidified. Hence the stress state was not reversed like it was in the dual shear specimen. In contrast, the dual shear specimen was substantially more stressed at high temperature than the component specimen, causing more creep and stress relaxation during the higher temperature hold time.

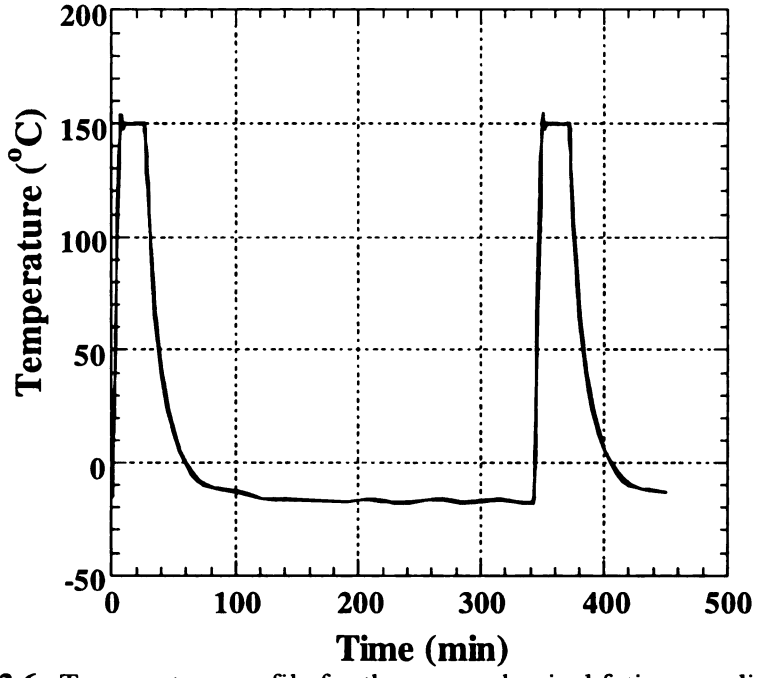

Figure 2.6. Temperature profile for thermomechanical fatigue cycling (-15°C to 150°C) .

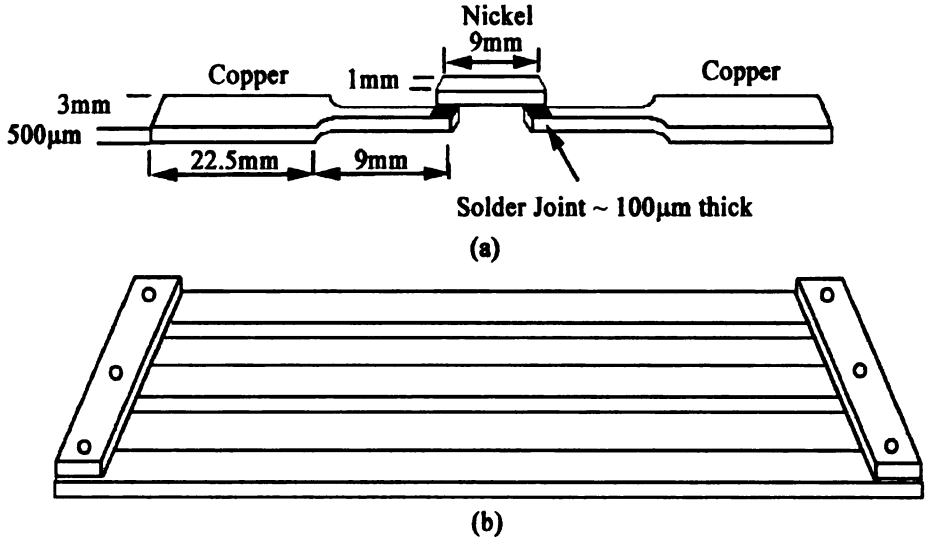

Figure 2.7. (a) Dual shear specimen with (b) copper block used to clamp it down during TMF cycling so as to simulate actual components.

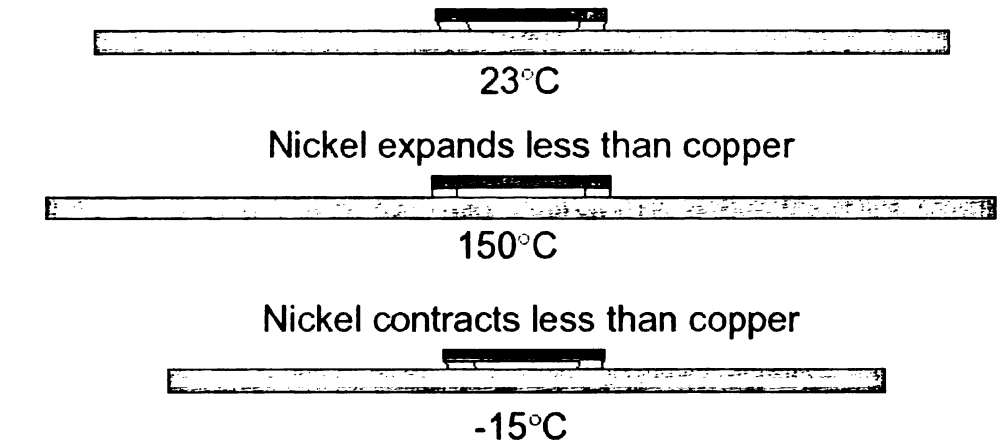

(a)

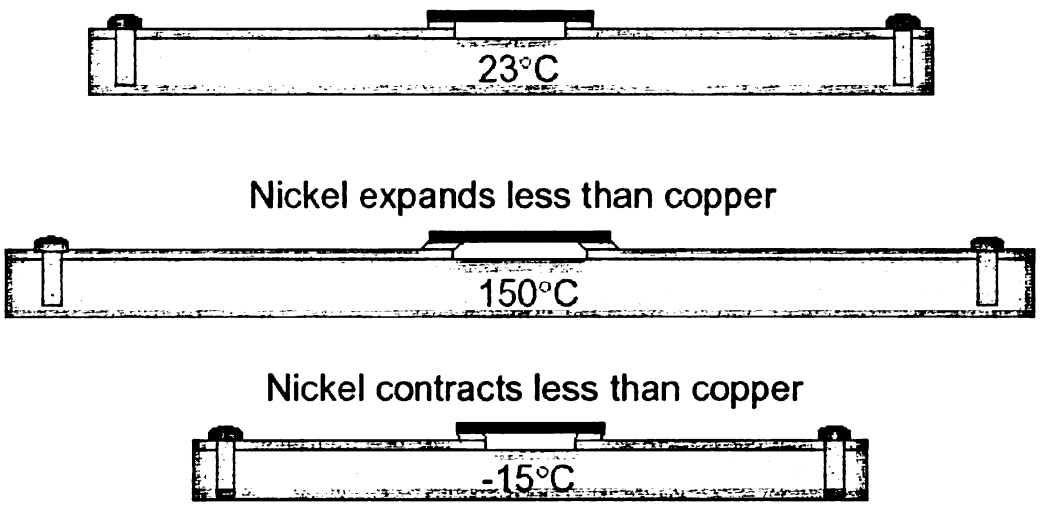

(b)

Figure 2.8. A schematic of the joints under cyclic loading (a) Component type specimen is stressed as it is cooled during fabrication, (b) dual shear specimen is stress-free at room temperature. Differential expansion (Ni–12.9, Cu–17.1, Sn–23 x 10^{-6}/°C) causes shear displacement at solder joints = $\Delta\alpha\Delta T$ (4.5mm) = 0.0031mm => γ = 0.031 shear per cycle.

2.3. CRYSTALLOGRAPHIC DATA COLLECTION AND TEXTURE MEASUREMENT:

OIM scans were carried out in the joint configuration on all specimens. The OIM data was collected on a CAMSCAN 44FE SEM using hkl Channel Acquisition software version 4.2 (HKL Technology, Inc., Blaakildevej, 17k, Hobro, DK-9500, Denmark) run on a PC at Michigan State University. A 25kV beam with a specimen current of about 2.3mA was used to generate EBSP's. A probe current greater than 5μA insured good scan conditions. The roughly polished (polished with 600μm paper) side of the joint was attached to the flat surface of a standard Aluminum stub using a carbon tape so that the polished side of the specimen could be seen when observed from the top. The specimen was oriented and placed into the microscope the same way every time; with the arms in case of the single shear lap joint lined-up along the x-axis i.e. the length of the joint along the x-axis and the thickness of the joint along the y-axis. The specimen stage was then tilted 70° about the specimen x-axis so that from the top to the bottom of the screen, one viewed a solder joint sandwiched between two copper substrates. Repeated mounting of the same specimen on separate days resulted in crystal orientation measurements in the same position that differed by less than 2° (in a few instances as much as 5° difference occurred in the first euler angle for rotation about the normal axis, associated with mounting the specimen holder onto the microscope stage). Coupled with the intrinsic 1° uncertainty in EBSP pattern indexing the absolute angular orientation certainty on a given specimen is accurate to ±3°. However within the same specimen, the misorientation angle between different grains is accurate within 1°. Most OIM scans were overnight

scans, collecting around 12,000 pixels of data with 1μm step size over a 120x100 μm^2 area of the solder joint. Several regions of the same specimen were scanned, to assess the similarities and differences in the microstructure in different regions of the joint. The crystal orientation data was collected by rastering the beam over the specimen in an automated manner. Crystal orientation information obtained from these scans was processed to obtain an OIM map; datasets collected from the hkl scans were processed and converted to TSL datasets (See Appendix I) which was then processed to obtain orientation maps, pole figures and misorientation plots using the TexSEM software version 3.0 (TSL Laboratories, Draper, UT), that provided more mapping and analytical tools than version 4.2 of the hkl software. To achieve consistency in the x-y-z coordinate system between the hkl and TexSEM software, the hkl datasets were rotated by +90° about the [001] direction (Normal Direction, ND) in the TexSEM software version 3.0 (See Appendix II) since the x-direction points down as defined by the TSL system and hence the lattice is rotated by 90° in the unrotated TexSEM OIM maps. Datasets were "cleaned-up" using a nearest neighbor criterion, so as to replace isolated unindexed pixels with the orientation of the nearest neighbor pixel that had the highest degree of confidence in the crystal orientation. Typically one round of cleanup was carried out on all scans, except for the VPSC simulations, where all pixels of a map required meaningful data to input into the VPSC code. Due to progressive aging and deformation, the detection of EBSPs was degraded and a light re-polish with 0.05μm silica in an alkaline suspension improved pattern sharpness; probably due to the removal of a surface oxide layer that formed.

Since the slip directions with the smallest Burgers vector in tin are in the c-direction [001] on {100} and {110} planes, crystals with the c-axis aligned with the solder joint x-axis will be most easily sheared by mechanical or CTE driven stresses in the solder joints. This easy direction of deformation was used to identify a reference crystal orientation scheme for OIM maps. When the c-axis was aligned with the x-axis, it is displayed as red on the orientation maps, based on the inverse pole figure color key. Increased c-axis misorientation from the x-axis reference direction by tilting towards the [110] or [100] crystal direction is represented by a transition to blue or green, such that a red orientation and a blue or green grain orientation is misoriented by ~90° about a <110> or <100> axis, respectively. Orientations in-between these three representative crystal directions are represented by colors obtained by mixing red, blue and green, as indicated on the inverse pole figure color key. Any crystal rotation about the specimen x-axis would give the same color. Black is used to represent pixels where patterns could not be indexed. The colors on these OIM maps do not completely define the crystal orientation (in three dimensions); to present a complete three dimensional representation of crystal orientations, 2 such OIM maps are needed, e.g. with different sample coordinate axis perspectives. To provide a better understanding to the reader, the actual crystal orientation is shown in exemplary places using the tetragonal unit cell prism (tin has a body centered tetragonal structure) for tin. See Figure 2.9.

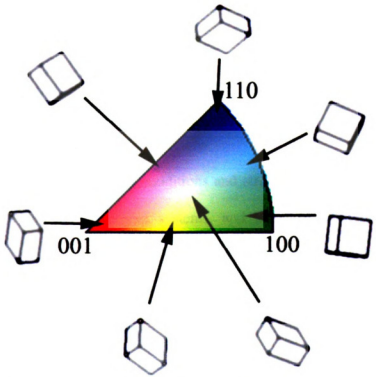

Figure 2.9. Inverse pole figure color key for inverse pole figure orientation maps in the [001] direction with sample crystal orientations having a particular color.

2.4. SIMULATIONS AND MODELING:

1. VPSC (Visco Plastic Self Consistent) Simulations:

It was anticipated that the VPSC model could be effective to evaluate deformation in tin by comparing experimental data with simulations based on hypothetical assumptions about active slip systems. However, before such models can be used with confidence, the material parameters for the slip systems need to be identified. Also, the stress state needs to be known to input into the VPSC code. Thus, a very simple approach was used; to assume that some particular combination of the known slip systems operate without hardening, with the same critical resolved shear stress for flow on each system, to determine whether particular slip systems affected rotations in a way that agreed with experimental observations.

In addition to boundary conditions and strain increments, the code also requires definition of the operative slip systems, and a set of discrete crystal orientations expressed in Bunge Euler angles. All possible slip systems found in the literature were used, and the discrete orientations were obtained from OIM measurements on the undeformed specimens. A small area of the OIM map was extracted from particular regions to provide about 1000 discrete orientations. The code output provided the new orientations for each pixel of the OIM scan, as well as statistics for the active slip systems, which accomplished the computational deformation. The orientations were computationally deformed to strains similar to those of actual experiments, and replotted with the OIM analysis software to compare with the experimental measurements.

2. Schmid Factor Analysis:

To assess how well the deformation state can be described by simple shear, a single shear lap specimen was modeled and computationally deformed elastically in a 2-D plane stress state using the finite element code ANSYS 6.1 and is shown in Figure 2.10. The left end had fixed (zero) x displacement, and the right end had a positive displacement of 0.03mm (to stay in the elastic regime) to simulate a "tensile" mode and a negative displacement was applied to simulate a "compressive" mode (TMF has reversals of stress states in single shear lap specimens). The shape of the solder fillets in the joint was also modeled to be close to the geometry typically obtained in these joints. The mesh was refined using h-refinement. The maximum stresses were always found at corners and places where the fillet met the copper. However, the main purpose of the computations was to determine a typical stress tensor in the main (central) part of the joint which would give a more characteristic stress state for majority of the solder joint where observations were made, rather than locations that had stress concentrations. An elastically deformed computational specimen with a stress similar to the creep experiment is shown in Figure 2.11, which is a good depiction of the elastic bending present in the copper arms from visual observation in the creep frame. Higher magnification of the joint (Figure 2.11) shows that the elastic shear stress within the joint is fairly uniform, except at the corners. The stress state obtained was relatively consistent in the middle 75% of the joint section, which had values of $\sigma_{11(avg\pm std)} = 11.4\pm1.9$, $\sigma_{22(avg\pm std)} = -7.8\pm2.3$, and $\tau_{12(avg\pm std)} = \tau_{21(avg)} = 5.5\pm2.2$ MPa with all other components zero. Particular values from a node at the center of the joint with a stress tensor σ_{11} =

10.4, σ_{22} = -9.6, and $\tau_{12} = \tau_{21}$ = 3.9 MPa were used, which is within the standard deviation of the average values. The stress state was examined along two lines; one near the interface of copper and solder and the other near the center of the joint. Remarkably, the stress tensor is quite similar in the center and the interfacial regions. Using Mohr's circle analysis, the angle made by the plane of maximum shear stress with the positive tensile direction was calculated for both the tensile and compressive cases and is shown in Figure 2.10. The variations in the direction of maximum shear near the interface and the center of the joint are similar in similar regions of the joint. This same stress tensor was also used for analysis of the dual shear lap specimen.

With this stress state, it is possible to determine how each slip system in a given crystal orientation is stressed, using a *generalized* version of the Schmid factor m^*. This generalized Schmid factor is defined by $m = \mathbf{T}_{ij}\,\mathbf{n}_j\mathbf{m}_i$, where $\mathbf{T}_{ij}$ is the normalized Cauchy stress tensor with $\|\mathbf{T}\| = 1$, $\mathbf{n}_j$ is the slip plane normal and $\mathbf{m}_i$ is the slip direction, all expressed in the specimen coordinate system. Using the (normalized) stress tensor from the FEM analysis and the measured crystal orientations, the slip systems with the highest resolved shear stress can be identified, and the plane trace and slip directions can be determined with geometry and compared with heterogeneous strain features on the deformed specimen.

---

* Note that the maximum value of m, as defined by the optimization problem

$$m_{\max} \equiv \max_{\substack{|\mathbf{n}|=|\mathbf{m}|=\|\mathbf{T}\|=1 \\ \mathbf{n}\cdot\mathbf{m}=0}} (\mathbf{T}\mathbf{m}\cdot\mathbf{n})$$

is $\sqrt{2}/2$ for an arbitrary stress state, not 0.5, which is the maximum for the special case of uniaxial deformation (not the usual Schmid factor that is defined for uniaxial deformation).

Table V. von-Mises Stress at each node shown in Figure 2.10.

Near Interface		NODE	SX	SY	SZ	SXY	SYZ	SXZ
Left	**1**	405	11.59	-9.88	0.00	3.54	0.00	0.00
	2	316	39.58	21.49	0.00	27.97	0.00	0.00
	3	385	27.74	3.77	0.00	13.39	0.00	0.00
	4	409	10.42	-9.85	0.00	3.90	0.00	0.00
	5	434	20.58	18.34	0.00	15.55	0.00	0.00
Right	**6**	18	3.18	0.36	0.00	4.94	0.00	0.00

Center of Joint		NODE	SX	SY	SZ	SXY	SYZ	SXZ
Left	**1**	410	10.22	-9.76	0.00	4.06	0.00	0.00
	3	237	19.51	9.71	0.00	15.46	0.00	0.00
	4	217	11.20	-10.08	0.00	4.42	0.00	0.00
	5	204	20.31	9.03	0.00	14.92	0.00	0.00
Right	**6**	22	9.89	22.23	0.00	15.34	0.00	0.00

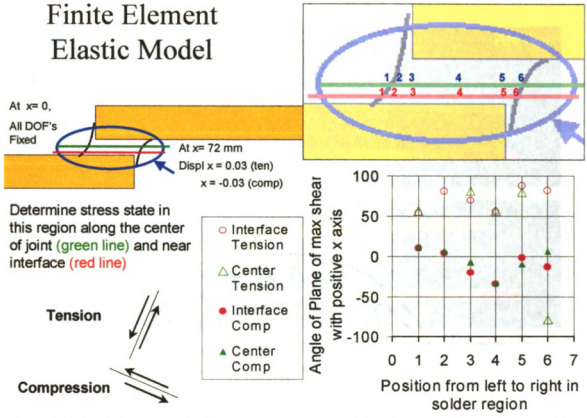

Figure 2.10. Illustration of the joint geometry and displacement imposed in ANSYS6.1 to obtain a generalized stress tensor to calculate the Schmid factors in the joint. Top right shows region in the joint from where stress states were collected. Bottom right, plot of the angle made by the plane of maximum shear stress with the positive x direction calculated for both the tensile and compressive cases using Mohr's circle analysis for locations shown in Figure on top right.

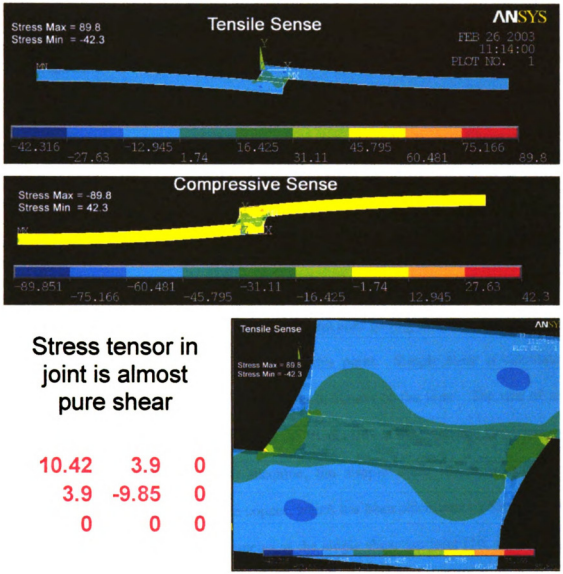

Figure 2.11. Elastic FEM simulation of joint showing magnitude of τ_{12} stress in "compressive" and "tensile" modes. The stress state is similar in middle region of the joint, whereas the highest stress state was seen in the fillet region. Left bottom, stress tensor from one location in the center of the joint.

2.5. SHEAR TESTING WHERE PLASTICITY DOMINATES:

Though TMF is a low strain rate deformation process ($\dot{\gamma} = 10^{-6} - 10^{-3}$), it is also important to see the effect of higher strain rate deformation ($\dot{\gamma} = 10^{-1} - 10^{1}$) on the solder texture so as to determine which slip-systems are activated in high strain-rate deformation. The high strain-rate shear test was carried out in a Rheometric Solids Analyser (RSA III) made by Rheometric Scientific Inc. The apparatus is extremely sensitive and measures small changes in displacement and load. Simultaneously, precise temperature control with no gradients in the joint is possible. Shear tests were carried out at room temperature 25°C at high shear strain rates up to the peak stress value. This allows OIM measurements of the joint before and after testing from the same region since the joint surface is not heavily damaged at this point. Simple shear is calculated by dividing the displacement of the joint by the thickness of the joint. The rate of simple shear was 0.1/sec and controlled using the displacement rate and the thickness of the joint. Since the RSA is a soft machine, the simple shear rate was corrected for compliance of the machine and the copper, which has been calculated by Rhee [9] using a copper specimen with similar geometry as the single shear lap joint [10, 11]. The joints were then taken for texture measurement immediately after testing. Ideally it would be desirable to deform the joint in the CamScan SEM and measure the texture changes in-situ.

2.6 REFERENCES:

1. S.Jadhav, Master's Thesis, Michigan State University, East Lansing, 2001.

2. F.Guo, Ph.D. Thesis, Michigan State University, East Lansing, 2002.

3. D.J.Jensen, Ultramicroscopy, Elsevier Science, 1997. **67**(25).

4. D.P.Field, Ultramicroscopy, Elsevier Science, 1997. **67**(1).

5. B.L.Adams, Materials Science and Engineering, A, 1993. **166**(59).

6. S.Choi, Ph.D. Thesis, Michigan State University, East Lansing, MI, 2002.

7. S.Choi, J.G.Lee, K.N.Subramanian, J.P.Lucas, and T.R.Bieler, J. Electron Mater., 2002. **31**(4): p. 292.

8. J.G. Lee, A.U. Telang, T.R. Bieler, and K.N. Subramanian, J. Electron. Mater., 2002. **31**(11): p. 1152.

9. H. Rhee, J.P. Lucas, and K.N. Subramanian, J. of Materials Science: Materials in Electronics, 2002. **13**(8): p. 477.

10. H. Rhee, and K.N.Subramanian, J. Elect. Mater., 2003. **32**(11): p. 1310-1316.

11. H. Rhee, F.Guo, J.G.Lee, K.C.Chen, and K.N.Subramanian, J. Elect. Mater., 2003. **32**(11): p. 1257-1264.

CHAPTER 3

AGING EFFECTS ON BULK PURE TIN, BULK Sn-3.5Ag AND Sn-3.8Ag-0.7Cu SOLDER ALLOYS

Scope

This chapter examines differences in the grain boundary character in bulk pure tin, Sn-Ag, and Sn-Ag-Cu (SAC) alloy ingots, as well as in slowly cooled reflowed Sn-Ag solder balls. The effect of aging is investigated in the ingot specimen microstructures. These changes will be compared with changes in boundary character that occur in solder joints [1-3] in subsequent chapters.

3.1 INTRODUCTION: Grain boundary sliding and grain de-cohesion appear to be the dominant mechanisms in failure of lead-free solder joints in thermomechanical fatigue [4, 5]. Joint reliability is an important issue and the constraints imposed in the joints can play a significant role in joint deformation. Solder joints are typically made up of a few dominant crystal orientations and can be considered multi-crystals or quasi-single crystals as discussed in the next chapter [1, 5]. Since deformation concentrated at grain boundaries is common in tin-based solders, it is important to characterize the grain boundary character and how it is affected by alloy composition and cooling rate to establish a foundation for understanding how it affects damage generation and mechanical properties. For example, a recent related work has identified how low angle boundaries in solder joints can slide [2]. It is known that deformation of bulk specimens is different from joints [6]. Differences in microstructure arise from differences in cooling rates, compositions, and strain paths while cooling, so it is likely that differences in properties are due to differences in microstructure and grain boundary character.

To identify trends in grain boundary character development from solidification, a set of experiments on pure tin and tin alloys in non-joint configurations were performed to examine the effects of composition, cooling rate, and aging on the grain boundary character, without the complications of joint fabrication. Samples with significantly different characteristics were investigated, including a pure tin ingot, a reflowed sample from the same ingot, an ingot of Sn-3.5wt%Ag and Sn-3.8wt%Ag-0.7wt.%Cu, and reflowed 1 mm solder balls with 1.63 or 3.0wt%Ag cooled at a rate similar to manufacturing conditions. The microstructure was characterized using OIM and SEM. After aging (150°C for 200 hours), the fine-grained polycrystalline microstructure in both

pure tin specimens grew considerably, revealing preferred misorientations and ledge formation at grain boundaries. In contrast, aging of the alloy ingots showed only slight grain growth, due to precipitate pinning. The microstructure of the reflowed solder balls showed some similarities in grain boundary character, but composition affected the microstructure and grain boundary character significantly. The role of alloying elements, cooling rate, and the anisotropy of CTE in tin on microstructural evolution, grain boundary character are discussed.

3.2 EXPERIMENTAL PROCEDURE: Slices of bulk pure tin (99.99%), eutectic tin-3.5 wt.% silver, and tin-3.8 wt.% silver-0.7 wt.% copper were cut out of an ingot obtained from a commercial source (Multicore Inc.). A reflowed pure tin specimen was made from a piece of the ingot by melting and re-solidifying in a ceramic crucible (CoorsTek 20 ml high form 60106 porcelain ceramic crucible) and cooled quickly at ~40°C/s by submerging the crucible in water to obtain a fine-grained polycrystalline microstructure. All specimens were then metallographically polished and final polishing was carried out with 0.05μm colloidal silica in an alkaline suspension. This surface finish was sufficient for Orientation Imaging Microscopy (OIM). OIM scans were then carried out in a location near the centers of the ingot and the reflowed specimen, and then aged at 150°C for 200 hours in a furnace. After aging, the same area was re-scanned with OIM. SEM images were taken both before and after aging in the locations scanned. The eutectic tin-silver specimen was given an additional 200 hours of aging and re-scanned in the same location.

1 mm diameter solder balls were made from a variety of Sn-Ag-Cu alloy compositions and cooled at 0.3/s cooling rate. These specimens were obtained from Professor E.J.Cotts at Binghamton University, Binghamton, NY 13902-6016 (more details of which can be found in Ref.[7]). Specimens were mounted in epoxy and polished, and observed using the cross polarization optical microscope system at Binghamton University, and selected specimens were scanned using OIM.

3.3 RESULTS AND ANALYSIS: The microstructural and grain boundary observations of the specimens examined are summarized in Table VI, and described in detail below.

Pure Tin

Ingot Specimen:

Figure 3.1 shows orientation maps for the pure tin ingot specimen before and after aging. The specimen normal is parallel to the long axis of the ingot, and the area scanned was near the center, as shown in the schematic diagram of the ingot. The as-received specimen had a polycrystalline microstructure with grains separated by high angle grain boundaries (thin white lines; twin boundaries near 60° are thicker). After aging, the grains grew substantially from 50-150 μm in the as-received condition to >500μm after aging. The pole figures for the same area showed an increase in the texture from 5.4 x random to 55.1 x random [1]. By comparing the pole figures, it is apparent that some of the prior orientations were retained and grew strong, while other orientations appeared that were not present on the surface in the as-received condition.

Figure 3.2 shows the grain boundary character map for this specimen. All boundaries greater than 3° are indicated with a thin black line, but special boundaries with specific misorientation ranges near 22, 43, 60, 70, and 80° [1] have thicker lines with various shades of gray instead. Grains with the same orientation before and after are represented by the same colors, and two such examples are marked with arrows.

Table VI: Summary of Microstructure and Misorientation Observations

Specimen, Cooling Rate	History	Grain Size	Grain Boundary Misorientation
Pure Tin Ingot, center	As received Aged 200 hr 150°C	50-150 μm equiaxed > 500 μm irregular	Sharp peaks seen initially at 45 and 60° After aging, fewer boundaries, peaks at 45, 60, 70°
Center of reflowed pure tin in ceramic crucible, quenched in water (~40°C/s)	Reflowed Aged 200 hr 150°C	100-250 μm equiaxed >500 μm irregular	Many small peaks Very strong peak at 45°, other smaller peaks.
Eutectic Sn-3.5Ag Ingot, center	As-Received Aged 200, 400 hr 150°C	10-30 μm equiaxed 20-60μm equiaxed	Nearly random distribution of higher angle grain boundary misorientation regardless of aging time
Eutectic Sn-3.8Ag-0.7Cu Ingot, center	As-Received Aged 200 hr 150°C	10-30 μm equiaxed 20-100μm equiaxed	Random + low angle, 60, 80° peaks superposed. Randomness decreases with aging, peaks sharpen
Solder Ball Sn-1.63Ag 0.3°/s	As-fabricated	15-20 μm equiaxed	Bi-modal; < 15° low angle, and large 50-70° peak
Solder Ball Sn-3.0Ag	As-fabricated	40-250 μm, irregular shapes	Several small peaks < 25°, 55-60°, 70-80°
Solder Ball Sn-3.0Ag-0.6Cu	As-fabricated	100-600 μm large, irregular	Not scanned

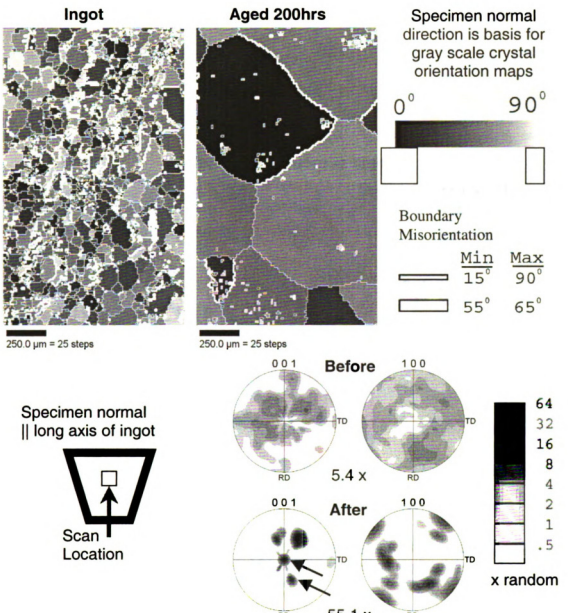

Figure 3.1. Pure tin ingot orientation maps and associated pole figures before and after aging at 150°C for 200 hrs. Gray scale keys are relevant for the orientation maps and pole figures that follow (unless stated otherwise).

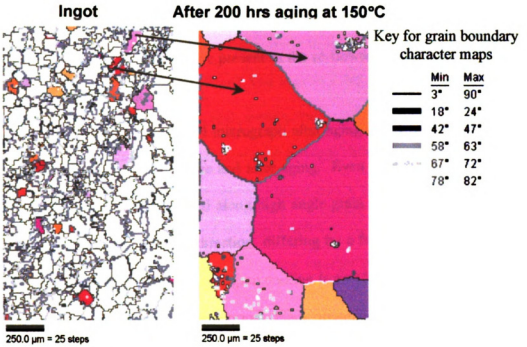

Figure 3.2. Grain boundary character map for pure tin ingot before and after 200 hr aging at 150°C. The gray scale key for special boundary misorientations is relevant for all other grain boundary character maps that follow.

Reflowed Specimen:

Figure 3.3 shows the reflowed pure tin specimen before and after aging using the same orientation and misorientation scales as Figure 3.1. Similar to the ingot specimen, the reflowed specimen had a 100-250 μm polycrystalline microstructure, which also grew to > 500 μm grains. The density pole figures show texture changes similar to the ingot specimen, with some orientations increasing in intensity, others disappearing, and some new orientations appearing (arrow). Figure 3.4 shows the grain boundary character map where less special boundaries are present in the re-flowed specimen than the as-received ingot (see bar chart shown later).

Figure 3.5 shows a SEM micrograph after aging of the reflowed specimen, along with the orientation maps before and after aging. Even though the original surface was polished and flat, ledges formed along high angle grain boundaries. The CTE of tin is anisotropic in the a- versus c-direction, differing by a factor of 2, as shown in the CTE plot adjacent to the image. Hence upon cooling from 150°C, the orientations with the c-axis nearly parallel to the surface normal (black orientations) contracted more than grains with other orientations with a lesser expansion coefficient in the normal direction, so they are more deeply set into the surface. Since the depth of the crystal beneath the surface is not known, nor the orientation of grains just below the surface, the height of the ledge can only be qualitatively related to the difference in expansion coefficient in neighboring grains, but larger ledges would be expected between larger grains having large misorientations.

A similar phenomenon must have occurred when the as-polished reflowed specimen was heated to the aging temperature. The high angle boundaries from the

initial microstructure developed relief in the reverse sense as cooling; grains oriented with higher expansion coefficient stuck out more than neighbors, as illustrated in two places with lines that cross such boundaries. The ledges were smaller, since the differential displacements were smaller due to the smaller grain size. Once formed, the ledges were retained throughout the aging process, even when grain boundaries moved. Since no grooves were observed, but only ledges, surface diffusion did not occur sufficiently to alter the ledges. This would provide some indication that surface diffusion did not occur at a level that would alter the ledges or pin the grain boundaries. Since surface diffusion was not significant, this suggests that ledges are formed due to grain boundary sliding, indicating that high angle boundaries can slide easily.

Figure 3.6 shows the misorientation histograms for the pure tin specimens before and after aging. After aging, the random component in the misorientation histogram also decreased after aging. Preferred misorientations of 22.5, 28, ~45, 59-62, 70, and 80° develop, which correlate with special low energy boundaries which have known coincident site lattices [1, 3].

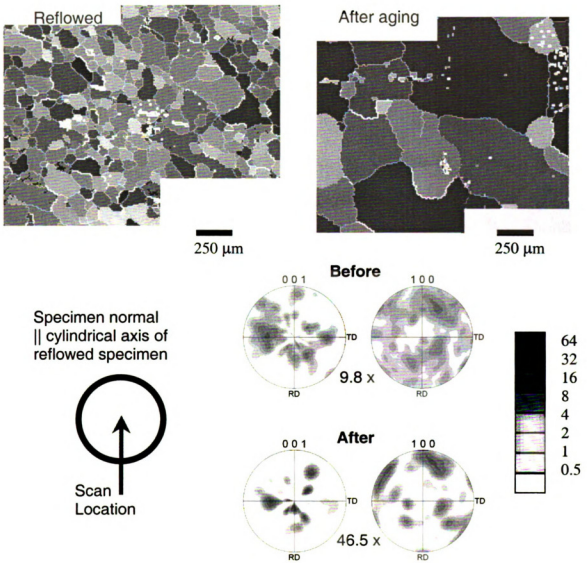

Figure 3.3. Orientation maps and associated pole figures for pure tin reflowed in a ceramic crucible and quenched in water, before and after aging at 150°C for 200 hrs.

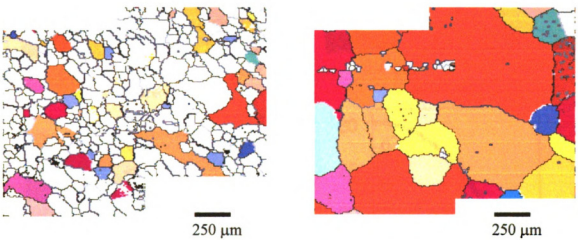

Figure 3.4. Grain boundary character map for reflowed pure tin before and after 200 hr aging at 150°C. The boundary misorientation is indicated using the same scale shown in Figure 3.2.

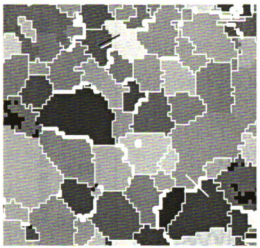

OIM of SEM shown below before aging

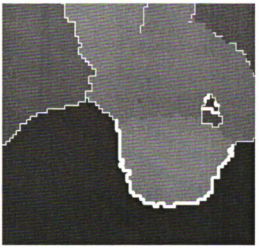

OIM of SEM shown below after aging

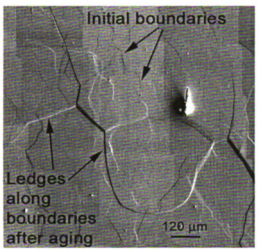

SEM of small region of the area scanned

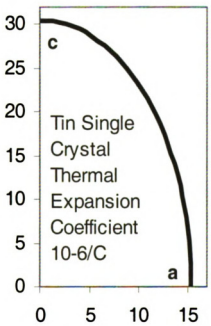

Figure 3.5. Secondary electron SEM image after 200 hr aging at 150°C of a small region of the scanned area in Figures 3.3 and 3.4. Locations of high angle grain boundaries before and after aging are evident as ledges that developed due to the anisotropic thermal expansion of tin.

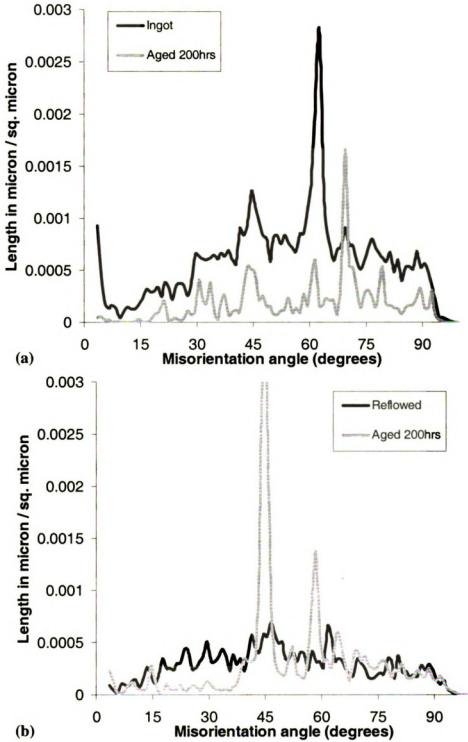

Figure 3.6. Misorientation histograms for (a) the ingot pure tin specimen and (b) the reflowed pure tin specimen. The maximum for the 45° in (b) was 0.004/μm.

Eutectic Sn-Ag and Sn-Ag-Cu Ingot Specimens

~40 ℃/s cooling rate in ingots

Figure 3.7 shows the secondary and backscattered electron SEM images from the eutectic Sn-Ag specimen, for the same region before and after 400 hours of aging. In contrast to pure Sn, comparison of the two images does not show ledges but only subtle changes in the micrographs, such as slight coarsening/spherodizing of the Ag_3Sn particles, and some boundary movement. It is apparent that the Sn grain size is approximately 10-30 micron for these samples. The grain boundary character maps in Figure 3.8 (using the same boundary scale as Figure 3.2) also shows a 10-30μm initial microstructure, but with 400 hours of aging only slight grain growth occurred. This microstructure is much more stable than pure tin, due to boundary pinning by Ag_3Sn particles.

Figure 3.9 shows the OIM map of the Sn-Ag-Cu (SAC) before and after aging. This ingot also showed a fine grain size of 10-30μm, but aging causes more grain growth than the Sn-Ag solder alloy (grains up to 120μm are observed in Figure 3.9).

Changes in grain size, texture, and grain boundaries are compared for the two alloys in Figures 3.10-3.13. Grain growth statistics in the Sn-Ag and the Sn-Ag-Cu alloy are compared in Figure 3.10, indicating very similar statistics, but grains >40μm appeared to have a more efficient growth advantage in the Sn-Ag-Cu alloy. Figure 3.11 shows density pole figures for both alloys, indicating only modest changes. The Sn-Ag texture changed slightly more than Sn-Ag-Cu (the Sn-Ag-Cu had a stronger initial texture than the Sn-Ag, but it strengthened less after aging). The misorientation histograms in Figure 3.12 show a systematic reduction in the number of grain boundaries with aging.

The Sn-Ag alloy has a random misorientation distribution but the Sn-Ag-Cu alloy shows preference for low angle, 43, 60, and 80° misorientations.

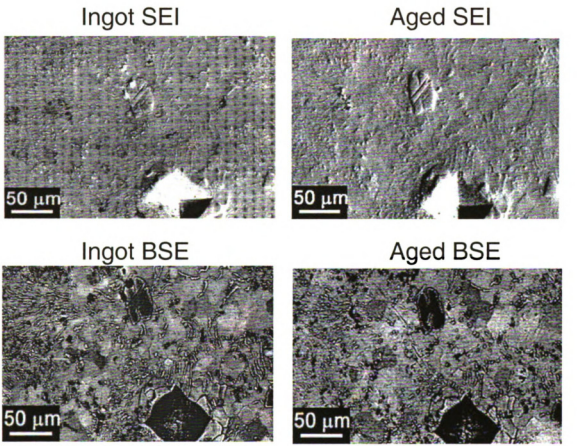

Figure 3.7. Secondary and backscattered electron images of Sn-Ag eutectic showing 10-30 μm grain size and coarsening/spherodizing of Ag_3Sn precipitates (dots in the ingot secondary electron image result from beam damage during the OIM scan).

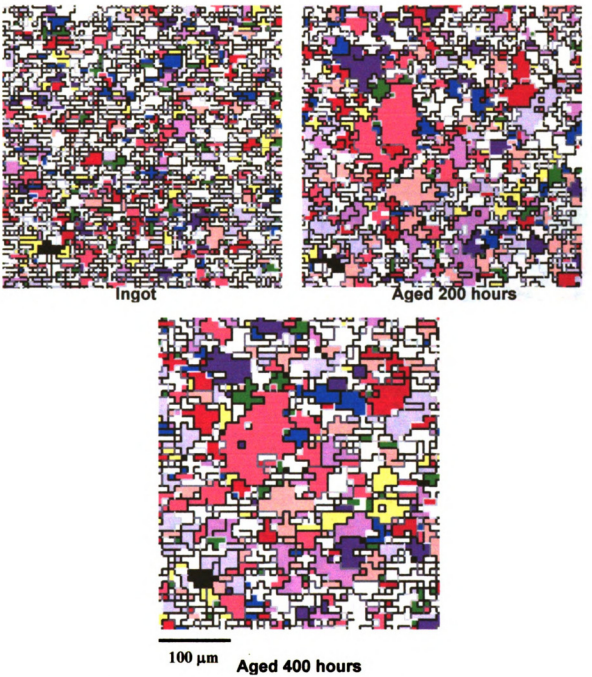

Figure 3.8. Grain boundary character map for eutectic Sn-Ag ingot before and after 200 hr and 400 hr aging at 150°C. An area similar to that used in the pure specimens was scanned, but a cropped image is shown to make the small grain size evident. Different step sizes were used in the three scans, but they are presented with the same scale.

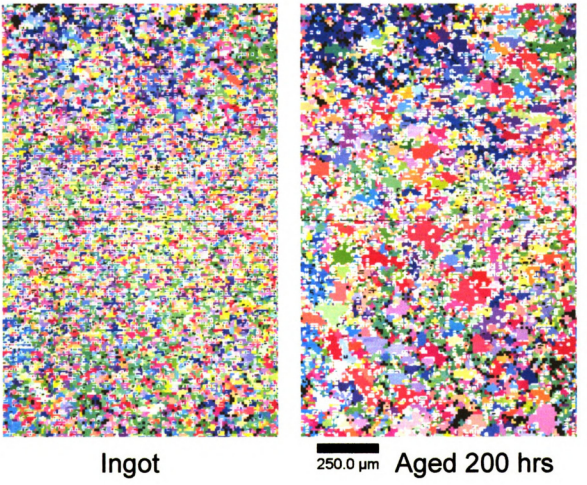

Figure 3.9. Orientation maps for Sn-3.8Ag-0.7Cu ingot before and after aging at 150°C for 200 hrs. The initial grain size of 10-30 µm grew to 20-100 µm.

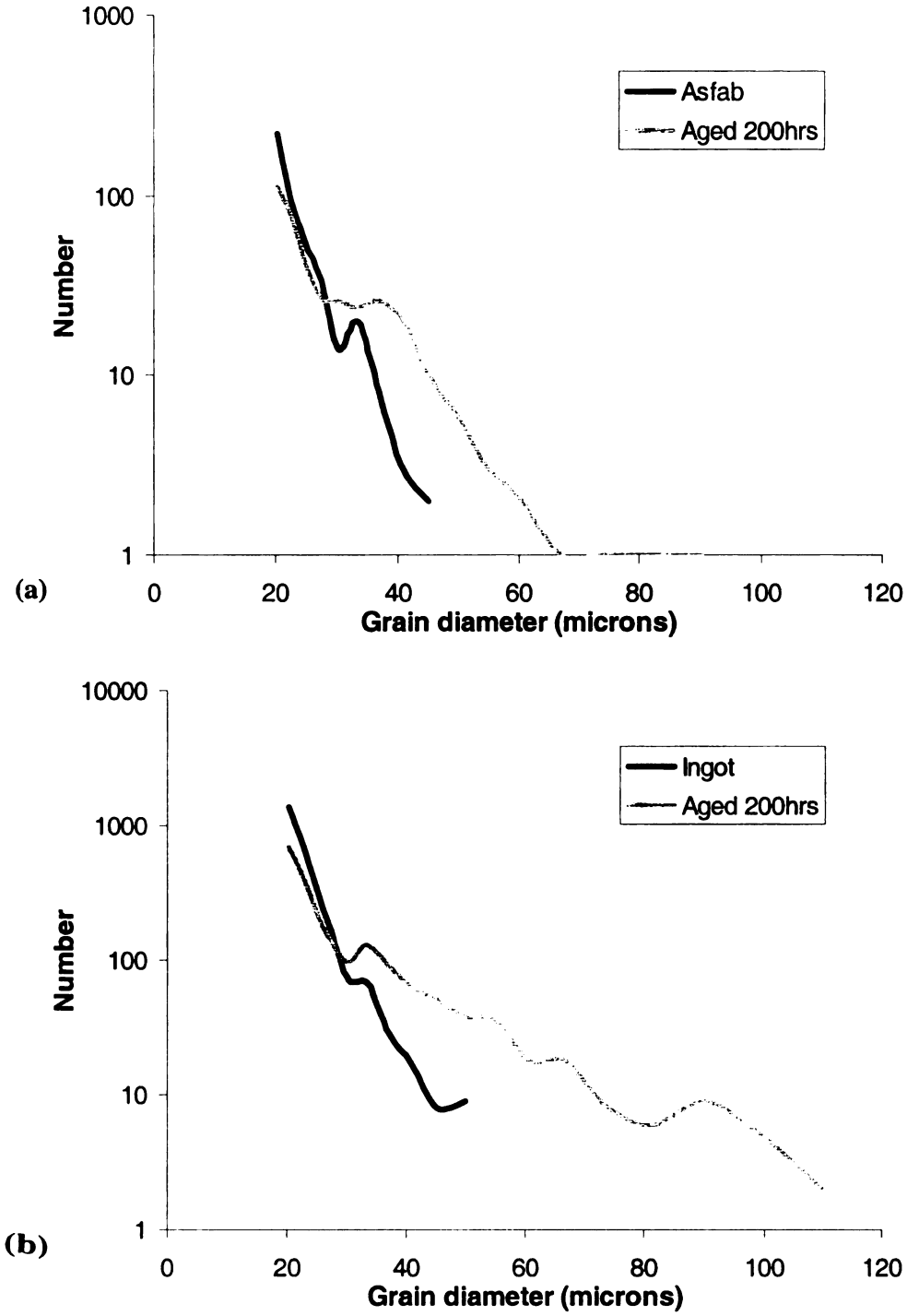

Figure 3.10. Grain growth statistics for (a) Sn-Ag ingot and (b) Sn-Ag-Cu ingot.

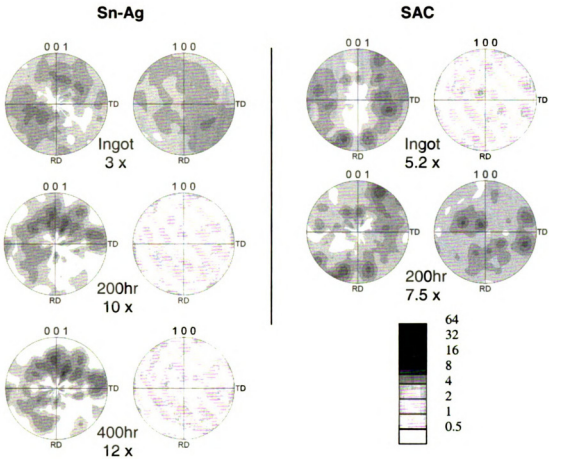

Figure 3.11. Density pole figures before and after aging for Sn-Ag and Sn-Ag-Cu alloy ingots so minor changes.

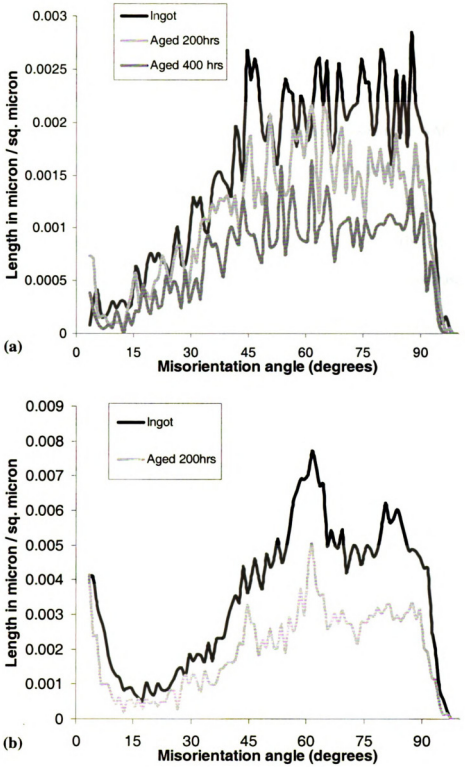

Figure 3.12. Misorientation histograms for (a) Sn-Ag and (b) Sn-Ag-Cu ingot specimens.

0.3 ℃/s cooling rate in 1 mm Solder Balls

A number of near eutectic Sn-Ag-Cu alloys in the Sn-Ag-Cu alloy system were cooled from 250°C to form a 1 mm solder balls at rates from 0.3-3.0°C/s [7]. A crossed polarized optical micrograph in Figure 3.13(a) [7] of a representative SAC alloy (Sn-3.0Ag-0.6Cu) shows only a few grains in the entire ball, so the grain size is hundreds of microns. However, without copper, the grain size is almost an order of magnitude smaller, though still somewhat irregular, as shown in Figure 3.13(b) [7]. The slow cooling rate of the solder ball resulted in grains larger than 100 μm, in contrast to the 10-30 μm grain size in the fast cooled Sn-Ag eutectic alloy ingot.

An OIM scan and associated pole figure of a region near the center of the Sn-3.0Ag solder ball is shown in Figure 3.14(a). The pole figure shows the presence of one dominant and two secondary orientations. The map is based upon black being the crystal orientation with the strongest intensity in the [001] pole figure, and other orientations are represented by shades of gray from 0 to 90 degrees from this reference orientation. The misorientation histogram in Figure 3.14(b) shows that the 3.0Ag alloy has a number of different misorientations, with slight preference for low angle, 43, 57, 72 and 80° misorientations.

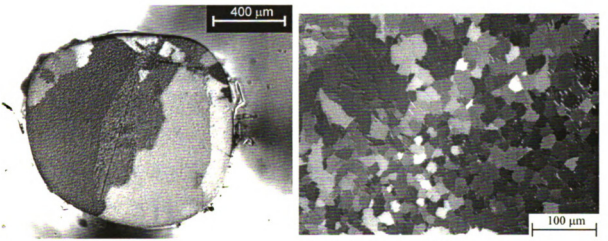

(a) (b)

Figure 3.13. Solder ball micrographs using cross polarized optical imaging (a) Sn-3.0Ag-0.6Cu, (b) Sn-3.0Ag.

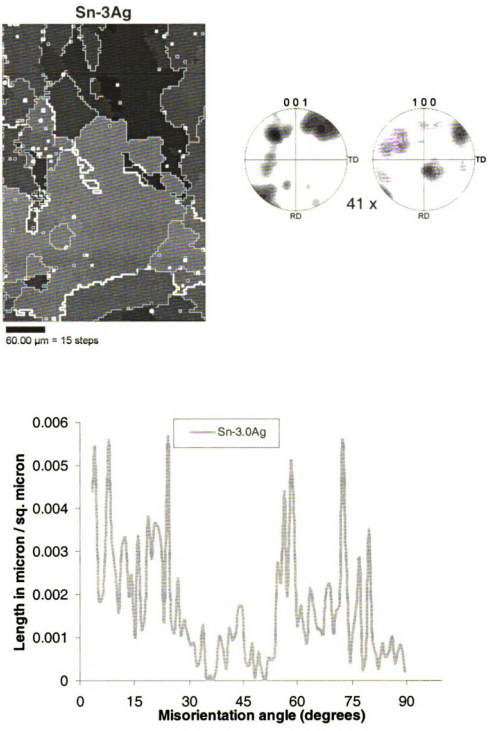

Figure 3.14. Crystal orientation map and associated pole figure for the Sn-3.0Ag solder ball. The black reference orientation is the strongest peak in the pole figure. (b) Misorientation histogram shows no highly favored peaks.

0.3 ℃/s cooling rate in Sn-Ag Hypoeutectic 1 mm Solder Ball

The importance of alloy composition, and cooling rate from the melt, in determining the microstructure of SnAgCu alloys is graphically illustrated with the microstructure of a binary hypoeutectic Sn-1.63Ag solder ball in the cross polarized optical image (Figure 3.15) [7]. This solder ball has a small grain size of 15-20 μm, which is similar to the alloy ingots that were cooled at a much higher cooling rate (Figures 3.8-3.10). The lack in variation of colors in this cross polarized image suggests a limited number of crystal orientations, which is confirmed in the OIM scan and an associated pole figure of a region near the center of this specimens Figure 3.16(a). The map is based upon black being the crystal orientation with the strongest intensity in the [001] direction (the pole in the 2 o'clock position), and other orientations are represented by shades of gray from 0 to 90 degrees from this reference orientation. Aside from the pixilated effect of the OIM scan, the appearance of the cross polarized optical image and the OIM map are very similar, indicating that information obtained in both techniques is correlated.

This hypoeutectic 1.63Ag alloy exhibited a 15-20μm fine grain size, in contrast to the 40-250μm grain size in the near-eutectic composition. Most surprisingly, there are essentially only 3 orientations present, related by 50-75° rotations about a [100] axis. This limited set of crystal orientation causes a strong peak near 60° in the misorientation histogram in Figure 3.16(b). 60% of the high angle boundaries in the scan are misorientations near twin type (59-62°) misorientations. Low angle boundaries are also present, accounting for 22% of the boundary length. The pole figure shows the presence

of three orientations with a common (100) axis close to the sample normal, a texture similar to the *beach ball effect* observed in some SAC alloy solder balls [7]. This is in contrast to the near-eutectic Sn-3.0Ag specimen, which had larger irregular grains than the Sn-1.63Ag alloy and a fraction of twin misorientations in the high angle boundary population of only 22%, much lower than the 1.63%Ag alloy.

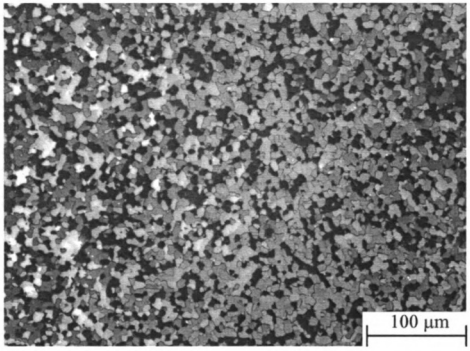

Figure 3.15. Solder ball micrographs using cross polarized optical imaging of Sn-1.63Ag.

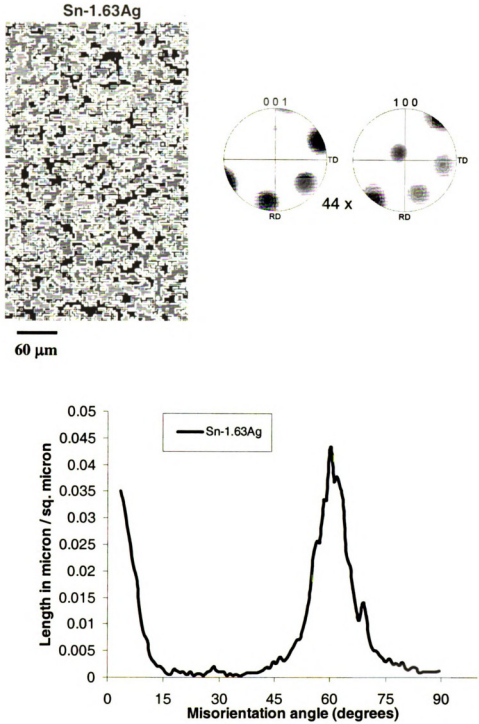

Figure 3.16. Sn-1.63Ag solder ball (a) crystal orientation map and associated pole figure. The three shades of gray represent the three dominant orientations in the 001 pole figure. (b) Misorientation histogram shows mostly low angle and 60-70° peaks.

3.4 DISCUSSION:

Variations in composition and thermal history cause a number of variations in the microstructure and grain boundary character of tin and lead-free solder alloys. Related studies in solder joints show many similar phenomena, such as the same set of highly preferred special boundaries in misorientation histograms [1]. Figure 3.17 shows the relative fractions of special boundaries in all of the specimens examined, for comparison. The distribution of special boundary fraction is similar for similar alloys and cooling rates, and the distribution does not change dramatically with aging. The differences imply that variations in composition and cooling rate have a strong effect on the formation of special boundaries during solidification, and hence on the microstructure, which should have a strong effect on material properties of solder joints in technical applications, where significant process and composition variations are typical [5].

Although pure tin and Sn-Ag-Cu alloys both show strong preference for particular misorientations between grains during solidification and aging (grain growth), there are anomalies, such as the lack of preferred misorientations in near-eutectic binary Sn-Ag alloys, and the exclusively preferred twin misorientations in the binary hypoeutectic alloy. Furthermore, the mechanisms and extent of grain growth are strongly affected by alloying and thermal history. Interpretations of how differences in composition and processing history of Sn-Ag-Cu alloys could cause such significant changes in microstructure follow:

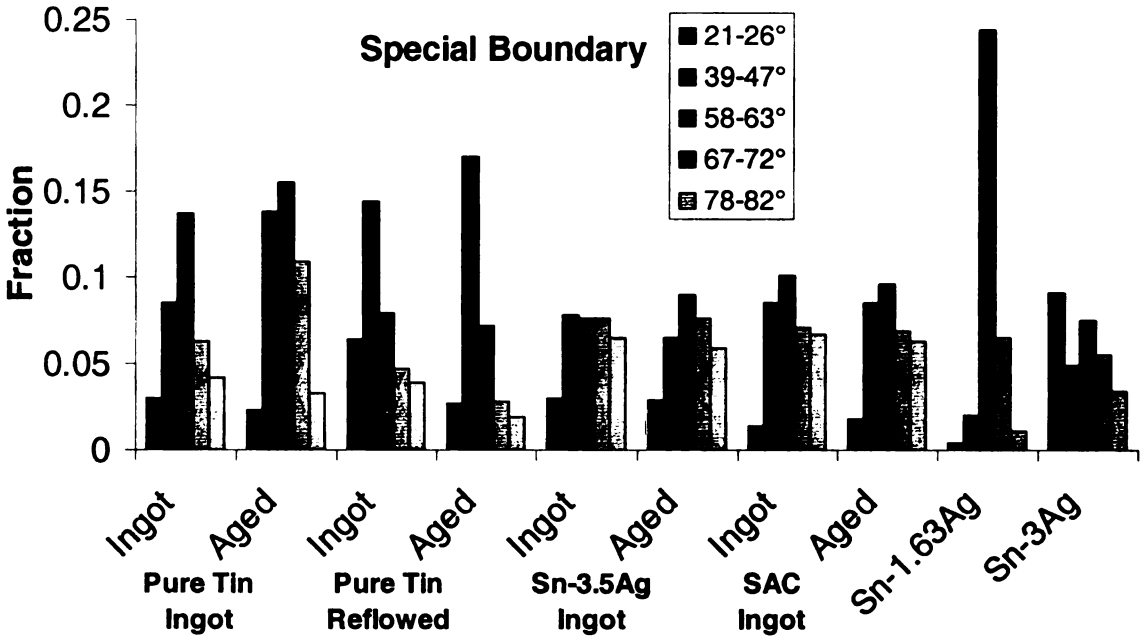

Figure 3.17. The distribution of special boundary area fraction differs in each specimen, the fraction of special boundaries remained similar after aging.

Grain growth in pure tin was unrestrained. Pure tin showed preference for the 22.5, 43, 59, 62, 70 and 80° misorientations, which are low energy boundaries with known coincident site lattices [1]. However addition of 3-3.5%Ag to Sn led to no preferred misorientations. Compared to pure tin, adding near-eutectic amounts of Ag increases the random component of the misorientation distribution (i.e. likelihood of preferred misorientations is reduced).

Addition of Cu to near-eutectic Sn-Ag alloy ingots, however, facilitated formation of preferred misorientations. In joints made with Sn-Ag solder alloys, copper is dissolved into the solder before solidification. Reflow experiments done by Guo et. al. [8, 9] showed that much more than the eutectic amount of copper was dissolved into the tin matrix, giving rise to Cu_6Sn_5 intermetallics upon cooling. Since solder joints show much stronger preferred misorientations than the Sn-Ag-Cu ingot specimen, then stronger peaks [1-3] may result from higher copper content in joints than in the SAC bulk alloy. A similar effect was observed by Lehman et. al. [7] in their study of many SAC alloy solder balls cooled at a variety of cooling rates. This implies that *cooling rate* does not strongly affect the degree that copper facilitates formation of preferred boundary misorientations, though it does affect the grain size; the ingot probably had the fastest cooling rate and it had the finest grain size. Hence, Ag apparently increases interfacial energy of special boundaries, while Cu apparently reduced the interfacial energy, making the special boundaries more likely to form during cooling. A lesser amount of Ag, but no copper also facilitates formation of preferred twin misorientations.

The anomalous result is that a lesser amount of Ag results in highly preferred twin misorientations, exclusive of other special boundaries. The fine grain size and the high

amount of near-twin boundaries indicates that with 1.63wt.%.Ag, the stacking fault energy must be very low, such that stacking faults form easily during solidification that form a high density of twin boundaries. If these boundary energies are consistently low, and evenly distributed spatially, this may explain why boundaries did not migrate, since junctions of grain boundaries with different energies were rare. This suggests that the effect of copper is to facilitate formation of a variety of different special boundaries with different boundary energies, such that differential energy in adjacent boundaries leads to preferred boundary motion of boundaries with relatively higher energy and thus irregular grain boundary motion, and irregular grain shapes.

Since grain boundary sliding is a commonly observed mechanism associated with localized deformation in tin and high tin solders, the alloy composition and cooling rate clearly affects grain boundary properties, which could impact the reliability of solder joints. Special boundaries are known to have high mobility [10, 11]. In pure tin, there are no precipitates to interfere with boundary sliding, and the formation of ledges due to only one thermal cycle implies that unless there are second phase particles in the boundaries, sliding is very easily accomplished. Sliding was not observed in the alloy ingot specimens, but the small grain size would not have caused ledges to be large enough to observe as clearly as pure tin, and furthermore, precipitates would assist in locking boundaries. Clearly, further work is needed to sort out how alloy composition and cooling rate affect the solidification microstructures of solder joints.

3.5 SUMMARY

This preliminary study of the effect of alloy composition and thermal history on the grain boundary character of tin and lead free solders shows that tin based alloys have strongly favored special boundaries. It appears that Ag tends to disrupt formation of the special boundaries that form naturally in pure tin, but Cu has a stronger tendency to favor the formation of special boundaries. This observation may be able to account for variations in the microstructure and hence, variations in properties of tin based alloys that are so commonly observed in the literature. These effects seem to be present regardless of the cooling rate, though in varying degrees. The cooling rate has a strong effect on the grain size of the material, as slower cooling rates delay nucleation and provide more time for grains to grow. Clearly more investigation of these effects is needed before these hypotheses can be evaluated and perhaps used in a predictive manner.

3.6 REFERENCES:

1. A.U.Telang, T.R.Bieler, S.Choi, and K.N.Subramanian, J. Mater. Res., 2002. **17**(9): p. 2294-2306.

2. A.U.Telang, T.R.Bieler, M.A.Crimp, and K.N.Subramanian, Material Science and Engineering A, 2004. **in review.**

3. A.U.Telang, T.R.Bieler, D.E.Mason, and K.N.Subramanian, J. Electron Mater., 2003. **32**(12): p. 1455-1462.

4. K.N.Subramanian, and J.G.Lee, J. of Materials Science: Materials in Electronics. **15**: p. 235-240.

5. D.W.Henderson, J.J.Woods, T.A.Gosselin, J.Bartelo, D.E.King, T.M.Korhonen, M.A.Korhonen, L.P.Lehman, E.J.Cotts, S.K.Kang, P.A.Lauro, D.Y.Shih, C.Goldsmith, and K.J.Puttlitz, J. Mater. Res., 2004. **19**(6): p. 1608-1612.

6. J.W.Morris, and H.L.Reynolds. *The Influence of Microstructure on the Failure of Eutectic Solders.* in *Design and Reliablility of solders and solder interconnects.* 1997. TMS Annual Meeting Warrendale, PA.

7. L.P.Lehman, S.N.Athavale, T.Z.Fullem, A.C.Giamis, R.K.Kinyanjui, M.Lowenstein, K.Mather, R.Patel, D.Rae, J.Wang, Y.Xing, L.Zavalij, P.Borgesen, and E.J.Cotts, J. of Electron. Mater., 2004(Dec).

8. F.Guo, S.Choi, J.P.Lucas, and K.N.Subramanian, Soldering and Surface Mount Technology, 2001. **13**(1): p. 7.

9. F.Guo, S.Choi, J.P.Lucas, and K.N.Subramanian, J. of Electron. Mater., 2000. **29**(10): p. 1241.

10. D.A.Molodov, U.Czubayko, G.Gottstein, and L.S.Shvindlerman, Scripta Metallurgica Et Materialia, 1995. **32**(4): p. 529-534.

11. D.A.Molodov, B.B.Straumal, and L.S.Shvindlerman, Scripta. Met., 1965. **13**: p. 1043-1048.

CHAPTER 4

DETERMINATION OF CRYSTAL ORIENTATION ON OPPOSITE EDGES IN SINGLE SHEAR LAP Sn-3.5Ag SOLDER JOINT SPECIMENS

Scope

Tin-based solder joints are near single crystal or multi-crystalline, and not polycrystalline, as determined by comparing crystal orientations measured using OIM on opposite sides of two solder joints. Comparison with 17 other joints indicated no preferred solidification orientation, though the tendency for tin c-axes to be in the plane of the joint is low.

4.1 INTRODUCTION: Characterization of Sn-3.5Ag solder using single shear lap joint specimens revealed that *heterogeneous grain boundary sliding and surface relief* developed during creep, stress-relaxation, reversed-shear and thermomechanical fatigue (TMF) experiments [1-7]. While microstructural evolution of second phases is easily and commonly characterized with optical and electron microscopy, microstructural evolution in the tin phase is challenging, since the grain boundaries are difficult to identify in the as-solidified microstructures using conventional metallography. Since a large volume fraction of Sn-3.5Ag solders consists of tin, the relationship between the crystallography of tin and deformation and failure processes *in the joint configuration* needs to be understood in order to identify failure mechanisms.

The primary goal of this section is to determine the microstructural characteristics and the crystal orientations present in the tin phase of solder joints. Previous studies [8-10] carried out on one surface / side of single shear lap joints have shown evidence of near single crystals or multicrystals, but not polycrystals *(The term multicrystal is used here instead of polyrcystals to bring out a difference in the number of grains seen in these solder interconnects).* This study evaluates the hypothesis that solder joints are nearly single- or at most, multi-crystals, by comparing crystal orientations measured on both sides of two solder joints to determine if they are the same. These measurements are compared with dominant orientations in 17 other solder joints, to determine if the solidification texture exhibits trends.

4.2 EXPERIMENTAL PROCEDURES: The single shear lap joint geometry was chosen in this study because it facilitated evaluation of mechanical properties of the solder in a mode similar to practical joints using a tensile loading configuration. These specimens were prepared as outlined earlier. The initial cooling rate was about 4°C/sec, which is on the fast side of the range of cooling rates used in industrial practice. Figure 2.1 shows the two categories into which the single shear lap joint has been classified depending on the geometry; left pointing or A oriented and right pointing or B oriented. These classifications will be frequently used in this chapter to describe the orientation of the specimen.

4.3 RESULTS AND DISCUSSION

1. Comparing orientations from two opposite sides of a joint:

Figure 4.1(a,b) show OIM maps from the left side and the center of joint 1 on opposite sides (A and B, see Figure 2.1). In this joint only one dominant orientation was observed in both locations, with low angle grain boundaries (thin black lines) traversing the microstructure. Encapsulated regions of minority orientations are also seen. Scans carried out on other joints have similar "multicrystal" microstructures. To scan the opposite side of the specimen, the specimen was rotated about the length of the joint (horizontal x axis), and hence the measured pole figures need to be rotated in a corresponding manner to observe both sides with the same perspective. Two types of rotations can accomplish this goal. First, the pole figure is rotated by 180° about the TD (x-axis in microscope coordinate system) as illustrated in Figure 4.1(c), which is a 3-D

representation of this rotation to show the equivalence of the two dominant poles in Figure 4.1(a,b): The left pole figure with side A in the front hemisphere shows the two dominant orientations as black circles. Gray crosses represent the corresponding poles on the back hemisphere. After rotation of the sphere (specimen) by 180° about the x-axis, the dominant poles marked by x's on side B are in front. Comparing the left and right spheres to pole figures in Figures 4(a and b) one can easily see that the orientation of the dominant poles are the same. If one looked at the front hemisphere of side B (right sphere) from behind (i.e. the same viewing direction as side A), it has the same appearance as side A on the front hemisphere on the left sphere. When projected on a 2-D surface, the as-measured pole figure (2-D image) on side B simply needs to be flipped about the vertical axis to give pole figures from sides A and B the same perspective, as illustrated in Figure 4.1(d). Though not shown, the same process was applied to (100) pole figures, and the same similarity in crystal orientation was confirmed. The OIM color maps are unaffected by these rotations due to the rotational symmetry. It is obvious that the orientations of the dominant and minority crystals are the same on sides A and B, with only minor differences in secondary poles and relative intensities arising from different fractions of minority orientations.

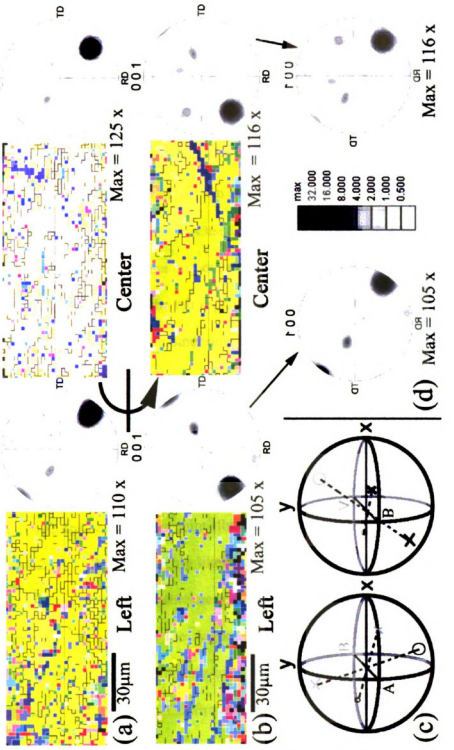

Figure 4.1. (a) Inverse pole figure OIM maps and density pole figures for the left and center regions of the joint. (b) OIM maps of the other side after rotating the specimen 180° about the horizontal x-axis. (c) 3-dimensional representation of the rotations showing similarity of crystal orientations on the two sides. (d) Density pole figures of (b) flipped about the vertical axis, which gives them the same perspective as pole figures as in (a).

Figure 4.2(a,b) shows inverse pole figure OIM maps and (001) density pole figures for specimen 2 with sides A and B, respectively. In Figure 4.2(a) the crystal orientation in the center and right region of the joint have the same pair of dominant c–axis crystal orientations (c-axis near the south pole), but the left region of the joint has two c-axis orientations (just above the equator) which differ by about 90° from the other region. This pair of c-axis orientations is twin related by a 60° misorientation about a 100 axis. The same rotational analysis was used as described above to confirm that the three crystal orientations were the same on both sides. The intensity for the left region of side A (Figure 4.2(a)) is higher than the left region on side B (Figure 4.2(b)), because one of the twin variants is stronger than the other on side B.

The measurements in Figures 4.1 and 4.2 indicate that nearly the same crystal orientations exist on opposite sides of the joint, implying that the volume between the two surfaces probably has the same orientation. The middle region of specimen 2 has a different texture on the two sides, suggesting that the joint consists of two crystal orientations as shown in the schematic joint illustration in Figure 4.2(d). The joints in Figures 4.1 and 4.2 show that it is highly likely that solder joints consist of one or two dominant orientations throughout the thickness. Recent measurements carried out using the Synchrotron radiation source at the Argonne National, Illinois by Lee et.al. [11] suggest that through thickness measurements using the penetrating X-rays also reveal just one or two dominant orientations. Confirmations are also seen from work done by Jackson et.al. [12].

Figure 4.3(a) shows a (001) and a (100) pole figure with the dominant and secondary orientations marked for 19 joints of the several joints that have been

characterized during the course of this study. For 45 scanned regions on these 19 joints, the average standard deviation of strongest and second strongest peaks are 70 (±33) and 11 (±11) x random, respectively. See *Appendix 3* for more details. Measurements had been made on both "A" and "B" sides of joints, so on the basis of the analysis above, the orientations of "B" type joints are flipped vertically (and thus specimen names appear mirrored about the vertical axis) to obtain the same perspective as side A. The c-axis pole figure (top) in Figure 4.3 shows that there is no common or dominant c-axis texture that forms consistently, though there are some orientations that are absent, such as c-axis parallel to the normal (z) direction, and the c-axis aligned with the x-axis. Figure 4.3(b) shows an overlay of quadrants 3 and 4 onto quadrants 1 and 2, respectively by a 180° rotation about the normal axis, which is a symmetric rotation for this sample geometry. The preference for c-axes in the second quadrant may result from the preference of heat flow along a diagonal direction down and to the right, since the upper copper strip was insulated from heat flow to the bottom of the jig by the glass spacer (Figure 1).

The orientations shown are typical; illustrating that crystal growth in the [110] direction parallel to the heat flow direction is common [13]. The lack of c-axis orientations in the x or z sample directions may result from the fact that the thermal expansion of tin is highly anisotropic (15 x 10^{-6}/°C in the basal (a-b) plane (a=b in tin), and 30ppm/°C in the c-direction [1]), such that crystal directions close to the basal (a-b) plane are more closely matched with the thermal expansion of copper (isotropic CTE 17.1 x 10^{-6}/°C), though the presence of Cu_6Sn_5 intermetallic interfacial layer (isotropic CTE 16.3 x 10^{-6}/°C) may reduce the need to match expansion coefficients upon crystallization.

Thus, after scanning a joint on two opposite sides, the same crystal orientations are found. The number of crystal / grain orientations present in such joints is very few, but low angle boundaries allow orientation spreads of ~5° to be present in different regions of the joint. This study shows that it is likely that majority of solder joints are single, bi- or at most, multi-crystals. When two or more orientations dominate, they are commonly twin related (60° about a [100] axis), such that the two orientations often interpenetrate each other. Furthermore, the variation in crystal orientations show that the surfaces are not artifacts of polishing, since polishing was consistently done in the same directions due to constraints of the jig used to support the joint, with respect to the sample coordinate system. These two specimens will be investigated using neutron diffraction for a full volumetric texture measurement, and will be reported in a future paper.

The presence of only one or two crystal orientations implies that formation of solidification nuclei is difficult. Tetragonal Sn has high entropy of fusion ($\Delta S_f = \Delta H_f/T_m$ =14 J/mol-K), compared to lead and other cubic metals (8-11 J/mol-K). Consequently formation of a solid nucleus requires more removal of heat than cubic metals, consistent with the 15-30°C of under cooling that has been observed during solidification of solder joints [14]. Once a nucleus forms, then the undercooling causes rapid growth, so stacking faults are more likely, that can develop into twins or other minority orientations that have low energy boundaries. Most of the peaks in misorientation statistics are related to coincident site lattice boundaries [9].

4.4 CONCLUSIONS:

1. Solder joints are typically made up of at most a few grain orientations, having low angle boundaries, implying a single or multicrystalline rather than a polycrystalline microstructure.
2. The OIM maps from two opposite sides of a joint show that the same crystal orientation is highly probable throughout the joint, implying that surface OIM scans are probably representative of the interior of the joint.
3. The dominant orientations obtained after solidification from several specimens indicate no highly preferred orientation, though there is a tendency for c-axes to be less likely in the plane of the joint. This may result from the large thermal expansion difference between Cu and Sn in the c-direction.
4. The small number of crystal orientations is probably a result of thermodynamic difficulty in forming solidification nuclei.

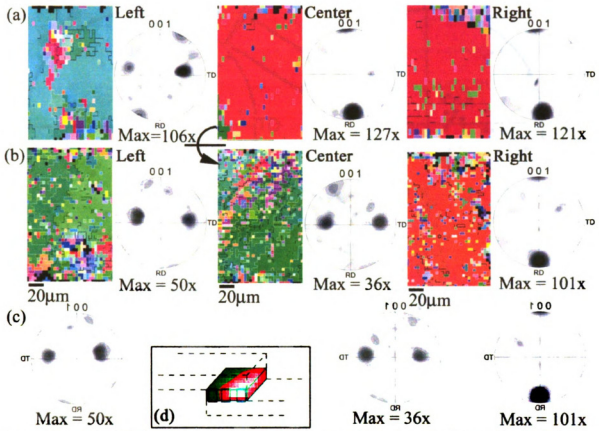

Figure 4.2. (a) [100] inverse pole figure OIM maps and density pole figures for the left, center and right regions of the joint. (b) [100] inverse pole figure and density pole figures measured after rotating the specimen 180° about the horizontal axis. (c) Density pole figures of (b) flipped about the vertical axis, showing similar poles as in (a). (d) Illustration showing the distribution of the two orientations through the thickness of the joint.

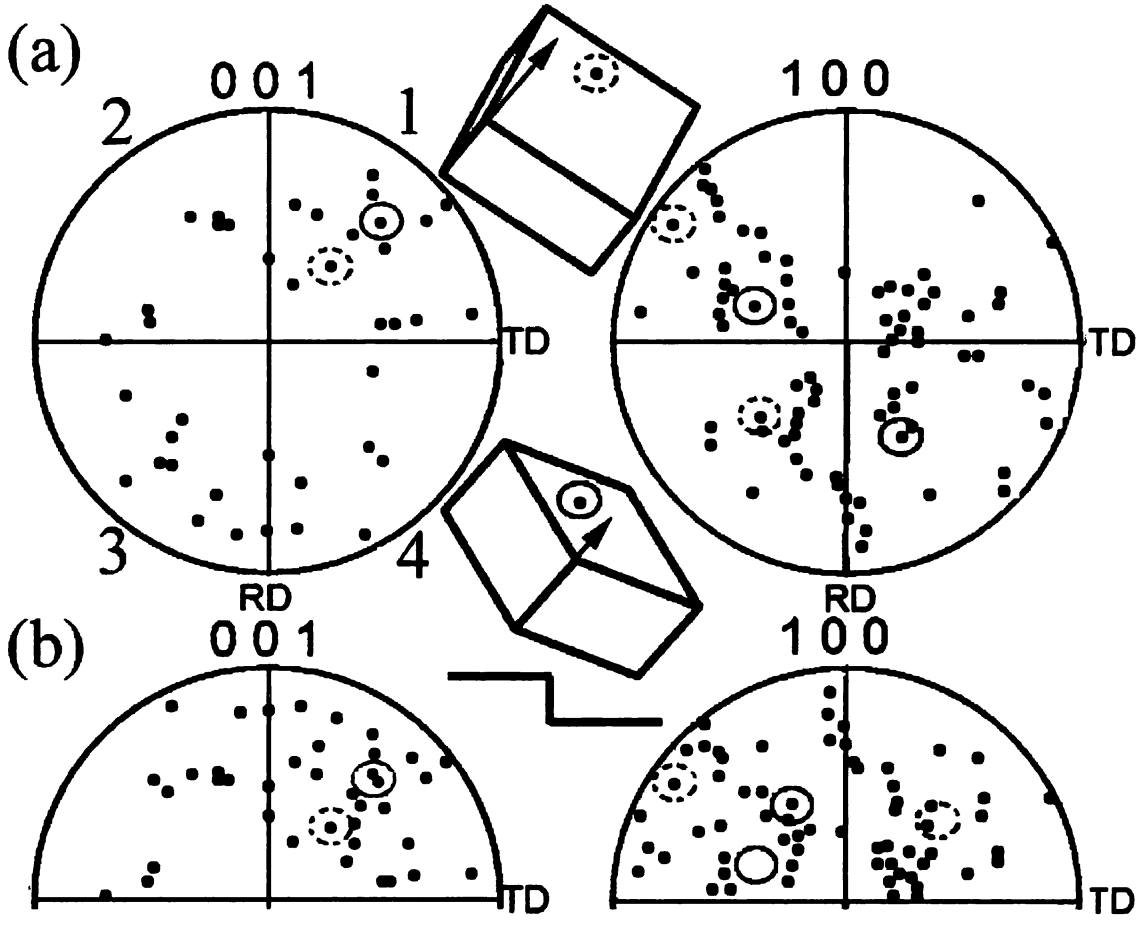

Figure 4.3. (a) Top – (001) and (100) pole figures showing location of the c- and a-axes for 19 different specimens. All the samples are represented in the same specimen geometry that of side A from Figure 2.1. (b) Bottom – (001) and (100) pole figures, with the 3rd and 4th quadrants overlaid onto 1st and 2nd quadrants respectively by a 180° rotation about the normal showing the spread of the c- and a-axis.

4.5 REFERENCES:

1. J.G. Lee, A.U. Telang, T.R. Bieler, and K.N. Subramanian, J. Electron. Mater., 2002. **31**(11): p. 1152.

2. D.R.Frear, JOM, May 1996: p. 49-53.

3. H. Rhee, J.P. Lucas, and K.N. Subramanian, J. of Materials Science: Materials in Electronics, 2002. **13**(8): p. 477.

4. S.Jadhav, Master's Thesis, Michigan State University, East Lansing, MI, 2001.

5. K.N.Subramanian, T.R.Bieler, and J.P.Lucas, J. Electron. Mater., 1999. **28**: p. 1176.

6. J.Siegelko, S.Choi, K.N.Subramanian, J.P.Lucas, and T.R.Bieler, J. Electron. Mater., 1999. **28**: p. 1184.

7. S.Choi, K.N.Subramanian, J.P.Lucas, and T.R.Bieler, J. Elect. Mater., 2000. **29**: p. 1249.

8. A.U.Telang, T.R.Bieler, S.Choi, and K.N.Subramanian, J. Mater. Res., 2002. **17**(9): p. 2294-2306.

9. A.U.Telang, T.R.Bieler, M.A.Crimp, and K.N.Subramanian, Material Science and Engineering A, 2004. **in review**.

10. A.U.Telang, T.R.Bieler, D.E.Mason, and K.N.Subramanian, J. Electron Mater., 2003. **32**(12): p. 1455-1462.

11. J.G.Lee, K.N.Subramanian, and A.Lee, Private Communication, 2004.

12. G.J.Jackson, H.Lu, R.Durairaj, N.Hoo, M.W.Hendriksen, C.Bailey, N.N.Ekere, and J.Wright, Presented at the TMS conference, Sept. 2004 in New Orleans, 2004.

13. R.E.Reed-Hill, *Physical Metallurgy Principles*. 1973, New York, London: Van Nostrand-Reinhold, .

14. D.W.Henderson, T.Gosselin, A.Sarkhel, S.K.Kang, W-K.Choi, D.-Y. Shih, C.Goldsmith, and K.J.Puttlitz, J. of Materials Res., 2002. **17**(11): p. 2775.

CHAPTER 5

AGING OF Sn-3.5Ag SOLDER JOINTS

Scope

Sn-Ag solder joints undergo aging at room and elevated temperatures. Microtextural evolution and grain growth is studied after aging at 85° and after 1 year of room temperature aging for the same joint. Aging causes grain growth, polygonization and low angle grain boundary motion at 85° but room temperature aging caused no obvious changes in the microtexture.

5.1 INTRODUCTION: Eutectic tin-silver, with its low melting point undergoes aging at room temperature. Room temperature (25°C) is about $0.6T_m$ for the Sn-Ag solder). Solder joints are subjected to temperatures of 85-150°C in service and hence aging carried out in the laboratory to study the microstructural evolution could be done in this temperature regime.

5.2 RESULTS AND DISCUSSION

By obtaining OIM maps of the same region of a solder joint before and after aging at 85°C, as illustrated in Figure 5.1(a,b), microstructural evolution due to aging in a particular location can be examined. Figure 5.1(a) shows the OIM map of the as-fabricated joint overlaid on the SEM image, and Figure 5.1(c) shows the OIM map of the same region after aging at 85°C for 100 hours. Figure 5.1(e) shows the OIM map of the same region after room temperature aging for 1 year after it was initially aged. SEM observations reveal coarsening of the Ag_3Sn particles, evident in the regions adjacent to the OIM scans, and discussed in more detail in Ref. [1, 2]. Prior to aging, the OIM scan indicated a single dominant orientation in the joint with fragments of low angle boundaries scattered throughout (essentially a single crystal in the region scanned). Within this orientation, there were many small grains with misorientation angles greater than 15° represented by the white boundaries. Only one continuous low angle boundary was observed (a twist boundary about the c-axis near the bottom in Figure 5.1(a)).

After aging, (Figure 5.1(c)) the dominant single crystal orientation was about the same, but the number of small grains with high misorientation angle decreased, and a number of 5-15° low angle boundaries (thicker black lines) developed. The one continuous low angle boundary present near the bottom of the micrograph of the as-fabricated specimen was no longer in the same position after aging.

The pole figures shown in Figure 5.1(b,d) for as-fabricated and aged specimens are very similar. Subtle changes did occur that reflect substantial motion of low angle grain boundaries. Point plots of the pole figures of both specimens are inserted in-between Figures 5.1(b,d) with as-fabricated orientations shown in black and the aged orientations in gray (each point represents one or more pixels of the scan). The orientations of the aged specimen in the (001) pole figure show 3 or 4 groups of orientations clustered near that for the unaged specimens. These groups show that the majority orientation is spread out over a larger angular space, such that the intensity of this composite peak is reduced, even though the minority orientations have largely disappeared. These disappearing minority orientations marked with a "+" (near (110)) or a "*" on the pole figures in Figure 5.1(b) are diminished in Figure 5.1(d).

After room temperature aging for one year (Figure 5.1(e)), the scan in the same region reveals no change in orientation. The location of the grain boundaries is unchanged. The small specs of different colored pixels in the top left and the lower right and center are probably due to the oxide development which obscured pattern indexing. The texture intensity in Figure 5.1(f) shows an increase to 111 x random. This implies that room temperature aging does not cause changes in the orientations present in the joint, though the Ag_3Sn and other intermetallics coarsen.

The misorientation distribution of the as-fabricated and aged specimens is shown in Figure 5.2. It shows an increase in the number of low angle misorientations of around 6-10° with initial 85°C aging, and a decrease in the number of high angle misorientations of 43, 60 and 70°. After one year the number of low angle boundaries decreased as some of the isolated low angle grain boundaries were annihilated by absorption into the other low angle grain boundaries. The increase in the number and misorientation of low angle boundaries (thick black lines in Figure 5.1(a,c)) after aging at 85°C, and the fact that the (001) peak is split into 3-4 distinct sub-peaks rotated by about 15° from the as-fabricated orientation, indicate that low angle boundaries swept through the microstructure one or more times during 85°C aging. The decrease in the number of high angle misorientations is due to the energy advantage that large grains have to consume small grains with highly misoriented grain boundaries [1, 3].

The high angle misorientation peaks in Figure 5.2 are similar in many of the specimen studied (see creep and TMF specimens in next few chapters). Such typical misorientation distribution for as-fabricated specimens, suggest that certain misorientations are energetically favored during the solidification process. These misorientations correspond to special boundaries and twins [1]: A coincident site lattice is seen when there is a 22.3° rotation about a [110] axis, or with a 43 or 71° rotation about a [010] axis. A 57.2 or 62° rotation about [010] axis gives a (011)[0 $\overline{1}$ 1] or (031)[0 $\overline{1}$ 3] twin, respectively.

Table VII. Typical Misorientation Peaks Observed in Sn-Ag Eutectic As-solidified Solder Joints

Angle/Axis	22.3°[110]	28°[001]	43°[100]	59°[100]	62°[100]	71°[100]	~80°
Σ #	27	17	21	twin	twin	21	

A few of the highly misoriented small grains did not disappear, particularly if they were part of a cluster with other highly misoriented grains, such as the circled clusters in Figure 5.1(a,c). These clusters appear to have existed in a smaller size in almost the same location prior to aging in Figure 5.1(a). A careful investigation of these clusters indicated a higher incidence of misorientations near 60°, than any other misorientation. Twins are known to persist even with long annealing times due to the low energy of their boundary structure [4] and Figure 5.2 shows that 60° twins were retained more than the other special boundary misorientations.

A similar OIM scan in a slightly overlapping region to the right of Figure 5.1 showed the same type of crystal orientations and changes due to aging, with differences only in the finest details.

A comparison of the MODF before and after aging (Figures 5.3, 5.4 and 5.5 respectively) reveals a decrease in the intensity of the 43° misorientations and an increase in the 0-15° misorientations (blue color) after aging, which is consistent with the result seen from the misorientation distribution histogram in Figure 5.2. The 5-15° misorientations are concentrated preferentially about the [100] crystal direction, though 0-5° misorientations have no preferred rotation axis (see Figure 5.4, 0° triangle). As dislocations are absorbed into low angle grain boundaries to increase the misorientation, some low angle boundary misorientations are more stable than others, such as the peak at

7.5°. After aging at room temperature for 1 year, the MODF shows a decrease in the number of <15° misorientations implying that the number of dislocations decreases.

Figure 5.6 presents the grain size distribution for the as-fabricated and aged specimens. While peaks in the grain size distribution shifted upward from 3 and 5μm to 4 and 8 and μm* (as noted by arrows), the area fraction of the small grains decreased for the 85°C aged specimen. This suggests that some of the small grains grew, but more of them disappeared. Since large grains are unbounded in the OIM map, the OIM software was not able to characterize grains larger than 10μm so they are not shown in the grain size distribution. After 1 year of room temperature aging, the 2-3 μm grains show an increase; however these are most likely artifacts of oxidation in different regions (top left and bottom center and right oxidation related region).

Low angle grain boundaries of about 8-12° developed due to high temperature exposure, without stress. The observed changes in the microstructure such as the elimination of small grains and the polygonization resulting in formation of low angle boundaries are consistent with general physical metallurgy principles. Thus isothermal aging caused strongly preferred orientations to persist, so that the joint maintained a nearly single crystal or multicrystal microstructure. Further aging causes growth and continuance of such multicrystals, and may cause smaller grains being absorbed into the most dominant of the multicrystals present in the joint. Since this is monotonic isothermal aging, dislocation are not generated and the existing dislocations have the thermal energy to climb and get absorbed into the grain boundaries.

* Since all plots are made using the same step size and bin definitions, small differences are statistically meaningful for comparison.

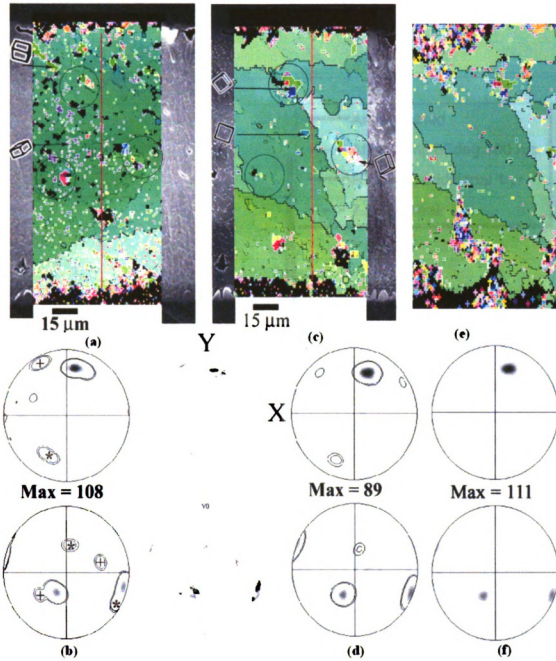

Figure 5.1. Effect of isothermal aging on as-fabricated eutectic Sn-Ag joint made from paste solder. (a) As-fabricated condition and with overlay of OIM map on SEM micrograph and (b) corresponding pole figures to (a), (c) aged condition with overlay of OIM map on SEM micrograph and (d) corresponding pole figures to (c). Small highly misoriented grains with a white boundary disappeared (near [110], marked with a "+" on the pole figure in (b), is diminished in (d)). Point plots of the pole figures of both specimens are inserted in-between (b and d) with as-fabricated orientations shown in black and the aged orientations in gray (each point represents one or more pixels of the scan). The aged orientations in the (001) pole figure show 3 or 4 orientation clusters.

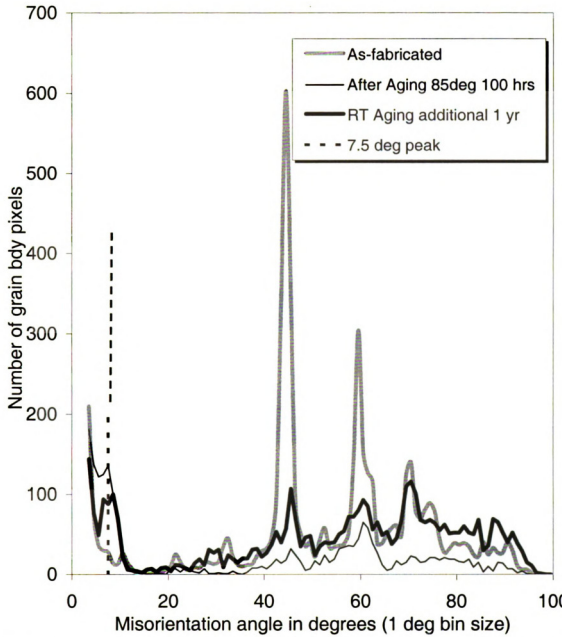

Figure 5.2. Misorientation angle histograms before and after isothermal aging. The number of misorientations at 43, 60 and 70° decrease after aging, and the number of misorientations in the 6-10° range increased.

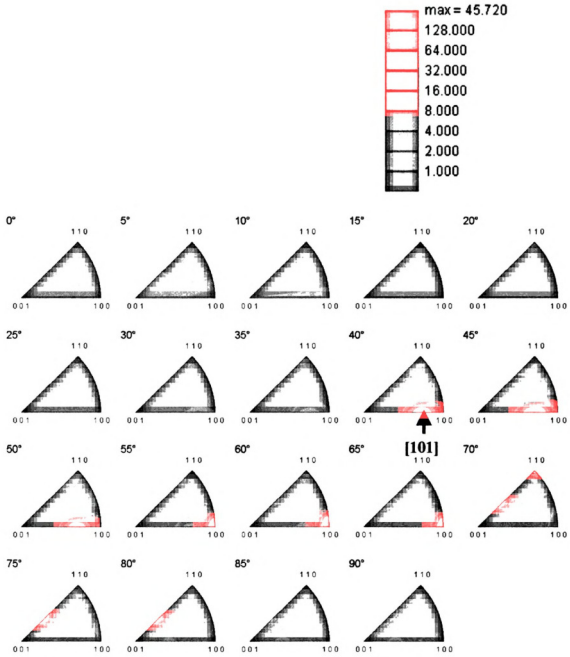

Figure 5.3. Misorientation distribution function for as-fabricated specimen showing 43° misorientations rotated about a [101] crystal direction and 60° misorientations rotated about a [101] crystal direction.

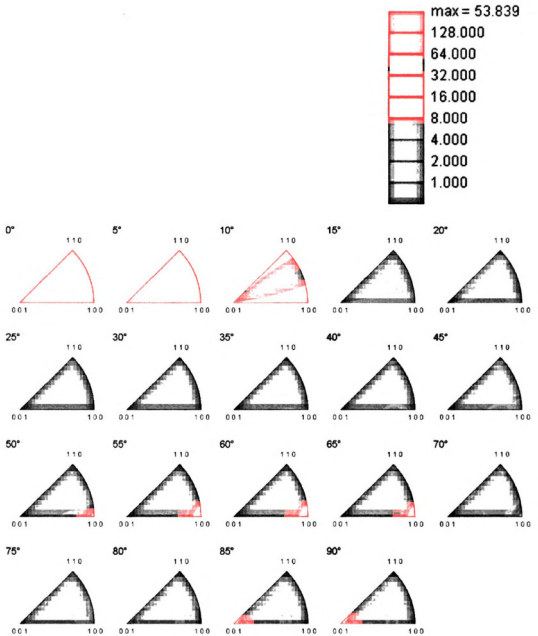

Figure 5.4. Misorientation distribution function after aging showing decrease in the intensity of the 43° misorientations and an increase in the <15° misorientations.

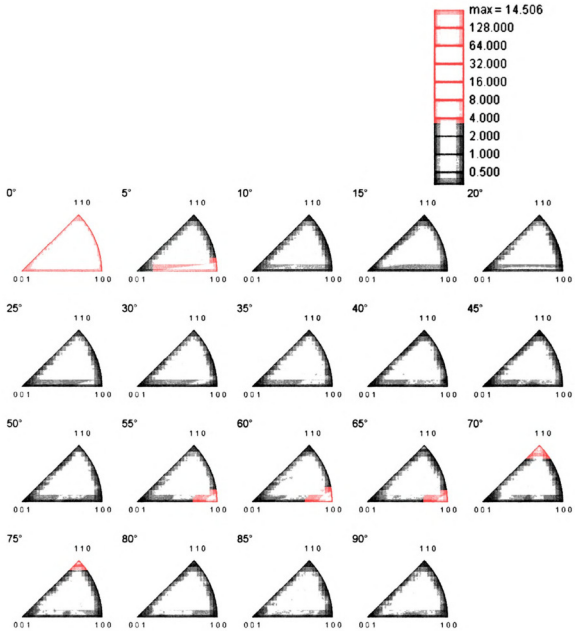

Figure 5.5. Misorientation distribution function after 1 year of additional room temperature aging showing decrease in the intensity of all misorientations.

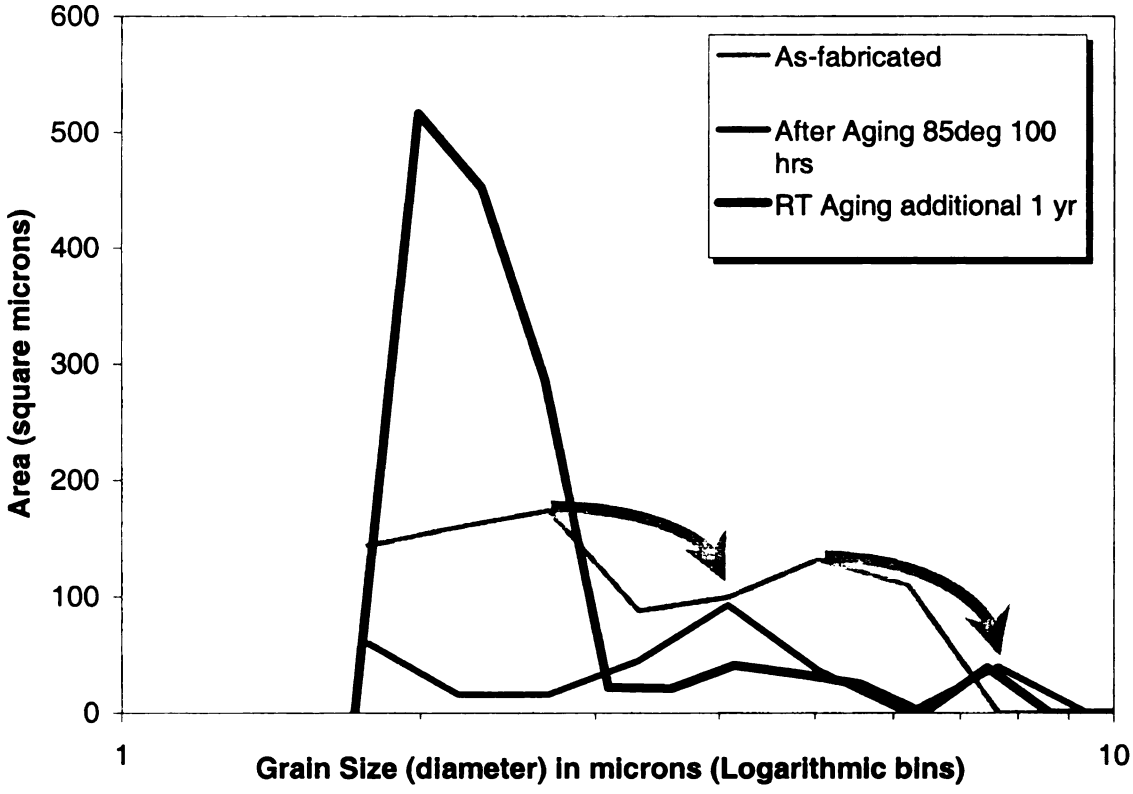

Figure 5.6. Grain size distribution for as-fabricated and aged specimen corresponding to the OIM maps in Figure 5.1. Aging at 85°C causes an increase in the size of the smaller grains characterized in this plot, but room temperature aging caused little change (the large peak is a result of surface degradation).

5.3 REFERENCES:

1. A.U.Telang, T.R.Bieler, S.Choi, and K.N.Subramanian, J. Mater. Res., 2002. 17(9): p. 2294-2306.

2. S.Choi, T.R.Bieler, J.P.Lucas, and K.N.Subramanian. in *Design and Reliablility of solders and solder interconnects, TMS Annual Meeting Warrendale, PA.* 1997.

3. R.W.Cahn, andP.Haasen, *Physical Metallurgy 4th ed., 28.* 1996: Elsevier Science.

4. K.L.Merkle, andD.Wolf, MRS Bulletin, 1990. 15(9): p. 42.

CHARACTERIZATION OF DEFORMATION IN SN-AG LEAD-FREE SOLDERS DURING THERMOMECHANICAL FATIGUE USING ORIENTATION IMAGING MICROSCOPY

Volume II

By

ADWAIT U. TELANG

A DISSERTATION

Submitted to
Michigan State University
in partial fulfillment of the requirements
for the degree of

DOCTOR OF PHILOSOPHY

Department of Chemical Engineering and Materials Science

2004

CHAPTER 6

CREEP OF Sn-3.5Ag SOLDER JOINTS

Scope

Sn-Ag solders experience high homologous temperatures in service where creep and stress relaxation is constantly occurring. It is imperative to study the deformation and the corresponding mesotextural evolution that accompanies this deformation. This section will highlight some of the differences in the creep behavior and damage observed in room temperature and high temperature (85°C) creep.

6.1 ROOM TEMPERATURE CREEP

Figure 6.1 shows SEM micrographs of an as-fabricated single shear lap specimen (a), the same specimen after 0.03 creep strain (b) and after 0.05 creep strain (c) at room temperature. This specimen was deformed with a load of approximately 15 MPa (actual stress was not determined from cross sectional area because the specimen was not deformed to failure). The interrupted experiments occurred after 1-3 months for 0.03 strain and up to 0.05 shear strain. The SEM image on the left side corresponds to a region in the center of the joint whereas the one on the right is 170μm to the right of the center region in the same joint. A scratch on the joint was used to measure the global creep strain. No observable surface topography is noted in these low magnification micrographs, however after 0.05 creep, high magnification images (Figure 6.2) shows cracks and grain pop-up features after 0.04 global strain in isolated locations. Ag_3Sn particles are seen embedded at the grain boundaries in Figure 6.2(b), but they were unable to prevent grain boundary sliding or intergranular separation. The bands containing the eutectic appear to be stronger and more resistant to fracture than primary tin dendrites as cracks in Figure 6.2(b) are arrested in the eutectic regions, and cracks open up in the interface between primary tin cells and the eutectic.

The [010] inverse pole figure OIM maps corresponding to the regions shown in SEM micrographs of Figure 6.1(a,b,c) are shown in Figure 6.3(a,b,c), respectively. The [010] OIM maps are drawn such that regions that have a red color have their c-axis oriented along the x-direction, which aligns the c-axis Burgers vector along the specimen shear direction. The OIM maps show subtle changes in crystal orientation as a function of creep strain; in particular the purple orientation increased in volume fraction with

strain. Room temperature creep does not change the overall crystal orientation and texture of the joint. In this joint, there is one dominant orientation and two secondary orientations in both OIM maps. The dominant orientation shown by a yellow-orange and a '+' on the pole figure in Figure 3(a), whereas the secondary orientations are represented by dark orange, purple, and green represented by 'o', 'p' and 'g' respectively on the pole figure maps. The dominant orientation represented by light orange, has its c-axis tilted towards the negative x-axis, 55° from the specimen normal, whereas the secondary orientation represented by dark orange has its c-axis tilted from the specimen normal by 65° towards the positive x-axis. For both these orientations, as well as the minority green orientation, the c-axis is tilted from the x-z plane of maximum shear by ~15°. This can be clearly seen in the density pole figures of Figure 6.4(a,b,c). The two stronger orientations are expected to deform easily in shear, since the c-axis vector is a close packed direction and a Burgers vector. The minority purple orientation has its c-axis tilted from the specimen normal by about 55° towards the negative y-axis. The 'o' and 'g' minority orientations are twin related by ~60° rotations of the "+" unit cell about the nearly vertical 010 axis, and the 'p' orientation is also twin related by rotating the '+' unit cell about the 100 axis by ~60°. Low angle and high angle grain boundaries are evident in the map. High angle grain boundaries are evident in places where there is a discontinuity in color. There are more twin high angle grain boundary misorientations in the range of 55-65° indicated by white lines than [1]. Many high angle grain boundaries are linked to low angle grain boundaries (thin for 3-5°, thick black lines for 5-15°) in several locations of the OIM map.

Figure 6.3 reveals texture bands between the top right and the bottom left, as identified by boundaries between purple, light and dark orange solidification twin misorientations. The OIM map of the right region has a lesser number of bands compared to the OIM map of the central region (left scan in Figure 6.3(a)).

The density pole figures in Figure 6.4 corresponding to the two regions show a single dominant orientation (+) along with 2-3 secondary twin misorientations (y-o, y-p, o-g). The maximum texture intensity 'x-random' is noted below the pole figures and tabulated for the dominant peaks in Table VII. There is a very small decrease in the texture intensity after 0.3 creep which may result from increased noise attributed to oxide formation, and small amount of growth of secondary orientations (especially in the polycrystalline band and the growth of the purple secondary orientation in the central region) since the overall texture does not change. However there are subtle changes in the position of both low and high angle grain boundaries. The overall texture remained unchanged and the high and low angle grain boundaries persisted and no major changes in grain shape were observed. These small changes imply that room creep deformation does not cause obvious changes in texture, though the strain was small enough to be near the OIM resolution limit, $\gamma \sim 0.05$ (a shear rotation of ~ 3°).

Table VIII. Texture Intensities for Twin Related Poles in the Room Temperature Creep Specimen #1

	Center				Right			
	+	o	p	g	+	o	p	g
As-fab	45.8	35.3	4.4	0	110.3	8	3.8	0.9
0.03	34.4	31.5	2.9	0.5	115.1	8.5	3.2	0.7
0.05	35.9	35	8.7	0.5	102.3	7.8	4.7	1.2

The grain boundary misorientation distribution shown in Figure 6.5 shows that only minor changes occurred as a function of creep strain. There are a large number of pixel pairs (~750) having low angle boundaries <3° and one can see notable peaks at 30, 43, 62 and around 70 and 75° misorientations. In the central region there is no change in the peak positions after 0.3 creep, however the trough of the 60° peak has widened and dual peaks are seen around 43°. There is an overall trend in the increase in the number of grain boundary pixels implying slight grain growth or noise caused by formation of oxides on the material. The widening of the base of the 60° peak suggests that dislocations may have accumulated near twin boundaries. The central region shows more changes that the right region which has a lower grain boundary area. The presence of smaller grains is correlated with larger changes in the misorientation profile.

Figure 6.6 shows the misorientation distribution function (MODF) for the as-fabricated specimen central region. The MODF indicates that there is a large number (~298 x random) of boundaries with a 62° rotation about the [100] crystal direction. Additional peaks for other grain boundary angle / axis pairs for this as-fabricated specimen are listed in Table IX.

Table IX. Preferred Angle / Axis Pairs Obtained From the MODF for the As-fabricated Creep Specimen (Figure 6.6).

Angle in degrees	Axis	Intensity (x random)
20°	[110]	1.2
30°	[100]	8.6
45°	[110] and [111]	4.1 and 7.3
62°	[100]	298
70°	[110]	50.5
77.5°	[829]	7.7
87.5°	[001]	24.4

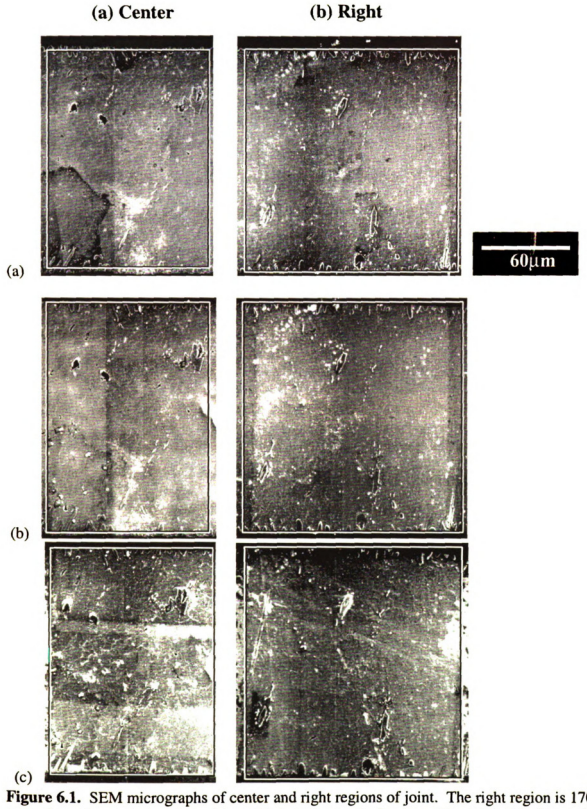

Figure 6.1. SEM micrographs of center and right regions of joint. The right region is 170μm away from the central region. (a) as-fabricated eutectic Sn-Ag solder joint, (b) after a global shear creep strain of 0.03 and (c) after a global shear creep strain of 0.05. No major changes in the microstructure can be observed from these SEM images, though microcracks develop after 0.05 strain.

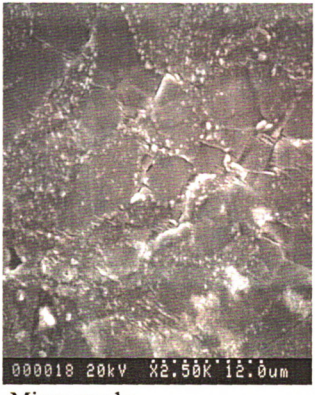

(a)

(b)

Figure 6.2. Higher magnification SEM micrographs of room temperature creep specimen after 0.05 strain from (a) center and (b) right regions of the joint. Both regions reveal microcracks and (a) shows grain rotation and shearing perpendicular to Ag_3Sn particle bands.

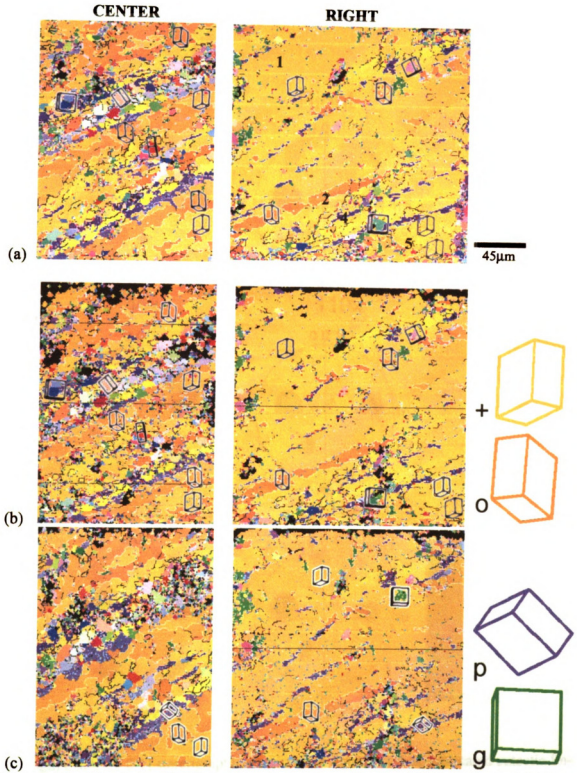

Figure 6.3. OIM maps of regions shown in low magnification SEMs in Figure 6.1 (a) as-fabricated eutectic Sn-Ag solder, (b) after a global shear creep strain of 0.03, and (c) after a global shear creep strain of 0.05. White boundaries 55-65° are twin boundaries, thin and thick black lines correspond to 3-5° and 5-15° misorientations respectively.

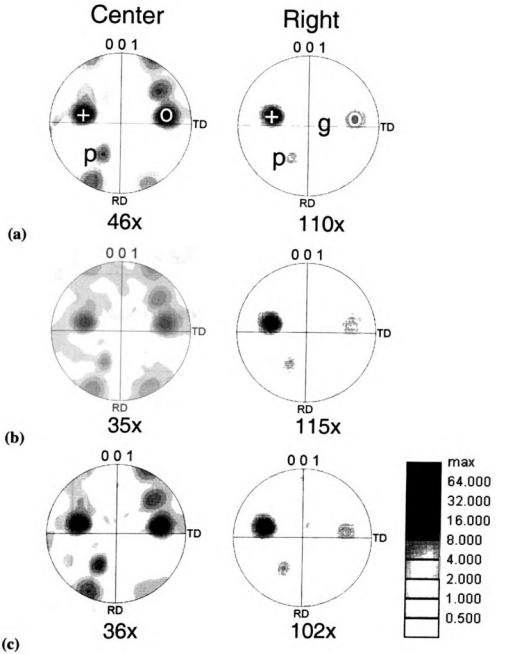

Figure 6.4. [0 0 1] stereographic density pole figures. (a) as-fabricated eutectic Sn-Ag solder, (b) after a global shear creep strain of 0.03, and (c) after a global shear creep strain of 0.05. Overall dominant orientation texture decrease may be due to slight grain growth of secondary orientations and oxide formation.

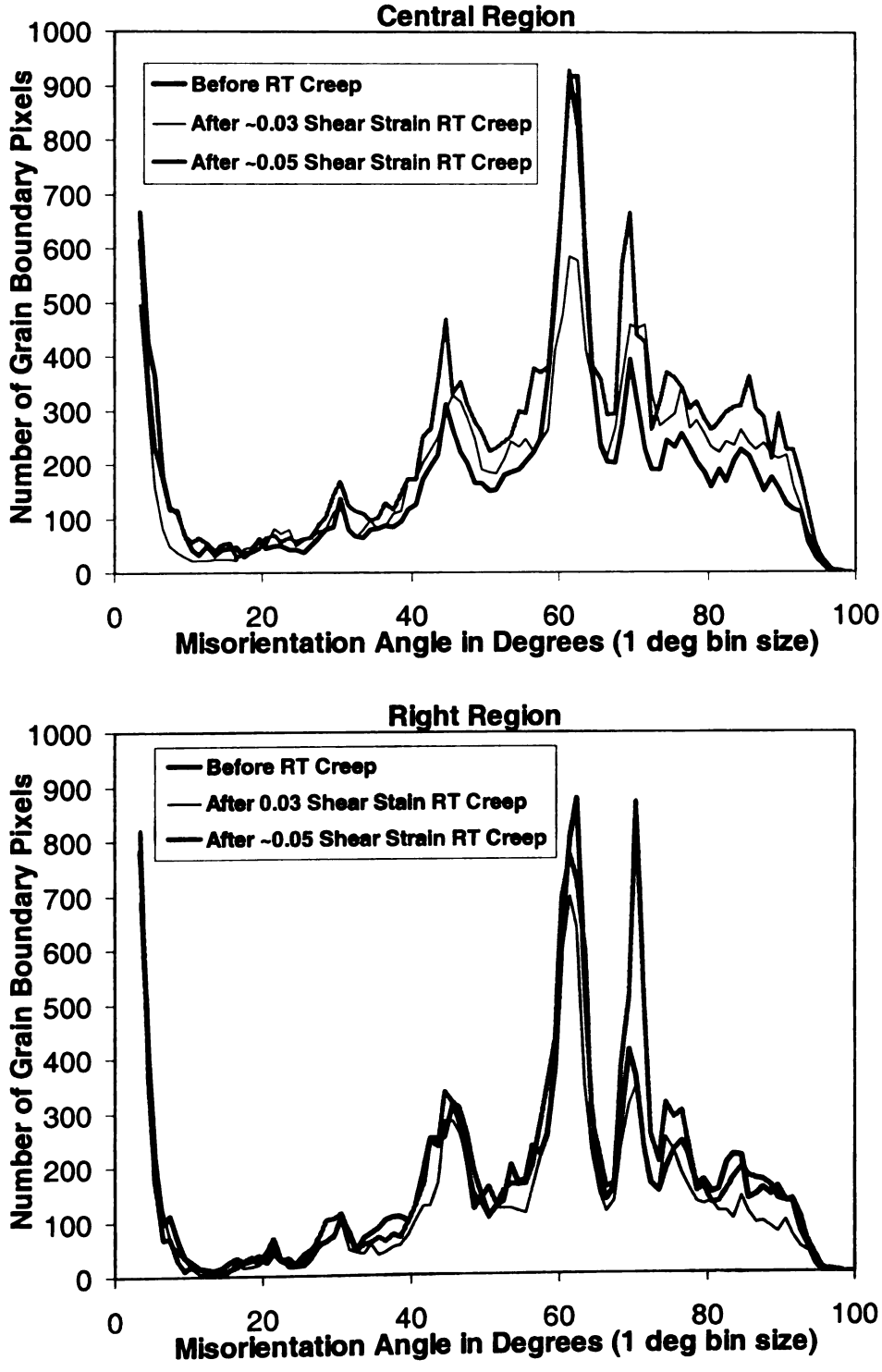

Figure 6.5. Misorientation histograms for the central and right regions as a function of creep strain. Subtle changes in peaks which correspond to dislocation activity and creep strain.

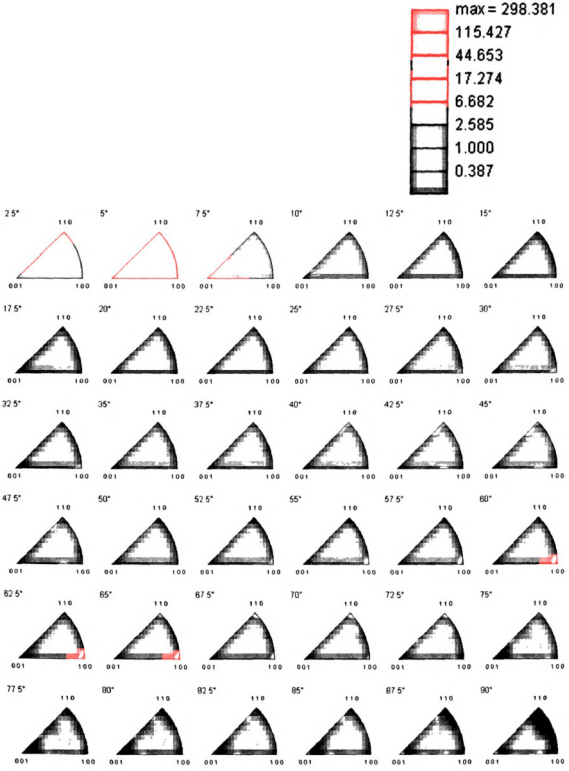

Figure 6.6. Misorientation distribution function for central region as-fabricated specimen with 2.5° bin size.

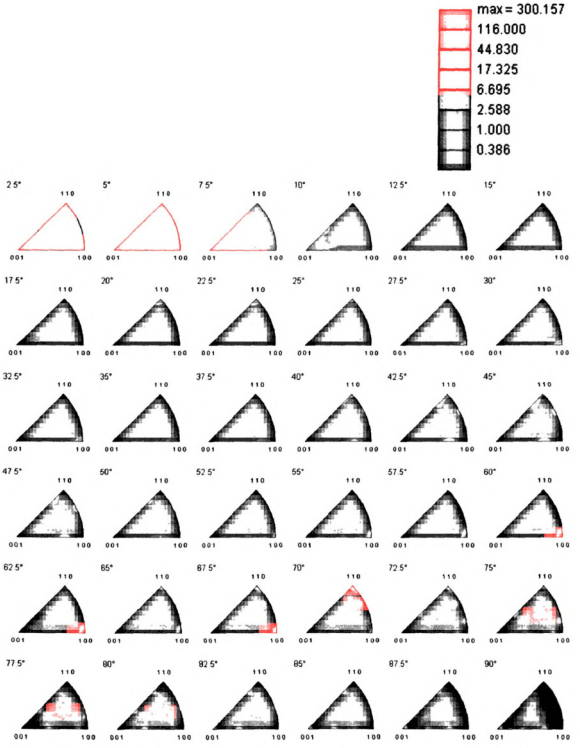

Figure 6.7. Misorientation distribution function with 2.5° bin size for central region of specimen after global creep to 0.05 shear strain. More spread of peaks seen near 45 and 60° which corresponds to the dislocation activity and small rotations in the polycrystalline bands.

6.2 SURFACE TOPOGRAPHY AND MICRO CRACK FORMATION DURING ROOM TEMPERATURE CREEP:

The following section will discuss the surface topography and micro cracks that developed after room temperature creep. Micro cracks were more common in these specimens as compared to high temperature creep specimens discussed later. Microcracks developed predominantly in minority twin orientations. A large amount of grain boundary sliding is not observed, however ledge initiation was seen in one case with presence on intermediary microcracks. Higher magnification SEMs are shown at the end of this section to illustrate some of the typical surface topography and micro cracks observed in room temperature creep specimens.

Case Study 1: Micro Crack Formation In The Central Region of Figure 6.3

Figure 6.8 shows the OIM and a high magnification SEM image obtained from an area in the central region of Figure 6.3. The SEM image corresponds to the boxed region in the OIM maps that correlated well with the boundary structure and orientation of individual grains in this region can be easily obtained. Microcracks and grain rotation developed after 0.05 creep strain at room temperature. The OIM map reveals a large number of twin type boundaries (55-65°, marked by thick blue lines), which correlate with crack formation during room temperature creep. The MODF of the cropped region after 0.05 shear strain in Figure 6.8 shows this to be true. The OIM map shown in Figure 6.8 has a misorientation histogram as shown in Figure 6.9(a). About a third of the high

angle grain boundaries are in the 50-70° range and another third of the boundaries are low angle grain boundaries <15° are present. The SEM image correlated well with the boundary structure and orientation of individual grains in this region can be easily obtained. Micro cracking and grain rotation is observed (see Figure 6.8). The grain rotation could cause inhomogeneous deformation and incompatibility, which can lead to micro cracks. Table X indicates rotations that occur along with the equivalent simple shear strains that could account for such a rotation (see Figure 6.8 and 6.3 for grain location for the center and right regions respectively). Grain 1 is the dominant orange orientation and the rotation observed corresponds closely with the shear strain imposed. Larger strain accompanies larger rotations, which show micro cracks in the specimen as shown in Figure 6.8, in which the grains analyzed in Table X are labeled.

Table X: Grain Rotations as a Function of Creep Strain from Central and Right Regions of Specimen #1 Figure 6.3

CENTER

		Euler Angle Degrees			Misorientation	Rotation axes			Rotation
		phi1	PHI	phi2	Angle (deg)	n1	n2	n3	Strain
Grain 1	Asfab	197.8	72.1	53.3					
	0.03	198.1	72.2	53.2	0.3	-0.954	-0.3	0.027	0.01
	0.05	200.5	70.7	51.9	2.78	-0.322	-0.927	0.193	0.05
Grain 2	Asfab	241.8	90.9	68.6					
	0.03	241.8	90	67.9	1.14	0.293	-0.733	0.614	0.02
	0.05	243.7	90	67.2	2.02	-0.867	-0.358	0.346	0.04
Grain 3	Asfab	210.1	145	54.7					
	0.03	211.8	144.3	56.1	1.21	-0.341	-0.94	-0.011	0.02
	0.05	209	143.9	53.2	1.8	0.871	0.346	0.35	0.03
Grain 4	Asfab	197.9	75.2	83.3					
	0.03	198.3	74.9	84	0.94	-0.373	-0.362	-0.854	0.02
	0.05	200.9	73.8	82.6	2.82	-0.836	-0.491	0.247	0.05
Grain 5	Asfab	191.8	64.8	66.8					
	0.03	191.1	65	69	2.02	0.254	0.21	-0.944	0.04
	0.05	191.5	65.1	67.8	1.1	-0.341	-0.037	0.939	0.02

RIGHT

		Euler Angle Degrees			Misorientation	Rotation axes			Rotation
		phi1	PHI	phi2	Angle (deg)	n1	n2	n3	Strain
Grain 1	Asfab	166.2	124.4	65.9					
	0.03	168.2	123.3	67.7	2.11	-0.519	-0.79	-0.325	0.04
	0.05	167.2	120.6	68.1	2.98	0.605	-0.733	-0.312	0.05
Grain 2	Asfab	188.3	64.6	68.9					
	0.03	188	64.1	69.1	0.57	0.754	-0.646	-0.122	0.01
	0.05	187.3	61.9	67.6	2.92	0.476	-0.621	0.622	0.05
Grain 3	Asfab	237.3	24.6	33.2					
	0.03	237.5	24.8	33.2	0.28	-0.753	0.14	-0.642	0.00
	0.05	244.1	23.1	26	3.38	0.045	-0.937	0.345	0.06
Grain 4	Asfab	243.5	127.3	25.8					
	0.03	241.2	131.9	24	4.94	-0.693	0.717	0.067	0.09
	0.05	234.5	130.1	16.8	6.05	0.57	0.679	0.462	0.11
Grain 5	Asfab	162.9	124.8	60.4					
	0.03	164	124.4	62.3	1.61	-0.373	-0.486	-0.79	0.03
	0.05	162.1	121	62.5	3.95	0.757	-0.575	-0.31	0.07

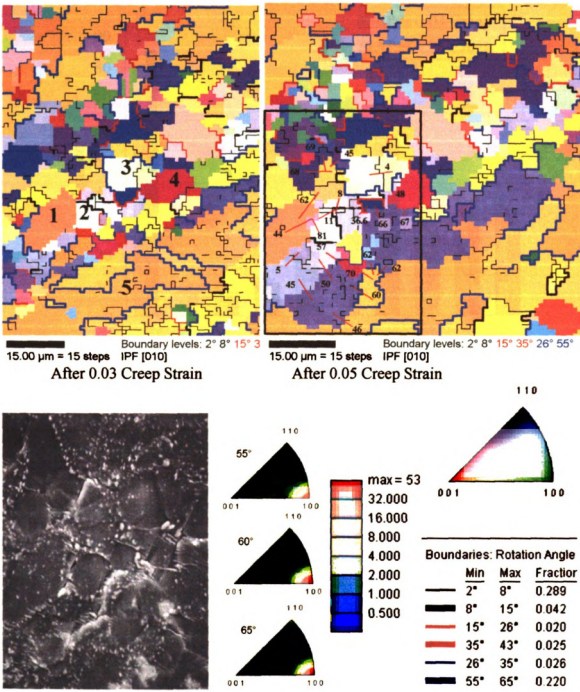

Figure 6.8. Higher resolution OIMs obtained from the center region above in Figure 6.3. OIMs after 0.03 and 0.05 creep strain and SEM after 0.05 creep strain (corresponding to boxed region in OIM map). Micro cracks and grain rotation developed after 0.05 creep strain at room temperature which can be correlated to the large number of twin type boundaries (55-65°, marked by thick blue lines in the OIM maps. The MODF of the cropped region reveals that these boundaries are twin-type, obtained by rotations of around 57 and 62° about [100].

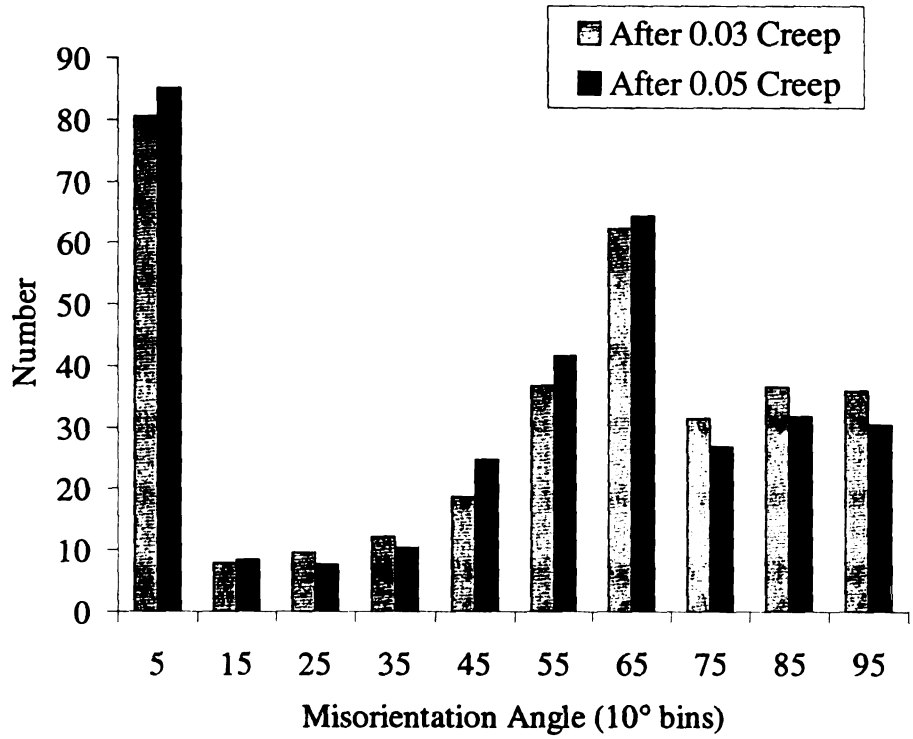

(a)

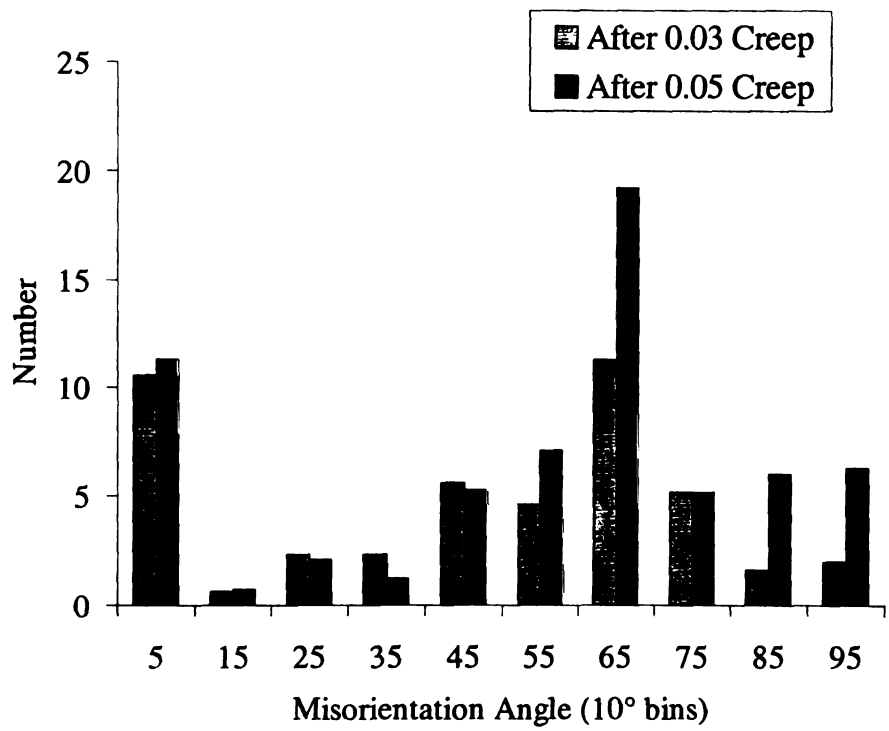

(b)

Figure 6.9. The misorientation histogram for the cropped OIM scans shown in Figures 6.8 and 6.10. (a) polycrystalline band from center region of joint and (b) left edge of right region.

Case Study 2: Micro Crack Formation in the Left Edge of the Right Region Of Room Temperature Creep Specimen #1 (Figure 6.10)

Figure 6.10 shows the OIM maps after 0.03 creep strain and 0.05 creep strain along with the SEM image after 0.05 creep strain (also shown in Figure 6.2(b)). The boxed region in the SEM image corresponds to the OIM scans. Grain boundary fracture is apparent in the SEM image, without any grain boundary sliding. Comparing the OIM maps after 0.05 creep strain to the SEM image, the cracks correlate predominantly with the twin boundaries having a 55-65° rotation about the [100] crystal direction marked by thick blue lines (note MODF for the cropped region in Figure 6.9). The twin boundaries are low energy coherent boundaries, which might resist climb-annihilation of dislocations, leading to pile-ups that give rise to micro cracks. The large number of low angle grain boundaries remain unchanged with creep (Figure 6.5, and MODFs) but this implies the presence of large number of dislocations, which must have moved through the material to cause strain, but also recovered to maintain the same low angle misorientation statistic. Some higher angle boundaries moved to consume grains with low angle misorientations between the green and pink grains present after 0.03 creep, so as to form a larger green grain after 0.05 creep. The green orientation has the c-axis normal to the surface and shear stress is maximized on the (100) plane in the direction of a slip, which makes this a harder orientation than the surrounding orange orientation. The microcracks correlate with these twin-type boundaries between the green and orange orientations, as well as present within the green orientation.

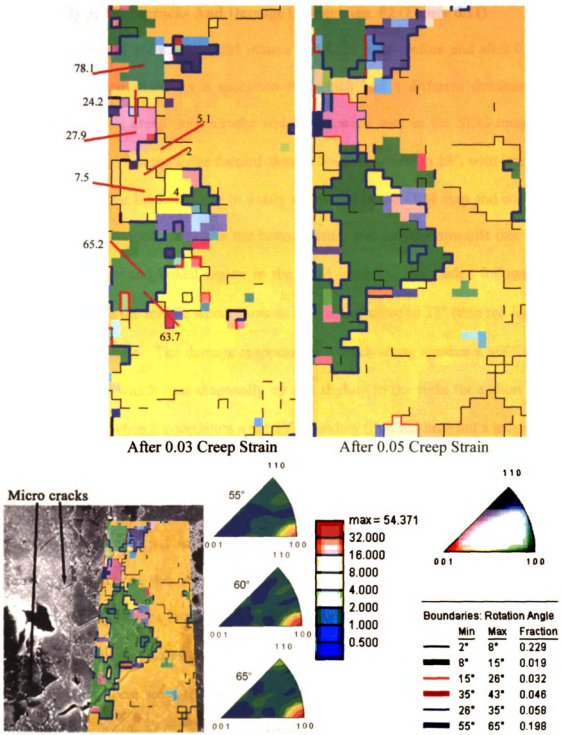

Figure 6.10. Higher magnification OIM maps obtained from the left edge of the right region in Figure 6.3 after 0.03 and 0.05 creep strain and SEM after 0.05 creep strain (OIMs correspond to boxed region in SEM). Cleavage-type micro cracks developed after 0.05 creep strain at room temperature which correlated with the large number of twin type boundaries (55-65°), marked by thick blue lines in the OIM maps. MODF reveals that these boundaries are twin-type obtained by rotations of around 57 and 62° about [100].

Case Study 3: Microcracks And Damage in Specimen #2 (Figure 6.11)

Figure 6.11 shows the SEM images and OIM maps before and after 0.07 room temperature creep strain for a specimen #2, which had a different dominant crystal orientation. After creep, microcracks and ledges were seen in the SEM images. The OIM maps reveal that the ledge formed along a boundary close to 28°, with intermediary micro cracks. The boundary can be easily delineated in the OIM map and compared to the ledge being formed starting at the bottom center and moving upwards (see thin blue line in OIM map and boxed region in the SEM images). The ledge follows the 28° boundary toward the middle where it meets a boundary close to 23° (thin red line) where the ledge disappears. The damage reappears as a crack along another a ~60° boundary (thick blue line) which runs diagonally up and slightly to the right for a short distance. The crack stops when it encounters a red 23° boundary (thin red line) but a ledge emerges at another 28° boundary above and to the left (see Figure 6.11(e)). The ledge formation is not observed as much in the room temperature creep specimens, as compared to the high temperature creep described in the next section. Other microcracks are observed in the boxed region of the SEM image after creep (see top right), but it is difficult to pinpoint the boundaries that align with the cracks since this scan was done with a 4μm step size, and hence smaller scattered boundaries / microcracks are harder to correlate. In this specimen, there are a few twin and 8-15° boundaries. Figure 6.12 shows a higher magnification image of the ledge and a small crack midway through the joint. The ledge starts from the tip of the Cu_6Sn_5 particle and proceeds to the left. Other SEM images in Figure 6.12 reveal different regions of this specimen (not in the region scanned) where grain boundary separation microcracks were observed.

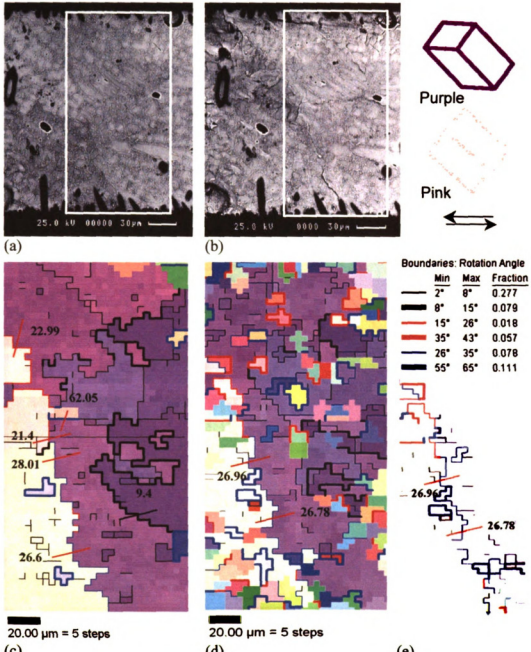

Figure 6.11. SEM images (a,b) and OIM maps of boxed regions (c,d) in undeformed (a,c), and after 0.07 strain (b,d) creep specimen #2 after 0.07 global creep strain, and (e) grain boundary map showing particular boundary relationships. Ledge and micro cracks developed after creep which correlate with the ~28° boundary marked by thin blue lines.

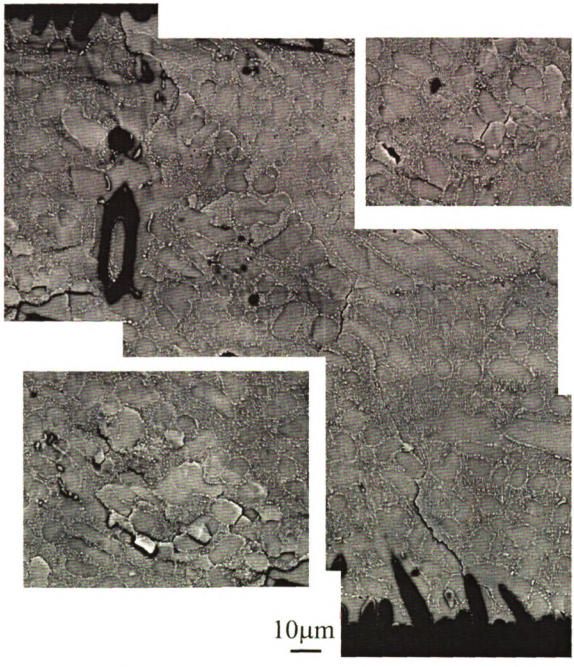

Figure 6.12. Higher magnification SEM of region shown in Figure 6.11 above. SEM images at the same magnification on top right and bottom left reveal micro cracks in different locations in the same specimen.

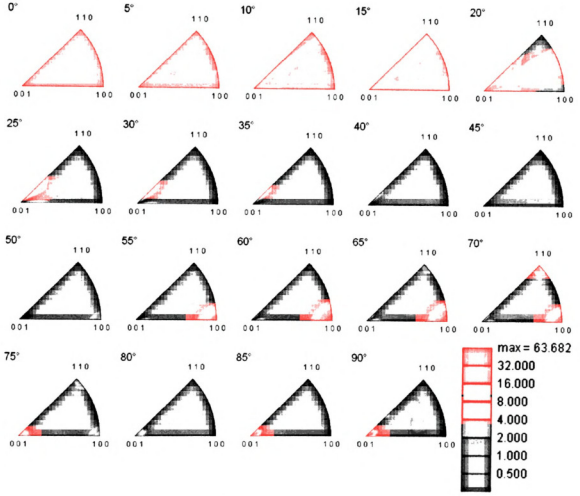

Figure 6.13(a). As-fabricated MODF reveals that these boundaries have a twin-type misorientation relationship obtained by rotations of around 60° about [100]. A large number of sub-grain boundaries (<15°) are present, implying the presence of a large number of dislocations.

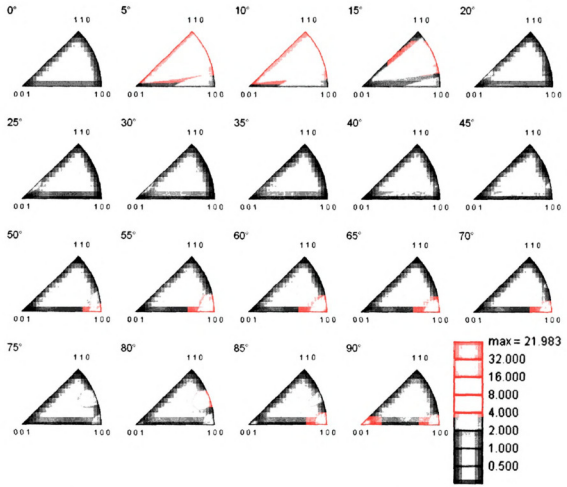

Figure 6.13(b). MODF and histogram for creep specimen #2 after 0.07 strain. Low angle boundaries have reduced, but increased misorientation, suggests substantial dislocation glide and/or annihilation processes occurred. The ~28° boundary misorientation can be obtained by a rotation about an axis close to [001].

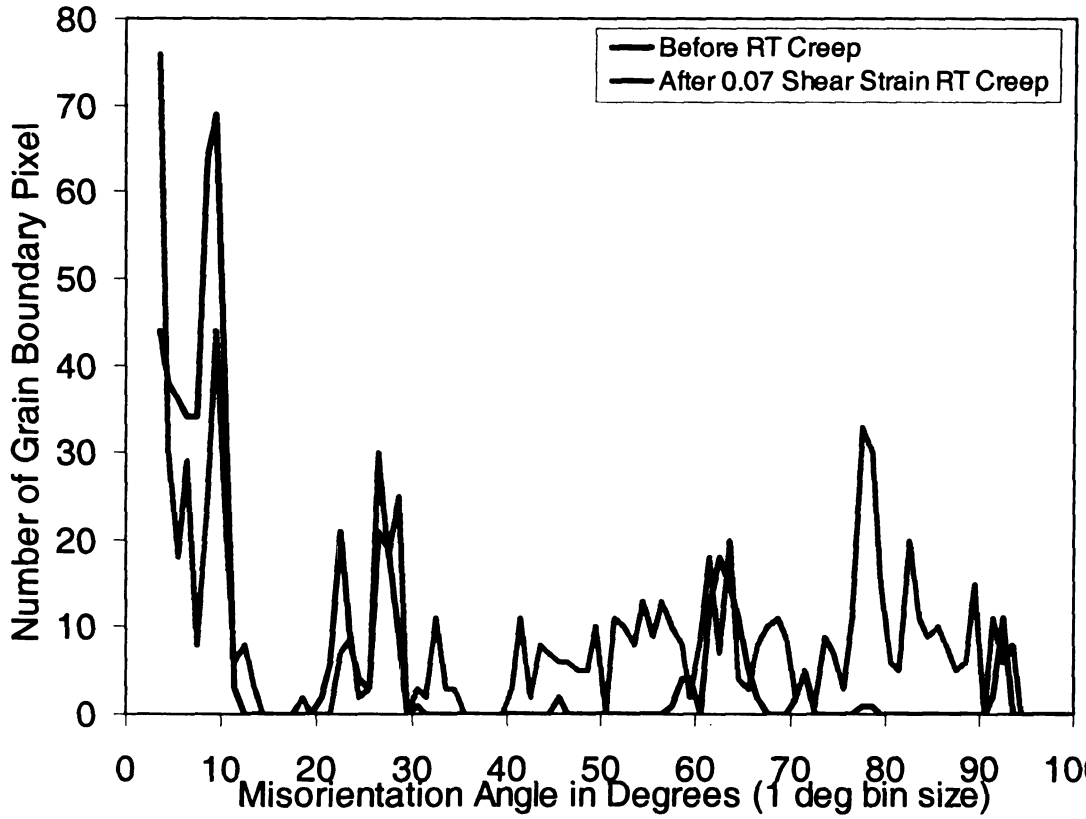

Figure 6.13(b) continued. MODF and histogram for creep specimen #2 after 0.07 strain. Low angle boundaries have reduced, but increased misorientation, suggests substantial dislocation glide and/or annihilation processes occurred. The ~28° boundary misorientation can be obtained by a rotation about an axis close to [001].

The MODF in Figure 6.13(a,b) reveals that this ledge is formed by a rotation of close to 28° about a [001] direction (there is also a strong peak for twins at 60°). Figure 6.13(b) shows an increase in the number of misorientations between 40-60° and 70-90°.

Case Study 4: Microcrack Features and Damage Observed in Room Temperature Creep Specimen #2

Creep specimen #2 revealed certain characteristic types of surface damage. Grain boundary separation type microcracks were observed in several regions, including regions close to the intermetallic layer interface with the tin matrix. Ledges / surface topography that formed started from the intermetallic interface and moved towards the interior of the joint. Figure 6.15 shows a low magnification image of the surface after room temperature creep to 0.07 shear strain in specimen #2. Extensive surface topography was observed with some regions showing microcracks. Figure 6.16 shows secondary and backscattered electron images for one such region not marked by an arrow but near the top center of Figure 6.15. 'A' marks a location where BSE contrast not present in the SE image indicates a probable subgrain boundary / dislocation wall. 'B' marks the location of apparent slip bands and 'C' shows a a low angle boundary or an incipient microcrack parallel to a primary micro crack. Several microcracks and other surface topography features are apparent in the SEM images. Figure 6.17 shows SE and BSE high magnification image revealing slip bands and microcracks. Figure 6.18 shows SE and BSE images revealing microcracks and dislocation substructure, which looks like it is looping away from the interphases intermetallic layer.

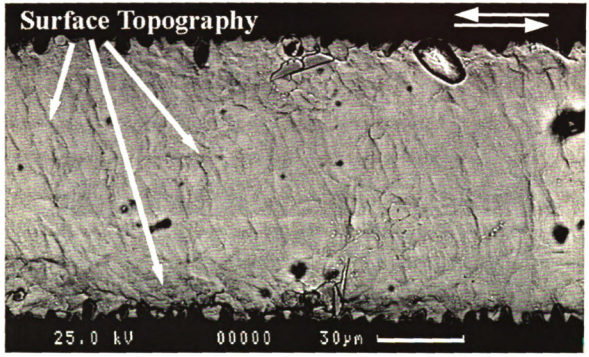

Figure 6.15. Surface topography seen after 0.07 creep strain on the BSE SEM image from a different location in the specimen shown in Figure 6.16-18. Shear bands are present coming out of the surface. Micro cracks are seen with higher magnification images in Figures 6.16-18.

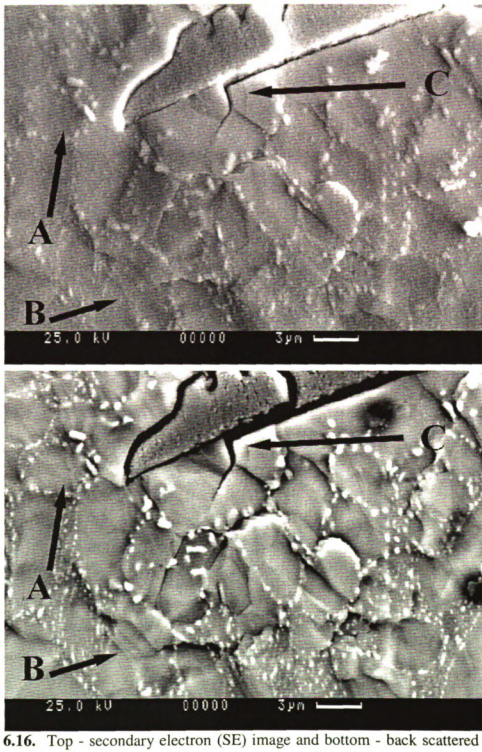

Figure 6.16. Top - secondary electron (SE) image and bottom - back scattered electron (BSE) images. These high magnification images are for a location in the top center of Figure 15 above. 'A' marks the location where subgrain boundary / dislocation wall can be seen (not seen in the SE image but present in the BSE image). 'B' marks the location of slip lines and 'C' shows an additional slip band or micro crack formed behind a primary micro crack. Several other micro cracks and surface topography is observed in the SEM images.

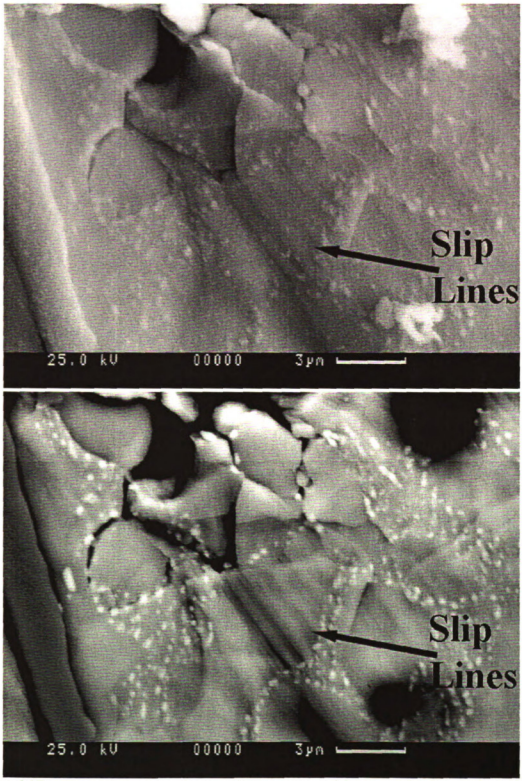

Figure 6.17. Top - secondary electron (SE) image and bottom - back scattered electron (BSE) images. Image revealing slip lines and micro cracks. These high magnification images are for a location in Figure 6.15 above.

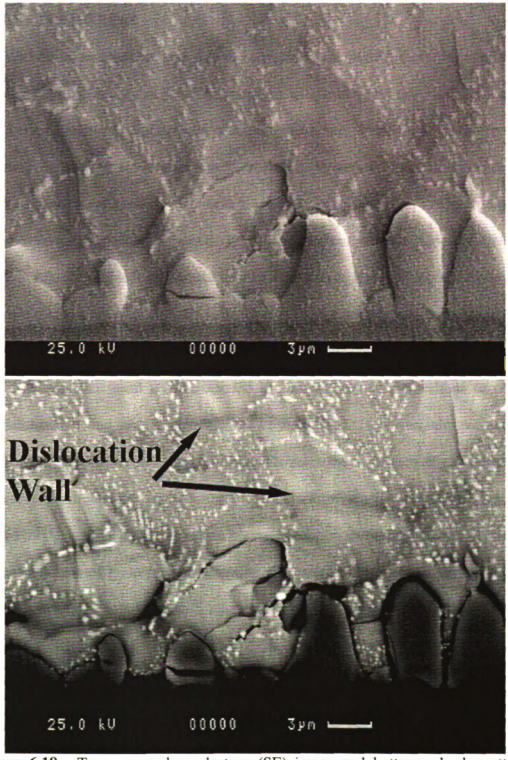

Figure 6.18. Top - secondary electron (SE) image and bottom - back scattered electron (BSE) images. Images reveal micro cracks and dislocation substructure. These high magnification images are for a location in Figure 6.15 above.

6.3 ASSESSMENT OF MICROSTRUCTURAL CHANGES DURING ROOM TEMPERATURE CREEP

With room temperature and global shear strains up to 0.07, there was apparently not enough thermal energy or local deformation to cause significant recrystallization, though dynamic recovery should occur at room temperature. From the reduction in very low angle boundaries in creep specimen #2, room temperature creep deformation occurs by a dislocation creep/recovery mechanism, which is consistent with the interpretation from conventional creep experiments [2] with a stress exponent greater than 5. Dislocation substructure and cells could be pinned by the Ag_3Sn particles which supports the experimentally observed n values larger than 5 [2, 3] for these single shear lap joint during room temperature creep. At elevated temperature, incoherent particles often cause threshold stresses that need to be exceeded to free the pinned dislocations to obtain plastic deformation, and such an approach has been used [4]. However, in regions where dislocations pile-up, high local stresses can lead to microcracks if recovery is hampered, that cause grain boundary separation [5]. The lack of significant recovery is also supported by the lack of large-scale grain boundary motion and little evidence of sliding. The small amounts of grain boundary motion and/or recovery observed from the OIM maps and statistics is consistent with microcrack formation due to ineffective recovery processes, which may be precluded by Σ boundaries that are unable to absorb dislocations.

The strong texture implies that small solder joints are multicrystals rather than polycrystals, and this can account for the greater variability of creep resistance in these single shear lap specimens consisting of single solder joints, as compared to the studies

with specimens containing multiple solder joints from Darveaux's study [2, 3]. The dominant and secondary orientations in the specimen are usually twin related, and they often exhibit some degree of symmetry with respect to the sample geometry. For example, creep specimen #2 has a different dominant crystal orientation than specimen #1, and consequently different grain boundary character and damage evolution processes. In specimen #1, the dominant crystal orientation was conducive for shear on many slip systems, whereas this was less true in the creep specimen #2 as seen from Table XI. Both the dominant orange and the minority green orientations in creep specimen #1 had highly stressed slip on (110) planes, but being twin related, slip on these planes were not compatible, so the dislocations that were generated may have piled up to cause stresses that can caused micro cracks in the vicinity.

Table XI. Comparison of Schmid Factors for the Dominant Slip Systems for The Two Specimens Described Above.

	Specimen 1		Specimen 2	
Slip Systems	**Orange**	**Green**	**Purple**	**Pink Left**
(010)[001]	-0.28	0.17	0.02	**0.48**
(010)[100]	0.04	0.21	**-0.37**	0.26
(010)[101]	-0.10	0.27	-0.31	**0.46**
(010)[10-1]	0.17	0.11	-0.33	0.00
(01-1)[011]	-0.25	-0.34	0.24	0.06
(011)[01-1]	**-0.55**	-0.15	0.26	**0.58**
(100)[001]	**0.38**	-0.24	**-0.48**	-0.20
(100)[010]	0.04	0.21	**-0.37**	0.26
(100)[011]	0.22	0.07	**-0.55**	0.13
(100)[01-1]	-0.15	0.30	-0.09	0.33
(10-1)[101]	-0.25	0.40	**0.55**	0.18
(101)[10-1]	0.16	0.13	0.03	-0.04
(110)[001]	0.07	-0.05	-0.33	0.19
(1-10)[001]	**0.47**	-0.29	-0.35	**-0.48**
(1-10)[110]	**0.43**	**0.61**	0.05	-0.30
(110)[1-10]	**0.43**	**0.61**	0.05	-0.30
(1-10)[111]/2	**0.57**	**0.46**	-0.08	-0.46
(110)[-111]/2	**-0.37**	**-0.58**	-0.16	**0.35**
(110)[1-11]/2	**0.42**	**0.55**	-0.07	-0.21
(1-10)[-1-11]/2	-0.23	**-0.67**	-0.17	0.11

6.4 HIGH TEMPERATURE CREEP RESULTS

SEM micrographs of creep specimens as-fabricated, after 0.06 global creep strain at 85°C, and 0.3 creep strain at 85°C are shown in Figure 6.19(a,b,c) respectively. This specimen was deformed with a load of approximately 12 MPa (actual stress was not determined from cross sectional area because the specimen was not deformed to failure). The interrupted experiments occurred after roughly 1 week for 0.06 strain and after roughly 2 weeks days when it reached 0.30 shear strain. The SEM images on the left correspond to a region on the left side of the joint whereas the one on the right is 320μm to the right, in a region at the center of the same joint. A dendritic microstructure with two different orientations is evident in the central region in the as-fabricated condition. After creep to 0.06 global creep strain, heterogeneous deformation was identified in different regions as shown in Figure 6.19(b) central region. Regions having local creep strains from 0.3 to almost undeformed regions were observed at this stage. Local shear strains were measured using intermetallic particles as markers. Incipient crack development via grain boundary sliding and ledge development was observed in the central region in Figure 6.19(b), below the words 'crack'. After more creep to a global strain of about 0.3, the crack was distinct in both regions (initially absent in the left region of Figure 6.19(b)), implying that the crack had propagated through the joint. Contrast in Figure 6.19(c) is disturbed due to the presence of dust particles and heterogeneous oxidation. Figure 6.20 shows higher magnification SEM images from the region marked by a white box after 0.3 creep strain in Figure 16.19(c). The high magnification SEM clearly shows grain boundary sliding or ledges formation with Ag_3Sn particles embedded in the boundary. Shearing between two grains at the boundary is also

evident. The dark surface topography in the center of this SEM image is due to an outward bulge and possible a particle that was charging, which obscured the image. EDS measurements confirmed that it was normal solder, and not an inclusion or intermetallic phase.

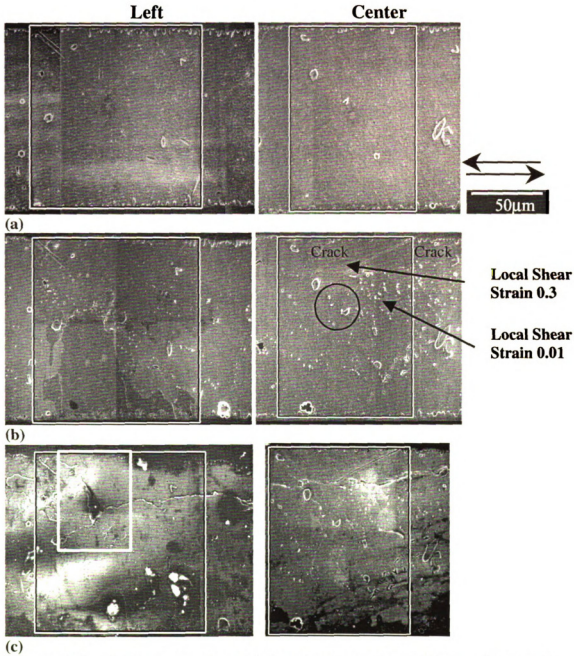

Figure 6.19. SEM micrographs of left and center regions of joint. The center region is 320μm away from the left region. (a) as-fabricated eutectic Sn-Ag solder joint, (b) after a global shear creep strain of 0.06 at 85°C, and (c) after a global shear creep strain of 0.3 at 85°C. Grain boundary sliding and ledge development, which leads to cracking, is seen after 0.06 shear strain.

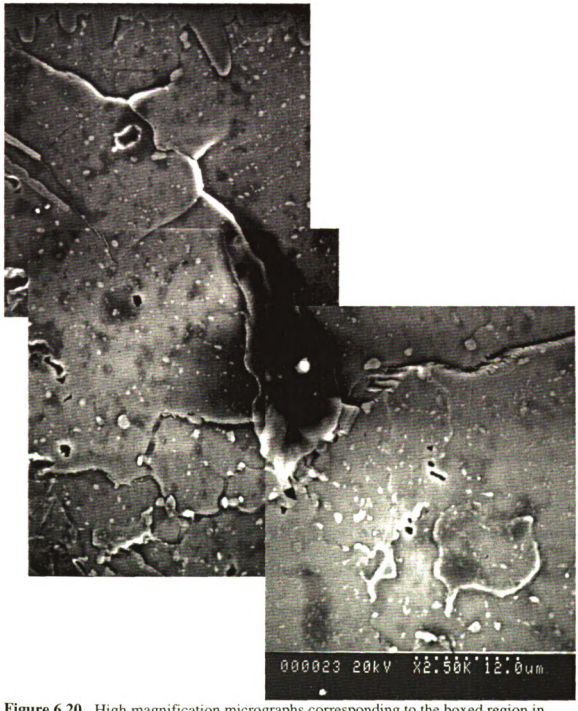

Figure 6.20. High magnification micrographs corresponding to the boxed region in Figure 6.19(c) revealing grain boundary sliding and decohesion, as well as grain pop-up or extrusion.

Figure 6.21(a,b,c) are the [010] inverse pole figure OIM maps corresponding to the regions shown in SEM micrographs of Figure 6.19(a,b,c). After creep deformation the scans look similar to the ones before creep with respect to the color representation of texture, however one can see changes due to creep by comparing the before and after maps. In both regions, there is still one dominant orientation with two other orientations close to the dominant one that remains similar to the as-fabricated specimen. The changes in orientation are shown by the pole figures in Figure 6.22(a,b,c). More low angle grain boundaries are present in the left region. In the OIM map for the central region, low angle grain boundaries traverse through the large pink grain, with mostly pink color on either side of the low angle (5°) grain boundary. Isolated regions represented by green and purple orientations are labeled in the pole figures. The left region shows predominantly three to four shades of blue separated by low angle grain boundaries. The pole figures shown in Figure 6.22(a) reveals that in both the scans there is one dominant orientation (blue in the left and pink in the center regions respectively), though there blue orientations have several close variants (misoriented by about 10-15°), forming a cluster. The pink and blue colors represent orientations that are misoriented by a twin rotation of about 62° about an [100] axis. The purple orientation (top part of central region in Figure 6.21(a)) is misoriented by a rotation of about 40° about an axis near [111] as inferred from the MODF shown later.

The texture intensity in the pole figures decreased with creep and all dominant peaks have rotated systematically toward the negative y-direction by about 10°. The left region has a lower texture maximum value due to the clustered peaks.

High temperature creep caused grain boundary motion. After creep to a shear strain of 0.06, the specimen shows changes with respect to grain boundary locations, particularly in central region of Figure 6.21(b), but overall there is not a significant change in the mesotexture. The changes in the positions of high and low angle grain boundaries imply their movement and consumption of small isolated grains (e.g. the salmon colored grains disappeared). The vertical high angle grain boundary in Figure 6.21(b) separating the pink and the blue orientations 'smoothened out'. Many low angle grain boundaries became more prominent due to polygonization of dislocations to form low angle sub-boundaries (e.g. upper left quadrant of left region of Figure 6.21(c). In such areas, recovery processes caused dissolution of low angle grain boundaries that were misoriented by only a few degrees, into low angle boundaries with a larger misorientation. In other places, low angle boundaries disappeared, such as in the top right of central region Figure 6.21(b).

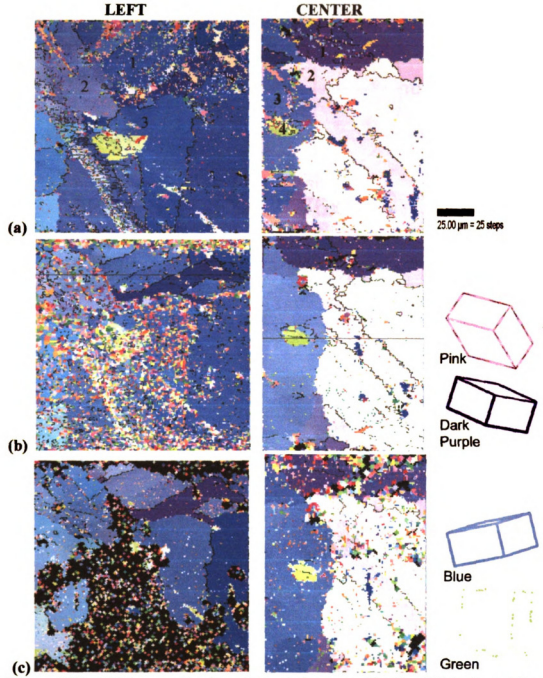

Figure 6.21. OIM maps of regions shown in low magnification SEMs above (a) as-fabricated eutectic Sn-Ag solder, (b) after a global shear creep strain of 0.06 at 85°C, and (c) after a global shear creep strain of 0.3 at 85°C. White boundaries 55-65° are twin boundaries, thin and thick black lines correspond to 3-5° and 5-15° misorientations respectively.

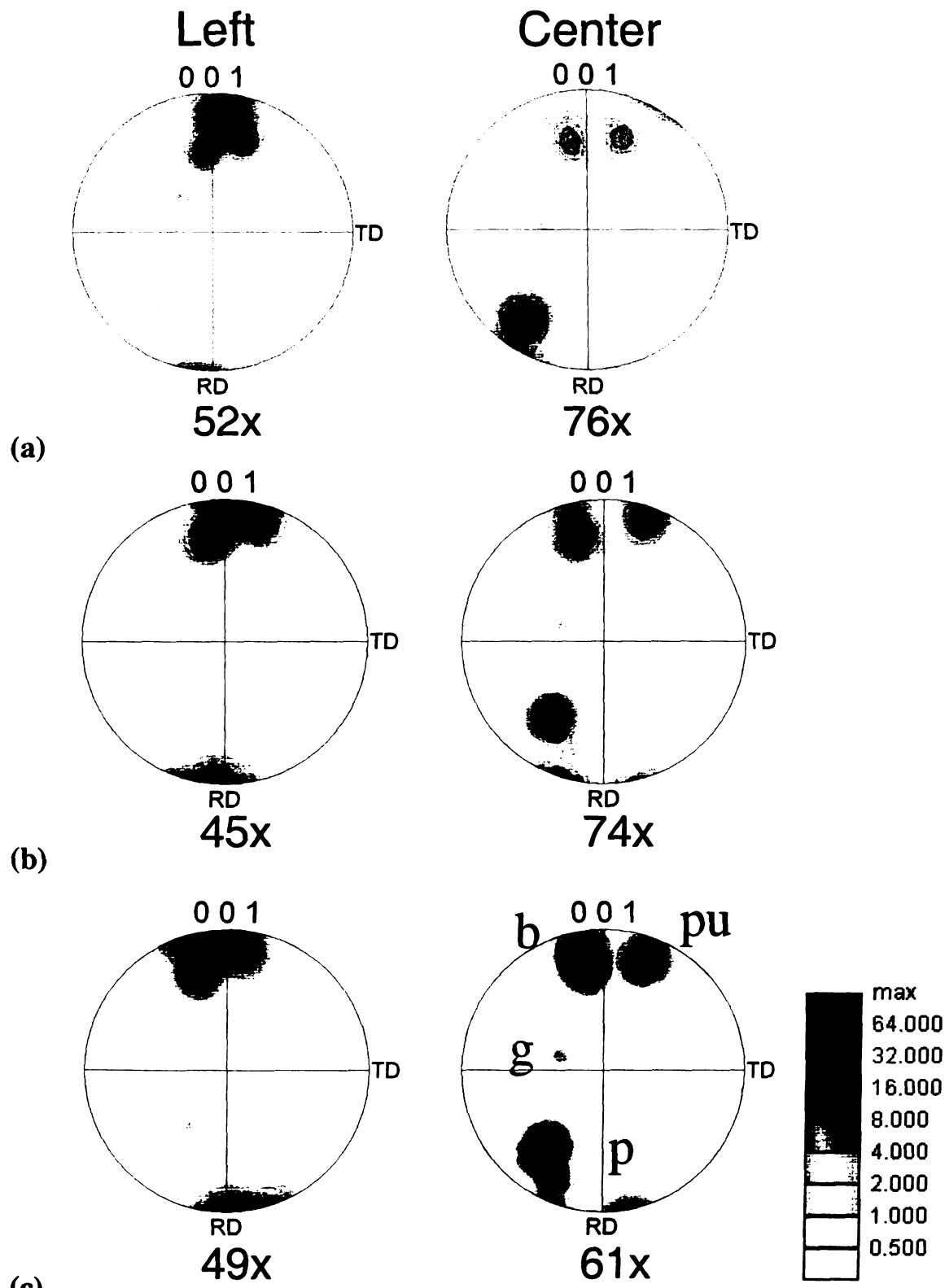

Figure 6.22. [0 0 1] stereographic density pole figures. (a) as-fabricated eutectic Sn-Ag solder, (b) after a global shear creep strain of 0.06 at 85°C, and (c) after a global shear creep strain of 0.3 at 85°C. Overall texture decrease seen due to slight grain growth of secondary orientation. Major peaks, with p=pink, b=blue, g=green, pu=purple.

Figure 6.23 shows the MODF for the as-fabricated specimen. The MODF has a maximum of 35.5 x random and shows prominent rotations of about 62° about the [100] axis and a second strong rotation of about 70° about the [110] crystal axis. These peaks are similar to those observed with the room temperature creep specimen. Also, there are a large number of low angle boundaries <7.5°. Figure 6.24 shows the MODF after high temperature creep to 0.3 strain (the MODF for the 0.06 shear strain is essentially the same as the as-fabricated specimen except for a slight increase in 20° rotation about the [110] crystal direction, hence not shown; this increase is even more evident after 0.3 strain). The maximum intensity after high temperature creep dropped to 25.5 x random.

Figures 6.25(a,b) show the corresponding misorientation angle histograms for the left and central regions. In the as-fabricated condition, notable peaks are seen at 43, near 60, near 70, 75 and 80°, with an additional peak at 90°. After 0.06 creep, the overall number of grain boundary pixels decrease, but after 0.3 creep the overall number of grain boundary pixels increased (probably due to degraded surface finish). There are peaks at misorientation angles on the lower side of 14 and 22.3°, and slightly off 43°, which are CSL misorientations for tin. The initial reduction in peaks after 0.06 creep implies that grain boundary length decreased, such that the grain boundary energy was reduced more by high temperature creep than at room temperature. This means that there is more grain growth and polygonization accompanying 85°C high temperature creep than at room temperature.

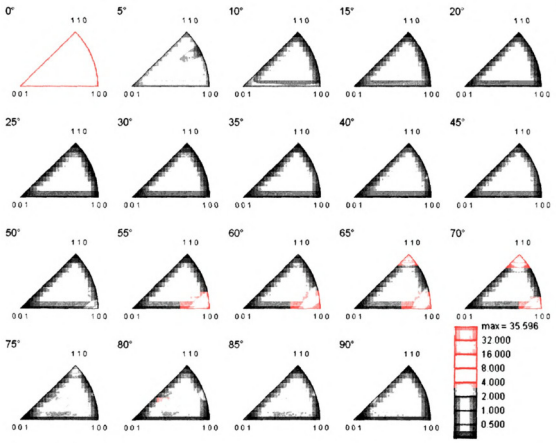

Figure 6.23. Misorientation distribution function for as-fabricated specimen with 2.5° bin size.

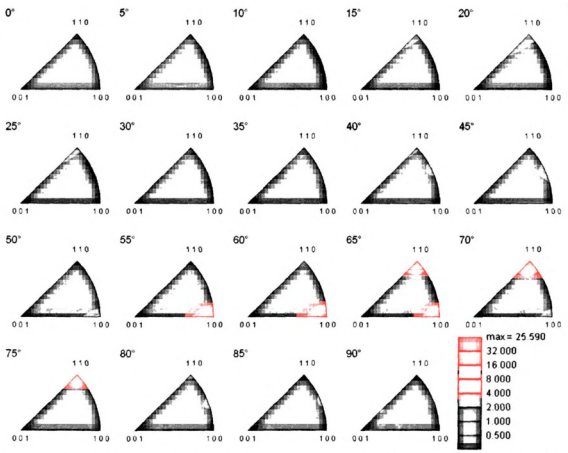

Figure 6.24. Misorientation distribution function with 2.5° bin size for specimen after global creep to 0.3 shear strain at 85°C. More spread of peaks seen <7.5°, near 22, 43 and 60° which corresponds to the dislocation activity and small rotations in the polycrystalline bands.

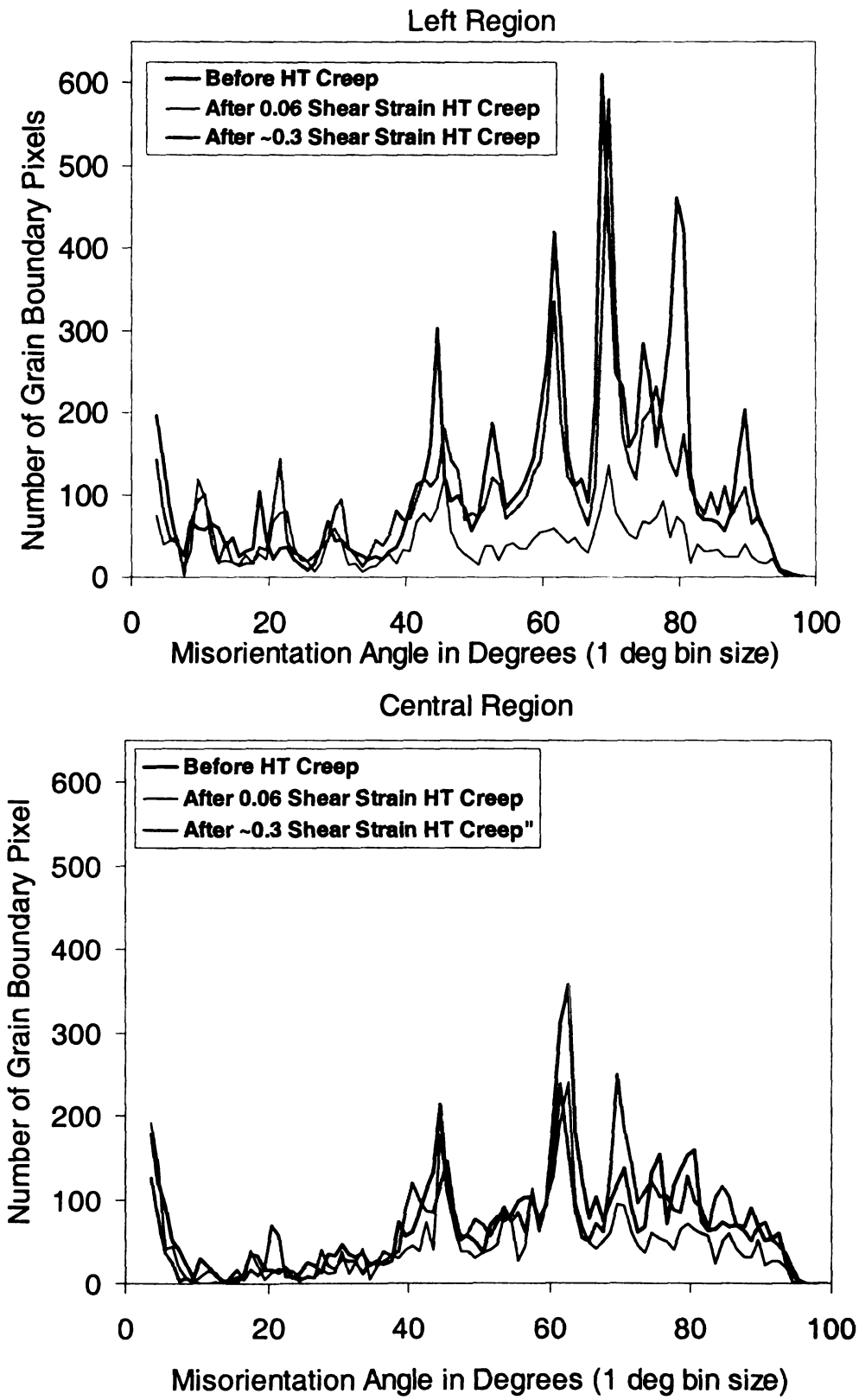

Figure 6.25. Misorientation histograms for the left and central regions as a function of creep strain. Changes in peaks correspond to dislocation activity.

6.5 CRYSTAL ROTATIONS DURING HIGH TEMPERATURE CREEP: Crystal rotations of 8-12° developed during high temperature 0.06 shear strain. See Table XII, which shows rotations occurring in grains numbered in Figure 6.21. This must be due to recovery processes and grain boundary motion since small strains cannot cause such large crystal rotations. The pole figures in Figure 6.22 illustrate such rotations about the specimen x-axis (a similar amount of rotation occurred in the high temperature aged specimen in Figure 5.1). Since the solder joint did not deform homogeneously in all regions during deformation, the observed rotations are too large for the region with local shear strain of 0.06 (3.4° rotation about the z axis, if homogeneously deformed). Since it is unlikely that the specimen could have been mounted at a different orientation by more than a couple degrees (this has been checked in Ref. [6]), the ~10° rotation and the large amount of boundary motion implies that there must have been more microstructural change due to recovery/annealing effects in addition to the shear strain.

Modest growth of moderate sized grains occurred with 85° creep, from about 20μm to 30-50 μm. The growth indicates motion or elimination of some of the grain boundaries, which removed some of the smaller grains (small isolated pixels are not being considered as small grains), but did not result in a significant change of the misorientation relationships between crystals during high temperature creep deformation.

These observations show that the single shear lap specimens are multicrystals rather than polycrystals. Thus, creep behavior may be made more repeatable with a finer grain size with a random texture that could homogenize the plastic deformation properties of the solder interconnect. The substantial motion of grain boundaries as well as significant crystal rotations implies that high temperature creep deformation occurs by a

process by which dislocation recovery by climb also causes grain boundary misorientation changes that alter crystal orientations, which is consistent with the interpretation from conventional creep experiments [7].

Table XII. Grain Rotations as a Function of Creep Strain from Left and Central Regions of High Temperature Creep Specimen #1 Figure 6.21.

LEFT

	Strain	Euler Angle Degrees			Misorientation	Rotation axes			Rotation
		phi1	PHI	phi2	Angle (deg)	n1	n2	n3	Strain
Grain 1	Asfab	109.8	118	37					
	0.06	98	109	35.2	14.4	0.949	0.241	-0.203	0.26
	0.3	98.2	108.3	34.2	1.29	0.363	-0.43	0.826	0.02
Grain 2	Asfab	238	72	63					
	0.06	256.7	83.9	61.6	21.9	-0.989	0.088	-0.115	0.40
	0.3	257.6	83.5	61.4	0.99	-0.604	-0.79	0.103	0.02
Grain 3	Asfab	273	74	58					
	0.06	265.7	87.4	59.4	15.2	-0.051	0.999	-0.014	0.27
	0.3	269.9	85.6	57.1	5	-0.524	-0.747	0.409	0.09

CENTER

	Strain	Euler Angle Degrees			Misorientation	Rotation axes			Rotation
		phi1	PHI	phi2	Angle (deg)	n1	n2	n3	Strain
Grain 1	Asfab	250	63	56					
	0.06	251.4	79.1	52.2	16.5	-0.638	0.744	0.201	0.30
	0.3	252	79.5	52.5	0.82	-0.864	-0.053	-0.5	0.01
Grain 2	Asfab	233.3	105.6	52.7					
	0.06	233.6	115.2	48.8	10.4	-0.605	0.698	0.384	0.18
	0.3	235.4	116.4	49.6	2.02	-0.997	-0.075	-0.008	0.04
Grain 3	Asfab	92	117	41					
	0.06	101.4	107.2	35.1	16.1	0.144	-0.799	0.583	0.29
	0.3	102.2	106.9	34.7	1.04	-0.185	-0.77	0.611	0.02
Grain 4	Asfab	186	143	84.8					
	0.06	163.6	146.6	75.6	16.2	0.746	0.351	-0.565	0.29
	0.3	162	145.8	72.1	2.48	0.435	-0.21	0.876	0.04

Note: The higher misorientations between the as-fabricated and 0.06 strain conditions are not fully understood, due to the as-fabricated data set having an apparent 180° rotation compared to later scans. An attempt is made to correct the euler angles, but the results are difficult to reconcile with the strain increment. This problem is not present for the 0.06 and 0.3 creep strain scans. Rotation strain is measured as the tangent of the misorientation angle.

6.6 EFFECT OF CRYSTAL ORIENTATION ON HETEROGENEOUS STRAIN:

Figure 6.26 shows the left region where heterogeneous deformation of the creep specimen occurred. Superposed on this SEM image are the projection of the unit circle for (110) slip planes, showing selected plane traces and the arrows representing Burgers vector directions for selected slip directions, with the generalized Schmid factor *m* values indicated next to the slip system. The solid arrows represent Burger's vectors with z components coming out of the page and dashed arrows represent Burgers vectors moving into the page; the direction of dislocation motion implies mass movement in the direction indicated.

Figure 6.26 shows the upper region of the creep specimen shown in Figure 6.19(c) after it was strained to 0.3 shear strain, focusing on a 37° misoriented grain boundary that sheared and cracked. The discontinuity between the upper and lower grains suggests that grain boundary sliding followed by microcracking occurred in this boundary. In the upper (purple) grain, whose crystal orientation is indicated by the upper purple wire prism, the (110) slip plane trace is nearly parallel to locations along the grain boundary. None except the [001] slip systems is likely to have been operational on this plane, with the highest Schmid factor of 0.21. The direction of shear in this grain is upwards towards the Cu interface, since the [001] vector is 17.5° above the specimen surface. A similar analysis of the lower grain shows that there are much larger Schmid factors, and arrows indicate the directions of dominant mass flow by shear. Assuming that the material deformed preferentially on systems with high Schmid factors, the lower grain was able to deform much more easily on two planes, one of which (1-10) has a trace about 30° from the orientation of the grain boundary. This difference in ease of

deformation clearly led to a disagreement about material flow in the grain boundary region that could be accommodated by grain boundary sliding or microcracking. The lower grain clearly had more significant mass flow than the upper grain, and the mass movement was away from the upper grain and in the outward direction (largest Schmid factor of 0.52 for slip on (1-10)[001] slip system is inclined outward by 17.5°, so grain boundary sliding and fracture are likely ways to accommodate this strain discontinuity. There was no measurable deformation above the grain boundary in the x-y plane, indicating that strain was accommodated by the grain boundary sliding process, with more mass / dislocation movement in the lower grain outwards and away from grain boundary. In Figure 6.26, heterogeneous deformation was observed and correlated with the operation of (110)[001] slip systems. Operation of this slip system is consistently correlated with heterogeneous deformation that precedes significant damage. If damage is highly correlated to operation of a particular slip system, then processing strategies that generate preferred orientation of solder crystals to minimize operation of this slip system may forestall damage nucleation, and hence lead to substantially improved reliability of a solder joint.

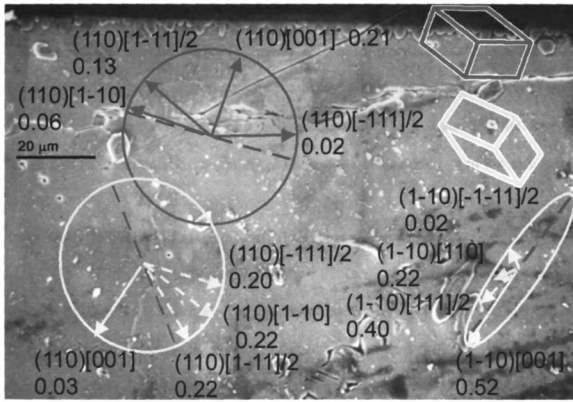

Figure 6.26. Enlargement of upper region of crept specimen after 0.3 shear at 85°C showing geometry of selected slip systems. ***m*** the generalized Schmid factor is shown along with the slip system. Arrows indicate the direction of mass movement due to dislocation slip, solid / dashed represent out of / into page respectively.

6.7 CRACK DEVELOPMENT DURING HIGH TEMPERATURE CREEP:

Cracks develop in high angle boundaries that are not twin boundaries but near CSL misorientations for tin. In Figure 6.19(b) a discontinuous crack traversing horizontally in the upper region, became continuous with further creep to 0.3 shear strain. This crack is located at high angle grain boundaries close to 22.3 and 38°, the details of which can be determined by studying the OIM data / maps as shown in the case studies below.

Case Study 1: Crack in Left and Central Regions of Figure 6.19(c).

The SEM image in Figure 6.27 shows the crack that developed after 0.3 creep strain at 85°C in the left region of the specimen discussed above. Grain boundary sliding is evident that developed into a crack, which has propagated throughout the specimen. Regions of *clean* grain boundary sliding are seen along the crack. In some places shear or ridges along the grain boundary are observed giving a sense of resistance to the sliding process, e.g. in the top right of the SEM where the boundary has a 'V' shape, ridges are seen on the exposed boundary region. In the center of the SEM image, the dark area is a bulge of tin that emerged from the bulk of the material. The OIM map reveals that the crack developed on the 22.3° (average misorientation) high angle grain boundary. Boundaries marked in red on the OIM map are fractured and / or show significant sliding. Certain other boundaries, for e.g. the 28.2 and 12.7° boundaries, which are delineated with thin blue and thick black color (also see black lines showing misorientation between adjacent grains in the OIM map) appear to have been dragged. The crack / ledges follow the 22.3° grain boundary very well. The MODF of the cropped region reveals that these 22.3° boundaries are misoriented around an axis close to [301]. Misorientation peaks at

60° are also visible in the MODF, which corresponds to the twin orientations (marked by thick blue lines). A large number of low angle grain boundaries are also noted from the MODF. Table IX shows the misorientation angle and axis calculated [8] (not using TSL TexSEM software) for the grains across the boundary at four locations, which gave an average of 22.3° for the misorientation angle and a [-30-1] as the rotation axis.

Figure 6.28 shows a focused part of the misorientation histogram (for the cropped region) for the cracked boundaries shown in Figures 6.27 and 6.29. For the left region, the histogram has a peak at 22.3°, but the peak is asymmetric, with many more boundaries having orientations smaller than the 22.3° CSL value. Boundaries near but not at a CSL value require misfit dislocations. This implied presence of more dislocations present in boundaries on the lower side of the 22.3° CSL boundary may facilitate grain boundary sliding.

Figure 6.29 shows the central region of the high temperature creep specimen described above. The SEM image shows the same crack that was investigated in the left region. Grain boundary sliding is evident that eventually developed in to a crack. The average misorientation across the high angle grain boundary that developed the crack is 38.35° and marked in red with misorientations labeled at certain locations. The average misorientation was calculated and shown in Table XIII for four different locations across the grain boundary. Certain other boundaries did not slide, such as the 32.8° boundary in the top left region in the OIM map marked by a thin blue line. The 62.2° twin boundary seen in the lower left of the OIM map and marked by a thick blue line revealed some sliding, but no sliding was observed after 0.06 shear strain. The crack / initial ledges follow the 38.35° grain boundary very well and continued on the left into the 17.3°

boundary. The MODF reveals a peak for a rotation of 38-40° about [140] axis, consistent with the [1-40] calculations seen in Table XIII. The misorientation histogram (Figure 6.28) also shows peaks at 36 and 38.5°, with a local minimum at the 38° CSL, implying that the slding boundary is probably a 38° CSL with misfit dislocations. A large number of low angle grain boundaries are also noted from the MODF.

In both the regions studied above, the crack followed boundaries that are close to 22.3 or 38° CSL misorientations. These cracks are located about 10-20 μm from the copper interfaces, and are present throughout the specimen after 0.3 creep strain. A large amount of grain boundary sliding is evident, that leads to the crack formation. Also, the crack seems to propagate across grains into boundaries, which are more susceptible to sliding. Boundary regions that were not suitable for sliding, were sheared to maintain continuity with the rest of the grain as it rotated.

Table XIII: Misorientation Angle and Axis for Several Locations Across the Cracked Boundary

Left Region		Euler Angle (°)			Misorientation	Rotation axes (unit vector)		
		phi1	PHI	phi2	Angle (°)	n1	n2	n3
Top Grain	Grain 1	102.6	110.1	45.9	22.11	0.88	-0.014	0.475
Bottom Grain	Grain 2	90.3	94.8	32.6				
Top Grain	Grain 1	102.9	109.7	46.2	22.81	0.854	0.014	0.52
Bottom Grain	Grain 2	90.2	94.7	31.5				
Top Grain	Grain 1	102.1	109.7	46.4	22.54	0.837	-0.044	0.546
Bottom Grain	Grain 2	90.8	94.4	31.6				
Top Grain	Grain 1	102.1	109.8	46.5	22.53	0.825	-0.044	0.564
Bottom Grain	Grain 2	91	94.7	31.3				
		Average			22.4975	0.849	-0.022	0.526
		Converted to Miller Indices				3.000	-0.078	1.014
		Miller Indices rounded off				3	0	1

Central Region		Euler Angles (°)			Misorientation	Rotation axes (unit vector)		
		phi1	PHI	phi2	Angle (°)	n1	n2	n3
Top Grain	Grain 1	252.3	79.8	52.4	39.46	-0.232	0.972	-0.038
Bottom Grain	Grain 2	236	115.9	51.6				
Top Grain	Grain 1	250.8	83.7	*49.9*	38.09	-0.288	0.956	0.057
Bottom Grain	Grain 2	234	118.1	*44.3*				
Top Grain	Grain 1	253.1	83.1	44.5	39.96	-0.207	0.952	-0.224
Bottom Grain	Grain 2	233.4	117	50.2				
Top Grain	Grain 1	252.8	82.6	45	35.88	-0.286	0.954	-0.091
Bottom Grain	Grain 2	236.1	114.4	45.8				
		Average			38.3475	-0.253	0.959	-0.074
		Converted to Miller Indices				1.000	-3.785	0.159
		Miller Indices rounded off				1	-4	0

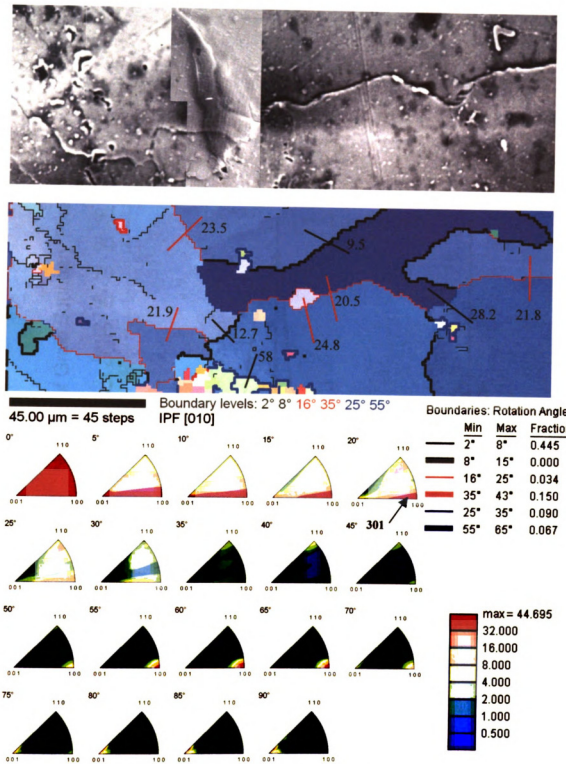

Figure 6.27. SEM shows crack after 0.3 creep strain at 85°C. A patch is applied over the SE image to show bulge. The [010] inverse pole figure OIM map reveals that the crack developed on the 22.5° (average misorientation) grain boundary. Boundaries marked in red on the OIM map are fractured and / or show significant sliding. These 22.5° boundaries are misoriented about a [301] rotation axis. The peak at 60° twin orientations is also visible in the MODF.

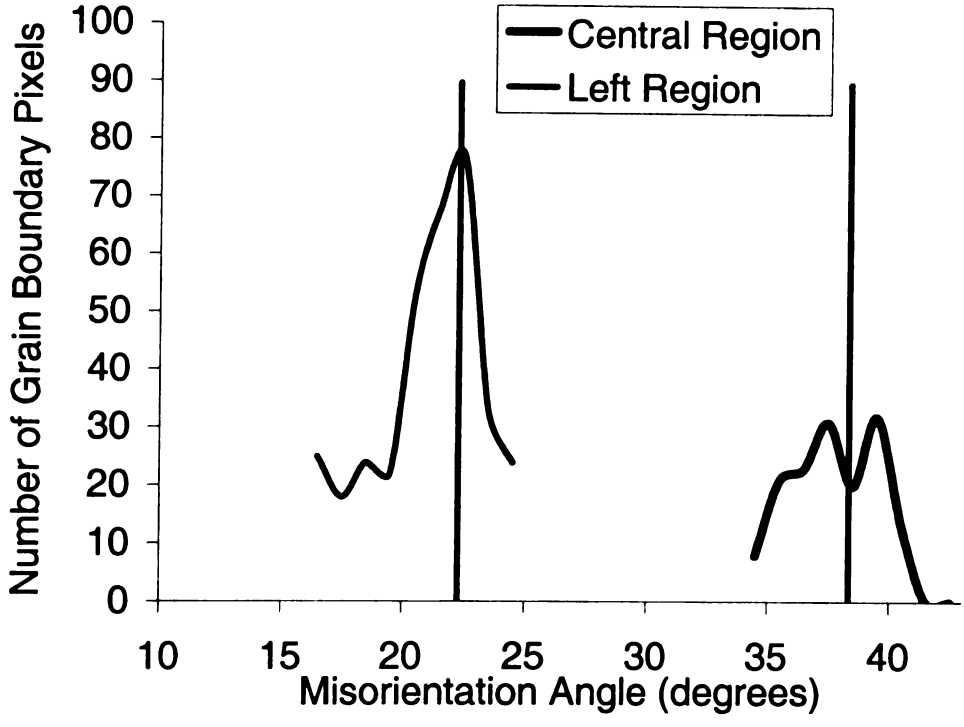

Figure 6.28. Misorientation histogram for the cropped regions in 6.27 and 6.29°.

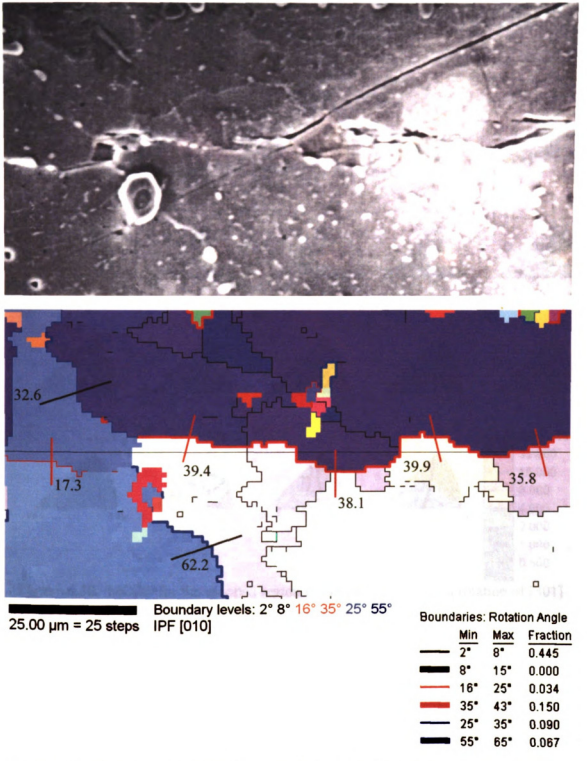

Figure 6.29. Central region SEM shows crack developed in 0.3 creep strain at 85°C. The [010] inverse pole figure OIM map reveals that the 38.35° (average misorientation) high angle grain boundary developed the crack. Boundaries marked in red on the OIM map are fractured and / or show significant sliding.

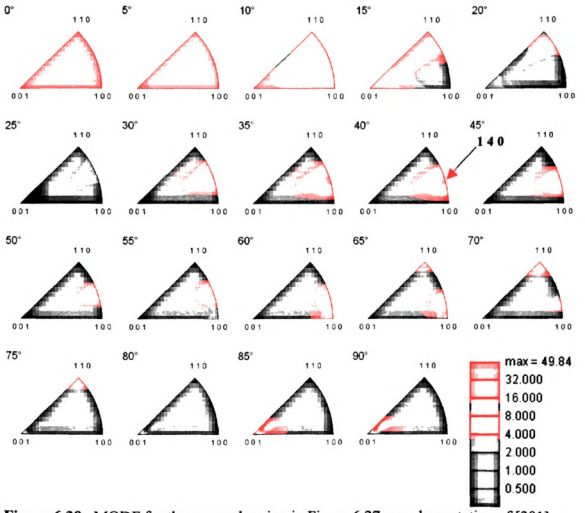

Figure 6.30. MODF for the cropped region in Figure 6.27 reveals a rotation of [301] about which these 22.5° boundaries are misoriented. Peak at 60° is also visible in the MODF, which corresponds to the twin orientations.

Case Study 2: Crack In Central Region Of High Temperature Creep Specimen 2

Figure 6.31 shows an SEM image of the central region of high temperature creep specimen #2, after 0.67 creep strain at 85°C. The stress imposed on this creep specimen was 12.7 MPa and the creep curve is shown in Figure 6.32. The SEM image shows the crack present at 0.67 strain. Grain boundary sliding is evident that eventually gave rise to the crack. The [010] inverse pole figure OIM map reveals that several low angle (15.1 and 15.7°) boundaries marked by thick black lines and high angle grain boundaries having a misorientation of 25.1° correlate well with the ledges that develop. The 61.6° boundary low-energy twin boundary, marked by blue on the right of the OIM map, resisted sliding. The MODF in Figures 6.33 reveals that many grains are misoriented by rotations of ~15° about the [140] axis, and Figure 6.34 shows a MODF peak at 20-25° about a [100] axis (red line in Figure 6.31. The misorientation histogram in Figure 6.35 also shows large peaks between 12-16° and near 26° for this central A region.

Figure 6.36 shows the SEM of the central region of specimen #2 high temperature creep specimen, after 0.67 creep strain at 85°C. The SEM image shows the crack that has developed which started from the fillet in the middle of the joint on the right side. The [010] inverse pole figure OIM map reveals that the crack follows a boundary close to 22° marked by red. A higher magnification micrograph of this region is shown in Figure 6.37. The MODF in Figure 6.38 reveals that grains are misoriented by rotation of 20° about an axis close to [112] axis. The misorientation histogram Figure 6.35 also shows large peaks between 20 and 22° and near 6-7 and 11-12° for this region.

In both the regions studied in case 2 above, just like case 1, the cracks were seen following boundaries close to special boundaries (CSL boundaries like 22.3 about 110, or

38° about [100]). However these are also CSL-type boundaries with rotation axes of [140], [301] or the [112] type to be more specific (see *Appendix 4* for CSL configuration about these axes). The cracks are present close to the interface between copper and the solder, and at times end at the interface. The cracks also run through the width of the specimen following the grain boundary. A large amount of grain boundary sliding is evident, that ultimately leads to cracking. Also, the crack can jump boundaries (through intermediate grains) and propagate into different boundaries which are more susceptible to sliding and thereafter cracking. In this case, intermediate grain boundary regions, that are not suitably close to a Σ boundary for sliding, are sheared.

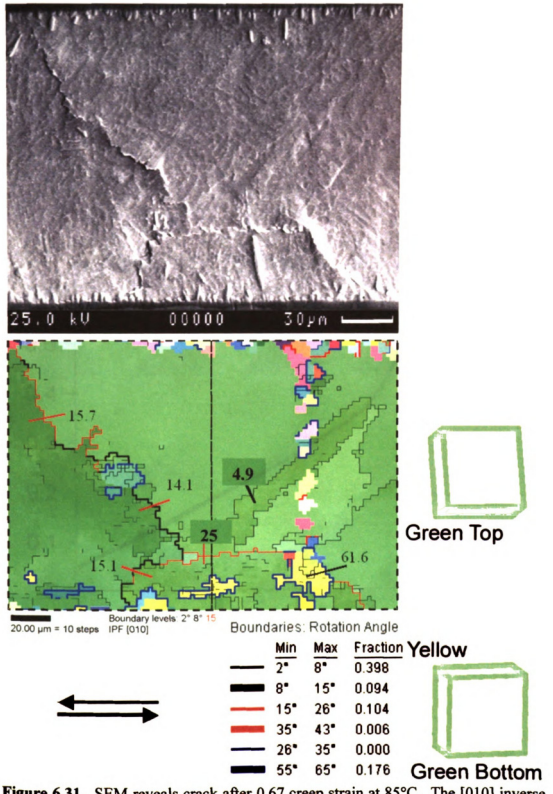

Figure 6.31. SEM reveals crack after 0.67 creep strain at 85°C. The [010] inverse pole figure OIM map reveals that the 22.5° (average misorientation) high angle grain boundary developed the crack. Boundaries marked in red on the OIM map are fractured and / or show significant sliding.

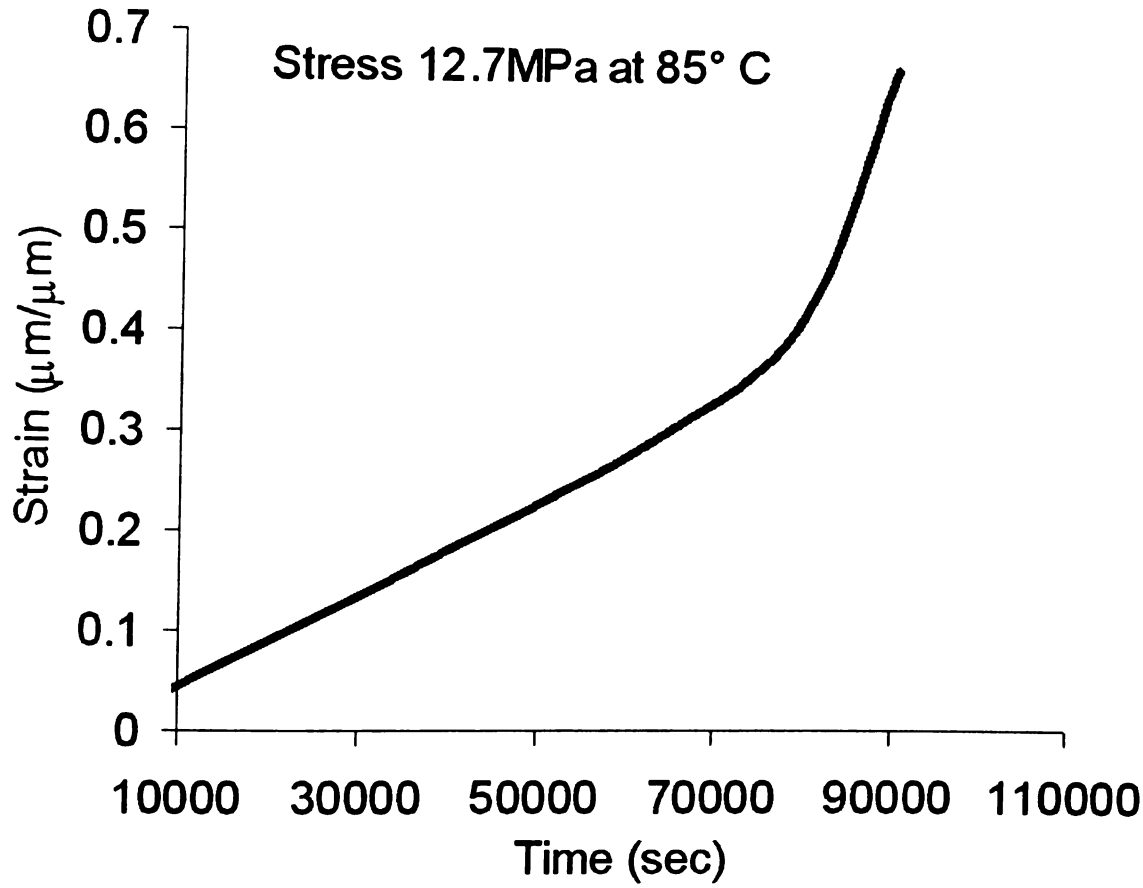

Figure 6.32. Creep curve for high temperature creep specimen 2 tested at 12.7 MPa at 85°C.

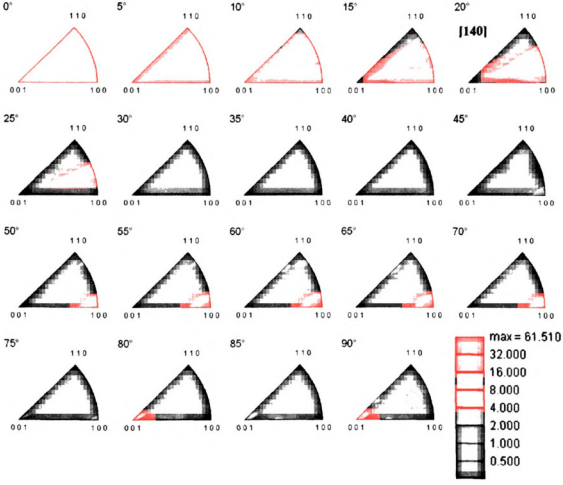

Figure 6.33. MODF of Region A of Figure 6.31.

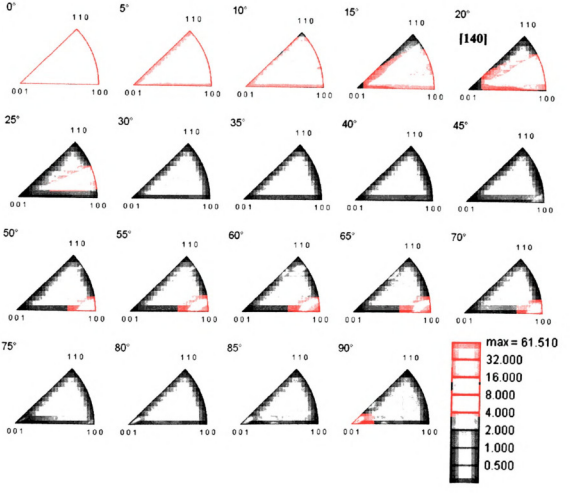

Figure 6.33. MODF of Region A of Figure 6.31.

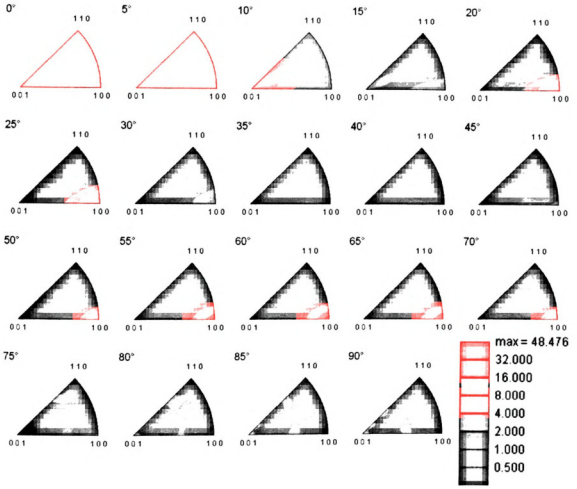

Figure 6.34. MODF of Region B of Figure 6.31.

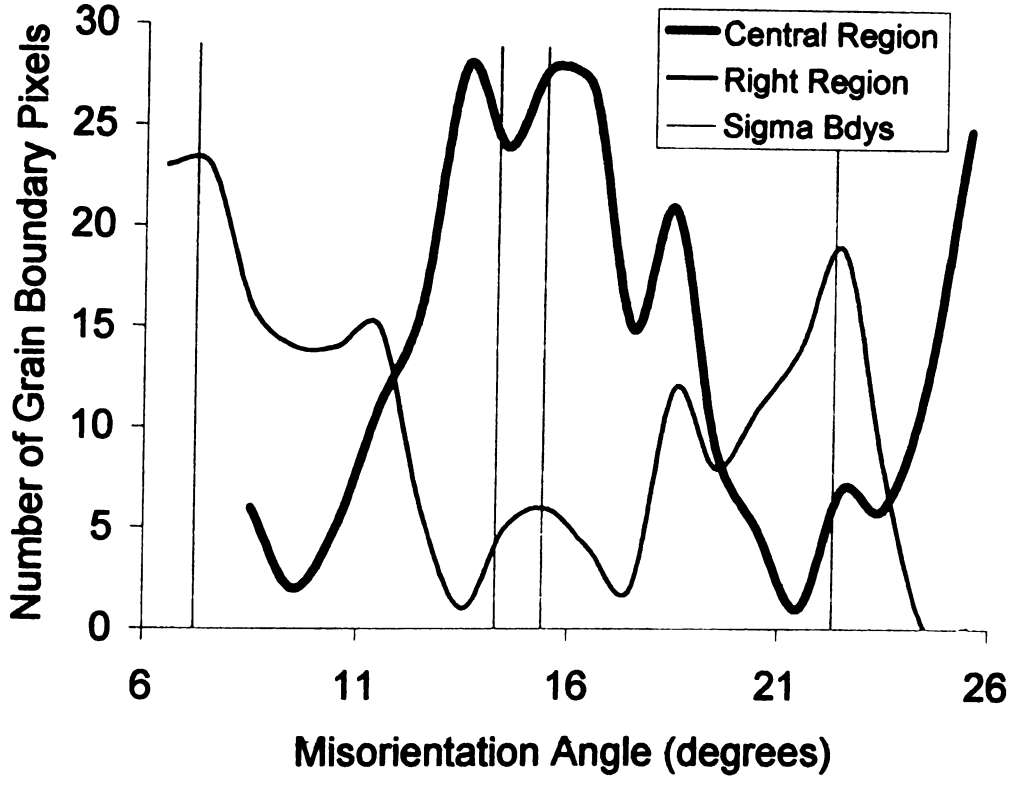

Figure 6.35. Enlarged version of misorientation histogram for the cracked boundaries shown in Figures 20 and 24 from central region A and right region of the joint. There is a Σ 29 of 15.4° about [140].

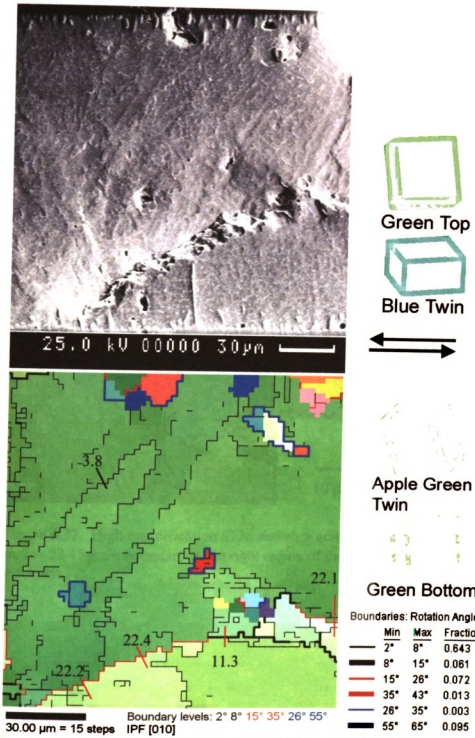

Figure 6.36. SEM and OIM of the central region of another high temperature creep specimen, after 0.67 creep strain at 85°C. The boundary that slides corresponds to a boundary close to the 22.5° CSL.

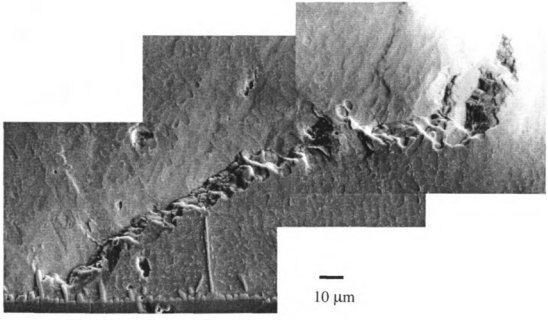

Figure 6.37. High magnification SEM showing grain boundary sliding along a high angle ~22.4° grain boundary in the right region of this high temperature creep specimen.

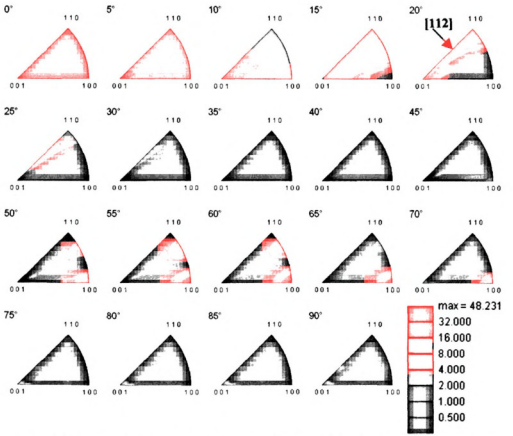

Figure 6.38. MODF of region shown in Figure 6.26. Grain boundary sliding is seen close to 22° which has a rotation axis near [112].

6.8 CONCLUSIONS FROM HIGH TEMPERATURE CREEP

With high temperature and global shear strains from 0.3-0. 7, extensive grain boundary sliding was observed along certain grain boundaries, thus concentrating strain to an interface. These grain boundaries were identified as ones close to a CSL configuration, especially those near 22.5 and 38°. The Ag_3Sn particles could not sufficiently pin the boundaries, which were able to slide. However the boundary orientation in the sample was important so as to have a shear force on it before any sliding could occur. This is seen in the left region in Figures 6.19,21 where the grain boundary traversing vertically does not show any sliding. The grain boundaries, which slide, have a misorientation close to a special boundary orientation such that during sliding a misfit dislocation sub-structure is formed in the boundary which facilitates the sliding process without loss of the low energy configuration of CSL. These sliding boundaries eventually develop cracks and cause failure in the interconnect. Polygonization at high temperature allows low angle grain boundaries to form, along with more rapid climb of dislocations. The strong texture once again implies the multicrystalline nature of these joints and, and this could account for the greater variability of creep resistance. However it is evident that it is easier for certain boundaries to slide more than others as explained above. More discussion on sliding boundaries will be carried out in Chapter 8.

Knowing the crystal orientation allows slip activity of the tin in solder joints to be investigated with computational models. Surface topography arising from differential slip activity appears to be associated with the {110}[001] slip system, and this slip system may be the one most responsible for damage nucleation in tin.

6.9 REFERENCES:

1. A.U.Telang, T.R.Bieler, S.Choi, and K.N.Subramanian, J. Mater. Res., 2002. **17**(9): p. 2294-2306.

2. R.Darveaux, and K.Banerji, IEEE, 1992: p. 538-551.

3. S.Choi, J.G.Lee, F.Guo, T.R.Bieler, K.N.Subramanian, and J.P.Lucas, JOM, June 2001: p. 22-27.

4. H.Mavoori, J.Chin, S.Vaynman, B.Moran, L.Keer, and M.Fine, Journal of Electron. Mater., 1997. **26**(7): p. 783-790.

5. M.A.Meyers, and K.K.Chawla, 1984: p. 300.

6. A.U.Telang, Masters Thesis, Material Science, Michigan State University, East Lansing, 2002.

7. R.W.Cahn, and P.Haasen, *Physical Metallurgy 4th ed., 28.* 1996: Elsevier Science.

8. U.F.Kocks, C.N.Tomé, and H.-R.Wenk, *Texture and Anisotropy, Preferred Orientations in Polycrystals and their Effect on Material Properties.* Vol. ch.11. 1998: Cambridge University Press.

CHAPTER 7

TMF OF SINGLE SHEAR LAP JOINT Sn-3.5Ag SOLDER JOINTS

Scope

The deformation in lead-free solder joints is very heterogeneous and sensitive to strain and temperature history. Surface topography develops in lead-free solder interconnects tested under different conditions in several different specimen geometries. Single shear lap specimens were subjected to thermomechanical fatigue (TMF) testing and observed using SEM and Orientation Imaging Microscopy (OIM). SEM micrographs of previously polished specimens revealed changes in surface topography after creep and TMF. Ledges and grain boundary sliding are frequently observed, correlating with both low and high angle grain boundaries, indicating a close relationship between deformation mechanisms and grain boundaries in tin-based joints. However, in joints where almost a single crystal was present (or developed during aging or TMF), the surface topography also revealed shear band features in grain interiors as well as ledges along certain grain boundaries. These shear band features frequently correlate with {110} plane traces. The underlying causes for these different surface damage features in grain interiors vs. grain boundaries will be addressed to examine how damage accumulation occurs in lead-free solder interconnects.

7.1 INTRODUCTION: Thermomechanical fatigue failure is the leading cause of failure in soldered joints. The stress state in joints is constantly changing with temperature excursions. Depending on the environment to which such joints are exposed, temperature cycling can occur anywhere from sub-zero to 150°C in automotive under-the-hood situations, or from room temperature to 85°C in household electronics and computer applications. Such cycling leads to premature failure of the joint and functionality of the component.

Lead-free solder joints based on tin silver solder have been characterized extensively in aging and creep and to a certain extent in thermomechanical fatigue (TMF), using either optical or scanning electron micrographs (SEM) [1-3]. However microstructural evolution in the *Sn phase* is difficult to track using only optical or SEM methods. There have been many investigations about intermetallic particle and interface evolution, and papers which reveal crack formation and failure of joints, but have no explicit explanation as to why such failure occurs with regard to deformation in tin. The use of Orientation Imaging Microscopy (OIM) to track microstructure evolution during TMF allows one to see the crystallographic evolution which was absent in earlier studies. This section attempts to characterize the crystal orientation changes that occurred with thermomechanical fatigue in a solder joint which underwent a total of 1500 TMF cycles, using Orientation Imaging Microscopy (OIM).

7.2 EXPERIMENTAL DETAILS:

A simple dog-bone single shear lap joint specimen made with eutectic tin silver (Sn-3.5%Ag) was used in this study. The solder joint was cycled through a total of 1500 TMF cycles, being subjected to thermal excursions with a short hold time at high temperature (150°C) and a long hold time at low temperature (–15°C), as explained earlier in the chapter on experimental procedures. The joint was intermittently removed from the automated setup to obtain crystal orientation data at the end of 370, 550, 750, 1000, 1200 and 1500 TMF cycles. The joint was lightly re-polished at the end of 1000 cycles since the oxide that formed frustrated pattern indexing. The amount of strain generated by TMF can be primarily attributed to the coefficient of thermal expansion (CTE) mismatch between the copper substrates (17.3×10^{-6}/°C) and the tin (a-direction = 15×10^{-6}/°C and c-direction = 30×10^{-6}/°C), as well as the intrinsic anisotropy of tin in the matrix. Since the joint was not clamped no external stress was imposed.

This study of microtexture evolution was carried out on one joint. Because the initial solidification texture was different in every joint that was characterized, the details of active deformation mechanisms and damage evolution differ from other specimens. Although the initial orientations were different, similarities still existed in the joints; single crystals were separated by low angle grain boundaries, and when the joints consisted of multicrystals, there was usually a twin type misorientation between the dominant and secondary orientation in all the joints studied. Though the initial texture in this joint was different from the texture in other joints, the similarities in the local regions for presence of low angle and certain special boundaries occurred in all specimens. Thus the phenomenological observations will be relevant to joints with other dominant

orientations. Moreover, this data adds to the knowledge of how crystal deformation affects deformation heterogeneity arising from TMF, which has not been explored with the perspective of TMF dependence on orientation. Further, studies done on dual shear and component type specimens show similar deformation in joints with difference stress history, which further strengthens this point. Hence, attempts can now be made to properly track the microstructural evolution of single shear lap lead-free solders during TMF using these means.

7.3 RESULTS: Figure 7.1 is an SEM of three different regions of the joint (left, center and right regions respectively) of the joint at the end of 370, 550, 750, 1000, 1200 and 1500 TMF cycles. This side of the specimen is the type A geometry – left pointing joint (see the notation used in chapter on experimental procedures). At the end of 370 cycles, the Ag_3Sn and Cu_6Sn_5 particles in the matrix coarsened, but no other surface topography was visible. After 550 TMF cycles some surface shear bands formed in the central region of the joint as well as some ledges / grain boundary sliding in certain regions of the joint (e.g. top left of left region). Surface topography developed near the bottom of the Cu_6Sn_5 particle in the top left region, which is very common. Shear bands ran horizontally through the joint. After 1000 TMF cycles, the surface topography and oxide formation obscured further OIM data collection, so a light re-polish was carried out to remove the oxide. However SEM images were taken prior to polishing to document the microstructure, which revealed strong surface topography that had developed after 1000 cycles as well as grain boundary sliding in regions close to the Cu-Sn interphases in the tin region. Some of the surface topography in the central region of the joint was partially

erased by the re-polish done at this stage and lost in subsequent SEMs. Further cycling to 1200 and 1500 TMF cycles revealed more of the already present grain boundary sliding, especially near the Cu-Sn interface.

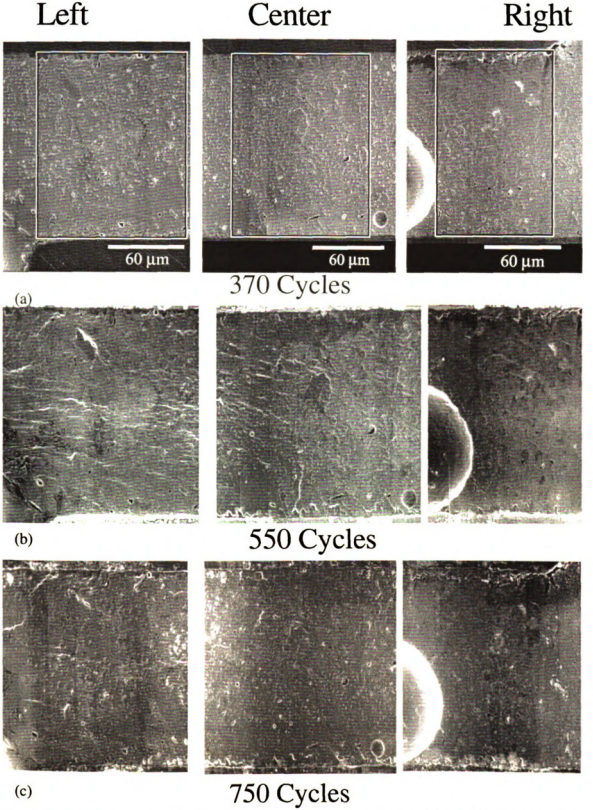

Figure 7.1. SEM images for the three different scanned regions. (a) 370 cycles, (b) 550 cycles, (c) 750 cycles.

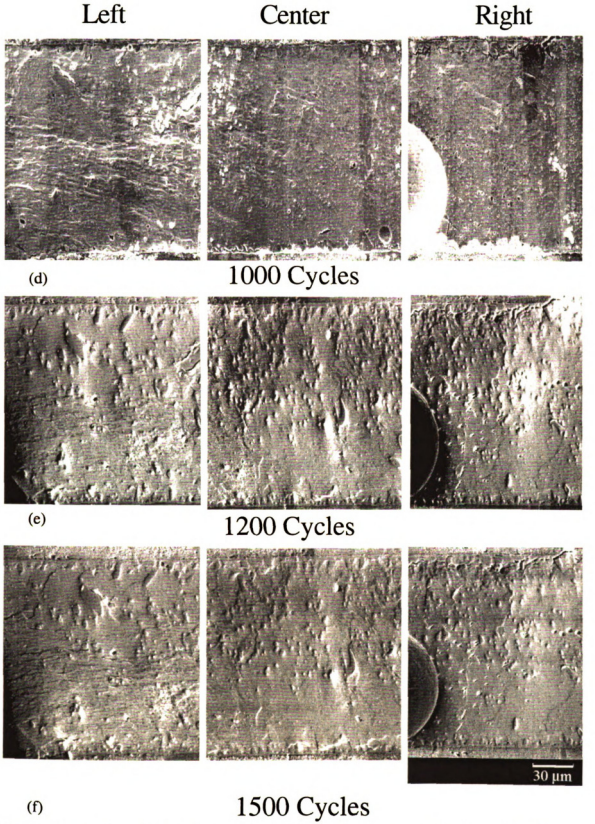

Figure 7.1 continued. SEM images for the three different scanned regions. (d) 1000 cycles, (e) 1200 cycles, and (f) 1500 cycles.

Figure 7.2,7.3, and 7.4 show the OIM maps for the center, left and right regions respectively as a function of number of TMF cycles. The EBSP pattern quality improved up to 550 TMF cycles, and then degraded with further cycling. This could be attributed to annealing initially, which eliminated small orientations followed by oxide and surface topography that frustrated pattern indexing during later cycles*. Microstructure evolution in all three regions shows growth of one orientation (darker gray or regions marked by 'A' and 'C' on the orientation map of the center and left respectively) at the expense of the other orientation marked by 'B' and 'D' respectively. There is a big change in orientation between 370 and 550 TMF cycles; all three regions show a total change of dominance from the primary orientation to the secondary one. After 1000 TMF cycles, a near single crystal orientation is seen in the different regions. Low angle grain boundaries (thin black lines) are seen traversing through them. These low angle boundaries are mostly seen close to the Cu-Sn interface, but some start at one interface and traverse across to the other interface. The nature of these boundaries and further details will be discussed later. Further cycling beyond 1000 TMF cycles shows smaller specks of orientation developing in the almost single crystal joint. These may be a result of oxidation. No further change in the texture was observed even after 1500 TMF cycles, however the low angle grain boundaries are more distinct after 1500 TMF cycles.

* Since no polishing was done between the fabrication and after 1000 cycles, the initial improvement of the map quality and elimination of small orientations shows that small minority orientations truly disappeared, and are not an artifact of the specimen preparation or measurement technique. Furthermore, the re-polish after 1000 cycles did not cause small embedded orientations, implying that polishing is not the cause of the initial high population of small embedded orientations – consequently the small orientations are there due to growth of stacking faults related to low energy boundaries during solidification.

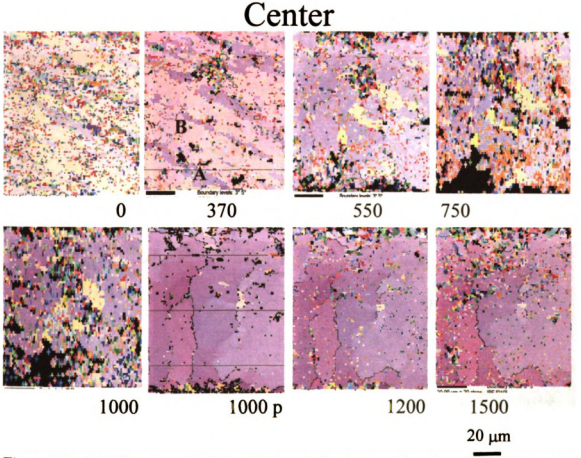

Figure 7.2. [010] inverse pole figure OIM maps for the central region as a function of TMF cycles. Nearly single crystal with low angle grain boundaries is obtained after 1000 TMF cycles.

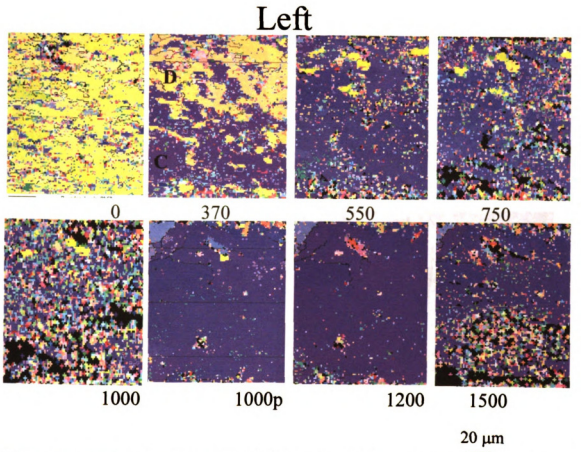

Figure 7.3. [010] inverse pole figure OIM maps for the left region as a function of TMF cycles. Nearly single crystal with low angle grain boundaries is obtained after 1000 TMF cycles.

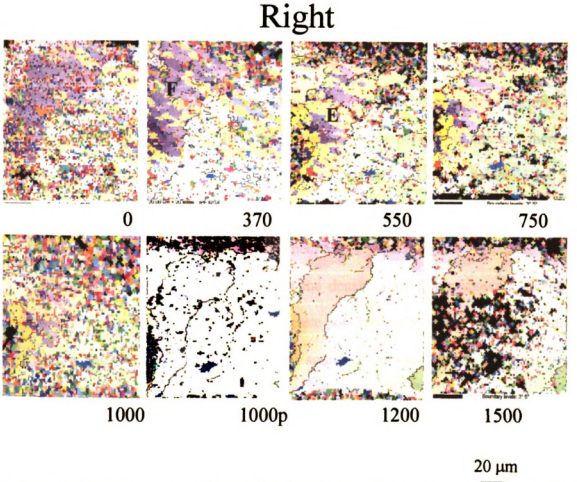

Figure 7.4. [010] inverse pole figure OIM maps for the right region as a function of TMF cycles. Nearly single crystal with low angle grain boundaries is obtained after 1000 TMF cycles.

Figure 7.5,7.6, and 7.7 shows the density pole figures for the center, left and right regions. In Figure 7.5, the density pole figures for the central region revealed a dominant orientation and a secondary orientation. Table XIV shows the texture intensities of the various dominant peaks in the density pole figures, in three scanned regions of the joint. The left region had one dominant orientation with texture intensity of 39.9 x random with secondary peaks with lower texture intensity 23.3 x random. After TMF cycling, and especially between 370 and 550 TMF cycles, in both the regions one can see a shift in dominance where the peaks corresponding to the A and C orientation in Figure 7.2 and 7.3 respectively (center and left regions respectively) become dominant whereas the initial dominant peaks B and D in the center and left regions respectively are losing intensity. Beyond 1000 TMF cycles peaks B and D have totally disappeared implying presence of a near single crystal. The near single crystal term is used here since the Gaussian interpolation used to construct the density pole figure shows a spread over several near-spread orientations. The discrete pole figure for the three regions after 1500 cycles is shown in Figure 7.8 to show the spread of the individual orientations over the roughly 5-10° space.

Figure 7.9 shows the changes in the lattice of the dominant orientations as a function of TMF cycles. The dominant orientation in the first row has its c-axis pointing upwards initially which changes and it points downwards after 550 cycles. Slight differences in crystal orientation (within 15°) for the three regions implies that the joint is essentially a single crystal having low angle boundaries at the beginning and end of the TMF process, but the crystal orientation changed during the process.

Table XIV: Texture Intensity Changes For The Two Dominant Poles Seen In The Density Pole Figure.

	LEFT		CENTER		RIGHT	
	Pole B	**Pole A**	**Pole D**	**Pole C**	**Pole F**	**Pole E**
0	39.9	23.3	66	18.8	90.0	4.8
370	55.1	27.4	69.5	30.1	44.9	58.63
550	25.5	44.2	17.4	77.7	4.9	137.5
750	25.4	40.6	17.5	45.4	6.3	112
1000	11.6	28	10	58.6	5.3	47
1000 pol	0	167	1.3	126	5.3	86
1200	0	121	0	110	0	83
1500	0	96	0	96	0	71

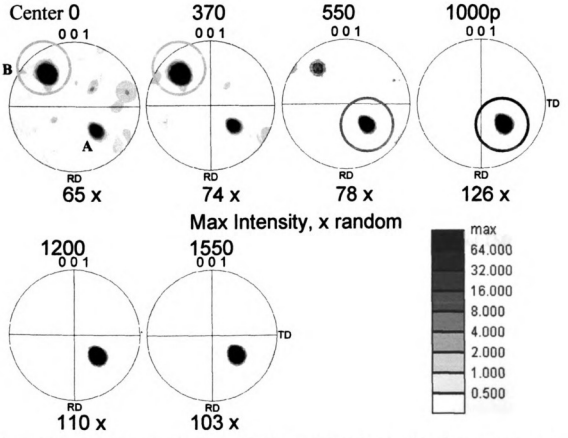

Figure 7.5. [001] density pole figures for the central region as a function of TMF cycles.

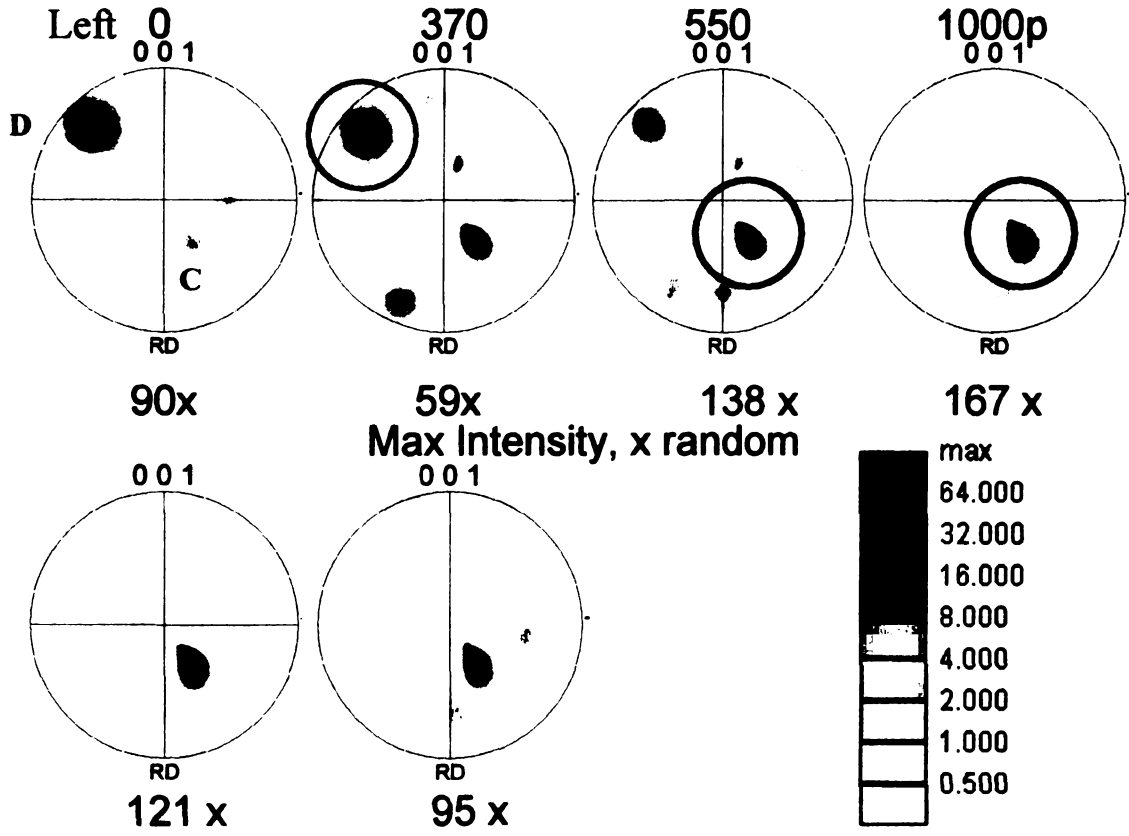

Figure 7.6. [001] density pole figures for the left region as a function of TMF cycles.

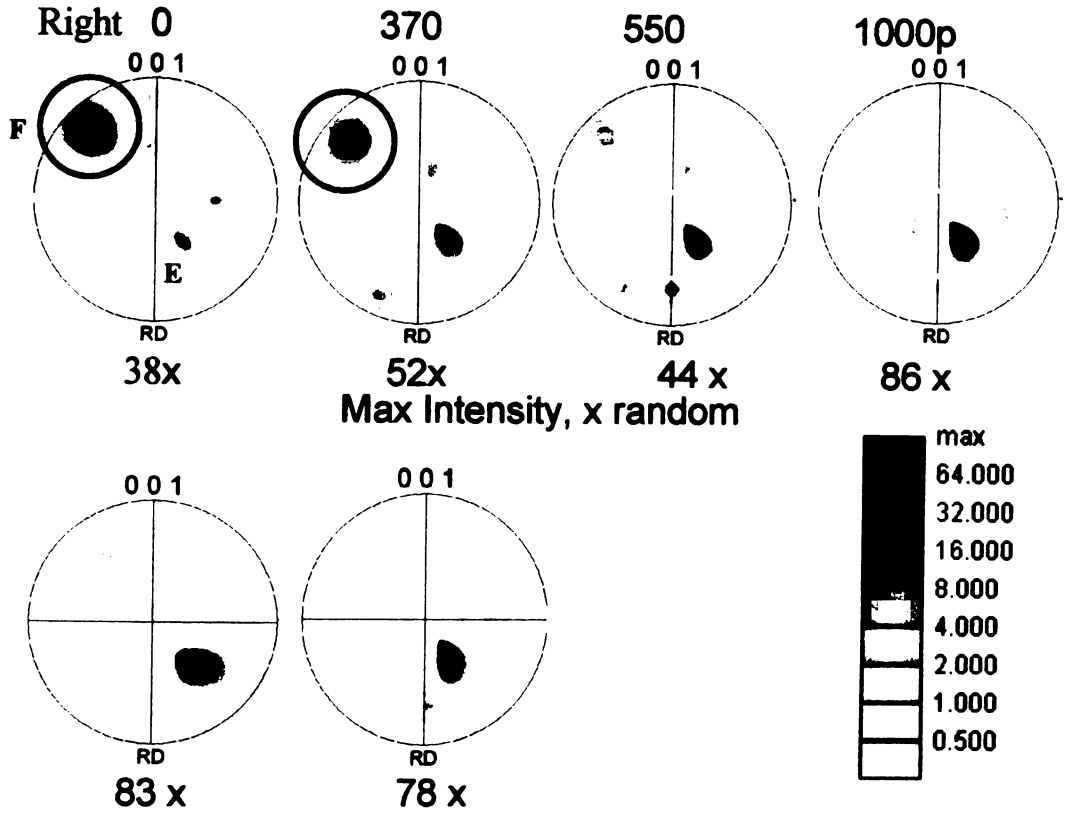

Figure 7.7. [001] density pole figures for the right region as a function of TMF cycles.

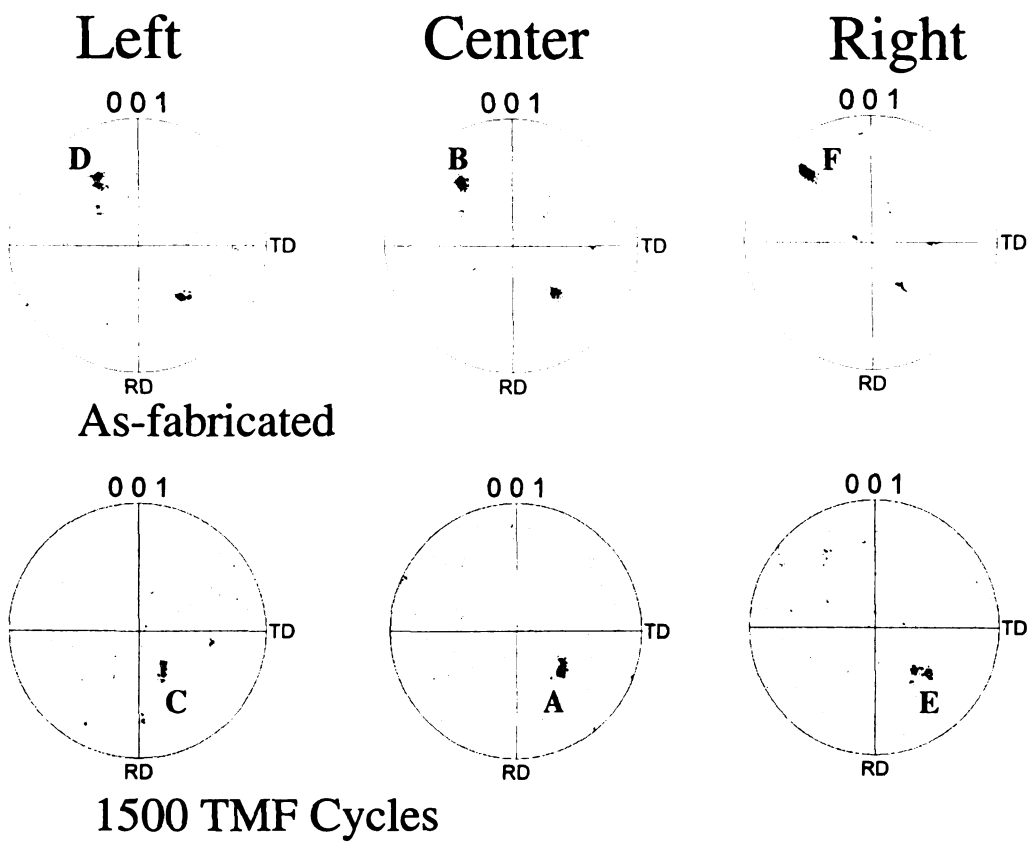

Figure 7.8. [001] discrete pole figures for the three regions after 1200 TMF cycles.

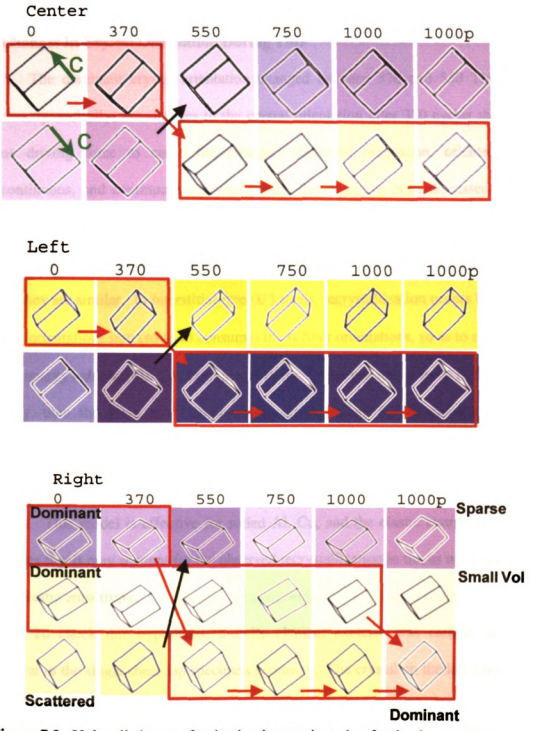

Figure 7.9. Unit cell changes for the dominant orientation for the three regions.

7.4 DISCUSSION

1. Changes In Crystal Orientation During TMF

The dominant crystal orientation changed between 370 and 550 TMF cycles. Thermodynamically, the changes in the crystal orientation after 370 cycles should have some driving force to cause the change. Oriented nucleation, oriented growth, discontinuous, and continuous recrystallization theories have been discussed for many years. For example, there is some uncertainty about recrystallization in steels that arises from difficulty in distinguishing deformation textures from recrystallization textures since they are similar. In interstitial-free (IF) steels, recrystallization occurs by growth of γ fiber orientations into (so as to consume) the α fiber orientations, so as to maximize the strain energy ***release*** [4]. For example, if two neighboring grains have high dislocation density, then the grain with lower elastic strain energy (lower dislocation density) consumes the grain with higher elastic strain energy (dislocation rich region), in a continuous recrystallization mechanism so as to reduce the overall strain energy of the system. This model is effective for rolled Al, Cu, and the elastic energy driving force indicates that it may account for the observed recrystallization in tin, as well, since tin has large elastic anisotropy.

To check this hypothesis, a finite element exercise was carried out using a bicrystal in the single shear lap specimen geometry. The crystal on the left was given the initial orientation (as-fabricated orientation, $\phi 1$, Φ, $\phi 2$ = 42.3, 105.1, 5.3) and the crystal on the right was given the final orientation after 1000 TMF cycles ($\phi 1$, Φ, $\phi 2$ = 34.7, 38.1, 12.4). These orientations were obtained from approximately the same location on the specimen before and after TMF cycling. The five elastic constants for tin were used

to develop the full 3-D fourth rank elastic constant tensor, and tensor transformations were used to identify the stiffness matrix for these two orientations before using them to describe the crystal elastic properties in an ABACUS™ Finite Element code, which was used for carrying out the simulation using the anisotropic thermal expansion coefficients. The bi-crystal in the joint geometry was then heated from -15°C and 150°C to determine the strain and the von-Mises stress that was generated in the joint due to heating. The system was unable to give valid data on cooling from 150° to –15°C and hence the heating cycle was used. It can be assumed that in this elastic analysis the sign on the stress will be reversed using the opposite cycle, but will not affect the magnitude of the stress. Figure 7.10 shows the stress distribution in the two crystals after heating. Though the finite element simulation is only an elastic estimation of the stresses that develop and does not account for plastic strain, it gives an insight into the differences in the strain energy in the two regions that occurred due to the differences in the crystal orientation. Also, the stress values obtained are reasonable, well below the yield point for tin. The region on the right has a much lower stress and hence is more compliant for the thermally induced stress. Hence lower stresses developed in this region, so the strain energy was lower. The left bicrystal however developed higher stresses, and changes in the stress across the boundary between the two bicrystals in Figure 7.10.

Figure 7.11 shows a single crystal simulation which is a simplified version of the bicrystal experiment, for two chosen idealized orientations (010)[100] and (100)[001]. For the (010)[100] orientation where the c-axis is perpendicular to interface, a-axis CTE is close to Cu CTE, low von-Mises stresses develop (~0.55 MPa in center, Max 0.9 MPa in corner). For the (100)[001] orientation, where the c-axis is parallel to interface, c-axis

CTE ~ 2 x Cu CTE, high von-Mises stresses develop (~3.5 MPa in center, Max 6.5 MPa in corner). When the same simulation is done with the crystal orientation that was present after 1200 TMF cycles in the central region, much higher stress developed as shown in Figure 7.12 (High von-Mises stress, ~5 MPa in center, max 9.3 MPa in corner). Stresses vary by ~50% in main part of CTE loaded joint. Externally imposed shear stress gave rise to elastic stress gradients that are different from the CTE loaded (internally loaded) joint. Stresses varied by at least 200% within main part of joint with external load as shown in Figure 7.12.

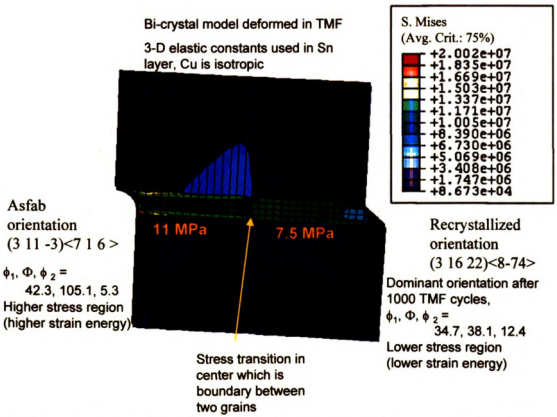

Figure 7.10. Bicrystal simulation using ABACUS for heating from –15 to 150°C for the as-fabricated orientation (left) and recrystallized orientation(right). The orientation on the right has lower von-Mises stresses and hence lower strain energy.

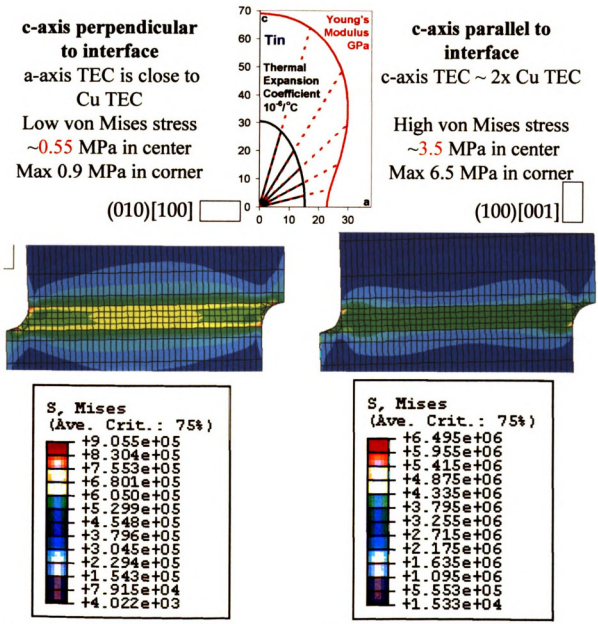

Figure 7.11. Single crystal simulation using ABACUS for heating from –15 to 150°C for two idealized cases (010)[100] and (100)[001]. Lower von-Mises stresses are seen in the (010)[100] case where the a-axis is aligned parallel with the Cu interface.

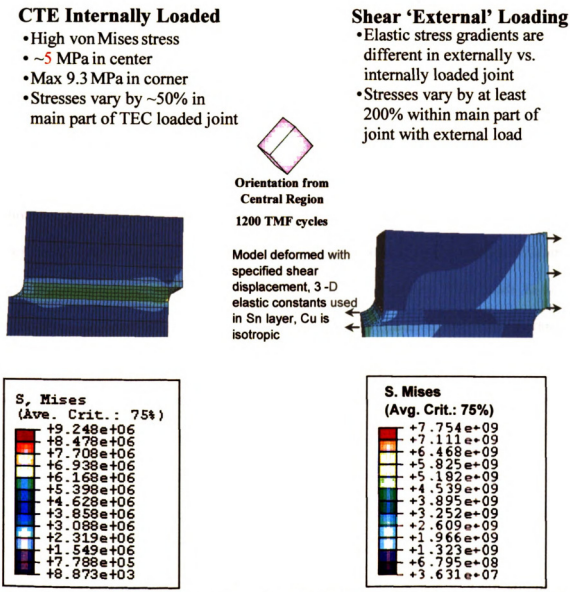

Figure 7.12. Single crystal simulation using ABACUS for heating from –15 to 150°C (left) and externally loaded shear case (right) for the orientation from the central region after 1200 TMF cycles. Stresses greater than the idealized cases in Figure 7.11 are observed in the internally loaded joint.

2. Ledge Formation On Low Angle Boundaries And Schmid Factor Analysis

The three different regions of this specimen have an almost single crystal mesotexture with low angle grain boundaries. The ledges that are seen correlate well with the location of these low angle grain boundaries, suggesting that the boundaries are responsible for their formation. A Schmid factor analysis was carried out for subgrains that formed along low angle grain boundaries in the three regions. From the plane trace analysis, this work shows that ledges which develop due to TMF are often parallel to {110) plane traces, and an analysis of Schmid factors for slip systems on {110) planes (as shown in Figure 7.13) follows to asses the role of slip on grain boundary sliding / ledge formation phenomena. The joints considered here were almost single crystals, with small differences in the tin orientations across low angle boundaries. This leads to small differences in the resolved shear stresses on a given slip system during TMF, leading to damage accumulation in the form of ledges and shear bands on the surface of the specimen. These ledges were along low angle tilt boundaries, and sliding was observed on boundaries with misorientations near 4 and 12°.

Figure 7.13 shows the Schmid factor analysis for the central region. The subgrains are marked 1,2,3,4 and a schematic of the elevation for three of the subgrains is also shown; with subgrain 3 having the lowest elevation. This analysis is based on a stress tensor for the observed crystal orientation after heating due to TMF simulation, given by σ_{11} = -0.03, σ_{22} = 0.14, σ_{33} = -0.82, $\tau_{12} = \tau_{21}$ = 0.19, $\tau_{13} = \tau_{31}$ = 0.19, and $\tau_{23} = \tau_{32}$ = -0.28 MPa, obtained from a FEM analysis for the crystal orientation of the central region.

The ellipses represent a tilted unit circle on the indicated slip plane, on which the thick solid or dashed line along the major axis represents the line trace of the slip plane on the surface, and arrows represent Burger's vectors for a particular slip system. Solid or dashed arrows represent the Burger's vector with a component coming out of, or into, the page, respectively, which allows one to visualize the correct inclination of the slip plane and the mass movement due to dislocation motion. The most highly stressed slip systems are identified in Table XV along with its Schmid factor, m, and the z component of slip (related to mass movement out of or into the page) on that system (note – the Schmid factor and z component are given for the slip plane and vector shown; for the opposite slip direction, the sign of the Schmid factor and the z component would be reversed). For the four orientations, the highest value of the Schmid factor, and the largest value of the z component are identified with bold font. For the most highly stressed slip systems, subgrain 3 had more instances of highest Schmid factor and/or highest z component of slip, causing the highest likelihood of mass moving into the page (dislocation movement into page), followed by grain 4. This corresponds well with the relative elevations of the grains indicated at the top of Figure 7.13. A similar effect is seen in Figure 7.14 with the (1-10) ½[111] slip system. For these subgrains, the (110) plane is fairly steeply inclined to the surface in a manner similar to the ledge geometry, and the plane trace lines up well with many of the ledges, so sliding on the (110) plane could account for the ledge geometry.

In the right region (shown in Figure 7.15), a similar analysis is presented for the ledge that developed; the right subgrain (subgrain 4) has a lower elevation than the left subgrain (subgrain 3). The ledge formed had a misorientation of 9-12° about the [110]

tilt axis moving along the boundary. Table XVI indicates the Schmid factors for various slip systems. The left grain (grain 3) has slip systems that would have cause more mass movement into the page than the right grain, contrary to the observations. Hence the observed ledge formation cannot be ascribed to slip activity alone.

Table XV. Schmid Factors For Various Subgrains In The Central Region.

	Grain 4		Grain 3		Grain 2		Grain 1	
Slip Systems	m	z	m	z	m	z	m	z
(1-10)[111]/2	**-0.62**	***0.78***	**-0.62**	*0.74*	-0.61	*0.75*	**-0.62**	*0.75*
(110)[1-11]/2	-0.58	*0.69*	**-0.59**	***0.73***	-0.58	*0.72*	-0.56	*0.72*
(110)[1-10]	-0.56	*0.49*	**-0.57**	***0.53***	-0.55	*0.51*	-0.55	*0.51*
(1-10)[110]	-0.56	***0.58***	**-0.57**	*0.54*	-0.55	*0.55*	-0.55	*0.55*
(101)[10-1]	-0.47	***0.36***	-0.47	*0.35*	-0.47	*0.35*	**-0.48**	*0.35*
(110)[-111]/2	0.47	*-0.23*	**0.48**	***-0.25***	0.45	*-0.24*	0.47	*-0.24*
(1-10)[-1-11]/2	0.44	***-0.31***	**0.45**	*-0.27*	0.42	*-0.28*	0.42	*-0.28*
(100)[001]	-0.28	*0.65*	-0.28	*0.65*	**-0.31**	***0.66***	-0.28	***0.66***
(1-10)[001]	-0.25	*0.65*	-0.24	*0.65*	-0.26	***0.66***	**-0.28**	***0.66***
(12 1)[-101]	0.38	***-0.36***	0.39	*-0.35*	**0.40**	*-0.35*	0.38	*-0.35*
(1-2 1)[-101]	0.30	***-0.36***	0.28	*-0.35*	0.27	*-0.35*	**0.32**	*-0.35*

Table XVI. Schmid Factors For Various Subgrains In The Right Region.

	Grain 3		Grain 4	
Slip Systems	m	z	m	z
(1-10)[111]/2	-0.60	**0.84**	**-0.61**	0.80
(110)[1-11]/2	-0.57	0.64	-0.57	**0.66**
(110)[1-10]	**-0.56**	**0.48**	-0.55	0.46
(1-10)[110]	**-0.56**	**0.69**	-0.55	0.60
(101)[10-1]	**-0.48**	**0.48**	-0.47	0.35
(110)[-111]/2	**0.48**	**-0.26**	0.46	-0.20
(1-10)[-1-11]/2	**0.44**	**-0.46**	0.42	-0.33
(100)[001]	-0.24	0.53	**-0.30**	**0.65**
(10-1)[101]	**-0.23**	**0.99**	-0.16	0.97
(1-10)[001]	-0.22	0.53	**-0.26**	**0.65**

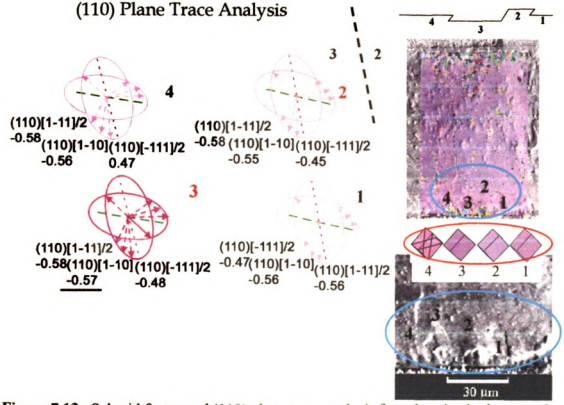

Figure 7.13. Schmid factor and (110) plane trace analysis for subgrains in the central region.

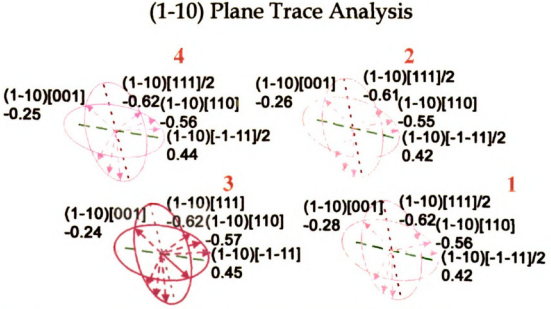

Figure 7.14. Schmid factor and (1-10) plane trace analysis for subgrains in the central region.

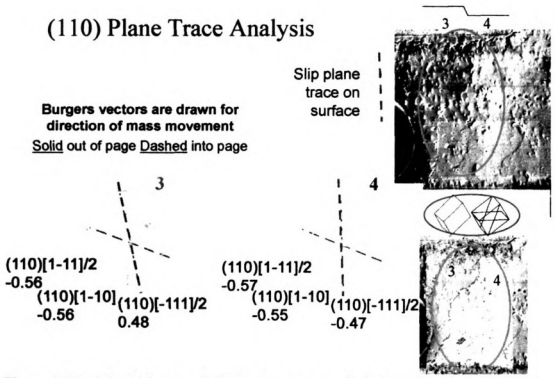

Figure 7.15. Schmid factor and (110) plane trace analysis for subgrains in the right scanned region.

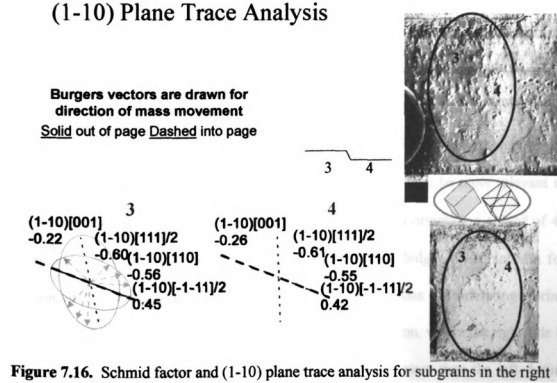

Figure 7.16. Schmid factor and (1-10) plane trace analysis for subgrains in the right scanned region.

Figure 7.17 shows the c-axis alignment for the central region, such that c-axis for this region makes an angle of 40° (blue) - 55° (red) from the surface normal. Red implies that the c-axis is furthest from the surface normal and hence has a lesser normal component of thermal expansion / contraction, whereas the blue orientation has a greater expansion / contraction component. Figure 7.17 shows the changes in the CTE going from c-axis to a-axis. As observed from this Figure the greatest rate of CTE change is between 30 and 70°. Cooling of the solder from high temperature would imply that the orientations with their c-axis closer to the normal direction would contract more and hence would be at a lower elevation, giving rise to the ledge that forms. The differential contraction (or expansion) effect is evident but not large at the ledges, since the color change across the boundary is small (very close orientations). Using a finer color scale at the bottom of Figure 7.17, subgrain 1 is blue / green in the orientation map, and has its c-axis closer to the normal, which would imply that it should contract more on cooling and hence be at a lower elevation. A similar argument can be made for subgrains 3 and 4 where 3 has a orange color (closer to normal) as compared to red (for subgrain 4) and has a corresponding lower elevation. Differences in the misorientation between the different subgrains is within 4°, implying that the effect of the expansion coefficient variations should be minor, such that the slip conditions described above may be more relevant to ledge formation in this area. The finely resolved region has an orientation spread of 4° and formation of these ledges implies that formation of such ledges could account for relaxation of the stress that gets accumulated with dislocations accumulating during TMF. Figure 7.18 shows the orientation maps for the right region, where the right side is at a lower elevation than the left side, and it would contract more than the left during

cooling since it has a c-axis closer to the normal (represented by the blue color). Thus, thermal contraction can account for the topography. The same slip systems are most active in both regions, and the significant difference between the two regions is the difference in the orientation of the c-axis. Initially the material is at the cold temperature where slip processes would be more active than diffusional processes. At high temperature, diffusion controlled recovery processes would be highly active, converting plastic deformation dislocations into extrinsic boundary dislocations, which may be mobile in the boundary plane. If they are transformed to boundary dislocations, they are not available to run backwards during cooling. Then upon cooling, sliding driven by thermal contraction mismatch may allow different deformation mechanisms to operate upon cooling in contrast to what occurred upon heating. The only way this sequence could work with the observations is if sliding is locked upon heating and facilitated upon cooling. *If recovery facilitates sliding at boundaries, then grain boundary sliding due to differential contraction during cooling may be more likely than sliding during heating.* More details of sliding and probable causes for sliding will be discussed in the next section.

Table XVII. Possible Grain Boundary Sliding Mechanism During TMF Cycling.

Stage of TMF Cycle	Hypothetical Events Occurring in the Boundary Between Two Differently Oriented Grains
Heating	Substantial Dislocation generation in neighboring grains due to ***major*** CTE stress differential; boundary does not slide due to lattice dislocation interacting with grain boundaries to form extrinsic grain boundary dislocations.
Short dwell	Diffusional assisted conversion of extrinsic dislocations into mobile grain boundary dislocations that relax stress, allow climbing of extrinsic dislocations that cause sliding to relax stress, restructuring to stabilize Σ boundary structure (attaining a lower energy boundary structure) if misorientation is near Σ character
Initial cooling	Sliding of grains via mobile intrinsic extrinsic boundary dislocations allows sliding to accommodate CTE change since no new lattice dislocations are generated that interfere until lower temperature is reached
Cold hold	Lattice dislocation generation during later stages of cooling, which are accumulated at the boundary; some climb recovery occurs as lattice dislocations are absorbed into grain boundary stay as extrinsic grain boundary dislocations, which block mobile GB dislocations
Heating	Dislocations continue to partially recover. As stress is reversed with heating, some dislocations move strain in reverse, but more need to be generated than are available to move due to being in low energy boundary locations.

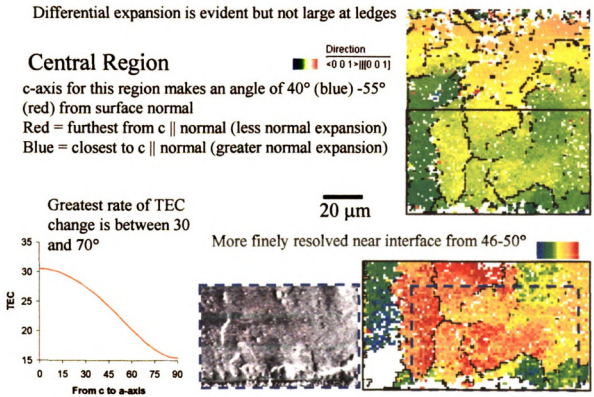

Figure 7.17. Orientation maps showing c-axis alignment with the surface normal for the central region. Differential expansion could give rise to surface topography and damage. Green colored regions have c-axis closer to the normal and hence larger normal expansion / contraction. Plot shows the change in the CTE going from a c-axis to a-axis; greatest rate of change is seen in between 30 and 70°.

c-axis alignment with surface normal

Right Region

c-axis for this region makes an angle of 48° (blue) - 68° (red) from surface normal

Red = furthest from c || normal (less normal expansion)

Blue = closest to c || normal (greater normal expansion)

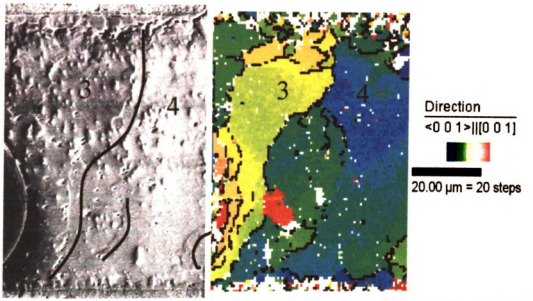

Figure 7.18. Orientation maps showing c-axis alignment with the surface normal for the right region. Green/blue for right grain have c-axis closer to the normal and hence larger normal expansion / contraction.

7.5 REFERENCES:

1. J.G.Lee, A.U.Telang, T.R.Bieler, and K.N.Subramanian, J. Electron. Mater., 2002. **31**(11): p. 1152.

2. J.G.Lee, F.Guo, K.N.Subramanian, and J.P.Lucas, Soldering and Surface Mount Technology, 2002. **14**(2): p. 11-17.

3. J.Howell, A.Telang, J.G.Lee, S.Choi, and K.N.Subramanian, Journal of Materials Science: Materials In Electronics, 2002. **13**(6): p. 335-344.

4. Hong, Choi, and Lee. in *J.J. Jonas Symposium, CIM*. 2001.

CHAPTER 8

TMF OF DUAL SHEAR JOINTS AND COMPONENT TYPE JOINT

Scope

To investigate the effect of external loads arising from differential thermal expansion between a substrate and a surface mount component, specimens with a nickel simulated surface mount component on a copper substrate were prepared to induce extrinsic shear in joints undergoing TMF cycling. The two solder joints had a 1 mm^2 joint area and solder thickness of about 100 μm. In the "dual shear specimen", the joints were not connected at the substrate during solidification, so they were not stressed during cooling. In the "component" type specimen, a continuous copper substrate caused these joints to be strained such that the component was put in compression during cool down. The first specimen was clamped onto a copper block to cause a significant reversal in sign of the shear imposed on the solder joint during TMF cycling. In the second specimen, the existing compressive strain in the component at room temperature was further increased with cooling, but it was nearly unstressed at 150°C. They were subjected to TMF cycling. The effect of these two strain histories on evolution of surface damage and microstructure was compared using SEM and OIM. The joints were almost single crystals. The specimen with the continuous compressive stress in the component exhibited less damage than the dual shear specimen that had reversed shear stresses. However, the orientations of the tin in the joints were roughly similar, but different in detail, leading to different amounts of resolved stress on slip systems involving c-slip. In both specimens, the joint with the largest resolved shear on the c-axis showed the most damage. Sliding of low angle tilt boundaries was observed, which was unanticipated, but analysis indicated that these were low-angle boundaries with a coincident site lattice.

8.1 INTRODUCTION:

It has been shown that the stress state of a solder joint developed during fabrication is complicated [1]. However, the fabrication of single shear lap joints can be considered to be stress free because there are no constraints on the motion of the copper substrates in the joint. This is different from joints that are fabricated on printed circuit boards, where differential thermal contraction typically causes surface mount components to be in a state of compression, with the solder joints carrying residual shear stresses [1, 2]. The effect of this residual stress and strain state on the thermomechanical properties could be considerable. This chapter describes microstructure evolution, deformation, and damage nucleation of joints similar to those used with surface mount components, with the stress states that occur in practical joints. Two different specimen geometries (*dual shear* and *component*-type), each comprised of two single shear lap joints, were used to examine the effect of realistic thermal histories representative of electronic systems in cold transportation settings. Analysis of SEM images and orientation imaging microscopy (OIM) was used to track microstructure evolution and damage accumulation during TMF. In this section we examine how the damage history develops in *component*-like dual shear lap solder joints (see Chapter 2 for more details on joint geometry), which have a residual stress/strain history imposed by the differential contraction between the component and substrate during cooling, and a *dual shear* lap solder joint, where the joints solidified without any externally imposed stress/strain history. The effects of these initial stress states on microstructural evolution and underlying causes for damage nucleation are examined and compared.

8.2 EXPERIMENTAL PROCEDURE:

The dual shear and component joints are prepared as explained in the experimental procedures in chapter 2. The dual shear joint was given a light re-polish after 160 cycles [3] and 800 cycles, to remove oxide and dust that degraded EBSP pattern recognition. The light re-polish increased the pole figure peak intensity slightly. The component type specimen was removed for OIM scanning after 400 and 700 TMF cycles.

8.3 RESULTS:

The results are presented in several composite figures starting with the *dual shear* specimen left joint (Figure 8.1), followed by the right joint (Figure 8.2) and then the *component*-type specimen left joint (Figure 8.3), followed by the right joint (Figure 8.4). Part a of the composite figures shows an SEM image of the entire joint with locations identified where OIM scans were made. Discrete orientation pole figures for these scans are adjacent to the orientation maps (these clearly show the presence of low angle boundaries), and density pole figures (with 'x-random' intensity contours) beneath the maps. The orientation maps have thin white boundaries for misorientations greater than 15°, but twin related boundaries are thicker. Low angle boundaries are defined by thin black lines, but 5-7° and 12-14° misorientations are thicker. Parts b and c of these composite figures show orientation maps and corresponding SEM images at intermediate and final stages of cycling, respectively. Part c also shows corresponding discrete and density pole figures.

Figure 8.1 shows the left joint of the *dual shear* specimen. The polished as-fabricated surface was smooth and flat (not shown). From the left to the middle, the orientation maps in Figure 8.1(a) show two different dominant orientations in the as-fabricated joint. The discrete pole figures for the left region indicate that the two major grains in the OIM map are slightly misoriented. While the orientations of the grains in the middle region are rotated by about 45° from the left region, the grains within the middle region are only slightly misoriented from each other. The small misorientations are evident in the OIM maps as low angle boundaries (various thickness of black lines) that traverse from top to bottom. After 550 TMF cycles the orientation maps (including dashed boxes) in Figure 8.1(b) revealed an increase in the number of low angle boundaries in both regions. The corresponding secondary electron SEM image shows ledges. These ledges correspond to the low angle grain boundaries in the orientation maps. After 800 TMF cycles the SEM image in Figure 8.1(c) showed more prominent ledge development and topography, and a corresponding increase in the number of low angle grain boundaries in the orientation map. The density pole figure maxima for the left region (boxed) show a decrease that can be attributed to peak splitting to form several different orientations that are slightly misoriented from the initial dominant orientation; this effect is also evident in the discrete pole figures.

In contrast to the low angle boundary evolution in the left joint of the *dual shear* specimen the right joint of the same specimen in Figure 8.2 showed almost no changes due to TMF, despite the fact that the joint was smaller and thus had a higher stress. The orientation maps in Figure 8.2(a) show the same dominant orientation in both of the regions, suggesting that a single dominant crystal orientation was present throughout the

joint (the right region has a band of a twin related secondary orientation). With cycling there was no ledge development observed in the SEM micrographs in Figures 8.2(b,c). The only observed change in the microstructure was coarsening of Ag_3Sn particles after 550 and 800 TMF cycles. The orientation maps get *cleaner,* suggesting that the initial dominant orientation consumed the secondary or other minority orientations, as confirmed by the increase in the texture intensity in the pole figures. The pole figure for the right joint is shown in Figure 8.2, which has the c-axis pointing close to the –y direction. Instead of weakening of the texture due to formation of subgrains as in the left joint, the secondary orientations disappeared, and there was no splitting of the peak in the discrete pole figure peak. Both sides of the specimen show systematic downward rotation of the pole figure peaks, and development/sharpening of low angle boundaries that spread out the peak shown in some of the density plots. However, in the right joint, the low angle grain boundary in the lower part of the right scan had an average misorientation of 6.5° and did not change in misorientation.

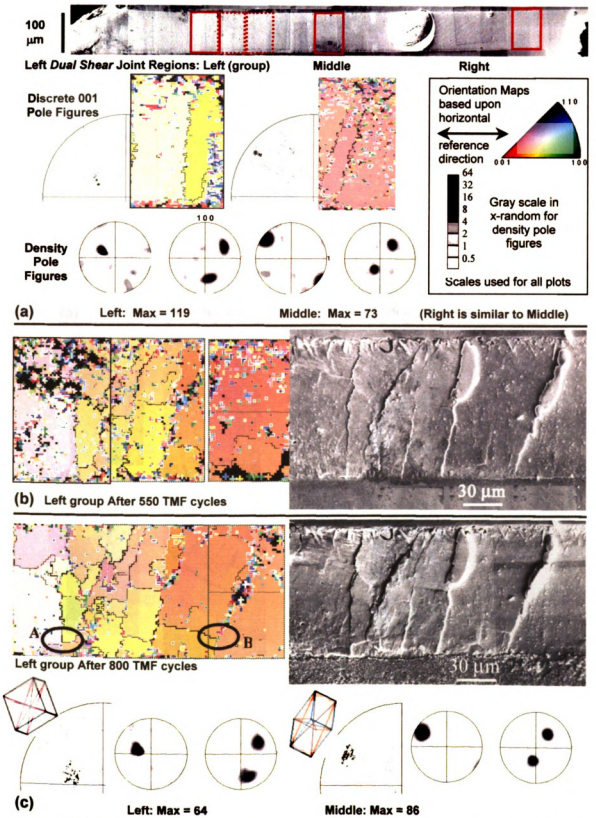

Figure 8.1. (a) Initial condition and (b,c) changes due to TMF cycling of the left joint of the dual shear specimen.

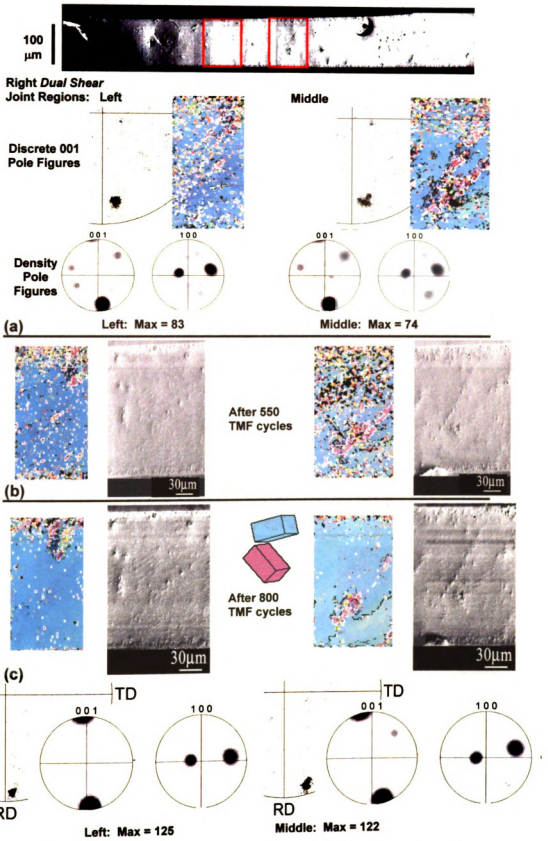

Figure 8.2. (a) Initial condition and (b,c) changes due to TMF cycling of the right joint of the dual shear specimen.

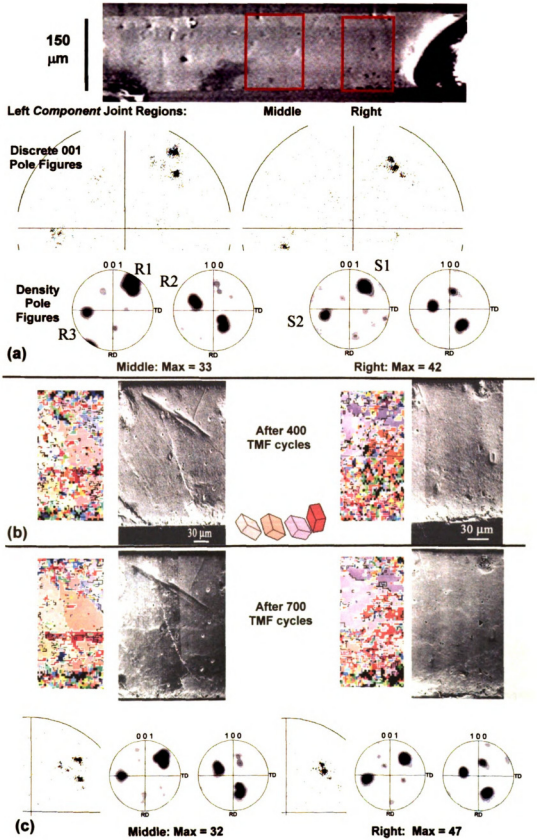

Figure 8.3. (a) Initial condition and (b,c) changes due to TMF cycling of the left joint of the component specimen.

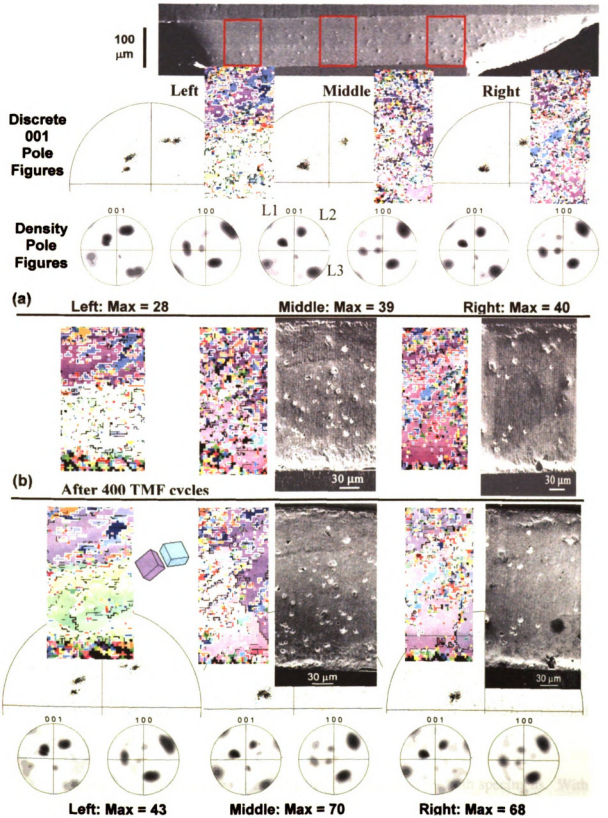

Figure 8.4. (a) Initial condition and (b,c) changes due to TMF cycling of the right joint of the component specimen.

Figure 8.3 shows the left joint of the *component* specimen. The orientation maps show three prominent orientations in the 001 pole figure, separated by high angle grain boundaries (shown as white lines in Figure 8.3(a)). The density pole figures display less intense texture compared to the *dual shear* specimen, indicating the presence of a dominant orientation and two secondary orientations in the middle region. The changes in the peak intensities are shown in Table XVIII. One orientation is misoriented by the 59 or 62° twin misorientation and the other is misoriented by ~20°. The SEM images after 400 TMF cycles in Figure 8.3(b) show that a ledge developed along the 20° high angle grain boundary. After 700 TMF cycles the ledge became more prominent (Figure 8.3(c)).

The right joint of the *component* specimen shown in Figure 8.4 is smaller and thinner, but it does not have any secondary orientations having a 20° misoriented boundary. The orientation maps from the as-fabricated condition in Figure 8.4(a) show one dominant and two secondary orientations with the same orientations in all three regions. The changes in the peak intensities are shown in Table XIX. Like the right joint of the dual shear specimen, the smaller right joint has a crystal orientations with the c axis close to the –y specimen direction. This joint appears to be a single crystal with some ~60° twin related secondary orientations embedded within the crystal. After 400 or 700 TMF cycles, no surface ledges developed, as shown in Figures 8.4(b,c). Some peak sharpening is evident in the density pole figures due to elimination of small-embedded orientations.

Figures 8.5 and 8.6 show the misorientation histograms for both specimens. With cycling, there is an overall decrease in random and 60°, twin misorientations, but

conspicuous peaks are seen at ~22, 45, 70 and 80° after 800 cycles in both joints. However, the 7 and 12.5° peaks that were present in the left joint before TMF cycling were not present at any time in the right joint. These strong peaks correspond to the low angle boundaries where ledges are evident in the SEM images in Figure 8.1. The initial 22° peak in the left *component* joint in Figure 8.6 was weakened, but retained. In contrast to the *dual shear* specimen, the *component* joints have a larger number of low angle grain boundaries, but no preferred misorientation peaks were present at 6-7 or 12-13°.

Table XVIII: Intensities For the Three Dominant Poles In The Left Joint Of The Component Specimen.

	Center			Right	
	R1	R2	R3	S1	S2
As-fab	33.4	30	10.1	42.3	15.3
400	25.4	23.3	10.0	38.6	18.3
700	32.7	29.3	13.6	47.03	21.4

Table XIX: Intensities For the Three Dominant Poles In The Right Joint Of The Component Type Specimen.

	Center			Right		
	L1	L2	L3	M1	M2	M3
As-fab	38.9	13.9	11.2	25.6	18.8	27.2
400	49.48	8.4	8.3	36.7	28	20.8
700	70.4	11.6	7.0	42.9	31.0	28.0

Figure 8.7(a) shows the first few sections of the misorientation distribution function (MODF) for the left region of the left *dual shear* joint. The number of very low angle boundaries decreases, indicating *polygonization* of low angle boundaries and their conversion into higher angle boundaries, but the boundaries misoriented by 7, 13, and 20° about a 110 axis are retained. Figure 8.7(b) shows that most of the boundaries in the region with many subgrains are misoriented by small rotations about an axis near {110}, but the tilt axis is different for boundaries that are perpendicular to each other.

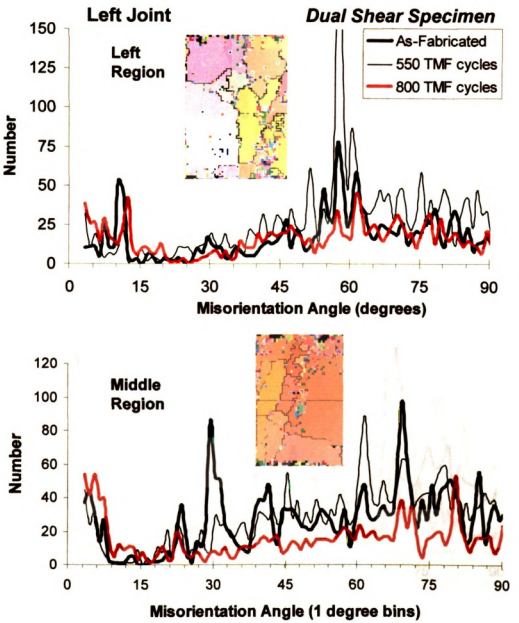

Figure 8.5. Misorientation changes due to TMF cycling of dual shear specimen.

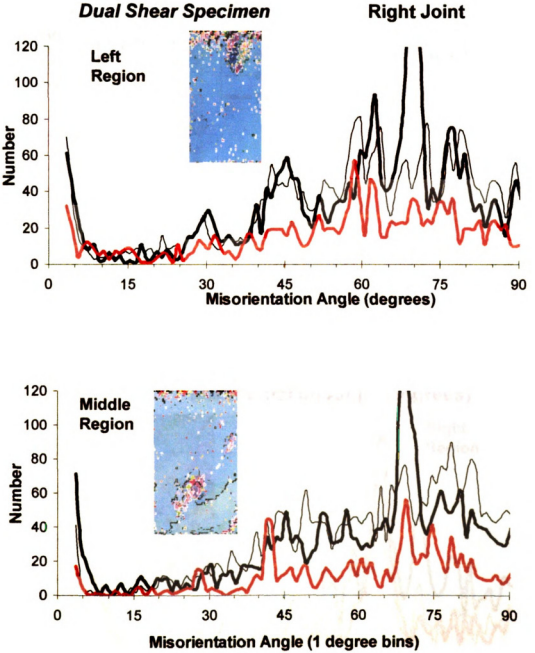

Figure 8.5 continued. Misorientation changes due to TMF cycling of dual shear specimen.

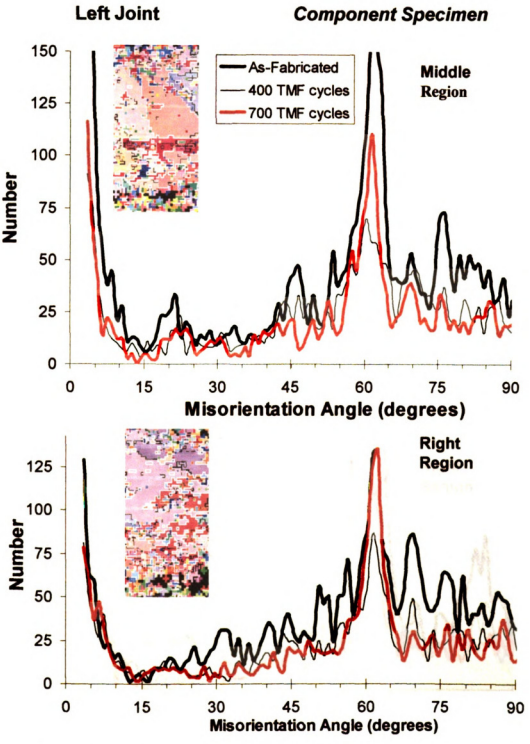

Figure 8.6. Misorientation changes due to TMF cycling of the component specimen.

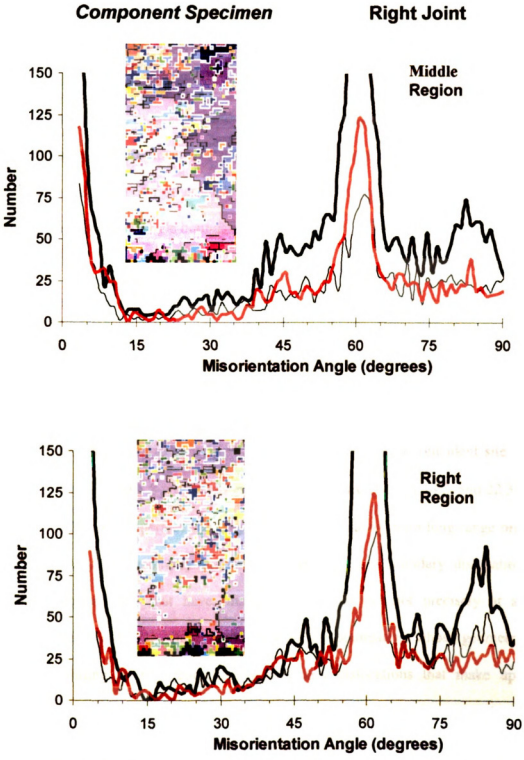

Figure 8.6 continued. Misorientation changes due to TMF cycling of the component specimen.

8.4 DISCUSSION:

Several new observations about deformation in tin based solder joints emerge from this work. Firstly, apparent grain boundary sliding was observed on low angle boundaries. Secondly, differences in the stress history for the *dual shear* and the *component* specimens, as well as differences in crystal orientations, strongly affected the nature of damage development in the solder joint. Both of these aspects are discussed in detail below, followed by further analysis and discussion pertaining to the activity of slip in the regions along low angle boundaries of Figure 8.1.

1. Ledge Formation On Low Angle Boundaries

Prior work in characterizing microstructure of the tin phase in solder joints has shown highly preferred boundaries with coincident site lattices at 22.3, 28 [9], 43, 70 and 80° misorientations, and twins at 59 and 62° [4]. The highly preferred low angle boundaries which appear to slide in Figure 8.1(b,c) are close to coincident site lattices (CSL) shown in Figure 8.8 with rotations about a {110) axis of 7.2, 14.3, and 22.3°. The low angle CSL's are imperfect and they cannot be maintained with long-range order for the simple rotational geometry presented. Periodic grain boundary dislocations are required in boundaries that have misorientations that are not precisely at a CSL misorientation [10,11,12]. These boundaries are tilt boundaries, whose geometry does not permit sliding of the geometrically necessary dislocations that make up these boundaries, though these sub-boundary dislocations could climb in a way that assists sliding. If misfit dislocations are contained in the boundary plane, and their glide plane is also the boundary plane, then sliding could be anticipated when the resolved shear stress

is sufficiently high. If the misfit dislocations have screw character on glide planes, they could slide when the resolved shear stress is sufficiently high.

Ledges that developed on the left side due to TMF are mostly parallel to {110) plane traces, which is confirmed in Figures 8.1 and 8.3(b,c) of this study as well. The *misorientation axis* (rather than misorientation angle) between subgrains in the left joint of the *dual shear* joint is characterized in the map in Figure 8.7(b), which shows that these sliding low angle boundaries are misoriented by a rotation about an axis within 5° of a {110) plane normal (note arrows in Figure 10(a)). Figure 8.7(c) shows that the (110) axes of rotation lies in the plane of the low angle boundaries, implying that these are low angle *tilt* boundaries (that is, the tilt axes for vertical and horizontal boundaries are perpendicular). The tilt axis for the sliding vertical boundaries is the [110] direction that is nearly in the plane of the paper. It is reasonable to expect tilt boundaries to form during polygonization, but not twist boundaries, as twist boundaries are made up of screw dislocations, which do not form low energy structures by assembling arrays [4].

Figure 8.9 shows the joint in Figure 8.1(b,c) tilted 70° (bottom edge of the joint is the high side) to reveal the 1-3 μm steps at the ledges. At the base of the 800 cycle image, a series of prisms for orientations near the bottom of the joint are rotated with the same 70° rotation about the x axis as the tilted joint, and the left two of these prisms has the 110 plane illustrated. The plane of shear of the left two steps is very close to the (110) plane illustrated, implying that sliding occurred on (110) planes. There are smaller magnitude steps on the right side of the image that cannot be ascribed to (110) planes, since the ledge step is nearly perpendicular to either (110) plane. Therefore, sliding that

formed the ledges on the right side must have occurred on another plane (such as the (100) plane that is nearly parallel to the ledge step for the right most ledge).

As misorientations of subgrains tend to increase with increasing strain, when a misorientation reaches an orientation close to, but not at a CSL, then misfit dislocations allow the boundary to exist with energy close to that of the CSL boundary. It is noteworthy that misorientation peaks are observed on the high side of the 7.3 and the low side of the 14.3° CSL misorientations (Left joint in Figure 8.5), which suggests that a significant number of boundary dislocations are required to maintain the favored CSL low energy boundary. If misfit dislocations have screw character and reside in the boundary plane, and if these dislocations are glissile, then sliding that forms ledges is plausible. Recent studies show that developing networks of CSL boundaries is beneficial for enhanced ambient temperature properties [13,14]. In contrast, the present study shows that low angle CSL boundaries may be undesirable for high temperature deformation if they facilitate grain boundary sliding and the heterogeneous strain that supports a damage nucleation processes. Furthermore, in the superplastic literature, it is commonly stated that high angle are required or must be developed for grain boundary sliding. On the basis of existing knowledge, observation of sliding on low angle boundaries is unanticipated.

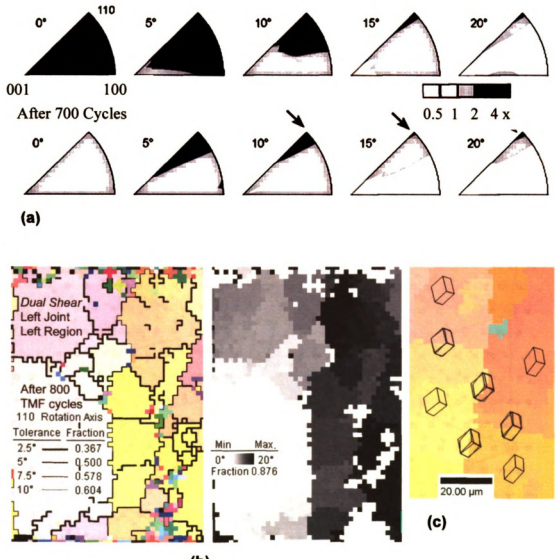

Figure 8.7. TMF in the *dual shear* specimen caused low angle boundaries to form with rotations about a [110] axis. (a) Changes in Misorientation Distribution (MODF) for the *component* specimen shows reduction in number of very low angle boundaries, and a preference for boundaries rotated about a {110) axis (arrows). The MODF is similar for the *dual shear* specimen. (b) More than 50% of the boundaries in a region with 20° of crystal orientation variation are within 5° of a 110 axis rotation. (c) prisms in adjacent subgrains are overlapped at the boundary to show that (110) rotation axes are in different directions for horizontal and vertical boundaries.

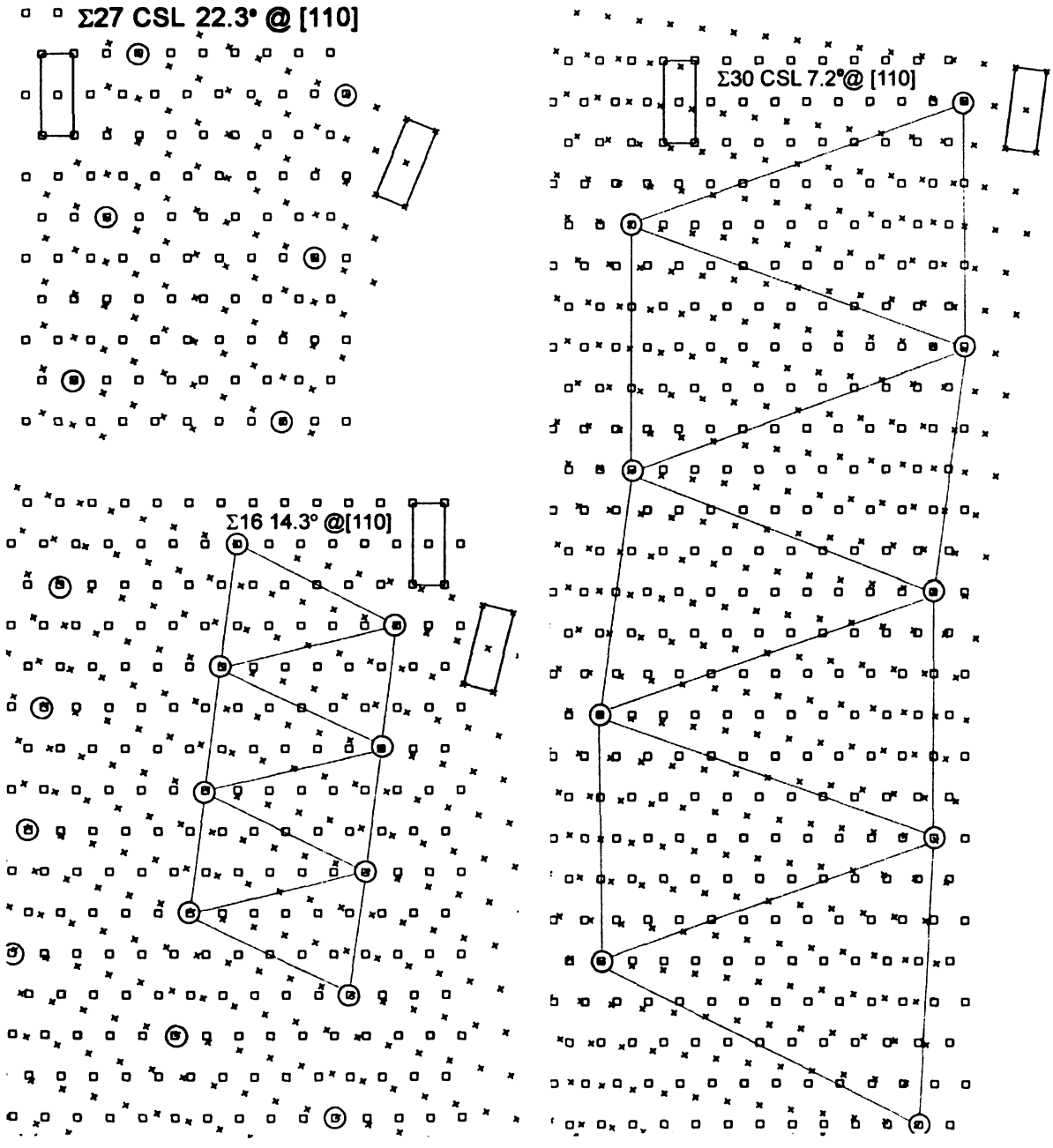

Figure 8.8. Coincident Site Lattice (CSL) arrangements for boundaries with rotations about {110) axes. These CSLs are not perfect; they cannot be maintained with long-range order for the simple rotational geometry presented; hence the ideal axis of rotation may be slightly different from {110).

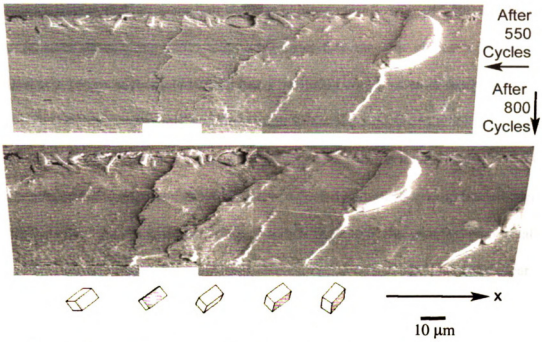

Figure 8.9. Images of the 550 and 800 cycle left group region of the *dual shear* specimen tilted 70° about the x-axis shows 1-3 micron displacements along low angle boundaries. Prisms rotated 70° deg about the x-axis with (110) or (100) planes highlighted show correspondence between the ledge planes of shear and crystallographic planes.

2. Heterogeneous Deformation At Low Angle Boundaries

In both TMF cycled specimens, the larger of the two joints developed more damage than the other, suggesting that the larger joints were weaker. In the *dual shear* joint, the left joint had 11% greater load carrying area, indicating that the overall shear stress was higher in the right joint. However, the orientation of the c-axis in the two joints was different; the left joint had the c-axis more closely aligned with the direction of maximum shear along the x-axis, suggesting that the slip modes with the smallest Burger's vector such as {110)[001] or {100)[001] could be more easily activated than slip in the more highly stressed right joint. In the left region of the left joint, the c-axis deviated 58° from the maximum shear direction, but in the middle it deviated 24° from the x-axis. The component of x-axis shear projected onto the c-axis on the left region was 53%, while it was 91% in the middle and right regions of the joint. When normalized by the 11% lower stress differential, the c-axis slip systems had 47-81% of the shear and the right joint had 24-32% of the shear projected on <001> slip directions, even though the left joint had a lower overall stress. Thus, the right joint was intrinsically more resistant to deformation in the c-axis direction. These values are tabulated for both joints in Table XX. In the *dual shear* specimen, the right joint of the *component* specimen was also more highly stressed, and it also had less of the resolved shear projected onto the c-axis. The right joint also had an orientation with a c-axis pointing near the –y specimen direction, as well as two orientations pointing closer to the z direction. The left joint was less damaged than the left joint of the *dual shear* joint specimen, where the c-axis was closer to the direction of maximum shear in the left joint, and damage was the greatest.

Two other factors may account for lesser amounts of damage in the *component* joint, the non-reversal of the shear stress direction, and the higher population of low angle boundaries. The sign of the shear stress reversed in the *dual shear* specimen. Reversal of stress sign has been shown to assist recovery processes (removal of mobile dislocations) [5, 6] which may account for less plastic accommodation of imposed stresses when reversals occur. The *component* specimen also had a higher population of low angle boundaries, indicating a higher initial population of dislocations that may have resulted from the strained cooling history, and since they were continually loaded in the same direction throughout its deformation history, the dislocation density in substructure may have been kept more constant. This suggests that retention of glissile dislocations is beneficial to prevent damage nucleation.

Table XX: Stress Parameters in *Dual Shear* and *Component* Joint Specimens

Dual Shear	Left Joint	Right Joint
Stress differential	11% lower	11% higher
angle between 001, x	58°, 24°	78°, 73°
% of stress along c-axis	53, 91	22, 29
normalized by differential	47, 81	24, 32
Component		
Stress differential	39% higher	39% lower
angle between 001, x	53°, 43°	60°, 51°
% of stress along c-axis	60, 74	51, 64
normalized by differential	74, 59	36, 31

3. Schmid Factor Analysis

Work above [1] has shown that ledges which develop due to TMF are often parallel to {110) plane traces, as is the case with most, if not all of the boundaries in this joint, and an analysis of Schmid factors on slip systems on {110) planes follows to asses the role of slip on grain boundary sliding/ledge formation phenomena. A Schmid factor analysis of possible slip systems in tin (BCT tin has many slip system families) was used to compare with observed slip phenomena associated with ledges and sliding. Schmid factor analysis was carried out in regions that showed ledges or grain boundary sliding. Slip on (110) planes correlated well with some of the ledges. This section focuses on microstructure evolution, deformation, and damage nucleation of joints similar to those used with surface mount components, and aims to ascertain the impact of slip in deformation by thermomechanical fatigue.

Figure 8.10 reveals the Schmid factor analysis for the two regions along low angle grain boundaries, regions (A) and (B) in Figure 8.1. This is based on a stress tensor σ_{11} = 10.4, σ_{22} = -9.6, and $\tau_{12} = \tau_{21}$ = 3.9 MPa, obtained from a FEM analysis described in Chapter 2, and it represents the hot part of the TMF cycle when the component is put into tension. The ellipses represent a tilted unit circle upon a slip plane, on which arrows represent a particular slip system. The thick solid or dashed line along the major axis corresponds to the plane trace of the slip plane. A solid, or dashed, arrow represents the Burger's vector with a component coming out of, or into, the page, respectively, which allows one to visualize the correct inclination of the slip plane. The most highly stressed slip systems are identified along with its Schmid factor, m, with the highest values circled.

In region (A), the upper grain on the right of the ledge slid out of the original surface more than the grain on the left. The Schmid factor analysis reveals that the upper grain is more highly stressed (m=0.61) on the (1-10)[111]/2 slip system than the left grain, (m=0.58). Because the Burger's vector comes out of the page, more mass would move out of the page for upper grain. The next most highly stressed slip system for these grains is (110)[1-11]/2, which has the Burger's vector going into the page. The Schmid factor for this slip system has a higher value in the left grain (m=0.54) than the upper grain (m=0.48), so more slip with an inward component would be expected in the left grain, which is also consistent with its lower surface elevation. On the basis of these two slip systems, there is more mass movement out of the page for the upper grain than the left grain. For both grains the (110) plane is fairly steeply inclined to the surface in a manner similar to the ledge geometry, and the plane trace lines up well with many of the ledges, so sliding on this plane could account for the ledge geometry.

In region (B), a similar analysis is presented on the right side of Figure 8.10. The ledge developed such that the right grain has a lower elevation than the upper or lower grains on the left. For the right grain, the most highly stressed slip system (1-10)[001] with m=0.67 has more overall mass movement into the page than the other two grains (m=0.63 and 0.58). The second most highly stressed slip system (100)[001] with m= 0.55 also has its Burgers vector going into the page. These slip systems in the other two grains have smaller Schmid factors. The crystallographic plane that best aligns with this ledge is the (001) plane, and the Schmid factors for [1-10] and [100] slip are above 0.53-0.67 in these grains, with similar kinds of inward and outward preference as described above. The sliding on the (001) plane, on which there is no Burgers vector with a small

value suggests that sliding by climb of (100)[001] dislocations may account for this deformation process.

Recent studies show that developing networks of high angle CSL boundaries is beneficial for enhanced ambient temperature properties [7, 8]. In contrast to these studies, this study shows that low angle CSL boundaries may stimulate heterogeneous deformation if they facilitate grain boundary sliding that supports damage nucleation processes. Furthermore, it is commonly stated that high angle boundaries are required or must be developed for grain boundary sliding in the superplastic literature. On the basis of existing knowledge, observation of sliding on low angle boundaries is unanticipated.

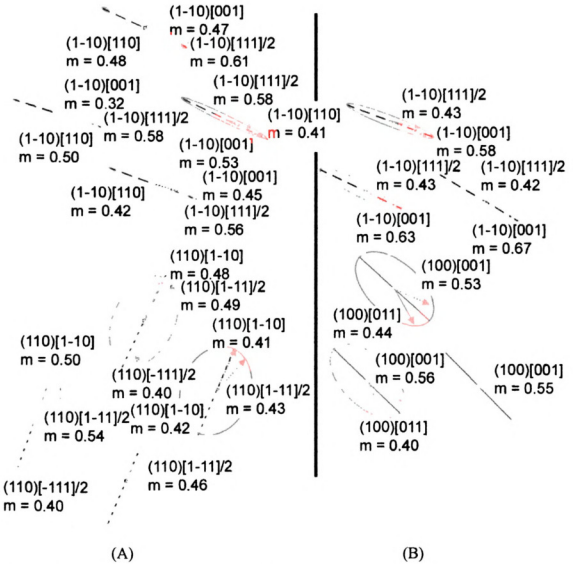

Figure 8.10. The most highly stressed slip systems and Schmid factors in the two circled regions (A) and (B) in Figure 8.1. Solid vectors come out of page, dotted vectors go into page.

8.5 CONCLUSIONS:

1. With increasing TMF, sub-boundaries were formed. Ledges developed preferentially in tilt boundaries with ~7, ~13 and ~22° misorientations about a (110) axis, which are near CSL misorientations. If misfit dislocations in the boundary plane have a screw character they may be able to account for the observation of sliding. Otherwise, climb of dislocations having a climb component in the boundary plane may also account for the sliding.

2. Differential slip activity on highly stressed slip systems on either side of a subgrain boundary can result in development of surface topography that is consistent with activation.

3. The *component* type specimen developed less damage than the *dual shear* specimen. This can be attributed to the differences in initial thermal stress history in the two joints, as well as the actual crystal orientations present in the joint. Joints with [001] orientation more closely lined up with the shear direction exhibited the most damage, whereas joints with orientations having the c-axis poorly aligned with the direction of shear may not have even deformed.

8.6 REFERENCES:

1. A.U.Telang, T.R.Bieler, D.E.Mason, and K.N.Subramanian, J. Electron Mater., 2003. **32**(12): p. 1455-1462.

2. J.W.Morris, and H.L.Reynolds. *The Influence of Microstructure on the Failure of Eutectic Solders.* in *Design and Reliablility of solders and solder interconnects.* 1997. TMS Annual Meeting Warrendale, PA.

3. A.U.Telang, Masters Thesis, Material Science, Michigan State University, East Lansing, 2002.

4. D.J.Rowenhorst, and P.W.Voorhees, J. Mater. Res., 2004. **Under Review**.

5. S.Choi, J.G.Lee, K.N.Subramanian, J.P.Lucas, and T.R.Bieler, J. Electron Mater., 2002. **31**(4): p. 292.

6. S.Jadhav, Masters Thesis, Materials Science and Mechanics, Michigan State University, East Lansing, 2001.

7. C.A.Schuh, K.Kumar, and W.E.King, Acta Mater., 2003. **51**: p. 687-700.

8. G.Palumbo, P.J.King, K.T.Aust, U.Erb, and P.C.Lichtenberger, Scripta Metallurgica et Materialia, Aug 1991. **25(8)**: p. 1775-1780.

CHAPTER 9

VPSC SIMULATIONS

9.1 INTRODUCTION:

VPSC simulations were carried out up to different global strains to capture crystal rotations as a function of high strain rate (0.1/sec) strain rate testing. Crystal rotations are represented with pole figures and comparison is made between as-fabricated, sheared final state and the simulations. The simulation captured activity of different slip systems with straining and allowed determination of progress of different slip systems that contribute to the strain. Since tin has several slip systems, the simulations allow us to determine the probability of their activity. Comparison was also made with creep straining, to see the differences between high and slow strain rate testing.

9.2 HIGH TEMPERATURE CREEP SIMULATIONS:

The visco-plastic self-consistent polycrystal plasticity code was used to simulate deformation in the regions examined by OIM. The boundary conditions imposed were a strain rate tensor with all zero terms except $\tau_{21} = \pm 1$ and $\tau_{12} = 0$ to impose a simple shear. This code can be used in a rate sensitive Taylor mode, which is computationally less time consuming than a self-consistent computation, and it provides an upper bound for stress in a polycrystal (in a preliminary run made with the visco-plastic assumptions, and the rotations of the crystals were qualitatively similar to the Taylor model). The Taylor model assumes that all grains deform with the same strain tensor that is imposed by the user. The visco-plastic self-consistent model (VPSC) assumes that every grain in the

material of interest can deform differently, as long as the total strain of the aggregate satisfies the imposed strain. In a preliminary run made with the self-consistent visco-plastic assumptions, the rotations of the crystals were qualitatively similar to the Taylor model. It is anticipated that the VPSC model will be effective to simulate deformation in tin due to its anisotropy, but before such models can be used with confidence, the material parameters for the slip systems need to be identified. Thus, a very simple approach was used, assuming that some particular combination of the known slip systems operated without hardening, with the same critical resolved shear stress for flow on each system, to determine whether particular slip systems affected rotations in a way that agreed with experimental observations.

In addition to boundary conditions and strain increments, the code requires definition of the operative slip systems, and a set of discrete crystal orientations expressed in Euler angles. The slip systems used are provided in Table XXI, and the discrete orientations were taken from OIM measurements on the undeformed specimen. A small area of the OIM map was extracted from particular regions of the creep specimen to provide about 1000 discrete orientations. These orientations were then computationally deformed to a strain of 0.06, and then replotted with the OIM analysis software to compare with the experimental measurements. The code output provides the new orientations for each pixel of the OIM scan, as well as statistics for the active slip systems by which the computational deformation was accomplished. Simulations using modes 1 and 2, 1,2,and 3, and 1,2, and 4 were done for all patches, and additional modes were checked with selected patches, but the rotations were essentially the same [1].

The regions of the creep specimens used for simulations had 3 primary grain orientations. The simulations in the creep specimen showed that mode 1 slip was the most active slip system when only modes 1 and 2 were allowed / present, and mode 3 slip was the most active slip system when modes 1,2 and 3 were used (Table XXI, Figure 9.2).

From comparisons of the experimental and computed rotations in the creep specimen, in Figures 9.2 and 9.3, it is clear that the experimental rotations are similar in magnitude but occur about a different {110} axis than the computed rotations for the creep specimen. Since the simulations did not account for recovery phenomena, the observed rotations may not be only due to slip. Conversely, if only slip were active, the sense of reorientation should have coincided for the experiment and simulation.

Table XXI. Slip Systems Used In Taylor Model Simulations For Creep Specimen

SLIP MODE	Plane Normal	Slip Direction
MODE 1 {100}<001>	(100)	[001]
	(010)	[001]
MODE 2 {110}<001>	(110)	[001]
	(0-10)	[001]
MODE 3 {100}<010>	(010)	[100]
	(100)	[010]
MODE 4 {110}<-111>/2	(110)	[-111]
	(110)	[1-11]
	(1-10)	[111]
	(1-10)	[-1-11]

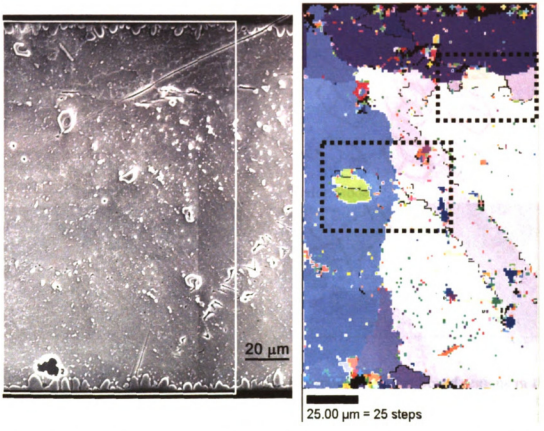

Figure 9.1. SEM and OIM map of creep specimen after 0.06 shear strain, 85°C.

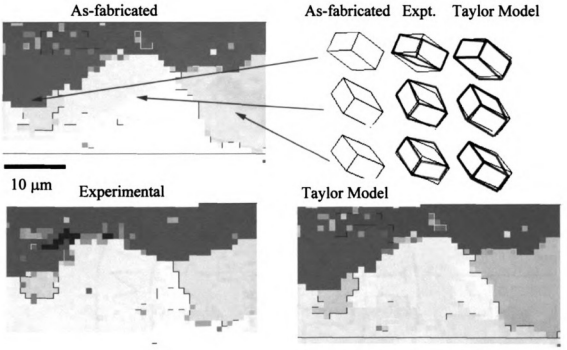

Figures 9.2. Smaller areas of the OIM maps corresponding to the boxed regions in the OIM maps of Figure 9.1 in the as-fabricated condition, after experimentation and after simulations. The wire frame unit cells show the orientation of the grains. With deformation, the lattice rotates to accommodate the imposed strain, as shown by the gray unit cell that is superposed on the undeformed orientation.

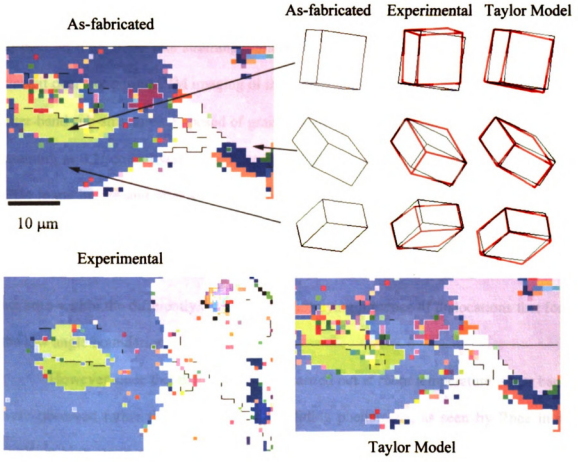

Figure 9.3. Smaller areas of the OIM maps corresponding to the boxed regions in the OIM maps of Figure 9.1 in the as-fabricated condition, after experimentation and after simulations. The wire frame unit cells show the orientation of the grains. With deformation, the lattice rotates to accommodate the imposed strain, as shown by the gray unit cell that is superposed on the undeformed orientation.

9.3. HIGH STRAIN RATE SIMULATIONS:

SEM images in Figure 9.4 reveal the microstructure before and after 0.8 experimental strain at 0.1/sec strain rate at room temperature. Extensive shear bands are formed on high strain rate straining. Shear testing was not done to failure in this case since it does not permit OIM imaging of the surface due to large surface deformation. An inter-band sub-structure composed of grain pop-up formed at higher temperature (150°C) straining at 0.1/sec and was carried out in Ref. [2]. Figure 9.5 shows the corresponding OIM maps before and after straining corresponding to the regions in Figure 9.4. OIM maps show that the initial near-single crystal region shows gradation in color after straining implying changes in crystal rotations in the joint. Low angle grain boundaries are seen within the differently colored grains implying presence of dislocations that form the low angle boundaries.

However since this deformation was carried out at room temperature, shear bands were observed rather than grain boundary sliding phenomena, as seen by Rhee in his work on high strain rate testing [2]. Pole figures illustrate rotations that are consistent with crystal rotations that would occur by rotations similar to the imposed simple shear, implying that primary recrystallization did not occur during room temperature creep. The pole figures also show that different grains have rotated by different amounts to accommodate the deformation in various regions of the joint.

Figure 9.6 shows the OIM maps and pole figures corresponding to simulations for 0.8 strain using the secant model with all slip systems present and with {112}<1-10> slip system having minimal activity (this slip system was given a critical resolved shear stress

of 10 times higher than all other slip systems). Figure 9.7 shows the OIM maps and pole figures for 0.8 strain using the VPSC models with minimal activation of {112}<1-10> and {101}<10-1> slip systems based upon secant and VPSC models. Switching off the two slip systems in this case shows better rotations, implying that these two slip systems do not contribute to the slip activity seen in tin. Figure 9.8 shows the activity for all the different modes for various cases shown above and Table XXII lists the different modes used. Modes 1, 2 and 4 ({100}<001>, {110}<001>, {110}<-111>/2) respectively) are most active and are responsible for causing the rotations.

Figure 9.9 shows the OIM maps and pole figures corresponding to simulations for 1.3 strain with {112}<1-10>, and both {112}<1-10> and {101}<10-1> slip systems having reduced activity (this slip system was given a critical resolved shear stress of 10 times more than all other slip systems). The simulations with 0.8 strain using the VPSC model showed rotations closer to the actual experimental observations, however the 1.3 simulations with reduced activity on two slip systems ({112}<1-10> and {101}<10-1>) show good correlation with the secondary peaks that develop after experimentation. This implies that different regions undergo different amount of strain depending upon the heterogeneities in the microstructure, which are also being captured by the VPSC code. Figure 9.10 shows the activity for all the different modes for various cases shown above.

Figure 9.11 shows the overlay of the (001) poles after rotation to make a better comparison. The simulation with {112}<1-10> and {101}<10-1> reduced activity using the VPSC model has closer rotations to the actual experiment shear. VPSC simulations showed better correlations.

Table XXII. Slip Modes Used for the High Strain Rate Simulations

MODE1	{100}<001>
MODE2	{110}<001>
MODE3	{101}<10-1>
MODE4	{110}<-111>/2
MODE5	{010}<101>
MODE6	{110}<1-11>
MODE7	{112}<1-10>

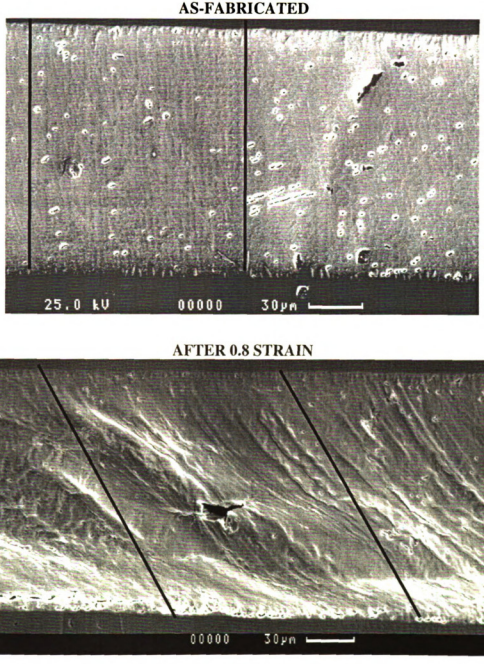

Figure 9.4. SEM images in as-fabricated and after 0.8 shear strain at 0.1/sec strain rate condition.

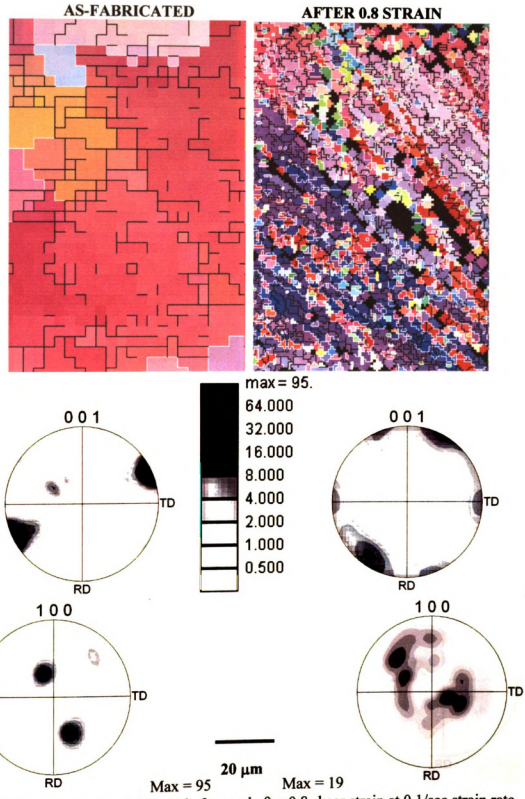

Figure 9.5. OIM and pole figures before and after 0.8 shear strain at 0.1/sec strain rate.

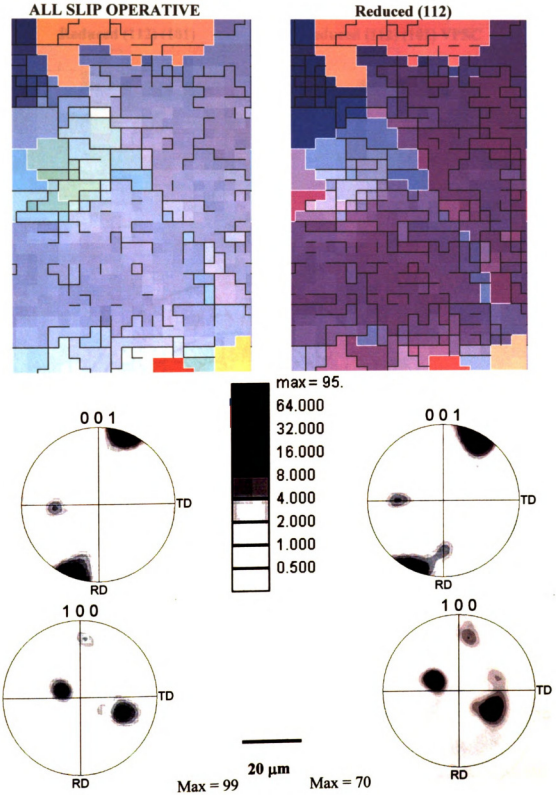

Figure 9.6. OIM and pole figures before and after 0.8 shear strain.

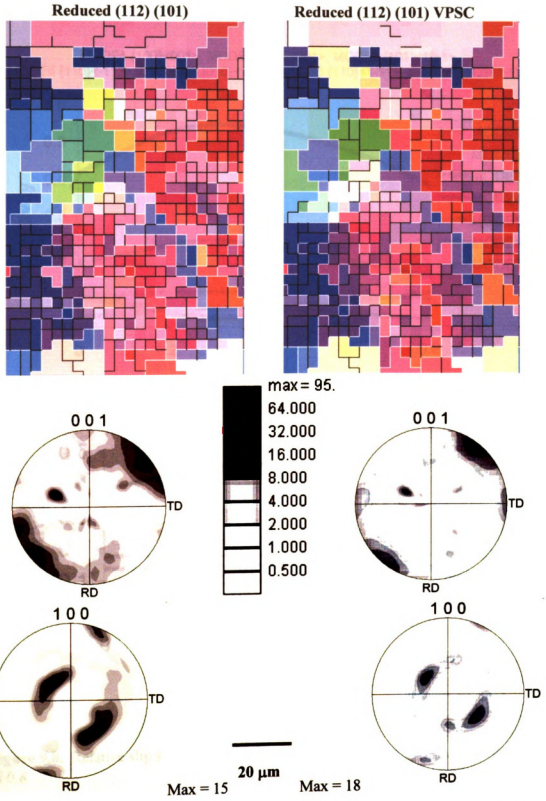

Figure 9.7. OIM and pole figures before and after 0.8 shear strain (a) (112) and (101) reduced and (b) (112) and (101) reduced using VPSC model.

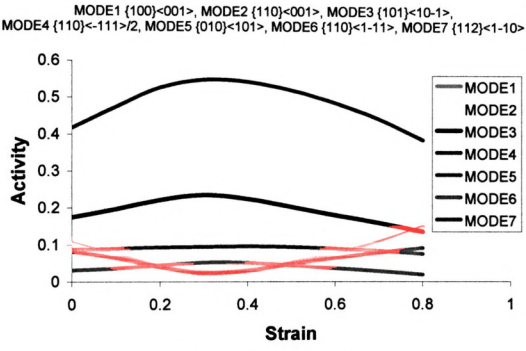

Figure 9.8. Relative slip system activity for various simulations shown above for strain of 0.8.

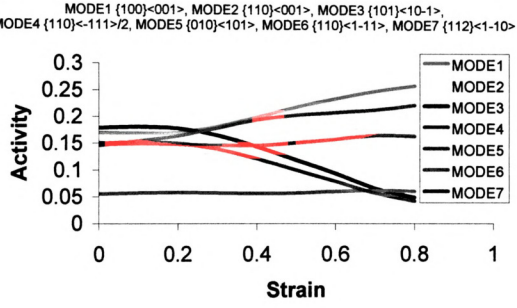

0.8 strain (112) and (101) reduced

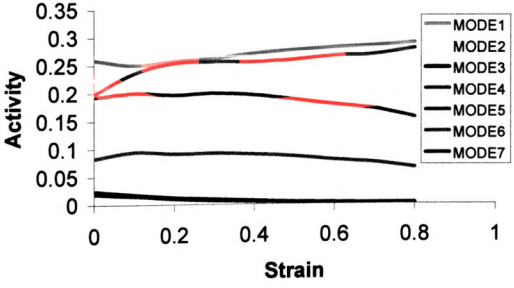

0.8 strain (112) and (101) reduced

Figure 9.8 continued. Relative slip system activity for various simulations shown above for strain of 0.8.

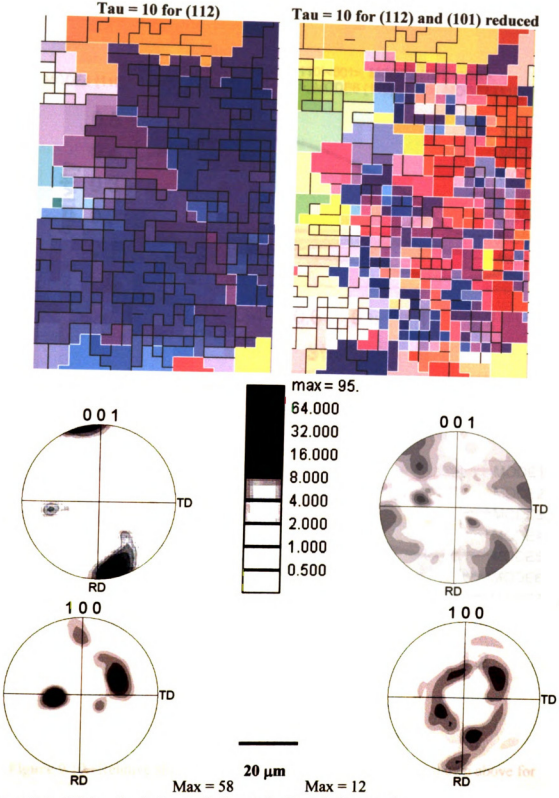

Figure 9.9. OIM and pole figures before and after 1.3 shear strain.

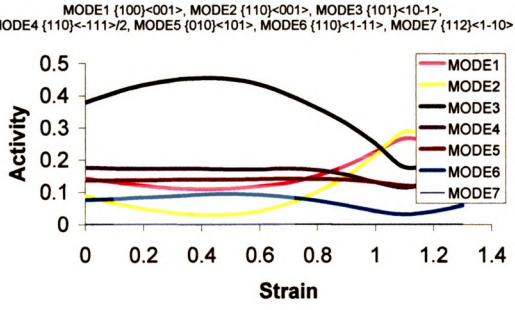

1.3 strain (112) reduced

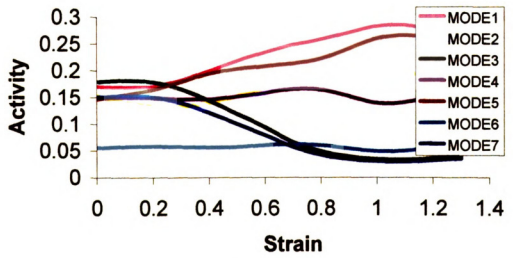

1.3 strain (112) and (101) reduced

Figure 9.10. Relative slip system activity for various simulations shown above for strain of 1.3.

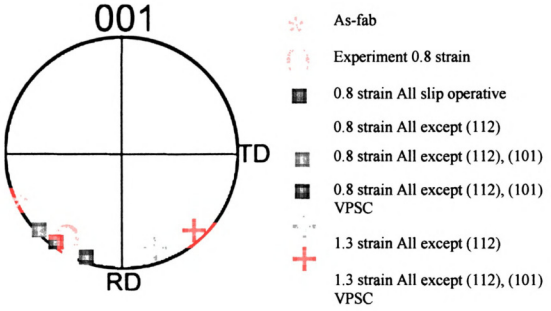

Figure 9.11. Overlay of the (001) poles to compare rotations to the experimental results. All simulations with either one or two slip systems reduced had increased critical resolved shear stress by a factor of 10 (τ = 10). The VPSC simulations with 0.8 strain and (112) and (101) slip systems inactive are closest to the experimental observations.

9.4 DISCUSSION:

The simulations match actual grain rotations and capture plastic deformation. Figure 9.8 shows the activity of different slip systems indicating that several slip systems are necessary to accommodate grain rotations, however modes 1,2 and 4 are most responsible for accommodation of the deformation implying that ({100}<001>, {110}<001>, {110}<-111>/2) are important for deformation systems in tin. This implies that in solder interconnects the grains deform to accommodate the strain with large number of dislocations being pumped into the matrix with fast straining.

These dislocations are probably absorbed and re-ordered into low angle grain boundaries due to the high stacking fault energy of tin, and are converted to higher angle grain boundaries such that the new grains that develop can cause sliding. Once boundaries are able to slide, then rotations due to slip are less likely to continue to develop to accommodate the deformation. Large number of low angle grain boundaries are formed Figure 9.12 which supports studies done by Rhee [2]. The VPSC model works better, which allows good compatibility between different grains that are formed during straining to accommodate deformation. These dislocations also account for the grain boundary sliding and pop-up seen in high temperature high strain rate deformation. Hence it is possible to simulate fast strain rate shear testing only, until boundaries become able to slide sufficiently to make slip based rotations unnecessary. Creep or recovery / diffusion based effects cannot be simulated at present.

Since damage is highly correlated to operation of particular slip systems, processing strategies that generate preferred orientation of solder crystals to minimize

operation of these slip system may forestall damage nucleation, and hence lead to substantially improved reliability of a solder joint [3].

9.5 CONCLUSIONS:

1. Knowing the crystal orientation allows slip activity of the tin in solder joints to be investigated with computational models.
2. A rate sensitive Taylor model can simulate the magnitude of rotations about a {110} crystal axis, but there is no good agreement between simulations and experiment about *which* {110} axis the rotations occurred in the creep specimen investigated.
3. However, the computed rotations for the high strain rate specimen were in agreement with the experiment with modes 1,2, and 4 i.e. slip systems {100}<001>, {110}<001>, and {110}<-111>/2 respectively being the most operative during high strain rate room temperature deformation, until grain boundary sliding effects contribute more to the total strain the slip.

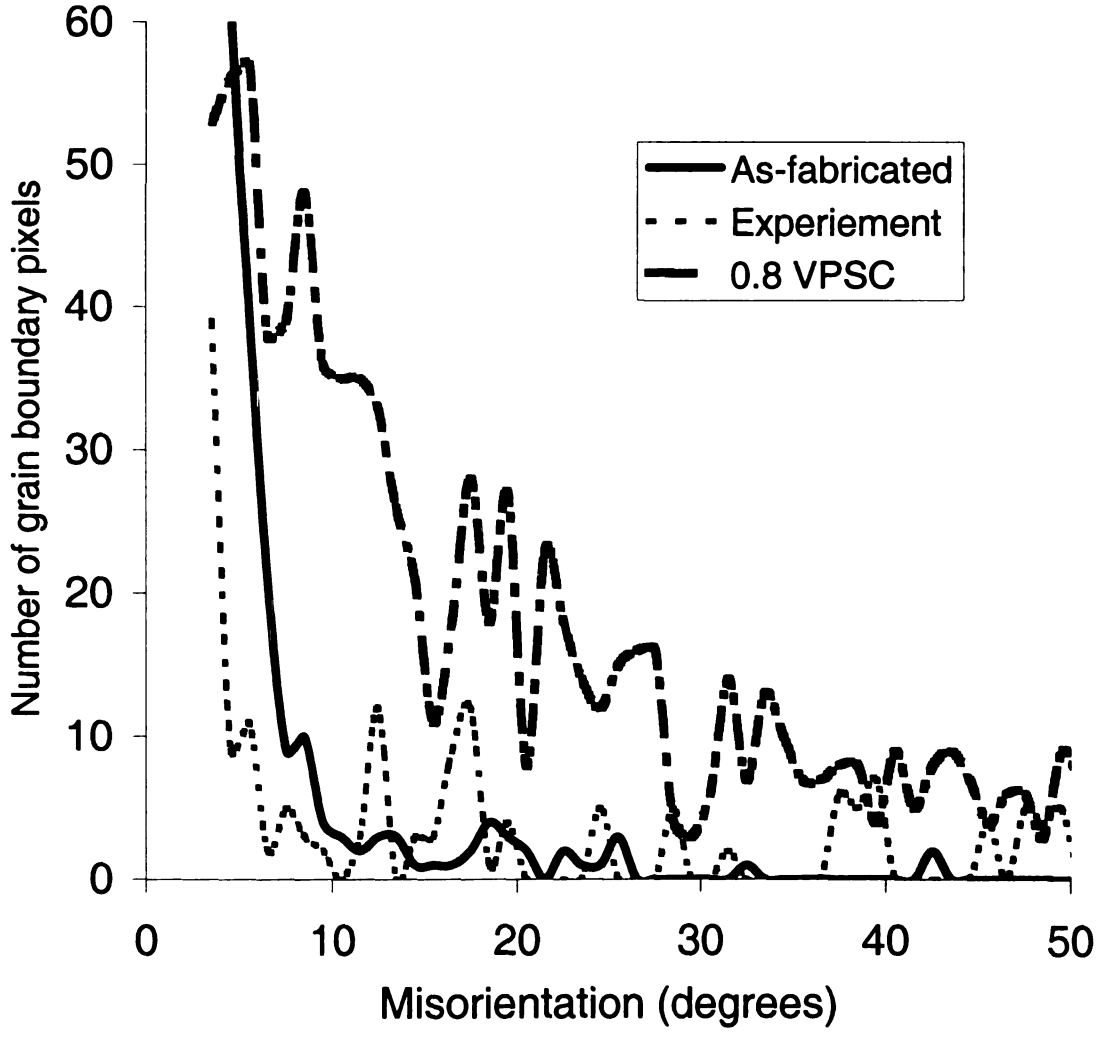

Figure. 9.12. Misorientation histogram showing the differences between as-fabricated, experimental and VPSC simulations after 0.8 strain with two slip systems having minimum activity.

9.6 REFERENCES:

1. A.U.Telang, T.R.Bieler, D.E.Mason, and K.N.Subramanian, J. Electron Mater., 2003. **32**(12): p. 1455-1462.

2. H.Rhee, Doctoral Dissertation, Chemical Eng and Materials Science, Michigan State Universtiy, East Lansing, 2004.

3. A.U.Telang, T.R.Bieler, M.A.Crimp, and K.N.Subramanian, Material Science and Engineering A, 2004. **in review**.

CHAPTER 10

DISCUSSION

10.1 DISCUSSION:

Solder joints are single or multicrystalline with a large number of CSL boundaries of secondary/minority orientations. Crystal orientation and grain boundary character affects properties and plays a major role in the final failure in these joints. Dislocation generation and annihilation is important, so understanding dislocation interaction with boundaries during deformation at rates and temperatures relevant to TMF is important. Table XXIII lists the most notable changes in the boundary character and the most important characteristics observed from each deformation process. Cumulatively, this enables us to identify the most important deformation mechanisms that occur in lead-free solder materials of interconnects. The following sections answer some of the general questions which have bearing on this study and which could be answered only after the completion of this work. Future recommendations and suggested experiments, which can be carried out to further research in this area, are highlighted and discussed at the end of this chapter.

Scope and Breadth of the Study:

This study has quantitatively assessed several important microstructural parameters needed to understand the deformation mechanisms of Sn-3.5Ag solder joints. However, deformation occurring during TMF is complicated and careful analysis is needed to more thoroughly understand contributions of different mechanisms. This dissertation has sought to identify subtle operative deformation mechanisms during different TMF processes. Since no prior studies had been performed using this approach (textural texture and microstructure approach) and limited knowledge base existed when

this study was undertaken, a survey of several related processes was undertaken in order to be able to identify common phenomena of deformation in pure tin that occured in different deformation conditions. This study aimed to provide an improved understanding of how solder materials respond to stress and expands our comprehension of the various deformation mechanisms in solder joints.

Characteristics of Joints:

Surface damage that accumulates is not fully representative of bulk. To carry out bulk studies, 3-D techniques utilizing 3-D texture analysis methods is desirable, and is only now becoming possible. Through thickness synchrotron radiation is possible, and has recently been done [1], but this does not provide misorientation relationships between adjacent crystal orientations. OIM provides spatially resolved orientation information in a convenient measurement setting. Data obtained is reliable and is justified on the following arguments:

1. Specimens were prepared in a consistent manner, but crystal orientations obtained were vastly different. This gives credence that the surface preparation had an insignificant effect on the overall crystal orientations. Polishing pure tin is difficult. However pure tin also showed crystals having the same orientation after re-polishing the same area.

2. Several joints showed dominant and secondary peaks from OIM demonstrating that these peaks are actually real and not artifacts. The orientation strength of the most dominant peak indicates that the joint material is a near-single crystal wherein the

secondary peak might be very small and barely measurable. If surface preparation caused characteristic damage, then such orientation strength distinction would not be observed.

3. Movies of solidification of solder balls [2, 3] reveal that they solidify at different times with substantial undercooling, and probably faster than the eye can see, implying rapid solidification and large amounts of undercooling needed for the solidification to occur.

4. The second strongest peaks are always twin related. This implies presence of solidification twins that are the secondary orientations, which are reasonable with high solidification rates.

5. Solidification area in the joint is 2 mm^2, which is rather small in comparison to large ingots that have many fine grains along the mold wall (chill zone). Solder joints do not have a chilled substrate during cooling so it is more of an isothermal process and hence there is much less of a driving force for nucleation. Single crystals are routinely grown in slow cooling conditions, e.g. super-alloy turbine blades.

6. Specimens also prepared by other researchers have shown the similar texture characteristics as those prepared by this author (see chapter 3 on bulk solders; see *Appendix 5* for statistics on OIM measurements of single shear lap specimens prepared by another researcher).

7. Most of the surface scans done as a function of time on the same region show that minority orientations present in the as-fabricated case disappear under the influence of time, temperature, and deformation. A different type of a noise develops with time that could be ascribed to oxidation. One should also bear in mind that surface roughness due to deformation degrades pattern indexing.

8. A light re-polish reveals the same dominant crystal orientation, but no minority orientations (polished 1000 TMF cycled SSL specimen Figure 7.2-7.4) with substantially improved pattern indexing. This indicates that light polishing removes the surface debris and does not introduce new crystal orientations, which further implies that the small freckled orientations in as-solidified joints are not artifacts of polishing.

Implications on Research in This Area and Joint Reliability:

Given that the OIM measurements are reliable, and can be interpreted with confidence, this study shows that the crystal orientation and misorientations have a large influence on the joint properties. This study is the first of its kind, which shows that crystal orientation in the joint affects deformation properties. It leads to practical recommendations concerning lead free solders wherein texture in the solders needs to be further understood as a parameter having great implications on reliability as discussed below. On a broader perspective, this study raises the level of identification and understanding of failure mechanisms active in these solders.

Low Angle Grain Boundary Changes:

On average, there is about 0.12 μm of low angle grain boundaries length per square μm in as-fabricated specimens. The low angle boundary length decreased with deformation in creep and single shear lap TMF, but the length increased in 100 hr aging in the dual shear and component TMF specimens. Figure 10.1 shows the changes in the length of boundaries in different processes. Low angle boundary length decreased in damaged specimens and increased in undamaged specimens, in several types of

deformation history. Sliding was often correlated with low angle boundaries in specimens that showed a decrease in low angle boundary length, suggests that the condensation, which correlates well with the low angle boundary fraction. The low angle grain boundary fraction decreases after all deformation processes, which also indicates that damage is correlated with the condensation of low angle grain boundaries in polygonized sub-grains that often slide. Most of the low angle boundaries that slid were on planes related to 110 tilt boundaries.

High angle, twin, and CSL Boundaries:

Sliding was observed on special boundaries in all creep and TMF specimens. One also sees a decrease in the number of random, CSL, and twin boundaries with time temperature, and/or strain in nearly every joint (with one exception, the right joint of the component specimen showed about a 30% increase in twins). The fraction of CSL boundaries also decreases with different processes.

Room temperature creep showed cracks due to higher strain during creep as compared to TMF testing. The only cracks observed were at 60° twin boundaries in the room temperature creep specimens due to their coherent nature that does not permit easy dislocation absorption into the boundary, due to the low temperature/low diffusivity conditions (see Refs. [4-8] for further discussion of this issue). Sliding along special boundaries, especially the 22.5 and 38° boundaries were seen in high temperature creep and TMF specimens. This type of sliding permits extensive strains to be accommodated without bulk deformation, and possibly delaying failure. The lower activation energy for migration of the CSL boundaries may permit migration that facilitates sliding with

minimal cavitation. No cracking was seen during TMF testing, only grain boundary sliding along both low angle and CSL boundaries was observed.

Table XXIII. Mechanisms And Important Features Seen In Different Processes.

Type of Experiment	Boundary Type		Deformation / Surface Features			Other Features
	Low Angle	Σ Bdy	Ledges	HAGB Crack	LAGB features	
As-fabricated	15% present.	14% specific CSLs at 22.5, 28, 43, 70° and 12% of 60° boundaries.	None present. Surface is polished flat.	None present	-	Solidification texture follows [110] crystal direction parallel to heat flow. Texture is dependent on the initial nuclei that form and grow. Entire joint made of either only 1 crystal orientation separated by low angle GB or 2/3 large crystals with specific CSL type misorientation between them usually 60° solidification twins. No control over the spread of Ag_3Sn particles. Microstructure very heterogeneous; Sn cells, Ag_3Sn poarticles + plates, Cu_6Sn_5 particles in matrix.
Aging – Bulk for 200hrs at 150°C	LAGB # decreases on aging, 4% present after aging.	Special GBs formed on aging, 20% are CSLs.	Sliding seen along many CSLs boundaries.	Lesser fraction of random HAGB	Did not show sliding along LAGB	Surface topography formed on heating/cooling corresponding to the grain structure due to CTE differences. Nano-indentation studies corroborated these findings.
Aging – Joint 100hrs at 85° + 1 year at RT	28% LAGB formed due to dislocation polygonization . No major migration evident.	30% CSL boundaries present.	No GB sliding or ledge formation	No cracks observed	None	Microstructure is cleaner. Coarsening of Ag_3Sn particles, which could reduce effectiveness of Ag_3Sn as obstacles to dislocation motion. Growth of both Ag_3Sn and Cu_6Sn_5. Volume changes of these particles cause misfit dislocations to be pumped into the system.
RT Creep	4% present.	9% CSL boundaries observed.	Ledges at 28° boundaries.	Cracks along 60° twins.	Slip lines present in sub-grains.	Dislocation substructure is important part of the failure in these solders. Room temperature creep has enough dislocations, which are not recovered. Pile-up can occur both at interface between Sn-Cu as well as along GBs. CSL bdys are better in creep resistance and will improve overall performance / life of the joint. Slip bands seen in center of the joint in the tin matrix.
85° Creep	4% LAGB, polygonization with HT creep.	6% CSL boundaries observed. 22.5 and 38° amongst	Sliding along special bdy, both 22.5 and 38°.	Crack at 22.5° developed initially however sliding prevented cavitation.	No sliding along LAGB since higher angle grain boundaries sliding prior.	No changes in the overall microstructure except bdy sliding and polygonization. Dislocations are necessary to accommodate the sliding. The sliding process itself provides dislocations, and hence the majority of the grain interior might not

		boundaries observed.				play a role in the deformation process (see Mykura's reference). The GB can act as source and sink for dislocations along with the sub-structure presence at CSL bdys slightly off the exact coincident site.
SSL TMF	8% of LAGB present after 1000 TMF cycles.	12% CSL boundaries present.	Ledges along LAGB after 1000 TMF cycles.	None	Polygonization of dislocations into LAGB causes sliding during cycling.	Near single crystal observed after 1000TMF cycles. Microtexture clears up initially during cycling. Low angle grain boundaries and dislocation dynamics play a vital role in formations of sub-grain boundaries, which slide and causes grain boundary decohesion. Dislocations accumulate. Can move more freely due to Ag_3Sn coarsening, and get piled-up at the interface between Sn-Cu followed by polygonization into low energy sub-boundaries. When they reach the correct slidable misorientation, they start forming ledges. Ledge formation could be due to both CTE and thermal contraction as well as from externally induced shear stresses.
DS TMF	LAGB fraction increases to 22%, as dislocations get polygonized into low angle sub grain tilt boundaries.	7% CSL present especially near 22.5°, the fraction does not change after deformation.	Ledges form along LA subgrain boundaries.	No HAGB cracks seen. Sliding and ledge development along 22.5° boundary.	Ledges along LAGB with 7 and 12° misorientations (lower side of exact CSLs).	Single crystal is broken down into subgrains which having sliding boundaries. Polygonization of dislocations into sub boundaries is responsible for breakdown of microstructure.
Component TMF	18% present after TMF.	16% CSL boundaries.	Ledge along 22.5° boundary.	No cracks seen, GB sliding at 22.5° bdy.	LAGB become distinct after 1000 cycles.	One joint shows grain growth and microstructure cleans-up. Other joint shows ledges that are formed along the CSL boundary.
High Strain Rate	Single crystal initial microstructure with no distinct LAGB.	None present in area scanned.	Ledges, shear bands present at HAGBs, that developed due to high strain rate testing.	No crack seen.	LAGB formed between high angle shear bands. Dislocations formed and absorbed into higher angle boundaries to form boundaries with higher misorientations.	Grain boundary sliding and pop-up seen along the low angle grain boundaries present between the high angle grain boundaries (shear bands). No recrystallization after high strain rate testing.
VPSC Simulations	No distinct LAGB present.	Not present	None	HAGB formed after simulation around certain grains.	LAGB are also seen formed due to crystal rotations.	LAGBs formed which make up the substructure responsible for grain pop-up.

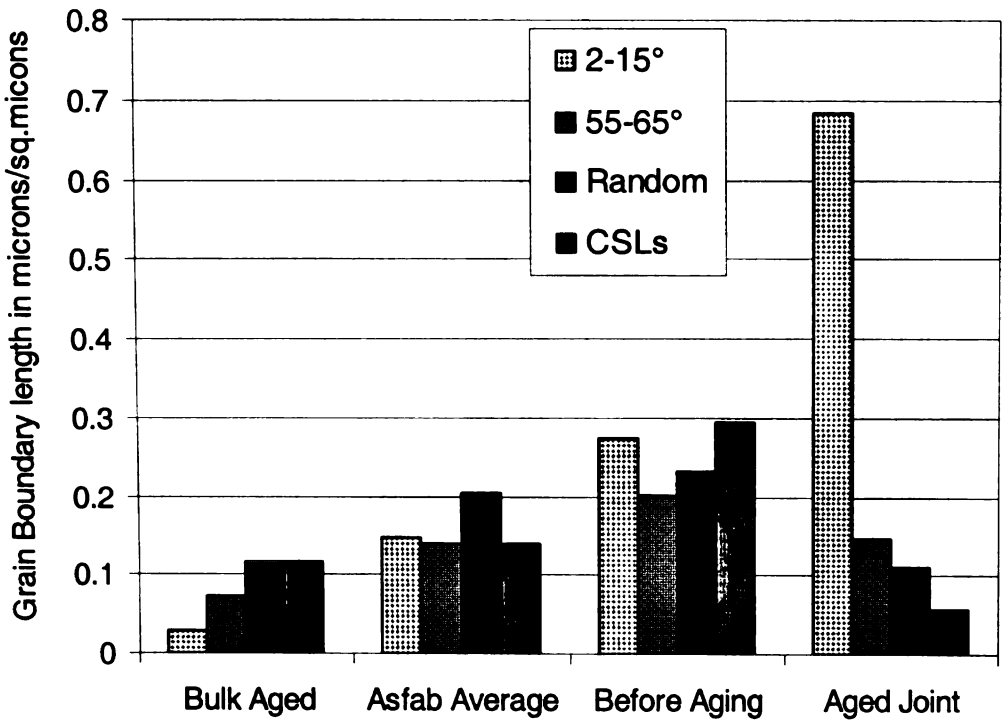

Figure 10.1. Fraction of grain boundaries in different processes.

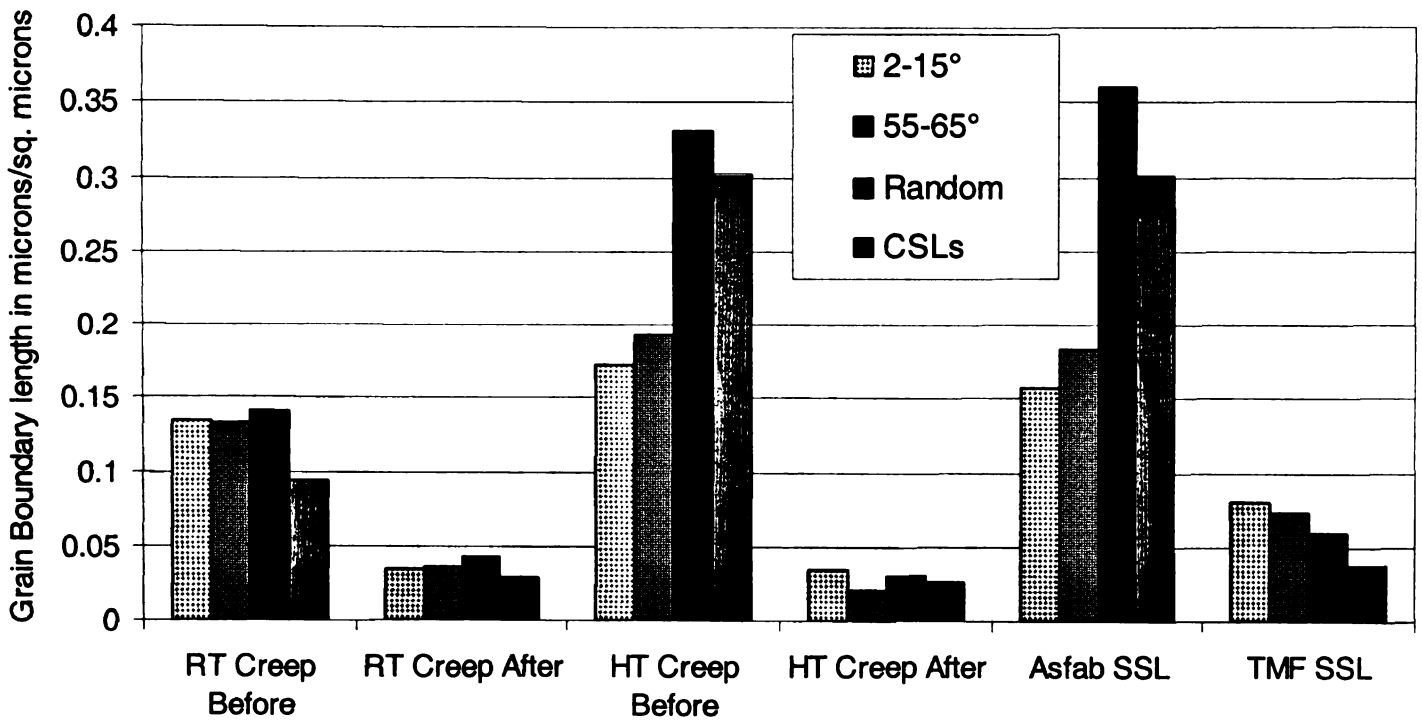

Figure 10.1 continued. Fraction of grain boundaries in different processes.

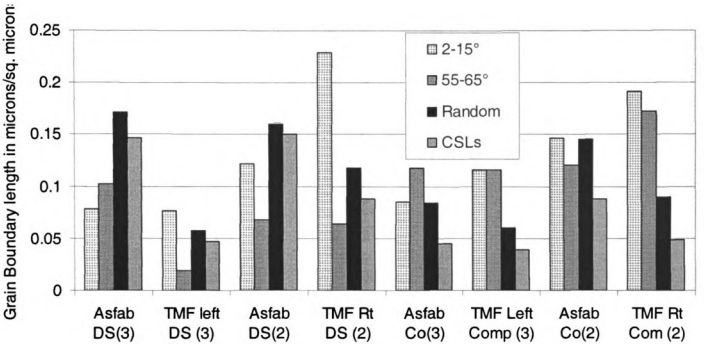

Figure 10.1 continued. Fraction of grain boundaries in different processes.

Further Theoretical & Experimental Investigations:

1. Dislocation dynamics seem to play a very important role in the response of these joints (a fact that is not well elucidated in literature). Future work should focus on characterizing such dynamics both, experimentally and theoretically. Dislocation interaction with grain boundaries, dislocation climb, special dislocations and polygonization are important processes to study in these solders.
2. With the current OIM measurements modeling of grain boundary sliding can be carried out using the CSL theory, polyhedral repeating units can also be used to represent the grain boundary structure, and sliding can be considered geometrically with respect to the polyhedral structure. It might be possible to assign a CRSS to grain boundary glide and resolve the shear in grain boundary. Further, the relationship between special grain boundaries and extrinsic dislocation configurations could be studied to determine how misfit dislocations can be formed from extrinsic lattice dislocations.
3. Experimental and theoretical characterization of mechanisms for grain boundaries that slide / fracture. A Focused Ion Beam (FIB) could be used to extract a small section of the grain boundary that slides and analyzed for their boundary structure in TEM. We know that the sliding boundaries are CSL type however it would be nice to ascertain the dislocation substructure present in these boundaries, which will elucidate the sliding mechanism.
4. Modeling of creep inside the VPSC code. Hardening and creep modeling is possible within the code, if a dislocation climb mechanism can be modeled. Dislocation climb could be implemented in the model, which could account for the recovery as

well as polygonization. Interaction between glide and climb would also need to be taken into account. The code has means to incorporate these features, by writing FORTRAN subroutines and making minor modifications. This could be done in collaboration with Dr.C.N.Tome at LANL.

5. Thermal and elastic anisotropy of Sn merits making an Elasto-Plastic self consistent calculation of thermally induced stress in grains. Neutron diffraction using the LANSE source at LANL would be a possible way to obtain stress states in the actual joint with cycling as well as in the as-fabricated condition.
6. It is important to determine if failure (crack propagation) starts at the free surface (ledge) and propagate inwards? Or does it always start inside and move to the surface? This could be done using 3-D computed tomographic techniques. However most fatigue failure starts at the surface and it is likely that results would point in this direction.
7. Thickness effect on the joint properties is an important consideration. It is important to understand changing the thickness of the joint affects the dislocation dynamics and dislocation mechanisms that operate.
8. A practical question is whether it is possible to control the texture and optimize it for avoiding fracture? Depending on the joint design, it would be necessary to find out what would be the ideal texture or grain configurations that would minimize the deformation, or conversely, maximize deformation but minimize heterogeneous flow. This could be done using a finite element analysis to determine its orientation using an optimization code. Given that grain boundaries slide, perhaps a single crystal would be more desirable than a multi-crystal; however the dislocation

substructure and their generation and movement needs to be controlled in the single crystal. On the other hand, dislocations need to be managed so that they will not become polygonized into sub-boundaries that can eventually slide in an undesirable manner. Conversely, effective stable strengthening phases can be introduced to make grain boundary sliding difficult, such as the Sn-Cu-Ni ternary intermetallics that have been identified by J.G. Lee [9] as beneficial.

9. It is desirable to understand the effect of texture in the joint on the shear strength of the joint. Joints can be fabricated and orientation determined after which it could be sheared to failure to determine the effect of orientation on the peak strength of these joints.

10. Effect of the copper substrate orientation on the texture in the joint is another subject of potential research. Rolled OHFC copper was used. However the texture in the $1mm^2$ surface area on which the joint is fabricated needs to be known to understand its effects on texture. Joints can be made with substrates having different copper texture to understand its implications on the solidification texture.

11. It would be possible to do nano-indentation traverses along a joint to determine if there are multiple deformation responses that depend on crystal orientations, and to correlate these property variations with measured crystal orientations.

12. This study has laid the basis for more focused research that could be done with respect to identifying statistically the boundary types that fail in different processes. For this, joints can be fabricated and put through some deformation process, for instance creep, before characterizing the texture. After creep the boundaries, which fail, can be checked in the OIM. Though this work indicates that these will

probably be special boundaries, it would help to know the probability of the type of boundaries that show damage more so than others.

13. All the work is done here looks at the texture and morphology of the free surface especially in the matrix of the joint. What happens at the interface between the solder and the copper substrate is also important. Focused deformation studies in tin near the interface are needed to identify how the tin deforms near the intermetallic interface.

10.2 REFERENCES:

1. J.G.Lee, K.N.Subramanian, and A.Lee, Private Communication, 2004.

2. K.S.Kim, K.Suganuma, J.M.Kim, and C.W.Hwang, JOM, 2004. **56**(6): p. 39-43.

3. K.Suganuma, K.S.Kim, and C.W.Hwang. *Solidification Phenomena in CSP Soldering with Sn-Ag-Cu Lead-Free Solder Alloy Using In Situ Observation System with COmputer Simulation.* in *TMS Annual Meeting Spring 2004*. 2004. Charlotte, NC.

4. G.S.Was, V.Thaveeprungsriporn, and D.C.Crawford, Jom-Journal of the Minerals Metals & Materials Society, 1998. **50**(2): p. 44-49.

5. T.Watanabe, Metall. Trans. A, 1983. **14A**: p. 531–545.

6. T.Watanabe, S.I.Kimura, and S.Karashima, Philosophical Magazine a-Physics of Condensed Matter Structure Defects and Mechanical Properties, 1984. **49**(6): p. 845-864.

7. L.C.Lim, and R.Raj, Acta Metall., 1984. **32**: p. 1183-1190.

8. L.C.Lim, and R.J.Raj, J. de Phys.supplement no. 4, 1985. **46**: p. c4-581–c4-595.

9. J.G.Lee, Doctoral Dissertation, Chemical Engineering and Materials Science, Michigan State University, East Lansing, 2004.

APPENDIX

Appendix 1

Procedure To Convert An 'hkl' Data Set As Obtained From An EBSP To A 'TSL' Data Set Which Can Be Read By The TexSEM Software.

Procedure:

1. Using the hkl software version 4 on the CamScan PC open the acquired data (*.prj) file. You will be prompted to convert the file to a *.cpr file. Click YES. Now you will have the file loaded as a working dataset.
2. Click on FILE (in the main menu) → EXPORT → CONVERT TO *.CTF. This will convert your file to the ctf (channel text format). Save the file with the desired filename.
3. Take the file to another computer for faster conversion. This can be done using a zip drive or by transferring the file to your M: drive using the *wsftp* software.
4. Open the *.ctf file with Microsoft Excel. Copy the data set excluding the headers. Only the actual data needs to be copied.
5. Paste this data into the 'hkl' spread sheet of the hkl2TSLdeg file. (This file can be obtained from Adwait or Dr.Bieler). Scroll down and find the last row to which the data extends. Remember this no.
6. Now in the same hkl2TSLdeg file move to the sheet named ext100180d2. Using the second row fill the cells till all the cells upto the above row number are filled. Now click FILE → SAVE AS → give name and save as a FORMATTED TEXT SPACE DELIMITED (prn) file.
7. Open this file using Microsoft Word.

8. Open ang.doc file for your specific crystal (This file can be obtained from Adwait or Dr.Bieler). Copy the contents from this file and paste in place of the first line of the *.prn file.
9. Click FILE → SAVE AS → save as *.ang file (to do this give file name and use 'ang' as your extension. You might have to use ' " ' before and after the name to do this.
10. This *.ang file can now be opened with your TSL TexSEM software.

Happy Analyzing ☺☺☺

Appendix 2

Rotations Given To As Received hkl Dataset To Attain Same Lattice Orientation In The TSL TexSem Software As Observed In The hkl Software August 5, 2003.

The data collected using the hkl channel acquisition software is analyzed using the hkl analysis software as a first insight of the recently collected data. The orientation of the lattice with respect to the hkl coordinate system (x-horizontal with respect to the page, y-vertical, z coming out of the page) is observed and documented for a particular set of Euler angles. The data is then transferred to the TSL TexSEM software and viewed in the TexSEM software as an Inverse pole figure OIM map. What one observes when looking at the lattice for the same set of Euler angles in the TexSEM software is that the unit cell is rotated by –90° about the z axis (to visualize this rotate the lattice by –90° about the z axis as shown In Figure 1). This is easily understood by knowing the fact that using the right hand coordinate system, in the TSL software the coordinate system is defined such that the x-axis points vertically downwards and the y-axis is aligned in the horizontal direction. Hence to achieve the same lattice orientation as that seen in the hkl software i.e. with respect to the hkl coordinate system (this coordinate system is consistent with the chamber ordinate system and would help in determining the sample alignment in the microscope chamber and further analysis thereon), one would have to rotate the TSL coordinate system by +90° about the normal direction (z-direction) to take into account –90° rotation brought into effect by the inherent differences between the two coordinate systems.

Further understanding why a +90° rotation about the normal direction is desired is exemplified by the following 4 Figures, which show the rotations of the lattice taken from the same position using the two different softwares. The first two figures shows (1)

the lattice as it appears in the hkl software, (2) the lattice as it appears in the TSL software using a (001) inverse pole figure, (3) the lattice after rotating the TSL coordinate system by +90° about the normal direction (notice the first Euler angle shows an addition of 90) and (4) the lattice after rotating the as is (as obtained dataset) TSL coordinate system in (2) by -90° about the normal direction (notice the first Euler angle shows a subtraction of 90 from the hkl Euler angles or the as is TSL Euler angles). Having seen the first two figures, the last two Figures show only (1), (3) and (4) discussed above for further clarity.

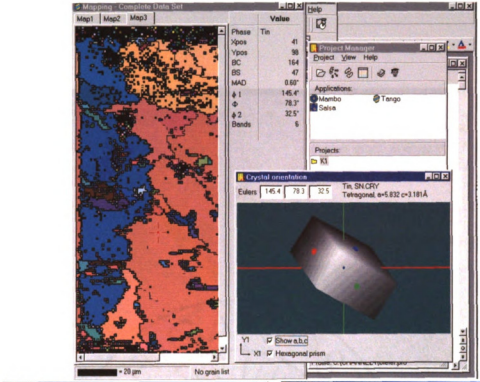
Mapping - Complete Data Set
Map1
Map2
Map3
Value
Phase Tin
Xpos 41
Ypos 98
BC 164
BS 47
MAD 0.60°
ϕ 1 145.4°
Φ 78.3°
ϕ 2 32.5°
Bands 6
Project Manager
Project View Help
Applications:
Mambo
Tango
Salsa
Projects:
K1
Crystal orientation
Euler 145.4 78.3 32.5
Tin, SN.CRY
Tetragonal, a=5.832 c=3.181Å
Y1
Show a,b,c
X1
Hexagonal prism
= 20 µm
No grain list

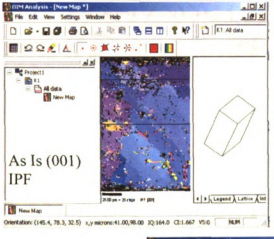
OIM Analysis - [New Map *]
File Edit View Settings Window Help
K1: All data
Project1
K1
All data
New Map
As Is (001)
IPF
New Map
Orientation: (145.4, 78.3, 32.5) x,y microns:41.00,98.00 IQ:164.0 CI:1.667 VS:0 NUM

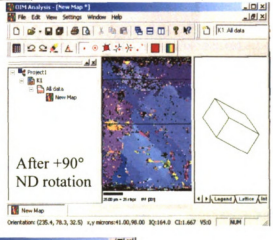
OIM Analysis - [New Map *]
File Edit View Settings Window Help
K1: All data
Project1
K1
All data
New Map
After +90°
ND rotation
New Map
Orientation: (235.4, 78.3, 32.5) x,y microns:41.00,98.00 IQ:164.0 CI:1.667 VS:0 NUM

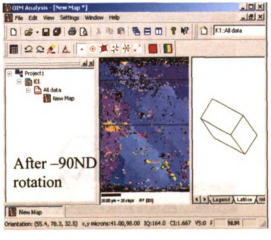
OIM Analysis - [New Map *]
File Edit View Settings Window Help
K1: All data
Project1
K1
All data
New Map
After –90ND
rotation
New Map
Orientation: (55.4, 78.3, 32.5) x,y microns:41.00,98.00 IQ:164.0 CI:1.667 VS:0 NUM

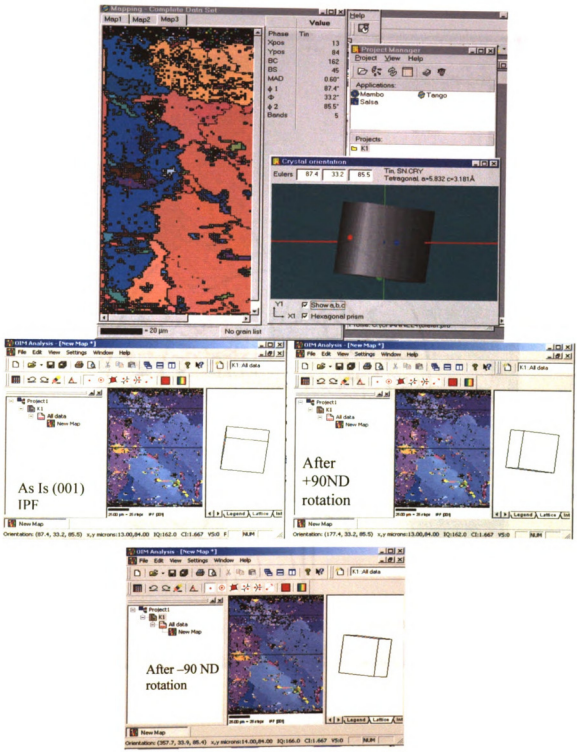
As Is (001)
IPF
After
+90ND
rotation
After –90 ND
rotation

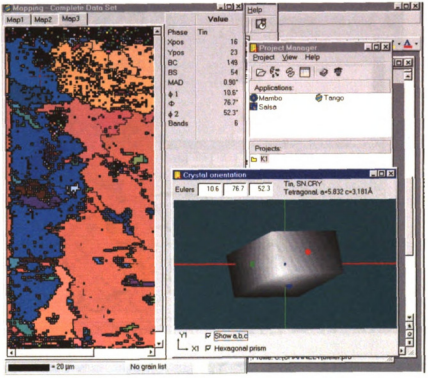
Map1
Map2
Map3
Value
Phase Tin
Xpos 16
Ypos 23
BC 149
BS 54
MAD 0.90°
φ1 10.6°
Φ 76.7°
φ2 52.3°
Bands 6
Help
Project Manager
Project View Help
Applications:
Mambo
Tango
Salsa
Projects:
K1
Crystal orientation
Euler1 10.6
76.7
52.3
Tin, SN.CRY
Tetragonal a=5.832 c=3.181Å
Show a,b,c
Hexagonal prism
= 20 µm
No grain list

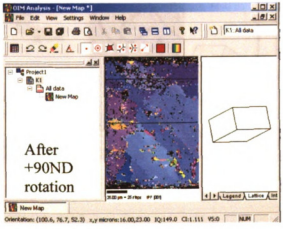
After
+90ND
rotation

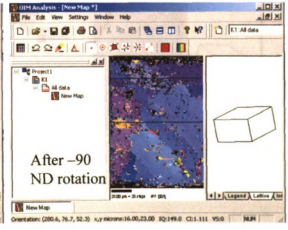
After –90
ND rotation

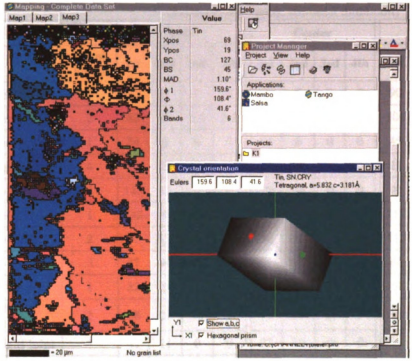
Mapping - Complete Data Set
Map1
Map2
Map3
Value
Phase
Tin
Xpos
69
Ypos
19
BC
127
BS
45
MAD
1.10°
φ1
159.6°
Φ
108.4°
φ2
41.6°
Bands
6
Project Manager
Project View Help
Applications:
Mambo
Tango
Salsa
Projects:
K3
Crystal orientation
Euler
159.6
108.4
41.6
Tin, SN.CRY
Tetragonal, a=5.832 c=3.181Å
Show a,b,c
Hexagonal prism
20 µm
No grain list

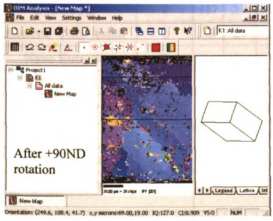
After +90ND
rotation

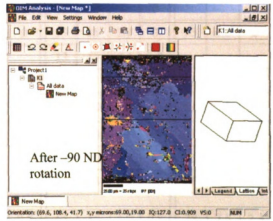
After –90 ND
rotation

Appendix 3

Table XXIV. Statistics Of Texture Intensities On The 19 Scanned Specimens.

	Texture Intensity of Dominant Peaks (1st=most dominant, 4th=least dominant)												
		Left				Center				Right			
	No. of Peaks	1st	2nd	3rd	4th	1st	2nd	3rd	4th	1st	2nd	3rd	4th
Thru thickness Sp A	1	73	0	0	0	125	0	0	0	90	0	0	0
Thru thickness Sp B	2	46	19	2.6	2.2	34	21	0	0	100	2.7	0	0
Thru thickness Sp C	1	74	0	0	0	84	0	0	0	45	0	0	0
Sp AG aging	4	21	15	15	0	22	12	11	6.7	21	12	11	0
Sp P aged+TMF	2	110	15	0	0	79	24	0	0	95	0	0	0
Sp Q aged+TMF	1	142	0	0	0	118	0	0	0	117	0	0	0
Sp R aged+TMF	2	87	6.7	6.2	0	98	0	0	0	112	23	0	0
Sp S aged+TMF	3	52	46	0	0	57	25	14	0	66	21	0	0
Aged 125+1year	1	82	0	0	0	91	0	0	0	131	0	0	0
Component left joint sc 123`2	2	28	27	18	7	39	14	12	5	40	25	19	0
Component right joint	1	41	11	0	0	33	10	0	0				
DS2 Sc 4,5	1	81	3.8	3.1	0	73	5.8	3.5	0				
DS2 Sc 1,2	2	117	2.9	0	0	71	3.2	0	0				
Eutectic TMF Asfab	2	39	21	0	0	69	18	2.4	0	93	4.8	0	0
Nano Eutectic	2					13	10	4.4	2.8				
Crep Sp G	2	66	13	0	0	46	6	0	0	16	15	0	0
Creep Sp F	2 same as ttB	36	34	8.5	4.3	102	7.9	5.2	0	84	5.9	4.3	0
Crep Sp K	2	52	0	0	0	50	40	11	0	38	0	0	0
Sp L RT CRP	2	49	41	0	0	74	2.2	1.9	0	122	2.1	0	0
Sp M HT Crp	2	35	32	2.1	1.7	53	15	4.6	1.8	85	8.2	2.6	0
Average		67	11	3.5	0.8	65	15	2.9	0.8	78	7.5	2.3	0
Std Deviation		31	11	4.7	1.9	32	15	5.4	1.9	36	8.9	5.3	0
Average All Data		**70**	**11**	**2.9**	**0.5**								
Average Std Dev		**33**	**12**	**5.1**	**1.3**								
Log (avg)		1.8	1	0.5	-0.3								

Appendix 4

Coincident Site Lattice (CSL) About Different Axes.

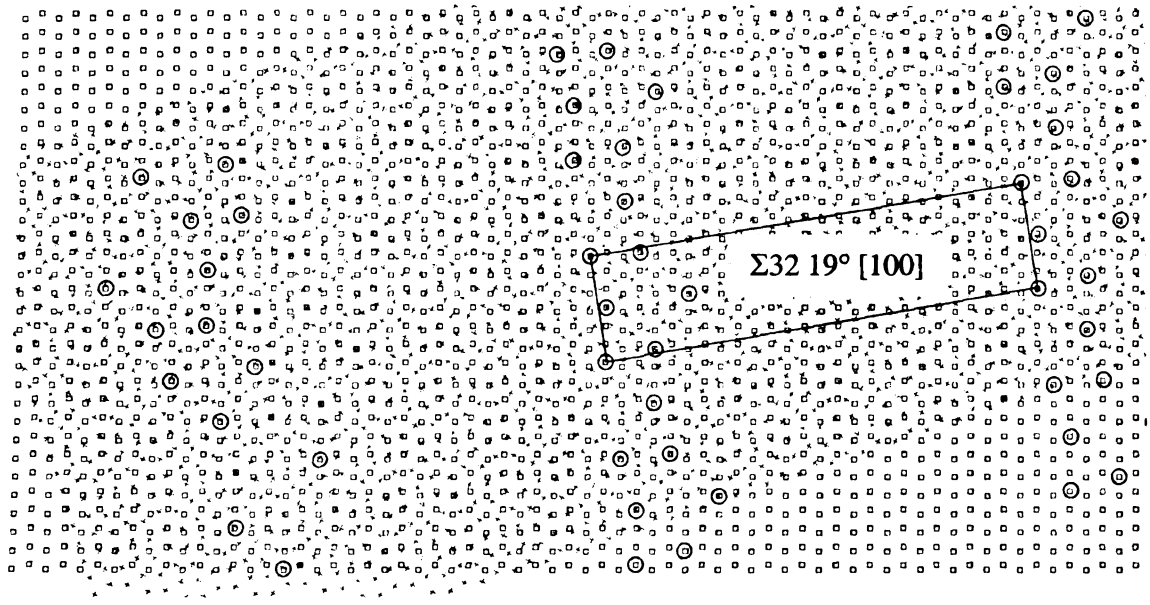

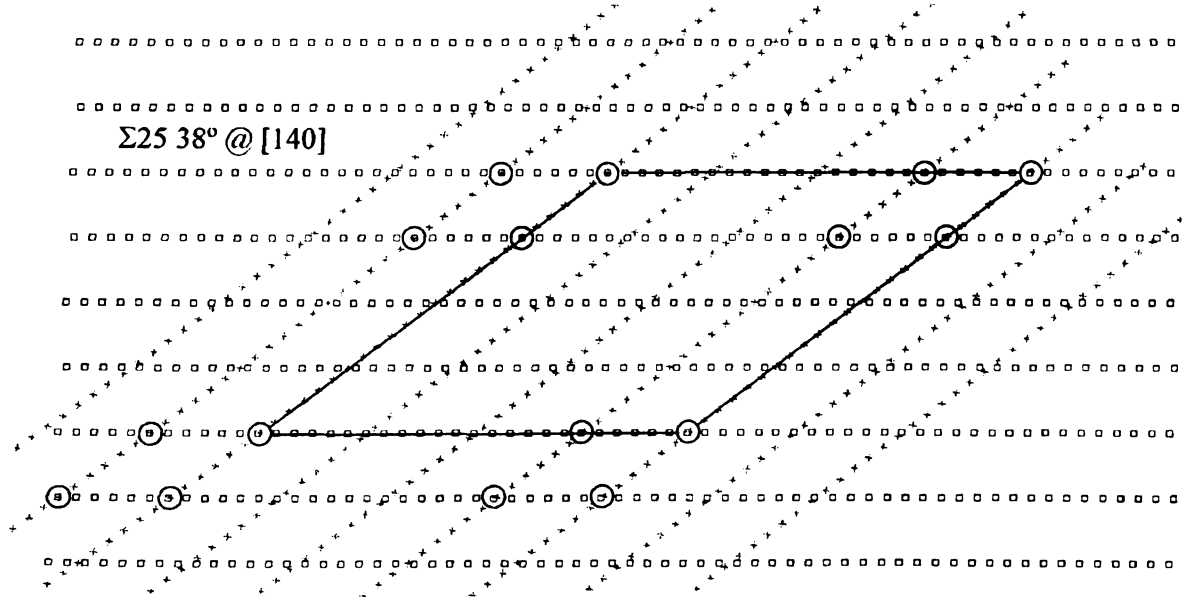

(1 0 –10) Σ8 20.3 @[301]

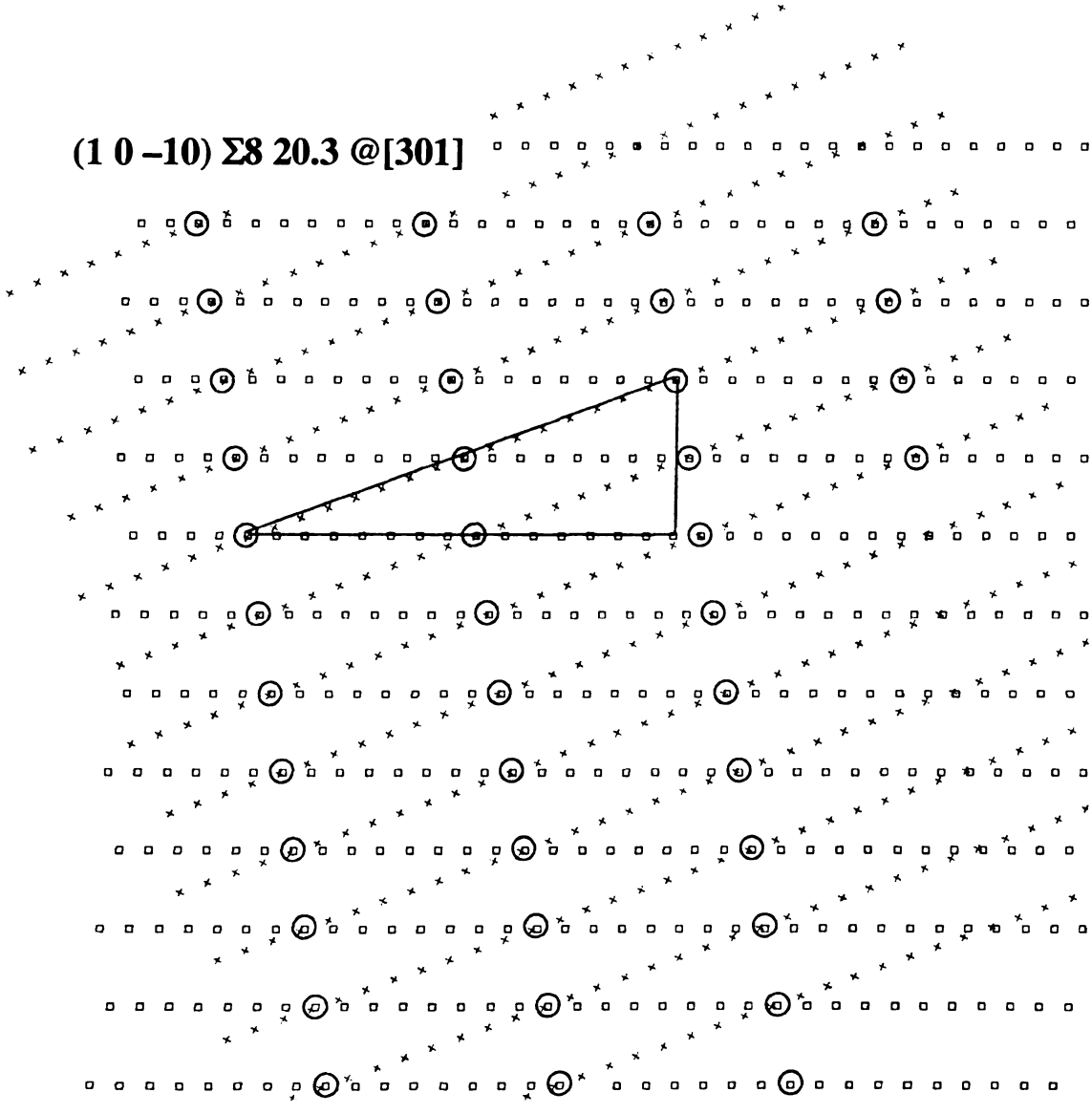

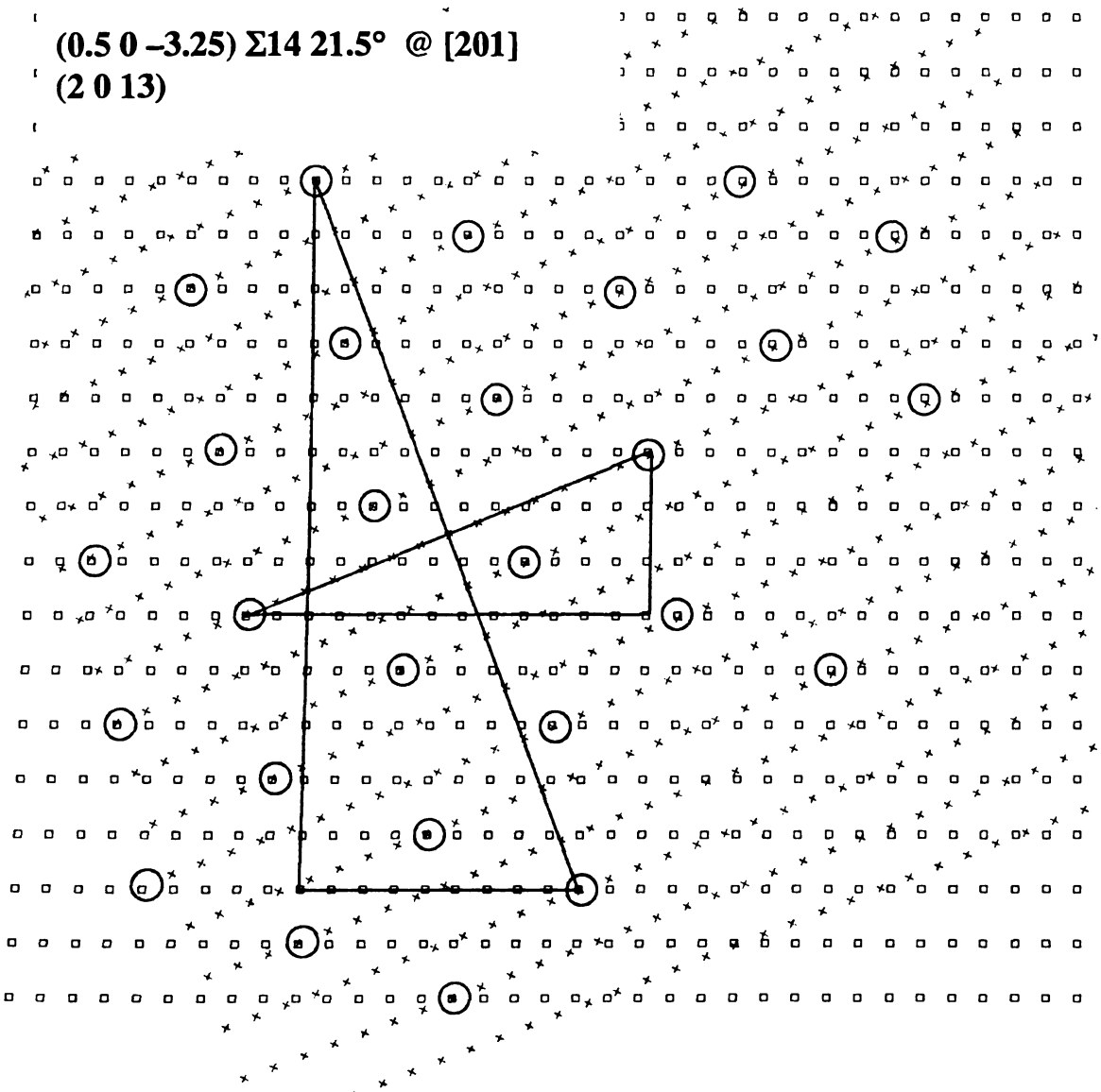
(0.5 0 –3.25) Σ14 21.5° @ [201]
(2 0 13)

(1 0 –6.25) Σ28 21.35° @ [401]

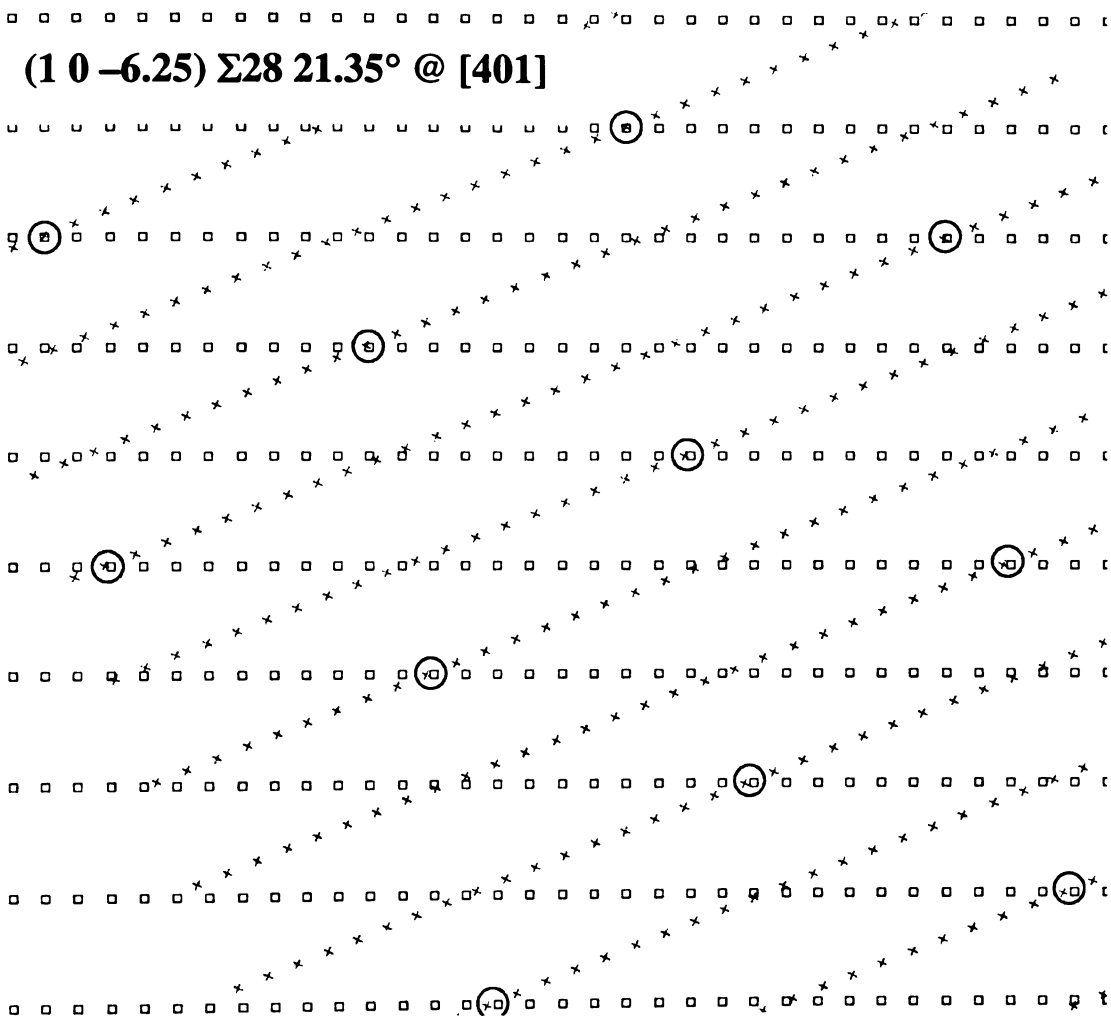

Appendix 5

OIM Maps For Joints Made By Other Researchers

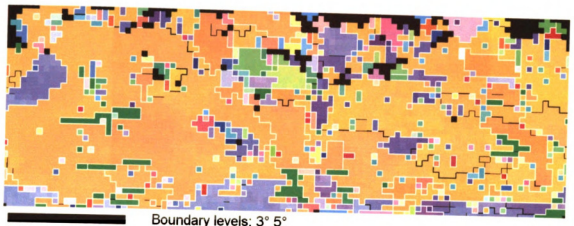

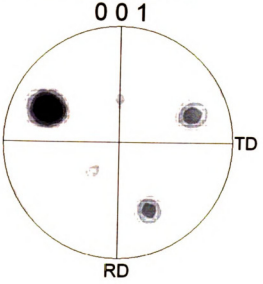

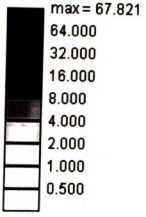

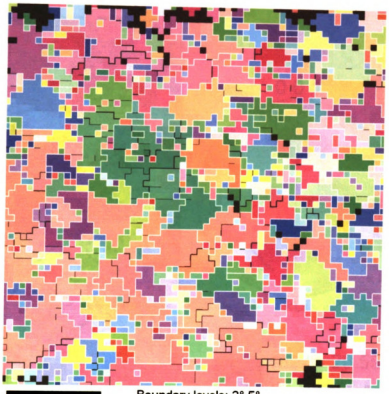
15.00 µm = 15 steps
Boundary levels: 3° 5°
IPF [010]

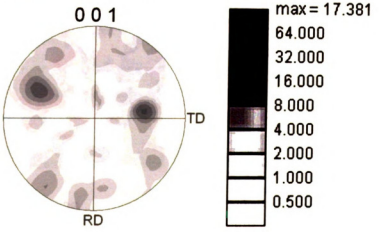
0 0 1
TD
RD
max = 17.381
64.000
32.000
16.000
8.000
4.000
2.000
1.000
0.500

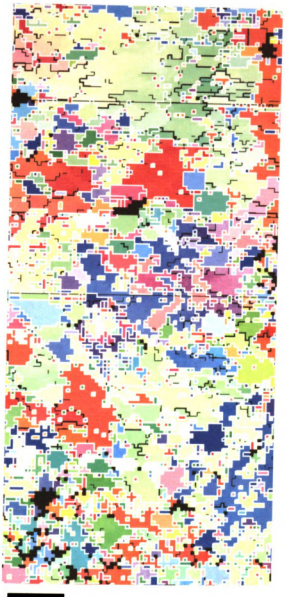

15.00 µm = 15 steps